

**Some pages of this thesis may have been removed for copyright restrictions.**

If you have discovered material in AURA which is unlawful e.g. breaches copyright, (either yours or that of a third party) or any other law, including but not limited to those relating to patent, trademark, confidentiality, data protection, obscenity, defamation, libel, then please read our [Takedown Policy](#) and [contact the service](#) immediately

# **Surface - plasma interactions in GaAs subjected to capacitively coupled RF plasmas**

**Carmen Cristina Surdu-Bob**

Doctor of Philosophy

The University of Aston in Birmingham.

September, 2002

This copy of the thesis has been supplied on condition that anyone who consults it is understood to recognise that its copyright rests with its author and that no quotation from the thesis and no information derived from it may be published without proper acknowledgement.

**Surface - plasma interactions in GaAs  
subjected to capacitively coupled RF plasmas**

Carmen Cristina Surdu-Bob

Doctor of Philosophy

2002

**SUMMARY**

Surface compositional changes in GaAs due to RF plasmas of different gases have been investigated by XPS and etch rates were measured using AFM. Angular Resolved XPS (ARXPS) was also employed for depth analysis of the composition of the surface layers. An important role in this study was determination of oxide thickness using XPS data. The study of surface - plasma interaction was undertaken by correlating results of surface analysis with plasma diagnosis.

Different experiments were designed to accurately measure the BEs associated with the Ga 3d, Ga 2p<sub>3/2</sub> and LMM peaks using XPS analysis and propose identification in terms of the oxides of GaAs. Along with GaAs wafers, some reference compounds such as metallic Ga and Ga<sub>2</sub>O<sub>3</sub> powder were used.

A separate study aiming the identification of the GaAs surface oxides formed on the GaAs surface during and after plasma processing was undertaken.

Surface compositional changes after plasma treatment, prior to surface analysis are considered, with particular reference to the oxides formed in the air on the activated surface. Samples exposed to ambient air for different periods of time and also to pure oxygen were analysed.

Models of surface processes were proposed for explanation of the stoichiometry changes observed with the inert and reactive plasmas used.

In order to help with the understanding of the mechanisms responsible for surface effects during plasma treatment, computer simulation using SRIM code was also undertaken. Based on simulation and experimental results, models of surface phenomena are proposed. Discussion of the experimental and simulated results is made in accordance with current theories and published results of different authors.

The experimental errors introduced by impurities and also by data acquisition and processing are also evaluated.

**KEYWORDS: GaAs, XPS, AFM, inert plasma etching, oxygen plasma etching, hydrogen plasma etching, SRIM**

## ACKNOWLEDGEMENTS

I would like to thank Professor John L. Sullivan for his help, guidance and kindness.

Many thanks to Dr. Sayah Saied for all her help throughout the project.

Special thanks go to Professor Geavit Musa for valuable help on various issues on plasma characterisation and also for constant support.

I am also grateful to George Pearce for technical help and advice.

I would also like to thank Andrew Abbot for his assistance with experimental work.

Special thanks go to Dr. Russell L. Layberry for his help with plasma modelling.

I would also like to thank all of the Surface Science research group for creating a pleasant working atmosphere.

I also thank my family for their constant support.

This work would have not been possible without financial support from Aston University.

To Alexandru, Sebastian and my parents.

## Table of Contents

	Page
<b>Chapter 1. Introduction.....</b>	<b>19</b>
<b>Chapter 2. Theory.....</b>	<b>23</b>
2.1 The GaAs semiconductor.....	23
2.1.1 Introduction.....	23
2.1.1.1 Fabrication of GaAs wafers.....	24
2.1.1.2 Physical parameters of the GaAs material.....	25
2.1.2 GaAs surface oxides.....	26
2.1.2.1 Introduction.....	26
2.1.2.2 Reported binding energies of GaAs oxides.....	27
2.1.2.3 GaAs native oxide.....	30
2.2 RF Plasma.....	30
2.2.1 General characteristics of RF capacitively coupled discharges.....	31
2.2.2 RIE plasmas.....	35
2.2.3 Plasmas of inert gases.....	36
2.2.4 Oxygen plasma.....	39
2.2.5 Hydrogen plasma.....	41
2.2.6 Ar + O <sub>2</sub> plasma.....	42
2.2.7 Ar + H <sub>2</sub> plasma.....	44
2.3 Plasma-induced surface modification.....	43
2.3.1 RIE plasma.....	43
2.3.2 Plasmas of inert gases and inert gas ion bombardment.....	47
2.3.3 Oxygen and mixtures.....	48
2.3.4 Hydrogen and mixtures.....	49
2.3.5 Air exposure after plasma treatment.....	50
2.4 Surface.....	51

	2.4.1	Introduction.....	51
	2.4.2	Surface - plasma interactions.....	52
	2.4.3	The stopping and range of ions in mater- the SRIM code..	59
<b>Chapter 3.</b>		<b>Materials and instrumentation.....</b>	<b>61</b>
	3.1	GaAs wafer.....	61
	3.2	Plasma treatment of GaAs.....	62
	3.2.1	The etching chamber and experimental setup.....	62
		3.2.1.1 Experimental errors.....	64
		3.2.1.1.1 Residual impurities and calculation of standard error.....	64
		3.2.1.1.2 Impurities introduced by gases.....	65
	3.2.2	Langmuir probe.....	66
	3.2.3	Mass/energy analyser.....	66
	3.3	Surface analysis.....	67
	3.3.1	X-ray Photoelectron Spectroscopy (XPS).....	67
		3.3.1.1 Calculation of oxide layer thickness.....	73
		3.3.1.2 Sources of errors in data acquisition and processing.....	74
	3.3.2	Atomic Force Microscopy (AFM).....	74
	3.4	Reference compounds.....	76
	3.4.1	Ga <sub>2</sub> O <sub>3</sub> powder.....	76
	3.4.2	Metallic Ga.....	77
	3.4.3	Boiled GaAs.....	78
<b>Chapter 4.</b>		<b>Experimental results.....</b>	<b>79</b>
	4.1	RF plasma diagnosis.....	79
	4.1.1	Plasma of inert gases: Ar and Ne.....	79
	4.1.2	O <sub>2</sub> plasma.....	84
	4.1.3	Ar + O <sub>2</sub> plasma.....	86
	4.1.4	H <sub>2</sub> plasma.....	88

4.1.5	Ar + H <sub>2</sub> plasma.....	89
4.2	XPS analysis.....	91
4.2.1	Identification of surface oxides of GaAs.....	91
4.2.1.1	Ga <sub>2</sub> O <sub>3</sub> powder.....	91
4.2.1.2	Metallic Ga.....	95
4.2.1.3	Virgin and clean GaAs wafer.....	97
4.2.1.4	Boiled GaAs wafer.....	98
4.2.1.5	The O 2s peak.....	99
4.2.2	Plasma-treated GaAs wafer surfaces.....	100
4.2.2.1	Inert gas plasmas .....	100
4.2.2.1.1	Argon plasma .....	100
4.2.2.1.2	Neon plasma.....	114
4.2.2.3	O <sub>2</sub> plasma.....	116
4.2.2.4	O <sub>2</sub> + Ar plasma.....	121
4.2.2.5	H <sub>2</sub> plasma.....	125
4.2.2.6	Ar + H <sub>2</sub> plasma.....	129
4.2.2.7	O <sub>2</sub> flow.....	134
4.2.2.8	Prolonged exposure to air.....	139
4.2.2.9	Experimental errors.....	140
4.3	AFM analysis.....	141
4.3.1	Topography.....	141
4.3.2	Shape of the etch pit.....	144
4.3.3	Etch rates.....	146
4.3.3.1	Argon plasma.....	146
4.3.3.2	Neon plasma.....	147
4.3.3.3	Oxygen plasma.....	148
4.3.3.4	Ar + O <sub>2</sub> plasma.....	150
4.3.3.5	Hydrogen plasma.....	151
4.3.3.6	Ar + H <sub>2</sub> plasma.....	151
4.4	Modelling of surface-plasma interactions.....	152

	4.4.1	Argon and neon.....	152
	4.4.2	O <sub>2</sub> .....	154
	4.4.3	H <sub>2</sub> .....	157
<b>Chapter 5.</b>		<b>Discussion of results .....</b>	<b>159</b>
5.1		Possible oxidation states on the surface of GaAs wafer.....	159
	5.1.1	The peak at $23.2 \pm 0.2$ eV.....	159
	5.1.2	The peak at $21.6 \pm 0.2$ eV.....	160
	5.1.3	The peak at $20.7 \pm 0.2$ eV.....	160
	5.1.4	The peak at $20.1 \pm 0.2$ eV.....	160
5.2		Virgin and clean GaAs wafer.....	161
5.3		Surface-plasma interactions in GaAs.....	162
	5.3.1	Contamination, sources of oxygen and hydrogen species in the plasma.....	162
	5.3.2	Non-reactive etching of GaAs.....	163
	5.3.2.1	Argon etching.....	163
		5.3.2.1.1 Air exposure after plasma treatment..	163
		5.3.2.1.2 Controlled neutral oxygen exposure after plasma treatment.....	166
		5.3.2.1.3 SRIM results.....	170
		5.3.2.1.4 Summary of results - argon.....	172
	5.3.2.2	Neon etching of GaAs.....	172
		5.3.2.2.1 Summary of results - neon.....	174
	5.3.3	Oxygen etching of GaAs.....	175
		5.3.3.1 Summary of results - oxygen.....	177
	5.3.4	GaAs etching with oxygen-argon plasma.....	177
		5.3.4.1 Summary of results - Ar + O <sub>2</sub> .....	178
	5.3.5	Hydrogen etching of GaAs.....	178
		5.3.5.1 Summary of results - hydrogen.....	180
	5.3.6	Hydrogen - argon plasma etching of GaAs.....	180
		5.3.6.1 Summary of results - Ar + H <sub>2</sub> .....	181

5.3.7	Summary of the overall processes.....	181
5.3.7.1	Physical processes.....	182
5.3.7.2	Chemical processes.....	183
5.3.7.2.1	Surface changes during plasma processing.....	183
5.3.7.2.2	After plasma processing.....	183
<b>Chapter 6.</b>	<b>Conclusions.....</b>	<b>184</b>
6.1	Peak assignment in the XPS of GaAs.....	184
6.2	GaAs surface modification.....	184
6.2.1	Inert-gas plasmas.....	184
6.2.2	Oxygen-containing plasmas.....	185
6.2.3	Hydrogen-containing plasmas.....	185
6.3	Relevance of the work to the general field.....	185
<b>Chapter 7.</b>	<b>Further work.....</b>	<b>187</b>
	<b>References.....</b>	<b>189</b>
	<b>Publications.....</b>	<b>198</b>

## List of Tables

	Page
Table 3.1 Gases used for plasma processing of GaAs.....	63
Table 3.2 As peak fitting.....	69
Table 3.3 Ga peak fitting.....	70
Table 3.4 Duration of etching for each level of argon ion bombardment of Ga <sub>2</sub> O <sub>3</sub> powder.....	76
Table 4.1 BE of the 3d peaks of Ga and As, the Ga and As Auger parameters (AP) and the FWHM intensity for the indicated compounds.....	92
Table 4.2 Surface composition of the reference compounds.....	94
Table 4.3 Surface composition of argon-bombarded Ga <sub>2</sub> O <sub>3</sub> powder at different stages of bombardment.....	94
Table 4.4 Peak positions and FWHM of the thermally evaporated metallic Ga.....	96
Table 4.5 XPS data used for calculation of oxide thickness of the metallic Ga samples. The calculated oxide thickness (d) is also given.....	96
Table 4.6 Calculation of the relative concentration of surface compounds from the total (the fourth column) and from As and Ga regions (the fourth column) respectively for Ar etching, 10 mT, 50 W, 30 min.....	103
Table 4.7 Calculation of the relative concentration of surface compounds from the total (the fourth column) and from As and Ga regions (the fourth column), respectively for Ar etching, 30 mT, 50 W, 30 min.....	105
Table 4.8 Calculation of the relative concentration of surface compounds from the total (the fourth column) and from As and Ga regions (the fourth column), respectively for Ar etching, 50 mT, 50 W, 30 min.....	107
Table 4.9 Calculation of the relative concentration of surface compounds from the total and from As and Ga regions, respectively for Ar etching, 70 mT, 50 W.....	108
Table 4.10 Calculation of the relative concentration of surface compounds from the total (the fourth column) and from As and Ga regions (the fourth column), respectively for Ar etching, 90 mT, 50 W, 30 min.....	110
Table 4.11 Relative concentration of surface compounds and standard deviation calculated for each surface component - errors due to plasma processing.....	140
Table 4.12 Relative concentration of surface compounds and standard deviation calculated for each surface component - errors due to XPS data acquisition.....	141
Table 5.1 Surface composition - virgin GaAs .....	161

## List of Figures

	Page
Figure 1.1 Basic MESFET structure (after Sze [1981]) .....	19
Figure 1.2 Schematic representation of pit shapes made by wet (a) and dry (b) etching ..	21
Figure 2.1 Cross-section of a GaAs MESFET (after Schwierz [2001]) .....	24
Figure 2.2 GaAs crystal structure (after <a href="http://jas2.eng.buffalo.edu/applets/education/solid/unitCell/home.html">http://jas2.eng.buffalo.edu/applets/education/solid/unitCell/home.html</a> ) .....	25
Figure 2.3 Capacitive voltage divider model of bias voltage formation in an asymmetric discharge (after Lieberman [1994]) .....	32
Figure 2.4 Cross-section data for Ar <sup>+</sup> collisions with Ar (after Phelps [1991]) .....	36
Figure 2.5 Variation of relative concentration of ions with power at different pressures in Ar plasma (after Rusu [2001]) .....	37
Figure 2.6 The ionisation cross sections for rare gases as a function of electron energy (after Man [1987]) .....	38
Figure 2.7 Cross sections for resonance charge transfer in Ne <sup>+</sup> on Ne. The keys in the graph represent data reported by different authors (after McDaniel [1964]).....	39
Figure 2.8 Cross sections for formation of a) O <sub>2</sub> <sup>-</sup> and b) O <sup>-</sup> in O <sub>2</sub> (after McDaniel [1964]).....	39
Figure 2.9 Charge transfer cross section for various ions in oxygen (after McDaniel [1964]) .....	40
Figure 2.10 Comparison of a) predicted and b) experimental results for the IEDs at the cathode of an rf oxygen plasma (after Layberry [PhD, 1999]) .....	40
Figure 2.11 Predicted variation of a) ion energy and b) ion flux with pressure (after Layberry [PhD, 1999]) .....	41
Figure 2.12 Variation of measured ion density with pressure (after Layberry [PhD, 1999]).....	41
Figure 2.13 Predicted variation of a) ion energy and b) ion flux with driving potential (after Layberry [PhD, 1999]).....	42
Figure 2.14 Mass spectrum of ions in Ar + 14% O <sub>2</sub> at 100 mT and V <sub>pp</sub> = 200 V (after Olthoff [1995]) .....	43
Figure 2.15 Variation of relative concentration of the species present in Ar + O <sub>2</sub> plasma with power (after Rusu [PhD, 2001]) .....	43
Figure 2.16 Variation of relative concentration of the species present in Ar + O <sub>2</sub> plasma with pressure (after Rusu [PhD, 2001]).....	44
Figure 2.17 Variation of relative concentration with oxygen volume fraction in the plasma of Ar + O <sub>2</sub> mixture (after Olthoff [1995]) .....	44
Figure 2.18 Cross sections for collisions of H <sup>+</sup> with Ar versus laboratory energy (after Phelps [1992]).....	45
Figure 2.19 Variation of the relative concentration of the species present in Ar + H <sub>2</sub> mixture (2.2:22) (after Rusu [PhD, 2001]) .....	45

Figure 2.20 XeF <sub>2</sub> and Ar etching of SiO <sub>2</sub> (after Roth [2001]) .....	46
Figure 2.21 Summary of target processes.....	54
Figure 2.22 Sputtering yield as a function of ion energy (after Roth [2001]) .....	55
Figure 2.23 Variation of sputtering yield, normalized for a surface - binding energy of 1 eV, with ion energy for normal incidence with atomic number Z <sub>1</sub> for a target specie having Z <sub>2</sub> = 70 (after Malherbe [1994]) .....	56
Figure 2.24 Variation of sputtering yield with angle of incidence. The curves represent data of sputtering reported by different authors (after Malherbe [1994]) .....	57
Figure. 3.1 Schematic diagram of the etching chamber.....	63
Figure 3.2 Schematic emission diagram of photoelectric process (top) and the Auger process (bottom), (after Wagner [1979]) .....	67
Figure. 3.3. Simple model of the layered structure of GaAs.....	73
Figure 3.4 The force sensor.....	75
Figure 3.5 Device for thermal evaporation.....	77
Figure 4.1 Variation of V <sub>dc</sub> with pressure in a) Ar and b) Ne plasma.....	80
Figure 4.2 Variation of V <sub>dc</sub> with power in a) Ar and b) Ne RF plasma.....	80
Figure 4.3 Sheath width in a) Ar and b) Ne RF plasma.....	81
Figure 4.4 Photograph of the plasma - cathode sheath region; a) 90 mT, 5 W and b) 90 mT, 150 W (argon).....	81
Figure 4.5 Variation of current density with a) pressure and b) power for Ar and Ne plasmas.....	82
Figure 4.6 a) Number of ions versus ion energy for a number of pressures in the range 20 ÷ 90 mT.....	83
Figure 4.6 b) Number of ions versus ion energy for a number of powers in the range 5 ÷ 200 W.....	83
Figure 4.7 Variation of V <sub>dc</sub> with power for pressures of 10 and 90 mT.....	84
Figure 4.8 Variation of sheath width power at pressures of 10 mT and 90 mT.....	84
Figure 4.9 Photograph of the plasma - cathode sheath region, 90 mT, 150 W (oxygen) ..	85
Figure 4.10 Variation of current density with pressure a) and c) for O <sub>2</sub> <sup>+</sup> ; with power b) and d) for O <sup>+</sup> .....	85
Figure 4.11 Variation of V <sub>dc</sub> with a) pressure and b) power .....	86
Figure 4.11 c) Variation of V <sub>dc</sub> with concentration of O <sub>2</sub> in Ar + O <sub>2</sub> mixture.....	86
Figure 4.12 Photograph of the plasma - cathode sheath, 90 mT, 150 W, a) Ar + 50% O <sub>2</sub> b) Ar + 75% O <sub>2</sub> .....	87
Figure 4.13 Variation of sheath width with pressure a) and b) power in Ar + 70% O <sub>2</sub> mixture.....	87
Figure 4.13 c) Variation of sheath width with O <sub>2</sub> concentration in Ar + O <sub>2</sub> mixture.....	87

Figure 4.14 Variation of $V_{dc}$ with pressure and power (hydrogen).....	88
Figure 4.15 Photograph of the plasma - cathode sheath region, 90 mT, 150 W ( $H_2$ ).....	88
Figure 4.16 Variation of sheath width with pressure at two different powers ( $H_2$ ).....	89
Figure 4.17 Variation of $V_{dc}$ with a) pressure and b) power in Ar + $H_2$ mixture.....	89
Figure 4.17 c) Variation of $V_{dc}$ with concentration of $H_2$ in Ar + $H_2$ mixture.....	90
Figure 4.18 Variation of sheath width with a) pressure and b) power (Ar + $H_2$ ).....	90
Figure 4.18 c) Variation of sheath width with $H_2$ concentration (Ar + $H_2$ ).....	90
Figure 4.19 Photograph of the plasma-cathode sheath, 90 mT, 150 W, a) Ar + 50% $H_2$ , b) Ar + 75% $H_2$ .....	90
Figure 4.20 Ga $2p_{3/2}$ , Ga 3d and Ga LMM spectra of: a) $Ga_2O_3$ powder; b) thermally evaporated metallic Ga; c) as-received metallic Ga.....	93
Figure 4.21 Argon ion bombardment of $Ga_2O_3$ powder.....	95
Figure 4.22 Ga $2p_{3/2}$ , Ga 3d and Ga LMM spectra of cleaned GaAs wafer.....	97
Figure 4.23 ARXPS analysis of a) virgin and b) cleaned samples.....	98
Figure 4.24 The 3d fit of GaAs a) before boiling; b) after boiling; c) Ga LMM of boiled wafer. For a better illustration of the increase of the element at 21.6 eV, this peak was shaded.....	98
Figure 4.25 Normalized spectra of Ga 3d and O 1s for: a) GaAs wafer etched in Ar plasma 5W, 90 mT; b) GaAs wafer etched in Ar plasma 200 W, 90 mT.....	99
Figure 4.25 (continued) Normalized spectra of Ga 3d and O 1s for: c) clean GaAs wafer; d) GaAs wafer etched in Ar plasma 150 W, 10 mT.....	100
Figure 4.26 XPS spectrum for GaAs exposed to Ar plasma, 10 mT, 50 W, duration of etching 30 min.....	101
Figure 4.27 Peak Table and Constraints Table for the As 3d region of all the XPS spectra acquired in this work.....	101
Figure 4.28 Best fit obtained for the As 3d region for the sample etched in Ar plasma, 10 mT, 50 W, 30 min.....	101
Figure 4.29 Peak Table and Constraints Table for the Ga 3d region of all the XPS spectra acquired in this work.....	102
Figure 4.30 Best fit obtained for the Ga 3d region for the sample etched in Ar plasma, 10 mT, 50 W, 30 min.....	102
Figure 4.31 XPS spectrum for Ar etching of GaAs at 30 mT, 50 W, 30 min.....	103
Figure 4.32 Best fit obtained for the As 3d region for the sample etched in Ar plasma, 30 mT, 50 W, 30 min.....	104
Figure 4.33 Best fit obtained for the Ga 3d region for the sample etched in Ar plasma, 30 mT, 50 W, 30 min.....	104
Figure 4.34 XPS spectrum for Ar etching of GaAs at 50 mT, 50 W, 30 min.....	105

Figure 4.35 Best fit obtained for the As 3d region for the sample etched in Ar plasma, 50 mT, 50 W, 30 min.....	106
Figure 4.36 Best fit obtained for the Ga 3d region for the sample etched in Ar plasma, 50 mT, 50 W, 30 min.....	106
Figure 4.37 XPS spectrum for Ar etching of GaAs at 70 mT, 50 W, 30 min.....	107
Figure 4.38 Best fit obtained for the As 3d region for the sample etched in Ar plasma, 70 mT, 50 W, 30 min.....	108
Figure 4.39 Best fit obtained for the Ga 3d region for the sample etched in Ar plasma, 70 mT, 50 W, 30 min.....	108
Figure 4.40 XPS spectrum for Ar etching of GaAs at 90 mT, 50 W, 30 min.....	109
Figure 4.41 Best fit obtained for the As 3d region for the sample etched in Ar plasma, 90 mT, 50 W, 30 min.....	109
Figure 4.42 Best fit obtained for the Ga 3d region for the sample etched in Ar plasma, 90 mT, 50 W, 30 min.....	110
Figure 4.43 Variation with pressure of the relative percentages of: a), c) all the GaAs surface components and b), d) Ga components only (argon plasma, etch time: 30 min, at indicated powers).....	111
Figure 4.44 Variation with power of the relative percentages of: a),c) all the GaAs surface components and b),d) Ga components only (Ar plasma, 30 min, at indicated pressures).....	112
Figure 4.45 Variation of oxide layer thickness with a) pressure and b) power (argon plasma, 30 min).....	113
Figure 4.46 Variation with depth of the relative percentages of: a), c) all the GaAs surface components and b), d) Ga components only (Ar plasma, 30 min,). Estimated depth was calculated with: $d = \lambda \cos\theta$ , where $\lambda = 26 \text{ \AA}$ .....	113
Figure 4.47 Variation with pressure of the relative percentage of a) all the GaAs surface components; b) Ga components only (neon plasma at 150 W, etch time: 30 min).....	114
Figure 4.48 Variation with power of the relative percentage of a) all the GaAs surface components; b) Ga components only (neon plasma at 150 W, etch time: 30 min).....	114
Figure 4.49 Variation of oxide layer thickness with a) pressure and b) power (Ne plasma).....	115
Figure 4.50 Variation with depth of the relative percentages of: a) all the GaAs surface components and b) Ga components only (Ne plasma, etch time: 30 min, at indicated pressures and powers).....	115
Figure 4.51 Variation with depth of the relative percentages of: a) all the surface components and b) Ga components only (Ne plasma, 30 min). Estimated depth was calculated with: $d = \lambda \cos\theta$ , where $\lambda = 26 \text{ \AA}$ .....	116

Figure 4.52 XPS spectra for oxygen etching of GaAs at 10 mT, 30 min at different powers.....	116
Figure 4.53 Variation with pressure of the relative percentages of: a), c) all the GaAs surface components and b), d) Ga components only (O <sub>2</sub> plasma, etch time: 30 min, at indicated powers).....	117
Figure 4.54 Variation with power of the relative percentages of: a), c) all the GaAs surface components and b), d) Ga components only (oxygen plasma, etch time: 30 min, at indicated pressures).....	118
Figure 4.55 Variation of oxide thickness with a) pressure and b) power - etching with oxygen plasma.....	118
Figure 4.56 Variation with depth of the relative percentages of: a), c) all the GaAs surface components and b), d) Ga components only (O <sub>2</sub> plasma, etch time: 30 min, at indicated pressures and powers).....	119
Figure 4.57 Variation with depth of the relative percentages of: a), c) all the surface components and b), d) Ga components only (O <sub>2</sub> plasma, 30 min). Estimated depth was calculated with: $d = \lambda \cos\theta$ , where $\lambda = 26 \text{ \AA}$ .....	120
Figure 4.58 XPS spectra for Ar+75%O <sub>2</sub> etching at 90 mT, 30 min at different powers...	121
Figure 4.59 Variation with pressure of the relative percentages of: a), c) all the GaAs surface components and b), d) Ga components only (Ar + 75%O <sub>2</sub> plasma, etch time: 30 min, at indicated pressures and powers).....	122
Figure 4.61 Variation with concentration of the relative percentages of: a) all the GaAs surface components and b) Ga components only (Ar + 75%O <sub>2</sub> plasma, etch time: 30 min, at 90 mT, 150 W).....	123
Figure 4.62 Variation of oxide thickness with a) pressure, b) power and c) O <sub>2</sub> concentration.....	123
Figure 4.63 Variation with depth of the relative percentages of: a), c) all the GaAs surface components and b), d) Ga components only (oxygen plasma, etch time: 30 min, at indicated pressures, powers and concentrations). Estimated depth was calculated with: $d = \lambda \cos\theta$ , where $\lambda = 26 \text{ \AA}$ .....	124
Figure 4.64 XPS spectra for H <sub>2</sub> etching of GaAs at 90 mT, 30 min at different powers..	125
Figure 4.65 Variation with pressure of the relative percentages of: a), c) all the GaAs surface components and b), d) Ga components only (hydrogen plasma, etch time: 30 min, at indicated powers).....	126
Figure 4.66 Variation with power of the relative percentages of: a) all the GaAs surface components and b) Ga components only (H <sub>2</sub> plasma, at 10 mT).....	126
Figure 4.67 Variation of the oxide thickness with a) pressure and b) power (H <sub>2</sub> plasma).....	127
Figure 4.68 Variation with depth of the relative percentages of: a), c), e) all the GaAs surface components and b), d), f) Ga components only (hydrogen plasma, etch time: 30 min, at indicated pressures and powers). Estimated depth was	

calculated with: $d = \lambda \cos\theta$ , where $\lambda = 26 \text{ \AA}$ .....	128
Figure 4.69 XPS spectra for Ar + 75% $\text{H}_2$ etching at 90 mT, 30 min at different powers.....	129
Figure 4.70 Variation with pressure of the relative percentages of: a), c) all the GaAs surface components and b), d) Ga components only (Ar + 75% $\text{H}_2$ plasma, etch time: 30 min, at indicated powers).....	130
Figure 4.71 Variation with power of the relative percentages of: a) all the GaAs surface components and b) Ga components only (Ar + 75% $\text{H}_2$ plasma, etch time: 30 min, at indicated pressures).....	130
Figure 4.72 Variation with $\text{H}_2$ concentration of the relative percentages of: a), c) all the GaAs surface components and b), d) Ga components only (Ar + $\text{H}_2$ plasma, etch time: 30 min, at indicated pressures and powers).....	131
Figure 4.73 Variation of oxide thickness with a) pressure, b) power and c), d) $\text{H}_2$ concentration.....	132
Figure 4.74 Variation with depth of the relative percentages of: a) all the GaAs surface components and b) Ga components only (Ar+5.5% $\text{H}_2$ plasma, at 90mT, 150W). Estimated depth was calculated with: $d = \lambda \cos\theta$ , where $\lambda = 26 \text{ \AA}$ .....	133
Figure 4.75 Variation with depth of the relative percentages of: a), c) all the GaAs surface components and b), d) Ga components only (Ar + 75% $\text{H}_2$ plasma). Estimated depth was calculated with: $d = \lambda \cos\theta$ , where $\lambda = 26 \text{ \AA}$ .....	133
Figure 4.76 Variation with pressure of the relative percentages of: a), c) all the GaAs surface components and b), d) Ga components only (Ar plasma, etch time: 30 min, under indicated conditions).....	134
Figure 4.77 Variation with power of the relative percentages of: a), c) all the GaAs surface components and b), d) Ga components only (Ar plasma, etch time: 30 min, under indicated conditions).....	135
Figure 4.78 Variation with $\text{O}_2$ dose of the relative percentages of: a), c), e) all the GaAs surface components and b), d), f) Ga components only (Ar plasma, etch time: 30 min, under indicated conditions).....	136
Figure 4.79 Variation of oxide thickness with a) pressure, b) power and oxygen dose at c) 90 mT, 5 W; d) 90 mT, 150 W; e) 10 mT, 5 W.....	137
Figure 4.80 Variation with depth of the relative percentages of: a), c), e) all the GaAs surface components and b), d), f) Ga components only (argon plasma, etch time: 30 min then $\text{O}_2$ exposure dose 48, at indicated pressures and powers). Estimated depth was calculated with: $d = \lambda \cos\theta$ , where $\lambda = 26 \text{ \AA}$ .....	138
Figure 4.81 Variation with time of exposure to air after plasma treatment of the relative percentages of: a), all the GaAs surface components and b) Ga components ..	139
Figure 4.82 Variation with depth of the relative percentages of all the GaAs surface components. Argon plasma, etch time: 30 min then air exposure for a) 20 min b) 13 months. Estimated depth was calculated with: $d = \lambda \cos\theta$ , where $\lambda = 26 \text{ \AA}$ .....	139
Figure 4.83 Variation of oxide thickness with time after Ar plasma treatment.....	140

Figure 4.84 Topography and roughness for the virgin GaAs sample.....	142
Figure 4.85 Topography and roughness for the 75% Ar + 25% H <sub>2</sub> plasma treated GaAs at 90 mT, 150 W, 30 min.....	142
Figure 4.86 Topography and roughness for the 50% Ar + 50% H <sub>2</sub> plasma treated GaAs at 90 mT, 150 W, 30 min.....	142
Figure 4.87 Topography and roughness for the 25% Ar + 75% H <sub>2</sub> plasma treated GaAs at 90 mT, 150 W, 30 min.....	143
Figure 4.88 Topography and roughness for the 25% Ar + 75% H <sub>2</sub> plasma treated GaAs at 30 mT, 150 W, 30 min.....	143
Figure 4.89 Topography and roughness for the H <sub>2</sub> plasma treated GaAs at 10 mT, 150 W, 30 min.....	143
Figure 4.90 Topography and roughness for the H <sub>2</sub> plasma treated GaAs at 90 mT, 200 W, 30 min.....	144
Figure 4.91 AFM image for determination of etch depth (Ar etching of GaAs at 150 W, 90 mT, 30 min).....	144
Figure 4.92 Zoomed 3D view of Figure 4.91.....	145
Figure 4.93 Profile of the etch pit for Ar plasma treatment of GaAs for 30 min, at 50 W and a) 10 mT; b) 30 mT.....	145
Figure 4.94 Profile of the etch pit for Ar plasma treatment of GaAs for 30 min, at 100 W and a) 10 mT; b) 90 mT.....	145
Figure 4.95 Profile of the etch pit for Ar plasma treatment of GaAs for 30 min, at 150 W and a) 30 mT; b) 90 mT.....	146
Figure 4.97 Variation of the etch rate with pressure at different powers (Ar plasma).....	147
Figure 4.98 Variation of sputtering yield with a) pressure and b) power (Ar plasma).....	147
Figure 4.99 Variation of etch depth with a) pressure and b) power (neon plasma).....	148
Figure 4.100 Variation of sputtering yield with a) pressure and b) power (Ne plasma).....	148
Figure 4.101 Variation of sputtering yield for O <sub>2</sub> <sup>+</sup> and O <sup>+</sup> with a), b) pressure and c), d) power (O <sub>2</sub> plasma).....	149
Figure 4.102 Variation of etch depth with a) pressure, b) power and c) O <sub>2</sub> concentration (Ar + O <sub>2</sub> plasma).....	150
Figure 4.103 Variation of etch depth with a) pressure, b) power and c) concentration (Ar+H <sub>2</sub> ).....	151
Figure 4.104 Predicted dependence of vacancy depth and depth of ion implantation on ion energy for a) argon and b) neon ion bombardment.....	152
Figure 4.105 Calculated variation of sputtering yield versus ion energy for a) Ar and b) Ne bombardment.....	153
Figure 4.106 Predicted spatial distribution of ions and atoms in the target after collision for a) argon and b) neon for 100 bombarding ions (red dots represent penetrated	

ions, green dots show displaced target atoms).....	154
Figure 4.108 Predicted dependence of vacancy depth and depth of ion implantation on ion energy for oxygen ion bombardment.....	155
Figure 4.109 Calculated variation of sputtering yield versus ion energy for oxygen ion bombardment.....	155
Figure 4.111 Predicted spatial distribution of ions and atoms in the target after collision for 100 oxygen bombarding ions.....	156
Figure 4.112 Predicted dependence of vacancy depth and depth of ion implantation on ion energy for hydrogen ion bombardment.....	157
Figure 4.113 Predicted spatial distribution of ions and atoms in the target after collision for 100 hydrogen bombarding ions.....	158
Figure 5.1 Layered structure of the surface of a virgin sample.....	161
Figure 5.2 Qualitative representation of the variation of the plasma strength with power and pressure for argon plasma.....	164
Figure 5.3 Model of surface layered structure at dose 1, for calculation of oxide thickness during plasma processing (denoted by x in the figure).....	168
Figure 5.4 Layered structure for Ar plasma treated GaAs at 100 W for 30 min and a) 10mT, b) 90 mT.....	170
Figure 5.5 Replot of Figure 4.104 a).....	171
Figure 5.6 Replot of Figure 4.104 b).....	172
Figure 5.7 Comparative profile of surface damage for Ar and Ne for the same ion energy. The dark areas represent the damage.....	173
Figure 5.8 Qualitative representation of the variation of the plasma strength with power and pressure for neon plasma. ....	173
Figure 5.9 Layered structure for Ne plasma treated GaAs at 150 W, for 30 min and a) 10 mT, b) 80 mT.....	174
Figure 5.10 Layered structure for O <sub>2</sub> plasma treated GaAs at 150 W, for 30 min and a) 10 mT; b) 90 mT.....	175
Figure 5.11 Layered structure for O <sub>2</sub> plasma treated GaAs at 5 W, for 30 min and a) 10 mT; b) 90 mT.....	177
Figure 5.12 Layered structure for Ar + O <sub>2</sub> plasma treated GaAs for 30 min at 150 W, 90 mT and a) 94.5% Ar + 5.5% O <sub>2</sub> ; b) 89.8% Ar + 10.2% O <sub>2</sub> .....	178
Figure 5.13 Layer structure for H <sub>2</sub> plasma treated GaAs at 200 W, 10 mT, 30 min.....	179
Figure 5.14 Layer structure for Ar + 75% H <sub>2</sub> plasma treated GaAs 150 W, 10 mT.....	181

# Chapter 1. Introduction

GaAs is one of the most important compound semiconductors, used either as a substrate for epitaxial growth or for direct ion-implantation [Schwierz, 2001], [Liu, 2002]. It has a key role in modern high speed and microwave devices. Sophisticated devices like high performance transistors, lasers, and far IR photodetectors [Bertolucci et al, 1998], [Ayzenshtat et al, 2001] have GaAs as base material [Takuo, 1985], [Stuart, 1983].

The progress in electronic device fabrication is driven by the ability to increase integration and performance and decrease cost. With device dimensions of the order of a micron, quantum mechanical effects become important. To overcome these problems, new fabrication techniques need to be developed. In order to achieve this, surface phenomena involved in the current fabrication processes should be better understood.

The first integrated circuit (IC) was made in 1958 and since then microelectronics technology has continuously been improved. It is possible now to fabricate millions of transistors on a single wafer.

The scaling law states that by decreasing transistor physical dimensions and operating voltage all by the same factor  $S$  ( $S$  being a factor less than 1) then transistor area will reduce by a factor of square  $S$ , gate delay will reduce by a factor  $S$  and power per gate transition will reduce by a factor of cubic  $S$ . Also, operating voltage must scale with gate length and oxide thickness to maintain reliability and to reduce power [Bohr, 1996].

The structure of an electronic device created on the wafer is given in Figure 1.1, where the dimensions  $a$  and  $L$  are known as the channel thickness and the physical gate length, respectively.

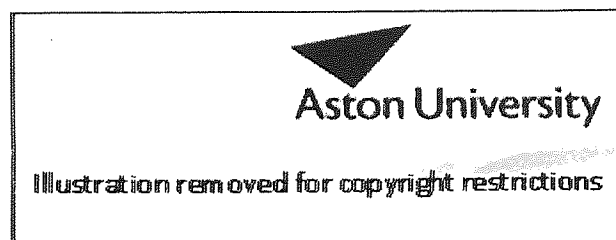


Figure 1.1 Basic MESFET structure (after Sze [48])

The fabrication process of this FET from the base wafer to the finished device consists of the following steps: cleaning, oxidation, deposition, doping, photolithography, patterning and deposition of metal for electrical contacts. For all these steps there are several techniques which can be used and which are under continuous development. The doping process, for example, can be done by diffusion or ion implantation. The deposition process can be realized by cathodic sputtering of the material to be deposited or vacuum

evaporation. The patterning step implies the transfer of the desired pattern into the underlying layer and it is accomplished by etching. Each of these techniques carries disadvantages and depending on the type of application the final substrate will be involved with, a certain technique can be better than another.

As this work is involved with etching, different aspects of this process will be presented in the following paragraphs.

Several general types of etching are known: wet chemical etching, plasma etching, ion beam milling or sputter etching, ion-assisted chemical etching, laser- or photo-assisted etching, and electron-assisted etching.

*Plasma etching* employs a plasma to generate reactive etchants and the semiconductor is bombarded with low energy ions (a few hundreds eV). Plasma is a partially ionized gas consisting of positive and negative charges. The degree of ionization of most of the usual plasmas used for semiconductor processing is typically  $10^{-4}$ . A comprehensive review of plasma characteristics is given by Chapman [1980].

*Ion beam etching* relies on physical momentum transfer process to remove material; no chemistry is involved [Aoyama et al, 1995]. Currently, ion-assisted chemical etching is the most important technique for GaAs-based device fabrication. It includes a number of techniques like: reactive ion etching (RIE) [Bond et al, 1998], [Singh et al, 1998], electron-cyclotron resonance RIE (ECR RIE), reactive ion beam etching (RIBE), ion-beam-assisted etching (IBAE), chemically-assisted-ion-beam etching (CAIBE), radical-beam-ion-beam etching (RBIBE). All these techniques involve both energetic ion bombardment and chemically reactive etchants.

*Laser or other high intensity photon etching* produce enhanced etch rates by thermal heating.

There are important characteristics to consider in selecting the best etching process for a specific application: etch rate, profile (anisotropy and morphology), selectivity and damage [Lee et al, 2002]. Wet chemical processing produces rapid etch rates, compositional selectivity and little damage. They also promote isotropic etching [Kumar et al, 1997]. In general, ion-based processes employ physical sputtering which causes damage, but anisotropic etching can be obtained. Also, low ion energies are essential to lessen the effect of channelling as described by Rahman [2001]. Therefore, a compromise has to be made between anisotropy and damage minimization in process selection.

Despite the advances in plasma-based etch technology, wet etching still remains important [Tereshchenko et al, 1999]. Wet etching is generally based on oxidation of GaAs and subsequent dissolution of the oxidized products by either acids or bases.

In wet etching, the chemical etches in an isotropic manner determining the formation of spherical etch pits (Figure 1.2 a)) which can extend to the areas under the masks. This process is a limit to the extent of miniaturisation. This leads to mask undercutting and poor pattern definition.

Wet etching is still used for some GaAs microwave and InP optical devices. The reason for this is that plasma etching causes "damage" to the material surface: contamination, crystalline defects and change of surface composition.

In inert ion etching, the surface layers are bombarded with chemically inert energetic ions. The energy used for ion etching of microstructures is usually in the range (0.5 - 5) keV. The upper limit of ion energies is determined by the maximum surface damage permitted. It is known [Raizer et al, 1995] that only 5% of the ion energy is usually spent for sputtering, the rest being spent for heating the target, surface damage, ion incorporation, secondary electron emission etc.

Ion chemical etching is more efficient because not only physical sputtering takes place; active ions induce chemical reactions on the surface, the resulting compounds being in most of the cases, volatile.

In dry etching, chemical reactions are thermally activated at temperatures of several tens of thousand degrees [Christmann, 1991]. The need of obtaining smaller and smaller devices required the development of new techniques of etching: etching with plasmas. The removal of surface atoms is made by the plasma constituents resulting vertical wall profiles (Figure 1.2 b)).

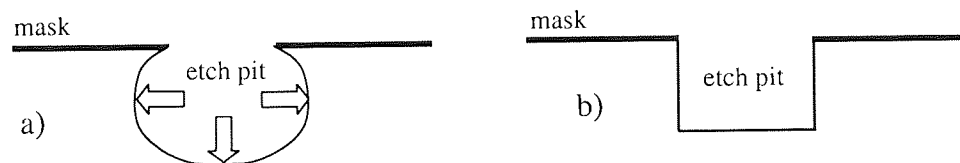


Figure 1.2 Schematic representation of pit shapes made by wet (a) and dry (b) etching

The present work is concerned with studying the etching step of the electronic device fabrication. One of the most commonly used methods for etching of semiconductors for applications in industry is Reactive Ion Etching (RIE). The reactive nature of the etch chemistry in RIE is important, as the enhanced etch rates lessen exposure time to the bombarding flux and remove damage quickly as it is created. This method provides a combination of physical and chemical processes on the surface of semiconductors [Lee et al, 2001], [Hahn et al, 1999].

For a better understanding of the phenomena taking place when the semiconductor is exposed to reactive etchants, a separation of the physics and chemistry involved is necessary. Therefore, etching with plasmas of non-reactive gases, like inert gases, is required. Even when etching with inert gases, the physical processes are not the only process taking place; surface oxidation process are also encountered. Therefore, for understanding the etching mechanisms with inert gases, a study of the GaAs surface oxidation was essential.

In the current literature, oxidation of GaAs is the subject of few papers, most of them reporting contradictory results [Wolan et al, 1998], [Passeggi et al, 1999], [Allwood et al, 2000].

It is hoped this work will provide useful information on surface plasma processing of GaAs for research projects as well as for semiconductor industry. An attempt was made here to identify, characterise and obtain controlled surface oxides of GaAs. Surface-plasma interactions of GaAs subjected to plasmas of inert gases, oxygen, hydrogen and their mixture with argon have also been investigated and a model of the main surface phenomena is proposed.

## Chapter 2. Theory

Surface - plasma interactions is a major subject in research and technology. The wide range of materials to be etched and the gases and techniques to be used makes the study very complex and very difficult to generalize [Choudhury, 1991]. Different theories and experiments are proposed in the current literature, some of them controversial, for explaining the various mechanisms that may be encountered when exposing different surfaces to plasmas.

In this work, surface - plasma interactions are studied using RF plasmas of pure argon, neon, oxygen, hydrogen and mixtures to etch the GaAs surface.

In the first section of this chapter some general information about the GaAs semiconductor is given. A literature review on RF plasma diagnosis and the results of reported surface-plasma interactions in GaAs are also presented in this chapter. The last section summarises the theory of surface-plasma interactions.

### 2.1 The GaAs semiconductor

#### 2.1.1 Introduction

Apart from the elemental semiconductors Si and Ge, semiconductor compound materials made from the elements of groups II to VI are also in use in industry:

group IV; SiC, SiGe

group III - V: GaAs, InP

group II-VI: ZnSe, CdTe

Group II-VI compounds have wide applications in IR detectors and window material.

III-V compound semiconductors have attracted much interest in recent years as the substrate material for electronic device fabrication because of their high electron mobility that allows the development of very high frequency devices (of the order of GHz).

GaAs materials have been investigated for 50 years [Brozel, 1996]. Since then, the efforts of scientists around the world have made possible the use of this material in industry. Research on GaAs continues due to the high complexity of the device fabrication process [Morgan, 1985], [Chester 1, 1993], [Nahlah, 1998], [Schmuki, 1999].

GaAs has advantages over silicon for certain applications mainly because it has a direct band gap (from D.C. to > 40 GHz) and higher carrier mobility both at low and high field

conditions which make it more suitable for high speed transistors [Lefebvre, 1997], [Lamontagne et al, 1995]. The high electron mobility transistor (HEMT) was the first device to use AsGaAs/GaAs heterostructure.

To date, 0.12  $\mu\text{m}$  gate length GaAs MESFET has been obtained (Figure 2.1 after [Schwierz, 2001]).

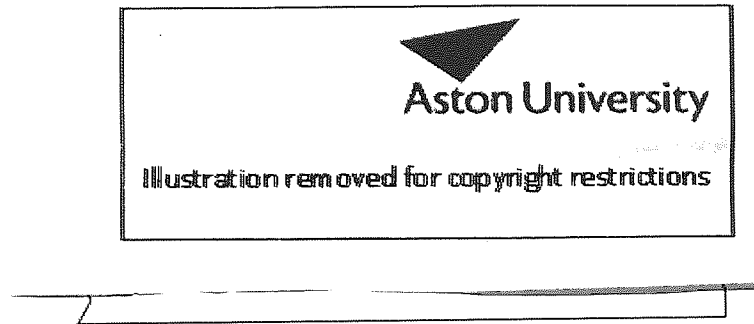


Figure 2.1 Cross-section of a GaAs MESFET (after [Schwierz, 2001])

Unlike silicon, whose oxide passivates the silicon surface leaving a low density of interface states, the native oxide of GaAs does not passivate the surface. The interface between the substrate GaAs and its native oxide, which is a mixture of different gallium and arsenic oxides, presents defects which affect the performance of electronic devices. Increased leakage currents in FETs and photodiodes are caused by these interface states [Aydil et al, 1993].

### 2.1.1.1 Fabrication of GaAs wafers

Bulk GaAs material can be obtained by different techniques which are used depending on the type of application the material is used for [Gatos, 1980]. A comprehensive review is given in [Brozel, 1996]. A general overview of growth techniques is presented in the following.

*Liquid encapsulated Czochralski (LEC) growth* is successfully used although some limitation is experienced in the growth of long crystals.

*Horizontal and vertical Bridgeman growth* of GaAs has been employed for optical devices such as laser diodes and LEDs. The main advantage over the LEC method is that it has a lower dislocation density due to a lower temperature gradient.

*Epitaxial growth* of GaAs is used for building complex device structures because it allows the formation of high quality layers with controlled thickness and conductivity as well as abrupt interfaces. This method consists of growing a material with monocrystalline

structure by deposition on a specially prepared substrate. Epitaxy is possible by several different techniques: molecular beam epitaxy (MBE) where elemental vapours are directed onto the substrate in ultra high vacuum, metal organic chemical vapour deposition (MOCVD) where gas phase organic and hydride compounds are pyrolyzed at the hot substrate surface, and liquid phase epitaxy (LPE) where a supersaturated solution is solidified over a cooler substrate [Croydon, 1981].

### 2.1.1.2 Physical parameters of the GaAs material

A listing of the important parameters of GaAs is given here.

The average interatomic space, or the distance from the centres of the atoms: 2.45 Å.

The density of pure GaAs is 5.31 g/cm<sup>3</sup>.

The crystal structure of GaAs is zincblende (shown in Figure 2.2).

In a GaAs crystal, the diffusion coefficients of Ga and As are very low at room temperature. Diffusivity for Ga in GaAs at room temperature is  $2.73 \times 10^{-54} \text{ m}^2 / \text{sec}$  and for As is  $1.8 \times 10^{-60} \text{ m}^2 / \text{sec}$ . If the atoms of GaAs receive energy (e.g. via ion bombardment), diffusion of Ga is expected to be higher than that of As.

The dielectric constant is: 13.1.

Lattice parameter:  $a_0 = 0.5654 \text{ nm}$ .

Energy gap at 300°C: 1.424 eV.

Vapour pressure: 1 Pa at 900°C.

Another parameter that may play an important role in diffusion of atoms within the lattice is the ionisation energy. For Ga and As, the value of this parameter is 5.99 and 9.81 eV, respectively. Ionisation energy is important in electronic stopping of bombarding ions in solids, as will be shown later.

Illustration removed for copyright restrictions

*Figure 2.2 GaAs crystal structure (after <http://jas2.eng.buffalo.edu/applets/education/solid/unitCell/home.html>)*

A correct value for surface binding energy is difficult to estimate, especially for compound systems. For elemental substrates this value is calculated using experimental data of heats of sublimation, by extrapolation to 273 K. For compounds, the correct value is uncertain due to the differential behaviour of the component atoms with temperature, sputtering etc. Surface binding energy for individual surface atoms may vary with its relative position, bonds. Thus, using different approximations, values of surface binding energy of 1.26 eV for As, 3.075 eV for Ga [Pan et al, 1997] and 2.82 eV for As, 2.876 eV for Ga [Malherbe, 1994] have been proposed. This subject is discussed in more detail by Wei [1995]. Also, a wealth of information on physical properties of gallium arsenide can be found in [Brozel, 1996].

## **2.1.2 GaAs surface oxides**

### **2.1.2.1 Introduction**

The GaAs oxides are very important in semiconductor and opto-electronic applications. The oxide films have an important influence on passivation of semiconductor surfaces, in mask diffusion and in preparation of wafers for epitaxy. There are several requirements for the oxide to be used in fabrication of electronic devices. The oxide should form a stable, uniform, protective coating on the substrate and also its dielectric properties must be suitable for the required device operation. The dielectric material must protect the surface of GaAs from degradation by chemicals present in the fabrication process of the device.

Although the thermal oxide of silicon was successfully used as passivating dielectric layer

on silicon, similar technique had no success in the case of GaAs. Therefore, other dielectrics grown on GaAs substrates are under investigation for improved electrical properties. Nevertheless, a better understanding of GaAs oxides would probably lead to a new era of GaAs based electronic devices. It is, therefore, of great importance to understand both the nature of oxides present on the surface [Thurmond et al, 1980] and the mechanisms by which these oxides can be removed for certain applications.

In the current literature the characterization of surface oxides of GaAs is still an open issue [Cossu et al, 1992], [Passeggi et al, 1998], [Breeze et al, 1980]. Following is an overview of the reported studies of GaAs surface oxides.

### 2.1.2.2 Reported binding energies of GaAs oxides

Considering the chemistry of Ga [Sheka et al, 1966], Ga forms the oxide GaO, the suboxide Ga<sub>2</sub>O, and the sesquioxide Ga<sub>2</sub>O<sub>3</sub>.

GaO has been detected only by spectroscopic means because it decomposes into Ga<sub>2</sub>O<sub>3</sub> and Ga<sub>2</sub>O.

Ga<sub>2</sub>O is stable in dry air and can be obtained by reduction of Ga<sub>2</sub>O<sub>3</sub> with hydrogen [Cochran, 1982]. The density of Ga<sub>2</sub>O is 4.77 g/cm<sup>3</sup> [Sheka et al, 1966].

Ga<sub>2</sub>O<sub>3</sub> is the most thermodynamical stable of the GaAs phases. Ga<sub>2</sub>O<sub>3</sub> is also the most dense oxide (density: 5.94 g/cm<sup>3</sup>) formed on GaAs, even more dense than the GaAs itself. The beta modification is formed above 650° C. Appreciable decomposition or volatilization is not observed up to its melting point (1740° C). Ga hydroxides are also possible and known are: GaOH, GaO(OH), Ga<sub>2</sub>O(OH)<sub>4</sub> and Ga(OH)<sub>3</sub>, GaOH.

The most important As oxides that can be formed on the GaAs wafer surface are:

As<sub>2</sub>O<sub>3</sub> - density 3.86 g/cm<sup>3</sup>, heat of decomposition 103 kcal, soluble in water [Quagliano, 2000].

As<sub>2</sub>O<sub>5</sub> - density 4.32 g/cm<sup>3</sup>, heat of decomposition 63.8 kcal, soluble in water.

There is much disagreement in the current literature concerning the correct assignment of the photoelectron energies and identification of the oxidation states to which these energies belong. In addition, not all oxidation states have been unequivocally identified; for example, the only Ga oxide which is covered by NIST (National Institute of Standards and Technology) XPS standard reference database is Ga<sub>2</sub>O<sub>3</sub> [<http://srdata.nist.gov/xps>]. Also, a large number of workers do not give the energy position of the photoelectron lines belonging to various oxidation states, but only give the energy-separation values between the photoelectron line of the bulk and that of the oxides [Gourier et al, 1985], [Vasquez et al, 1983], [Mihailova et al, 1997], [Massies, 1985], [Tone et al, 1992], [Masuda et al, 1995].

The majority of workers have concentrated on the Ga and As 3d lines, but both the 2p<sub>3/2</sub> and the LMM Auger lines are required if the surface is to be properly characterized. Accurate identification of 2p<sub>3/2</sub> peaks is as important, since these peaks represent smaller sampling depths and hence are more sensitive to surface modification than 3d peaks. This has not been generally recognized as can be seen from the NIST XPS database where there are few entries for 2p<sub>3/2</sub> lines of GaAs as opposed to the large number for the 3d lines. In addition the identification and quantification of the components using the 2p<sub>3/2</sub> line could be more accurate than using the 3d region due firstly to the simple line shape of the 2p<sub>3/2</sub> peak, which is only a single photoelectron line, not an unresolved spin-orbit doublet. Secondly, the Ga 2p<sub>3/2</sub> and As 2p<sub>3/2</sub> peaks have the highest intensities in XPS spectra of GaAs, which statistically give more accurate identification of the peaks in a shorter collection time.

In the XPS spectra, the As oxide components may be more easily identified and with greater accuracy than those of Ga, since chemical shifts of oxidized As are considerably greater than those of oxidized Ga. This together with the fact that the predominant oxides are those usually of Ga, is why a considerable amount of work is currently employed to determine different chemical states of Ga.

Although much work has been conducted in this area, in many references the peaks have different assignments [Ballutand et al, 1995], [Mikhailov et al, 1992], [Senemaud et al, 1985]. One of the peaks that has been detected and not consistently identified is the peak having a binding energy of around 23.2 eV. Different assignments are proposed for this peak in the current literature. Albanesi [Albanesi, 1992] suggested that 23.2 eV is the binding energy of a chemical state of Ga, Schwartz [Schwartz, 1979] proposed that this peak is the result of an "intrinsic photoemission process", whereas others assigned the peak to O 2s [Bresse, 1994], [Leyral et al, 1981].

Further, there is some uncertainty on the assignment of the peak around 21.6 eV in the literature. The main chemical state proposed for this peak is the hydroxide Ga(OH)<sub>3</sub> [Vasquez et al, 1983], [Massies, 1985]. The other possible compound is GaAsO<sub>4</sub>, but with this there is a corresponding peak at 45.2 eV in the As 3d region [Wolan et al, 1998], [Albanesi et al, 1992], [Schwartz et al, 1979], [Massies, 1985].

There is general agreement about the assignment of the peak with a BE of around 20.6 eV, where most authors agree that it originates from Ga<sub>2</sub>O<sub>3</sub> [Aydil et al, 1993], [Shin et al, 1991], [Beerbom et al, 2000].

Of the various oxidation states of Ga, there is more uncertainty about formation of Ga<sub>2</sub>O than the others. Obtaining Ga<sub>2</sub>O by hydrogen treatment of Ga<sub>2</sub>O<sub>3</sub>, with C 1s as internal reference at 284.6 eV, Carli [1994] reported a binding energy of 19.0 eV for Ga<sub>2</sub>O. Chemical shifts between Ga<sub>2</sub>O and Ga<sub>2</sub>O<sub>3</sub> of 0.4 eV or 0.5 eV were also noted by Aydil [1993] and Ballutand [1995], respectively. The chemical shift of about 1 eV from the bulk

observed by other authors was attributed to  $\text{Ga}_2\text{O}_3$ , rather than to  $\text{Ga}_2\text{O}$  [Lu et al, 1993], [Yokoyama et al, 1985], [Kikawa et al, 1994]. Also, Cuberes [1992] suggested a new Ga oxide ( $\text{GaO}_x$ ) from comparison of the Auger spectra of different thermally treated GaAs samples. The mechanism of  $\text{GaO}_x$  formation is not explained in the paper, but the fact that its structure was different from that of  $\text{Ga}_2\text{O}_3$  has been outlined by another interesting experiment made by the same authors. Nevertheless, the shift value 0.9 eV relative to the B.E. for bulk emission corresponds to  $\text{Ga}_2\text{O}$  rather than  $\text{Ga}_2\text{O}_3$ . A number of authors [Hollinger et al, 1994], [Chester, 1993], [Pearson, 1994] suggest that the GaAs surface contains a single-phase oxide instead of having separated well-defined oxidation states. For example, using thermal oxidation of n-type (100)GaAs, Hollinger [1994] showed that the presence of  $\text{As}^{3+}$ ,  $\text{As}^{5+}$  and  $\text{Ga}^{3+}$  peaks is correlated to a single-phase oxide made up of a mixture of different molecular units (such as  $\text{AsO}_3$ ,  $\text{AsO}_6$ ,  $\text{GaO}_4$ ,  $\text{GaO}_6$ ).

In the identification of photoelectron lines ( $2p_{3/2}$  and  $3d$ ) of bulk Ga(-As), a large number of workers do not report binding energies. Instead, they use the line as a reference for energy assignment of peaks for other chemical compounds, and quote the energy difference between them for identification of these compounds.

Using an appropriate reference peak for calibration of the BE scale is essential for obtaining reliable values of peak positions. The standard procedure of using the C 1s line as calibrant for this system gives erroneous results [Bertrand, 1981], [Li et al, 1996]. This problem has been identified by many workers in the field who chose to use a different reference material. Deng [2000] and Debiemme [1993] used Au  $4f_{7/2}$  as a calibrant. Iwami [1987] reported the BE of the Ga  $3d$  Ga(-As) peak as  $19.2 \pm 0.2$  eV from the energy difference between the Ga  $3d$  peak and the top of the valence band.

The binding energy ranges for the GaAs components found in current literature and NIST XPS data base are: (23 - 24) eV for O 2s, (20.2 - 21.6) eV for  $\text{Ga}(\text{OH})_3$  or  $\text{GaAsO}_4$ , (19.7 - 20.9) eV assigned to  $\text{Ga}_2\text{O}_3$ , (19.6 - 20.1) eV for  $\text{Ga}_2\text{O}$ , (18.5 - 19.8) eV for Ga(-As) and (18.2 - 18.9) eV for elemental Ga. There are few measurements of the Ga  $2p_{3/2}$  line, but the corresponding ranges are: (1116.4 - 1118.1) eV for elemental Ga, (1116.4 - 1117) eV for Ga-As and (1116.9 - 1118.9) eV for  $\text{Ga}_2\text{O}_3$ . The overlap in these ranges leads to obvious problems in accurate identification [Ghidaoui et al, 2002]. No Ga  $2p_{3/2}$  data appear to have been reported for  $\text{Ga}_2\text{O}$ .

There is less dispute in the case of the As oxides. In the As  $3d$  region, the following BEs have been reported: (40.7 - 41.2) eV for As(-Ga), (41.6 - 42) eV for As metal, (44 - 44.9) eV for  $\text{As}_2\text{O}_3$  and (45.2 - 46) eV for  $\text{As}_2\text{O}_5$ . The As  $2p_{3/2}$  BEs are (1322.7 - 1323) eV for As(-Ga), (1323.2 - 1323.8) eV for As-metal, (1325.8 - 1327.3) eV for  $\text{As}_2\text{O}_3$  and (1327.7 - 1328) eV for  $\text{As}_2\text{O}_5$ .

### 2.1.2.3 GaAs native oxide

Barrett [1990] used glancing angle X-ray absorption spectroscopy to elucidate the local structure around Ga and As atoms in the oxide of polished GaAs(100) wafer. They reported an oxide layer thickness of 7 - 9 Å and a surface which was As depleted. Their opinion is that the presence of a sequence of ordered layers of chemically defined oxides is unlikely, since 3 - 4 monolayers of an oxygen rich phase are found at the surface. The surface is more likely to consist of a random microscopic oxide comprising tetrahedral and octahedral sites.

According to Massies [1985], storing a virgin sample in deionized water resulted in a strongly arsenic-deficient oxidized phase. They found that the oxide thickness increased with time spent in deionized water (the growth rate: 15 Å per hour). This fact also implies that the surface of a virgin sample will suffer compositional changes upon exposure to ambient air due to the presence of water. Also, rinsing the sample in running deionized water after etching did not produce a chemically stable oxide film on the surface. In the same paper, it is also shown that the surface oxidation can be avoided by handling the sample under an inert atmosphere. Ageing of GaAs surface stored under a variety of conditions was studied by Allwood [2002].

## 2.2 RF Plasma

RF plasma reactors are used for a large range of applications, both for commercial production and for laboratory research. They are used in thin film deposition for microelectronic circuits, etching, for plasma assisted surface catalysis and polymerization, and to promote different surface chemical reactions [Stuart, 1983], [Kaminsky, 1976]. RF plasmas are also used to modify the surface of materials exposed to a plasma, for changing adhesion, wettability or antistatic properties of the surface of materials.

RF etching systems for surface treatment were developed because of the impossibility of using DC systems for etching insulating targets. This is because of the build up of positive charge on their surface. The employment of a high frequency alternating potential permits periodic neutralization of the target surface, allowing insulating materials to be processed.

RF plasmas are far more efficient in transferring the power from the supply into the plasma than the dc systems. Also, RF plasmas produce much lower energy ions at the cathode than the dc ones, resulting in a reduction of surface damage of the sample [Liu, 1990].

Surface changes depend on the target sputtering yield and thus on the energy of bombarding ions. Due to collisions of ions with plasma constituents, ion energy is influenced by the gas pressure in the chamber and the applied voltage. The control of all the parameters is the main problem of the etching process. The energy and fluxes of ions

striking the surface are therefore important in studying the etching process. RF discharges can be subdivided into inductive and capacitive discharges.

An effort has been made here to collect reported data which are of the greatest interest for a good characterization of plasmas used in this work for surface treatment of GaAs. This information will be used for discussion of results of the surface analysis in Chapter 6.

### **2.2.1 General characteristics of RF capacitively coupled discharges**

Many different frequencies of driving potential have been studied but, because of interference with communications, the 13.56 MHz frequency is used in industry, although with better screening technology some systems using other frequencies (e.g. 100 kHz, 90 MHz) are now being introduced onto the market. The cathode is almost always capacitively coupled [Raizer, 1995]. Additional inductive or microwave couplings are often applied to increase ion density without increasing ion energy. In this work, an asymmetric capacitively coupled RF discharge was employed.

The complete self-consistent model of such a discharge is quite complicated, even in the simplest plane-parallel geometry. This leads to various simplifying assumptions (or models), as will be shown in the following paragraphs.

In asymmetric RF discharges, the dc voltage between the plasma and the driven electrode is larger than the dc voltage between the plasma and the grounded electrode. This can be seen from a model of the rf voltage drop across the two sheaths connecting the driven electrode to ground, as shown in Figure 2.3. In this figure, the dc voltages are taken between the plasma and the electrodes. Since the voltage drops across the sheaths are inversely proportional to the sheath capacitances (Lieberman [1994]), the sheath with the smaller area has a smaller capacitance and therefore a larger voltage drop. This fact is very important in industry because the power can be used more economically by driving it mostly at the electrode where the samples are processed, e.g. at the powered electrode (also named cathode).

Illustration removed for copyright restrictions

*Figure 2.3 Capacitive voltage divider model of bias voltage formation in an asymmetric discharge (after Lieberman [1994])*

The time variation of the plasma potential is driven by the cathode potential. In the positive part of the cycle, the electrons bombard the cathode, the breakdown of the sheath occurs and the plasma potential increases. In the other part of the cycle, the plasma potential is given by the floating potential. Therefore, in an RF plasma, the plasma potential is variable, changing with alternating field.

The time varying potential at the cathode can be described by

$$V_C(t) = V_{dc} + V_0 \sin(\omega t + \phi) \quad (3)$$

where  $V_{dc}$  is the cathode dc self bias,  $V_{dc} < 0$ , generated due to the difference in ion and electron mobilities within the plasma and  $V_0$  is the driving potential [1999].

The maximum positive potential of the cathode is given by  $V^+ = V_{dc} + V_0$  where  $V^+ > 0$  and the most negative potential is given by  $V^- = V_{dc} - V_0$  where  $V^- \ll 0$ .

Secondary electrons are emitted at the impact of an electron or ion with the electrode surface. The probability of electron emission by collisions of ions is independent of the ion energy because the time taken for the process to occur is much less than the time taken for the surface impact. Electron emission probability from the walls due to electronic impact depends strongly on incident energy of electrons.

Secondary electrons help sustain the discharge. They gain energy either in the sheath or in the plasma bulk and cause ionizations, depending on the cross section of the process. Both types of electrons cause ionizations in the sheath or at its edge. It is therefore expected that the number density of ions throughout the plasma will be higher than that at the electrodes.

In the plasma bulk, the number of electrons and ions are equal, conserving the neutrality condition of the plasma. In the sheath, the number of ions exceeds the number of electrons, resulting in a positive space charge. Theoretical and experimental investigations

in the current literature showed a maximum yield of ions at the sheath edge [Kushner, 1985].

### ***The RF sheath***

RF sheaths separate electrodes from the plasma body. They strongly influence the external electrical and plasma characteristics in capacitively driven RF discharges. The physical processes in the RF sheaths influence the surface reactions that occur in the plasma processing reactor. Many models have been proposed to predict RF sheath characteristics [Godyak et al, 1993], [Lieberman, 1988], [Turner, 1998].

The light ions cross the sheath in only one or two RF cycles whereas the heavier ions need more cycles to arrive at the cathode. Therefore, ions at the electrode acquire an energy dependent upon both their initial velocities on crossing the plasma - sheath boundary and the phase and therefore the extent of the sheath at the time. The resultant ion energy has a saddle like structure with an average energy given by the average sheath potential and a peak width given by the ion mass, sheath width and RF frequency.

The effective RF sheath width ( $S$ ) is difficult to measure due to the fact that the sheath is diffuse at the plasma edge. The visible sheath width is taken to be the distance between the RF electrode and the point of maximum plasma brightness, but this introduces errors since no accurate measurements of the plasma brightness can be performed. A more reasonable way to find  $S$  is to determine the point of maximum contrast in luminosity which corresponds to a sharp fall in the electron density [Layberry, 1999].

Depending on the processes taking place in the sheath, two different sheath regimes are distinguished: collisionless and collisional regime. Following is a description of the models to predict the electrical properties of RF sheaths [Lieberman, 1988].

#### **a) Collisionless sheath**

For low pressures ( $p < 0.01$  mbar) the ions pass the sheath without colliding. Their energy is determined by the voltage drop between the plasma potential and the electrode potential ( $V_s$ ). In this case, the ion flux is constant and ion flux density satisfies Poisson's equation whose integration gives the well known Child-Langmuir law [Godyak, 1993]. Using this equation, the mean sheath thickness can be written as:

$$S = \lambda_D \left( \frac{q V_s}{k T} \right)^{3/4} \quad (1)$$

where  $\lambda_D$  is the Debye length,  $q$  is the ion charge,  $k$  is Boltzmann constant.

The thermal energy of the ion at the bulk-sheath interface is usually small compared to

sheath potential. If ions have no collisions in the sheath, their velocity is directed completely perpendicular to the surface.

## b) Collisional sheath

At higher pressures, collisions within the sheath take place. Thus, ions are scattered and slowed down. With collisions, different processes may take place: charge transfer of an ion to a neutral, dissociation, electron attachment etc. Therefore, determination of ion energies is more complicated than in the case of collisionless sheath and cross sections of the processes must be taken into account by modelling.

Determination of ion distribution functions was the aim of several investigations over the past few years. Many models have been proposed to predict electrical properties of RF sheaths and relate them to dynamics of particles. An overview of current models for ion and electron energy distributions is given by Layberry [PhD, 1999]. The thesis also includes computer modelling of RF capacitively coupled methane/hydrogen plasmas which was extended and used in this work for argon plasma. The input parameters were experimentally determined  $V_{dc}$ , floating potential ( $V_f$ ), sheath width and also pressure and number of incident ions.

In general, for capacitively coupled plasmas, where most of the applied voltage falls across the sheath, the initial ion thermal energy is negligible and momentum transfer scattering is necessary to produce significant ion incident angles. Although ions are scattered in the sheath, most of their energy is still directed towards the electrode since the sheath electric field accelerates them towards the surface.

More useful information on ion energies and densities at the cathode would be obtained by placing a mass/energy analyser behind the cathode and sample particles from the sheath through an aperture in the cathode. This experimental arrangement was used by many authors and a review article on this subject is presented by Olthoff [1995]. Additional information about the plasma constituents, like ion mean free path, current density and ion sputtering yield can be experimentally determined as following.

### *Mean free path ( $\lambda$ )*

The mean free path of the ions in the plasma can be approximately calculated using the formula:

$$\lambda = \frac{RT}{\sigma P N_A} \quad (2)$$

where  $R$  is the general gas constant 8.31 J/mol K,  $T = 300$  K,  $\sigma$  is the total cross section,  $P$  is the gas pressure,  $N_A$  is Avogadro number  $6.022 \times 10^{23}$  mol<sup>-1</sup>.

This formula was employed here for the plasmas of the following gases: argon, neon, oxygen. As shown later in this chapter, the main process taking place in the sheath of these plasmas is charge transfer. Its cross section was approximated to have a constant value in the range of ion energies 100 - 500 eV. Thus, values of  $5 \times 10^{-19} \text{ m}^2$  for Ar,  $2 \times 10^{-19} \text{ m}^2$  for Ne,  $1.3 \times 10^{-19} \text{ m}^2$  for  $\text{O}^+$  and  $1.9 \times 10^{-19} \text{ m}^2$  for  $\text{O}_2^+$  were used (see the following section where cross sections versus ion energy are presented for these gases).

### ***Current density ( $J_i$ )***

Current density  $J_i$  at the cathode may be calculated from experimental data using the Child-Langmuir law [Godyak et al, 1993]:

$$J_i^{1/2} = \frac{1.07}{S^{5/4}} \epsilon_0^{1/2} \left( \frac{e \lambda}{M} \right)^{1/4} V_{dc}^{3/4}$$

where  $S$  is the measured sheath width,  $M$  is the ion mass,  $e$  is the ion charge,  $\lambda$  is the ionic mean free path (see above),  $V_{dc}$  is the experimentally measured DC bias.

### ***Ion sputtering yield ( $Y$ )***

The experimental ion sputtering yield,  $Y$ , can easily be evaluated using the following formula:

$$Y = \frac{er \times N_{GaAs}}{\phi}$$

where  $N_{GaAs} = 5 \times 10^{22} \text{ atoms/cm}^3$ ,  $er$  is the measured etch rate and  $\phi$  is the ion flux density.

The spatial distribution of excited states in radio frequency electrical gas discharges have been observed to be dynamic functions of plasma parameters: gas mixture, pressure and applied voltage [Rauf, 1997]. Obviously, the detailed etching mechanisms are different for different gases. Following is a brief review of plasma characteristics for the gases used in this work.

## **2.2.2 RIE plasmas**

In industry, the usual etchant for GaAs is  $\text{CH}_4/\text{H}_2$  plasmas. These plasmas are very complex and accurate information of the type of ions present and their energies is very difficult to obtain. Collisional processes in methane (and mixtures) were experimentally investigated by many authors [Tosi, 1995], [Ando, 1998], [Naito, 1995], [Vodjdani, 1987], [Kuypers, 1988]. Computer codes were also generated to reveal variation of ion energies and fluxes with gas type, pressure and RF power [Layberry, PhD, 1999].

Furthermore, the surface reactions induced by these ions are complicated. Therefore, a separation of chemical effects from physical effects is necessary for a better understanding of these complex processes. For this purpose, plasmas of inert gases and mixtures with hydrogen and oxygen were employed in this work.

### 2.2.3 Plasmas of inert gases

#### *Argon plasma*

Collision cross sections were used in this work to calculate ion density and sputtering yield (as shown earlier in this chapter). These cross sections also provide the basis of modelling of electrical discharge in weakly ionized Ar.

A compilation of collision cross sections of  $\text{Ar}^+$  with Ar is given by Phelps [1991] (Figure 2.4). In the diagram,  $Q_m$  is momentum transfer (or scattering),  $Q_{CT}$  is charge transfer,  $Q_{UV}$  is the cross section for excitation of the UV radiation emitted by the resonance states of Ar,  $Q(e)$  is the electron production (or ionization cross section for  $\text{Ar}^+$ ) and  $Q(811)$  and  $Q(488)$  are Ar excitation lines (the numbers in parenthesis denote the wavelength in nm). In the energy range of interest (a few tens eV to a few hundreds eV), only momentum transfer and charge transfer are high-probability events.

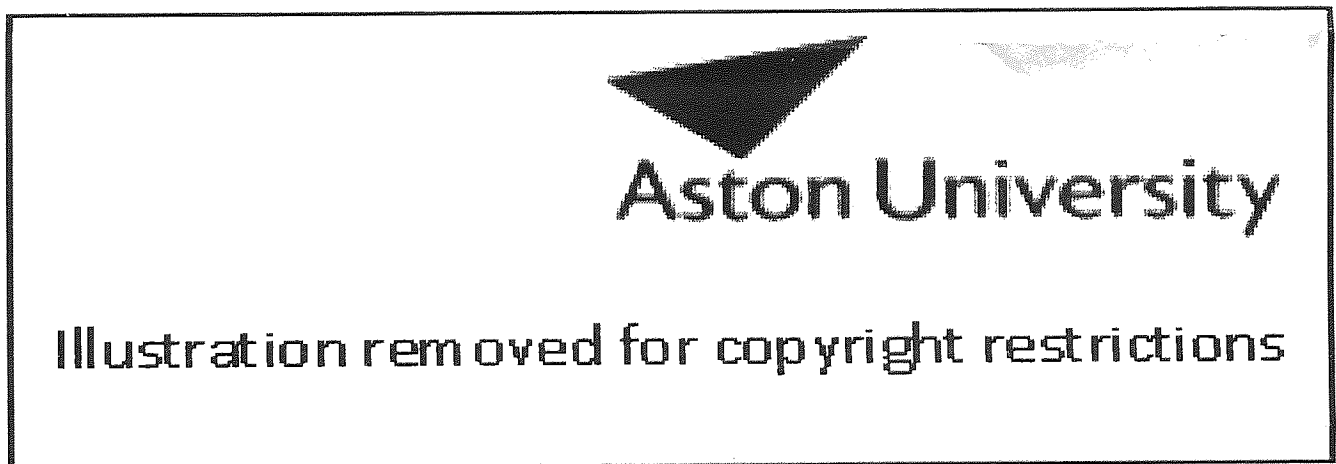


Figure 2.4 Cross-section data for  $\text{Ar}^+$  collisions with Ar (after Phelps [1991])

Based on the two cross sections mentioned above, a computer model of RF capacitively

coupled plasmas realised by Layberry [1999] was used in this work for determination of ion-energy distributions in different plasma conditions.

The model consisted of a Monte Carlo code which followed electrons and ions through the plasma and sheath whilst taking account of collisions with background gas molecules. The ionisation profile output from the electron module was used as input for the ionic module. Using this code, the variation of ion distribution energies with power and pressure for argon plasma were calculated and are presented in Chapter 4.

Argon plasma has been intensively studied by many authors [Kushner, 1985], [Snijkers et al, 1993], [Rauf 1997], [Wild, 1991], [Ventzek et al, 1994]. In RF capacitively coupled argon plasmas, the following ions were found:  $\text{Ar}^+$ ,  $\text{ArH}^+$  and  $\text{Ar}^{++}$  [Rusu, PhD, 2001]. The major ion formed in the plasma at any power - pressure combination is reported to be  $\text{Ar}^+$ . The  $\text{ArH}^+$  ions are believed to be formed due to the presence of  $\text{H}_2\text{O}$  in the plasma chamber. A decrease of the relative concentration of each ion with pressure was observed, as shown in Figure 2.5. With power, an increase of the relative concentration of all ions in the plasma is also observed.

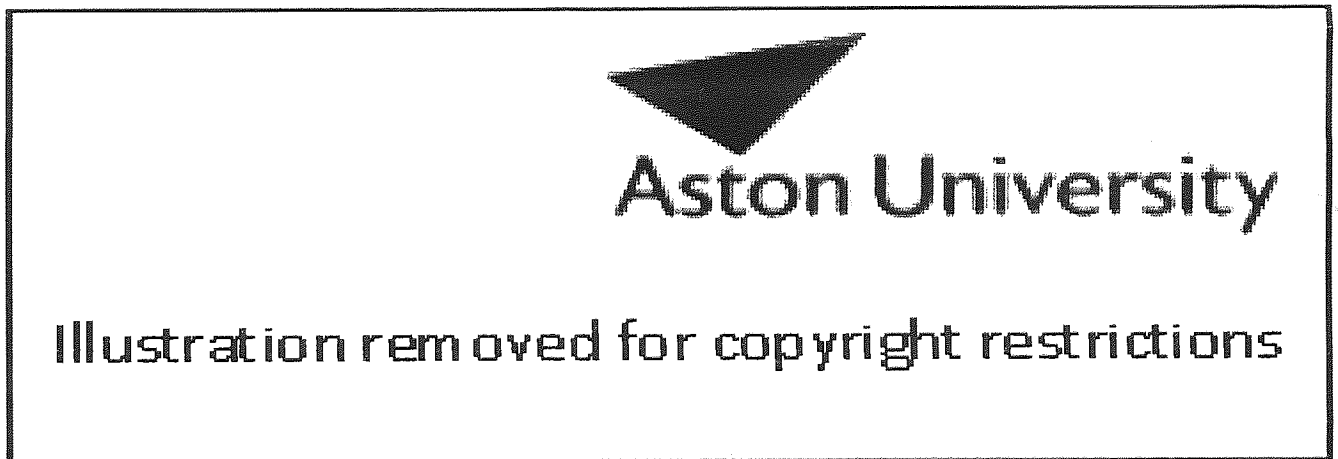


*Figure 2.5 Variation of relative concentration of ions with power at different pressures in Ar plasma (after Rusu [PhD, 2001])*

Other workers also reported that the dominant ion was the parent ion of the feed gas (e.g.  $\text{Ar}^+$  in argon) with minor ions contributing less than 10% to the total ion current [Rauf,

1997].

### *Neon plasma*

Research on diagnosis of capacitively coupled RF neon plasma in the current literature is very scarce. Analogies with argon plasma and plasmas of other rare gases may be useful.

Measurements of electron impact ionisation of rare-gas ions (Figure 2.6) [Man et al, 1987] show that the magnitude of cross sections increases with increasing atomic number along the group. This fact is in agreement with the expectations of decreasing ionization energy of the outer electrons with increasing atomic number of the element. In the paper mentioned above, analogy of Ne and Ar is presented. Thus, similar behaviour of ion energy and density with RF power and gas pressure for Ne and Ar plasmas is assumed to take place but a more abrupt dependence in the case of argon is expected.

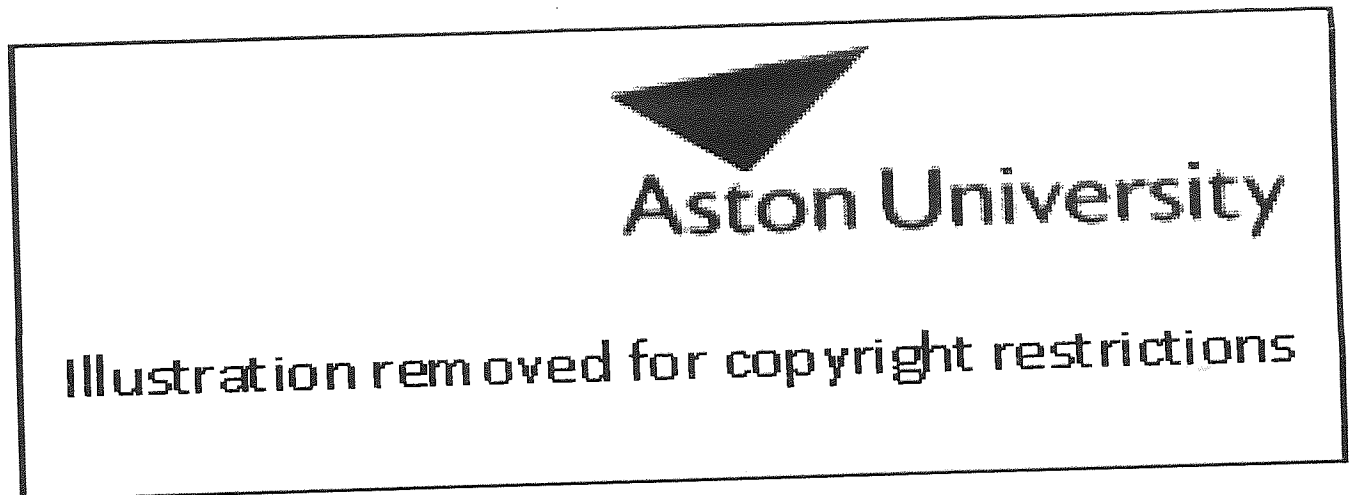


*Figure 2.6 The ionisation cross sections for rare gases as a function of electron energy (after Man [1987])*

Argon is much more efficient at slowing down electrons than Ne [Christophorou et al, 1979]. For neon plasmas charge transfer is also the most important process, as in the case of argon. The cross section associated with this process is presented in Figure 2.7 [McDaniel, 1964].

Illustration removed for copyright restrictions

*Figure 2.7 Cross sections for resonant charge transfer in  $Ne^+$  on  $Ne$ . The lines in the graph represent data reported by different authors (after McDaniel [1964])*

#### 2.2.4 Oxygen plasma

RF discharges in electronegative gases are also of interest for industry, especially in mixtures with an electropositive gas. In an oxygen plasma, negative  $O^-$  and  $O_2^-$  and also positive  $O^+$  and  $O_2^+$  ions are formed. Cross sections for formation of  $O^-$  and  $O_2^-$  are high (see Figure 2.8) and these ions form the majority of ions in the bulk plasma. Due to the fact that the cathode is "seen" negatively charged by the negative ions, they never arrive at the cathode. Therefore, they are of no interest for the present study.

Illustration removed for copyright restrictions

*Figure 2.8 Cross sections for formation of a)  $O_2^-$  and b)  $O^-$  in  $O_2$  (after McDaniel [1964])*

Charge transfer cross sections for  $O_2^+$  and  $O^+$  in molecular oxygen are given in Figure 2.9 [McDaniel, 1964].

Illustration removed for copyright restrictions

Ion energy  $\sqrt{eV}$

Figure 2.9 Charge transfer cross section for various ions in oxygen (after McDaniel [1964])

Models of the processes taking place in an oxygen plasma are also presented by Janes [1992]. They believe that charge exchange collisions creating low-energy  $O^+$  ions are improbable and elastic scattering of  $O^+$  at thermal  $O_2$  is the dominant collision process responsible for the moderation of ion impact energies in their IEDs. Dissociative ionization is assumed to occur, also. They also reported that with increasing  $V_{dc}$  the high energy peaks slowly vanish. This is interpreted as being caused by a higher scattering probability of high energy  $O^+$  in the sheath.

Meichsner *et. al.* [1998] also investigated an oxygen plasma formed in an RF capacitively coupled system, similar to that used in this work and reported that  $O_2^+$  ion energies increase with power and decrease with pressure. Similar results were presented by Wild [1991].

In Figure 2.10, the ion energy distribution at 150 W and 10 mT (equivalent to a dc bias of 488 V) is presented.



Figure 2.10 Comparison of a) predicted and b) experimental results for the IEDs at the cathode of an rf oxygen plasma (after Layberry [PhD, 1999])

## 2.2.5 Hydrogen plasma

Predicted average energies and flux distributions of  $H^+$ ,  $H_2^+$  and  $H_3^+$  with pressure presented by Layberry [PhD, 1999] are given in Figure 2.11. Also, Langmuir probe measurements of ion density in hydrogen plasmas at 50 W and 150 W with pressure are given in Figure 2.12.

### *Reported types of ions in $H_2$ plasmas*

Three ionic species,  $H^+$ ,  $H_2^+$  and  $H_3^+$  are formed in a pure hydrogen plasma [Layberry, PhD, 1999]. The variation of their flux and density with pressure and power is presented in the following paragraphs.

### *Reported pressure dependence*



Figure 2.11 Predicted variation of a) ion energy and b) ion flux with pressure (after Layberry [PhD, 1999])

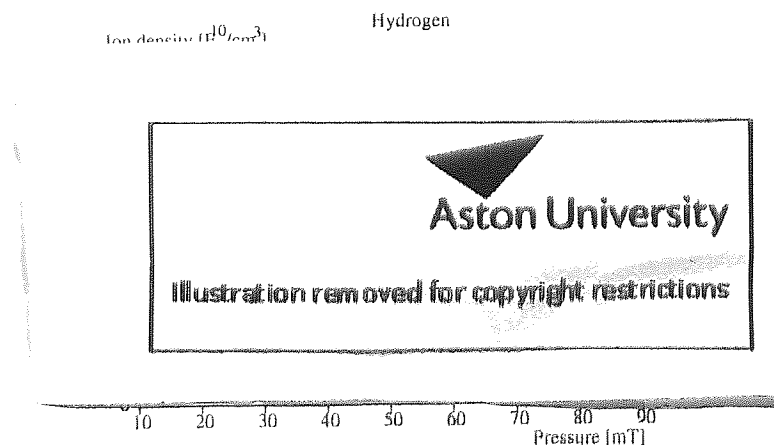


Figure 2.12 Variation of measured ion density with pressure (after Layberry [PhD, 1999]). The lines join the data points to lead the eye.

### *Reported power dependence*

With increasing RF power and consequently driving potential, the ion energies of all hydrogen species increased (Figure 2.13 a)). It is interesting to note that only the relative concentration of  $H_2^+$  increased with driving potential (Figure 2.13 b)).

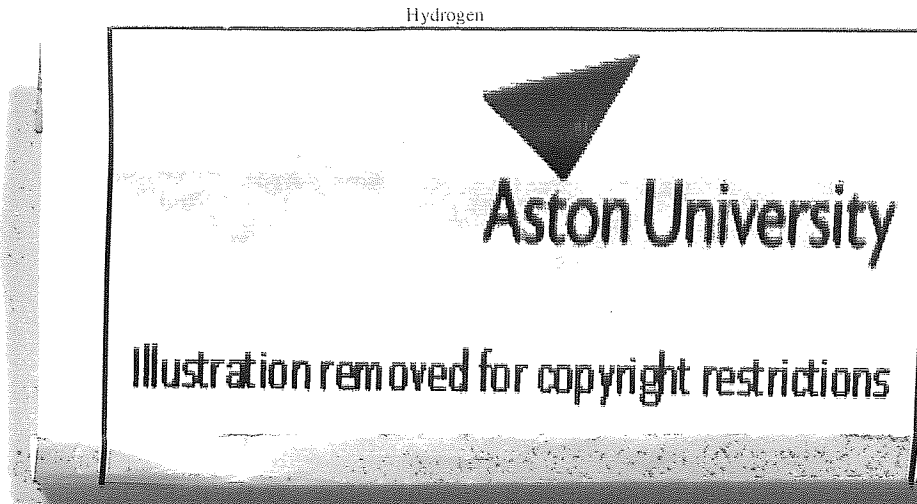


Figure 2.13 Predicted variation of a) ion energy and b) ion flux with driving potential (after Layberry [PhD, 1999])

### **2.2.6 Ar + O<sub>2</sub> plasma**

In dry etching, the addition of certain gases significantly changes the activation energy of the reaction. In Ar + O<sub>2</sub> mixtures, addition of O<sub>2</sub> was found only to decrease the excited Ar density due to quenching of Ar\* by O<sub>2</sub> and O [Rauf, 1997]. Due to the fact that O<sub>2</sub> is an electron attaching gas, an important loss of electrons was observed.

### *Reported types of ions in Ar + O<sub>2</sub> plasmas*

The relative concentration of ions formed in an Ar + 14% O<sub>2</sub> plasma reported by Olthoff *et. al.* [1995] is presented in Figure 2.14. As it can be observed in this figure, Ar<sup>+</sup> and O<sub>2</sub><sup>+</sup> are the major ions present in the plasma of the mixture, as in the case of pure argon and pure oxygen plasmas. Very similar results were reported by Rusu [2001] for an Ar + 10% O<sub>2</sub> plasma and by Flesch [1990], also.



Illustration removed for copyright restrictions

Figure 2.14 Mass spectrum of ions in Ar + 14% O<sub>2</sub> at 100 mT and V<sub>pp</sub> = 200 V (after Olthoff [1995])

#### *Reported power dependence*

In Figure 2.15 variation of the relative concentration of the species present in the plasma with power is given. As it can be observed, the formation of O<sub>2</sub><sup>+</sup> and O<sup>+</sup> ions in the plasma has a fast increase with increasing power whereas formation of Ar<sup>+</sup> ions tends to saturate at about 30 W. With pressure, a depletion of the concentration of all species was observed, except for that of O<sub>2</sub><sup>+</sup> which remained constant.



Illustration removed for copyright restrictions

Figure 2.15 Variation of relative concentration of the species present in Ar + O<sub>2</sub> plasma with power (after Rusu [PhD, 2001])

#### *Reported pressure dependence*

In Figure 2.16, pressure dependence of the relative concentration of active species in the plasma of Ar + O<sub>2</sub> mixture is presented. With increasing pressure, a decrease of the relative concentration of all plasma species is observed.

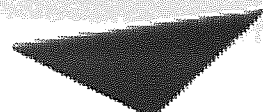


Illustration removed for copyright restrictions

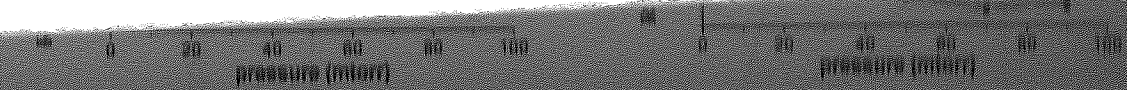


Figure 2.16 Variation of relative concentration of the species present in Ar + O<sub>2</sub> plasma with pressure (after Rusu [PhD, 2001])

**Reported dependence on concentration**

Figure 2.17 shows the variation of relative concentration of the ions present in Ar + O<sub>2</sub> plasma with increasing concentration of O<sub>2</sub> in the mixture.

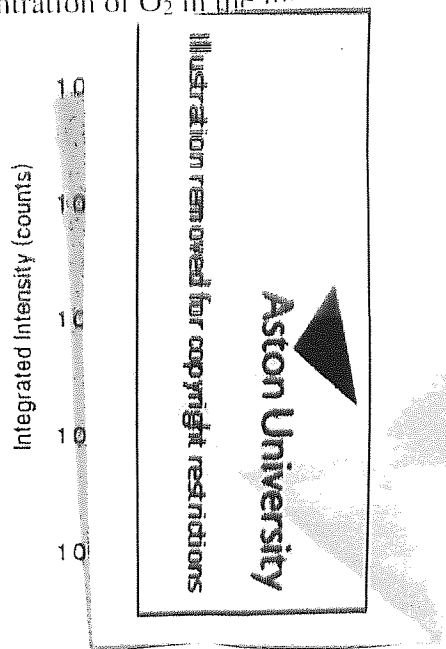
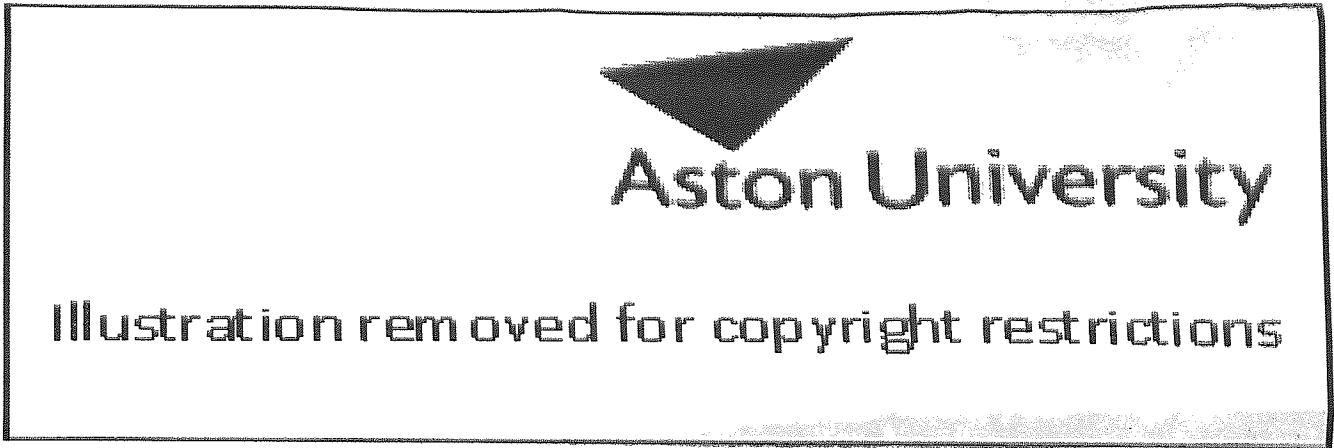
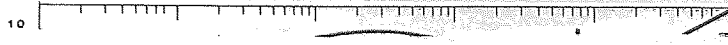


Figure 2.17 Variation of relative concentration with oxygen volume fraction in the plasma of Ar + O<sub>2</sub> mixture (after Olthoff [1995])

**2.2.7 Ar + H<sub>2</sub> plasma**

Cross sections for collisions of H<sup>+</sup> with Ar versus laboratory energies are given in Figure 2.18 [Phelps, 1992]. The symbols and collisions processes are: *Q<sub>m</sub>* momentum transfer, Ar<sup>+</sup> charge transfer to form Ar<sup>+</sup>, *e* electron production by ionization of Ar; *Ly $\alpha$* , *Ha* production of the Lyman and Balmer  $\alpha$  line; the curve labelled *L<sub>m</sub>* is the momentum loss function and that labelled *L<sub>s</sub>* is the stopping power for H<sup>+</sup> in Ar.



10<sup>-1</sup> 1 10 10<sup>2</sup> 10<sup>3</sup> 10<sup>4</sup>  
Laboratory energy (eV)

Figure 2.18 Cross sections for collisions of H<sup>+</sup> with Ar versus laboratory energy (after Phelps [1992])

The most important ions detected in argon - hydrogen plasma are: Ar<sup>+</sup> (major component), Ar<sup>++</sup>, Ar<sub>2</sub><sup>+</sup>, ArH<sup>+</sup> (see Figure 2.19 after Rusu [PhD, 2001]).

Ar:H



Figure 2.19 Variation of the relative concentration of the species present in Ar + H<sub>2</sub> (2.2:22) (after Rusu [PhD, 2001])

## 2.3 Plasma-induced surface modification

### 2.3.1 RIE plasma

Free radicals contained by RIE plasmas cause extensive chemical effects at surfaces due to the high reactivity of their unsatisfied bonds, thus producing enhanced etch rates [Law et al, 1991], [Kuen-Sane, 1991]. Combination of chemical reactive gases with hydrogen or inert gases has been found to increase the etch rates further. An example of this is shown in Figure 2.20.



Figure 2.20  $XeF_2$  and Ar etching of  $SiO_2$  (after Roth [2001])

Reactive ion etching of GaAs using  $SiCl_4$  is reported by Rahman [2001]. For obtaining low damage they demonstrated that etch parameters that minimize atomic ion content in the discharge should be used.

Using  $CCl_2F_2$ , high etch rates of GaAs have been reported [Webb, 1984]. Rough surfaces were obtained due to the chlorine ion content which has a very high etch rate. Also, by adjusting the angle of incidence of the ion beam with respect to the target, optimum conditions to fabricate structures with perpendicular walls are reported. The introduction of oxygen into the  $CCl_2F_2$  gas allows the concentration of carbon containing compounds to be decreased, but leads to formation of oxides at the surface. The oxides hinder or prevent the etchant access to the substrate atoms. Grigonis [1999] found that the thickness of oxide layer depends on etching rate. It decreases with increasing oxygen concentration in  $CF_2Cl_2 + O_2$ .

The gas of most interest in the reactive etching of III-V semiconductors is methane hydrogen. Using  $CH_4/H_2$  plasmas, surface changes of GaAs have been found to be due to

physical and chemical etching, as well as deposition in some cases [Layberry, PhD, 1999]. The results showed arsenic depletion and formation of a wholly Ga oxide surface covering. Hydrogen removal of arsenic and methane removal of gallium were found to be the main reactions responsible for surface changes.

Because of the great complexity of the  $\text{CH}_4/\text{H}_2$  plasmas, phenomena taking place at the surface of GaAs subjected to these plasmas is still an open issue in current literature. Much of this work is based on replacing  $\text{CH}_4$  by an inert gas. Studies of GaAs etching with inert gases (and mixtures with hydrogen) have also been reported, as will be presented in the following sections.

### **2.3.2 Plasmas of inert gases and inert gas ion bombardment**

In the current literature, a great deal of work on ion bombardment has been reported [Sanghera, 1998], [Malherbe & Odendaal, 1999] much more than on plasma treatment of GaAs. Given the fact that ions are the most important species in the plasma responsible for surface changes, and also that ion energies and fluxes are more easily controlled in ion bombardment, reported work on ion bombardment of surfaces is very useful for studies of plasma-surface interaction.

#### *Changes in surface composition*

Surface compositional changes by inert ion bombardment of GaAs are reported to be mainly related to changes in the As/Ga ratio [Singer et al, 1981].

Most surface composition studies of ion bombarded GaAs have reported an As - depleted surface [Singer et al, 1981], [Sullivan et al, 1994]. It is interesting to note that sputtering of GaAs was not observed in the initial stages of bombardment. After removal of hundreds of monolayers of material, preferential sputtering of As was observed resulting in a Ga rich surface [Malherbe et al, 1992]. Smentkowski [2000] also reported that Ga enrichment of the GaAs surface increased with increasing Ar ion bombarding energy or ion current density. The large difference in sublimation energy of Ga and As was interpreted as being responsible for the preferential sputtering of As.

From a thermodynamic point of view, there should always be a difference between the components of a multicomponent system. One of the components is preferentially driven from the bulk towards the surface to maintain minimum surface free energy. Mass effect is based on classic collision mechanics and it has been given as an explanation for the preferential sputtering in the low keV regime, as pointed out by Wei [PhD, 1995]. The momentum and energy of the incoming ions are redistributed differently to the target constituents. The lighter component is usually dislocated rather than the heavier one.

Other explanations for differential sputtering correlated to binding energy are also discussed.

Wei [PhD, 1995] reported that Ar<sup>+</sup> sputtering of GaAs (3 keV, 1 mA, dose 10<sup>17</sup> ions/cm<sup>2</sup>) at an working pressure of 5×10<sup>-4</sup> Pa removed the contaminant overlayer and an As rich surface layer (made of one or two monolayers) above a As depleted surface occurred. This was explained in terms of Gibbsian segregation.

Scandurra [1996] studied surface changes after irradiation with rare gas ions. The surface composition after argon ion bombardment with ion energies in the range of a few hundreds eV to 5 keV is reported to be As rich in the topmost surface layer and As depleted underneath it. It is also interesting to observe the influence of lighter bombarding ions, (He and Ne) having the same energy on the surface. Another result presented in the paper was that with increasing energy, for the same ion bombarding specie, sputtering becomes more important than segregation.

### *Etch rates and damage*

In the paper of Ching-Hui et al [1995], a model for studying the low energy (500 keV) argon ion-induced damage is proposed. The higher etch rate results in lower total accumulated damage. The critical process here is the rapid removal of the highly damaged surface on a time scale that is smaller than that required for diffusion. However, although the total integrated damage is reduced in samples with higher argon etch rates, the damage at the surface is higher. The paper presents the benefits of high etch rates that generally produce low depth damage but high modification of the damaged layer by argon ion bombardment. The dependence of the etch rate of GaAs with argon ion energy was studied also by Webb [1984] using argon ion bombardment of 200 - 800 eV. Changes of the cross section of the etch pit with beam angle are reported.

As observed by Masuda et al. [1995], impinging ions sputter the surface leading to a modification of surface stoichiometry due to a preferential sputtering of the arsenic component. The thickness of the modified layer depends linearly on the substrate bias and its composition exhibits a departure from stoichiometry due to arsenic loss, a factor which increases with plasma power.

On channelling, energy is dissipated into the bulk. A decrease in the sputtering yield due to channelling was reported [Hollinger, 1994]. In this paper, the most important sputtering theories are reviewed and comparisons with published experimental data of sputtered GaAs are given.

### **2.3.3 Oxygen and mixtures**

Reported work on oxygen ion bombardment is important in studies of surface changes in oxygen plasma. Oxidation of GaAs by irradiation with oxygen with energies from 0.5 to 5 keV was studied by Alay [1995]. It was found that Ga is preferentially oxidized compared to As which is explained by heat of formation of corresponding oxides. The formation enthalpy of Ga<sub>2</sub>O<sub>3</sub> per metallic atom (-5.54 eV/metal atom) is lower than for As<sub>2</sub>O<sub>3</sub> (-3.38 eV/metal atom).

Besides surface oxidation, sputtering can also occur with oxygen ions. Preferential removal of As by O<sub>2</sub><sup>+</sup> bombardment was reported [Alay, 1992].

Policrystalites of Ga<sub>2</sub>O<sub>3</sub> in the oxide layer were observed. During etching of GaAs in O<sub>2</sub> plasma, the adsorbed oxygen is thought to form chemical bonds on the surface or penetrate to the deeper layers as a result of segregation of arsenic to the surface (interdiffusion between arsenic and oxygen atoms). When etching with O<sub>2</sub>, the near surface layer is As depleted and Ga enriched. Arsenic depletion is explained by the interdiffusion with oxygen, i.e. the As atoms segregate to surface and their sites are occupied by adsorbed oxygen atoms.

XPS and ISS studies of Ar<sup>+</sup> sputtered GaAs(001) before and after neutral oxygen exposure are presented [Wolan et al, 1998]. The authors reported a Ga<sub>2</sub>O<sub>3</sub> rich surface also containing GaAsO<sub>4</sub>, As<sub>2</sub>O<sub>3</sub> and As<sub>2</sub>O<sub>5</sub>. The oxide layer thickness was 25 Å and the Ga:As ratio increased from 1.1 to 1.6 during oxidation. The ISS study indicate a more electrically insulating oxide on the oxygen exposed sample.

### 2.3.4 Hydrogen and mixtures

Hydrogen implantation is widely employed in GaAs device technology for isolation and or current-guiding applications [Pearton, 1990]. Hydrogen is present in every step during the processing of III-V devices, as part of the plasma used for dry etching, or as a component of the chemical used for conventional wet-etching or solvent cleaning. In many situations hydrogen is an unintentional contaminant as, for example, water vapour in vacuum systems or OH species in oxides. Hydrogen can alter the electrically active dopant profile in the near-surface region.

Atomic hydrogen is found to electrically passivate all shallow dopant impurities and some deep level states. The passivation is due to formation of neutral hydrogen complexes at the defect point [Sullivan et al, 1998]. In GaAs it is observed that all shallow donors (Si, Ge, Se, Te) and shallow acceptors (Be, Mg, C) are passivated by atomic hydrogen (a review can be found in [Brozel, 1996]).

Lower frequency plasmas ( $\leq 100$  kHz) are reported to be more effective in producing larger incorporation depth due to their higher average ion energies [Dautremont-Smith, 1988]. At higher plasma drive frequencies the lower ion energies can lead to a higher

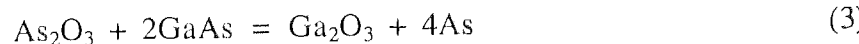
hydrogen concentration at the immediate surface.

### 2.3.5 Air exposure after plasma treatment

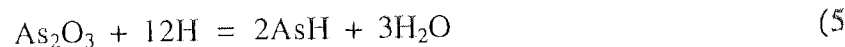
The surface quality is very important for the growth of epitaxial layers on III-V semiconductor substrates. Currently, the cleaning and etching processes performed in situ, prior to growth, are being replaced by pretreated, ready-to-use wafers, named "epi-ready" surfaces. The wafer fabrication gives clean and oxide free substrates, but unfortunately these surfaces are easily contaminated with carbon during air exposure. This carbon contamination is hard to remove. An epi-ready surface has an oxide overlayer which is thin (to be easily removed thermally) and homogeneous (to prevent direct access of contaminants to the surface). However, these surfaces are unstable (they are normally kept in a nitrogen atmosphere) and their lifetime depends on ambient conditions.

Passeggi [1999] reported studies of surface evolution in air, depth profiling and chemical etching. The results show a fast increase of oxide in the first month of exposure to air (following a power law) and a linear increase for the next 4 months.

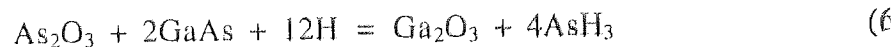
Air exposure after treatment did not alter the surface composition [Aydil et al, 1993] of GaAs. The samples exposed to plasma for a shorter period of time are less stable in ambient air [Aydil et al, 1993]. The idea of the influence of ambient air humidity on the surface composition depending on the quality of the Ga oxide is proposed. Another conclusion of the work of Aydil is that the oxygen atoms from adsorbed water vapour and/or  $O_2$  can diffuse through the gallium oxide to the GaAs interface and react with GaAs to form  $As_2O_3$  which can further react according to reaction (3) to form As defects.



Removal of both As and  $As_2O_3$  from the surface via the following reactions:



reduces the As defects. Another interesting result of the work is the observation that the samples exposed for shorter time have less and different type of gallium oxide on the surface than those exposed for longer time. The samples exposed to plasma for a shorter period of time are less stable in the ambient air. It is also mentioned the importance of H atoms in the gallium oxide formation when the reaction:



takes place.

Air-exposed GaAs surfaces analysed by Wilmsen [1990] had a logarithmic growth with time. The oxide  $Ga(OH)_3$  was found in air grown oxides. The authors believe that water

vapours in the air accelerate the oxide growth. It is shown that the surface oxidized phases can be avoided by handling the sample under an inert atmosphere. Also, after the chemical treatment, no trace of oxidation was found on the surface of the samples manipulated under dry nitrogen showing that the oxidation observed on substrates exposed to air is due to the atmospheric oxygen [Massies, 1985].

The air-exposed cleaved GaAs showed preferential oxidation of Ga at the surface, as reported by Ingrey [1986]. Three Ga oxide phases are reported with  $\text{Ga}_2\text{O}$  as major compound. According to these authors, the layered structure of the surface of a cleaved sample has  $\text{Ga}_2\text{O}$  on top of a layer of Ga-enriched GaAs. They explain this by the dissociation of the oxygen molecules at the surface defect sites leading to oxidation.

The article of Lu [1993] reports on a study of the ultraviolet (UV)-ozone oxidation of GaAs. It is very interesting that the angle resolved analysis showed no variation of the  $(\text{Ga}/\text{As})_{\text{substrate}}$  ratio. This suggests that Ga and As are simultaneously oxidized, which is in agreement with Ingrey [1986] (see above).

Barrett et al [1990] used glancing angle X-ray absorption spectroscopy to elucidate the local structure around Ga and As atoms in the oxide coating of polished GaAs(100) wafer. The oxide layer thickness was 7 - 9 Å and the surface was As depleted. Their opinion is that the presence of a sequence of ordered layers of chemically defined oxides is unlikely, since 3 - 4 monolayers of an oxygen rich phase are found at the surface. The coating is more likely to consist of a random microscopic oxide comprising tetrahedral and octahedral sites.

If a metal forms several stable compounds with a particular gas under a given pressure the compound richest in metal will be nearest the metal surface, and that poorest in metal nearest the gas phase [Kubaschewski, 1953]. In the ideal case, each compound will constitute a separate layer within which the concentration of metal decreases from the inside to the outside; growth of layers will take place by diffusion, the concentration gradients acting as the driving force. The relative thickness of the various layers will depend mainly on the diffusion rates (of the cations or anions as the case may be) through the layer, but also on the differences of the chemical potentials at the interfaces. Alnot [1985] attributed the oxidation of GaAs to air exposure after chemical etching with  $(5\text{H}_2\text{SO}_4:\text{H}_2\text{O}_2:\text{H}_2\text{O})$ . As-rich surface layers obtained by anodic polarization oxidize in air forming agglomerates of  $\text{As}_2\text{O}_3$ , as reported by Steer et al [2000].

## 2.4 Surface

### 2.4.1 Introduction

*Surface* is the region of the solid where the interaction forces differ from the bulk. This

region may consist of several layers. Here, the symmetry of the binding forces existent in the bulk is perturbed and therefore its peculiar behaviour leads to phenomena like surface tension, chemical reactivity. Due to the asymmetric binding forces in the surface, the first few monolayers are contracted by about 1 to 10% of the nominal bulk layer distance. The distance between two surface layers is called *relaxation parameter* [Christmann, 1991].

The solid bulk material is usually polycrystalline but depending on external parameters (temperature, ambient pressure, type of ambient gas) its surface can exhibit a different structure and composition. This is due to the fact that the surface atoms are driven to *reconstruct* the surface by minimization of surface free energy.

#### 2.4.2 Surface - plasma interactions

Current literature on general theories on surface-plasma interaction is very scarce. This is because of the complexity of the plasma and also due to the multitude of materials and experimental procedures that can be involved. Also, plasmas have a multitude of plasma constituents with different energy and angle distributions which cannot be completely determined. Therefore, simplifications of the real plasmas have to be employed. As explained earlier in this chapter, from the multitude of the RF plasma constituents that interact with the sample surface, the most important effects are induced by positive ions. Thus, studies of ion bombardment interactions with surfaces play an important role in understanding plasma - surface interactions.

In this section, a background of general phenomena taking place at a surface exposed to ion bombardment is given.

Although an ion approaching the surface is neutralized before impact by the lattice electrons [Stuart, 1983] so it is no longer an ion, in the current literature on surface science the term *ion* is still used for this particle, to be distinguished from the target *atoms*. As an ion approaches the surface, firstly interaction of its electronic structure with that of surface atoms usually takes place. This interaction may consist on:

- direct energy transfer to the target electrons
- excitation or ionization of target atoms
- excitation of band - or conduction-electrons (weakly bound)
- excitation, ionization or electron capture of the projectile itself

Ion bombardment can induce different surface processes, depending on its energy, angle of incidence and chemical reactivity. With increasing energy, the ion bombardment may induce the following phenomena:

- 1 Adsorption, desorption of adsorbed gases and activation of chemical reactions

- among adsorbed gases or with the surface atoms
- 2 Removal of surface atoms by momentum transfer (sputtering)
  - 3 Intermixing of atoms and crystallographic damage within the top 10 layers
  - 4 Diffusion of target atoms
  - 5 Implantation of ions to hundreds of layers deep and crystallographic disordering

## 1 Adsorption

When a particle is brought so close to the surface that noticeable interaction can occur, a lowering of the energy of the combined system can take place resulting in a bound state and any excess energy is released as heat of adsorption. In order to remove the particle from the bound state (to the surface), an energy at least equal to the adsorption energy is necessary.

All gases are adsorbed to some extent by any surface. Adsorption is divided into two different classes: physisorption and chemisorption. Noble gases physisorb via weak van der Waals interactions. The surface must be kept at very low temperatures (below liquid nitrogen temperature) in order to reach appreciable surface concentration of these species.

If a stable molecule is dissociated by the molecule-surface interaction, the resulting atomic products will then form strong chemical bonds with the substrate. On the other hand, if the molecule is not dissociatively adsorbed the resulting bond is much weaker and is due to polarization forces [Blakely, 1975].

## 2 Sputtering

Sputtering is the erosion of the surface when the surface is bombarded by a particle beam.

The mechanisms of sputtering have been studied theoretically and experimentally for decades [Malherbe et al, 1992], [Malherbe, 1994], [Wolan et al, 1998], [Roth, 2001], [Blakely, 1975], [Pearton, 1996].

There is still no comprehensive theory of sputtering that can explain the experimental observations. The simplest model of sputtering is that of the billiard balls, where the interactions ion - target atom are treated as binary collisions, without taking into account interatomic potentials. This model is not too unrealistic [Chapman, 1980] because the interatomic potentials are short range and therefore interactions only between immediate neighbours need to be considered even in detailed calculations of sputtering. One of the fundamental problems of science is determination of these interatomic potentials.

Potentials used in collision models include: the Coulomb potential, the Lennard-Jones potential, the Morse potential, ionic potentials, the overlap potential etc. All these have limitations. Details of models using these potentials can be found in [Smith, 1997]. A comprehensive review of collision theories is also given by Wei [PhD, 1995].

Depending on the energy of the incident ions, the following phenomena may take place at the impact with a solid surface (see also Figure 2.21):

- a target atom may be ejected from the surface
- a secondary electron may be ejected
- the incident ion may be implanted
- the incident ion may be ejected
- the ion impact may result in collision cascade and reordering of surface layers

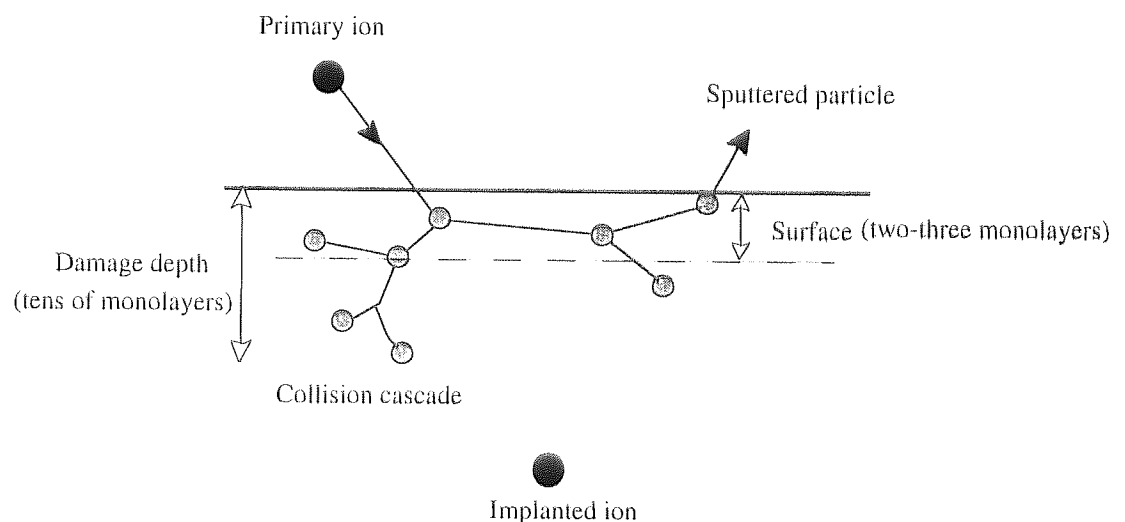


Figure 2.21 Summary of target processes

Sputtered particles come from the first two - three monolayers of the surface. The sputtering yield is defined as the ratio between sputtered atoms and number of incident particles. Electrons and neutrals rarely sputter atoms from surfaces in industrial plasmas. This is because electrons are not heavy enough and neutrals are not energetic enough. Significant sputtering yields are usually the result of ion bombardment.

Sputtering yield ( $Y$ ) is usually represented as a function of ion energy as in Figure 2.22 [2001]. With increasing energy after the threshold value for sputtering, the sputtering yield increases. For values of  $Y$  lower than 1, ions remove target atoms by direct knock on collisions and not all incoming ions remove atoms from the surface. For  $Y > 1$ , all incoming ions participate to sputtering and collision cascades take place with increasing energy. After a point where a maximum value of  $Y$  is obtained, any further increase of ion energy decreases sputtering yield. At this stage, the collision cascade reached its maximum depth.

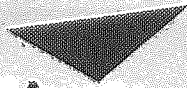


Figure 2.22 Sputtering yield as a function of ion energy (after Roth [2001])

The sputtering yield is not only a dependence of ion energy. Target atomic mass, projectile mass, incidence angle and dose also influence sputtering yields. All these factors will be described briefly in the following.

#### *Projectile mass*

The increase of the sputtering yield with atomic mass number of the bombarding ion ( $Z_1$ ) striking a surface of a material with 70 atomic mass number ( $Z_2$ ) is presented in Figure 2.23. Similar data for different  $Z_2$  is also presented in [Malherbe, 1994].



Aston University

Content has been removed due to copyright restrictions

Ion Energy /keV

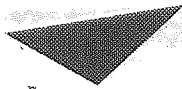
*Figure 2.23 Variation of sputtering yield, normalized for a surface - binding energy of 1 eV, with ion energy for normal incidence with atomic number  $Z_1$  for a target specie having  $Z_2 = 70$  (after Malherbe [1994])*

If the mass of the incident ion is lower than the mass of surface atom, the incident ion may be ejected from the surface and the surface atom in this collision may be driven towards the bulk. For large ion-to-target mass ratios, the mean depth of damage is smaller than the ion range [Smith, 1997].

If the mass of incident ion is greater than the mass of the surface atom, both ion and atom will be directed towards the bulk. A surface atom is ejected only if the acquired velocity is directed away from the surface. In the case of perpendicular incidence, this is achieved via secondary collisions. If there is an increased difference between the mass of the ion and surface atom, the sputtering yield is lower [Stuart, 1983]. Thus, sputtering yield for lighter ions can be greater than for heavier ions.

#### *Incidence angle*

The sputtering yield for amorphous and crystalline materials subjected to inert gas bombardment varies with the angle of incidence as shown in Figure 2.24 [Malherbe, 1994].



Aston University

Content has been removed due to copyright restrictions

Figure 2.24 Variation of sputtering yield with angle of incidence. The curves represent data of sputtering of GaAs reported by different authors (after Malherbe [1994])

### *Ion dose density*

The threshold dose density for amorphisation of the surface of most semiconductor materials is typically of the order of  $10^{14} \text{ cm}^{-2}$ . This is equal to the dose density required to sputter remove two atomic monolayers of the semiconductor surface. A summary of published data on sputtering is presented by Behrisch [1981] and a review of sputtering theories is given by Wei [PhD, 1995].

Sputtering of multicomponent samples usually induces enrichment in one component; this phenomenon is called *differential sputtering*. The probability of sputtering of an atom raised above the surface is higher than that of the other atoms contained in the target material. Practical applications of sputtering are most important at low ion energies.

## **2 Diffusion**

The atoms of a substrate material can move (diffuse) to minimize the surface free energy. Two main diffusion theories, the continuum diffusion in solids and the atomic theory are used to theoretically explain diffusion in solids [Sharma, 1970]. In this book, possible diffusion mechanisms are presented:

- exchange mechanism - when two neighbouring atoms may directly interchange their position.
- vacancy mechanism - when an atom exchanges place with a vacancy

In vacancy diffusion, the main criteria is the difference in ionic radius between the diffusing particles and those of the major constituent [Boltaks, 1963]. Thus, the greater the difference in size between the diffusing particle and the particles of the solvent, the larger the diffusion coefficient will be.

According to Sharma [1970], when diffusing interstitial atoms have a size comparable to that of lattice atoms, the interstitial atom moves into a normal lattice site by pushing the lattice atom into the adjacent interstitial site. In addition to the above mechanism, diffusion via dislocations can be encountered. Atomic radii of gallium and arsenic are 136 and 114 picometers, respectively. According to the argument above, neon (38 picometers radius) should have a higher diffusion coefficient than argon (71 picometers radius) and also higher diffusion coefficient than oxygen (48 picometers radius).

Reactive diffusion is the appearance of a new phase in the diffusion region with the new phase being a chemical compound. Diffusion can occur in surface and in the bulk and is mainly due to the existence of large atomic concentration gradients. If a concentration gradient does exist, then the atoms move in such a way as to remove it. Diffusion takes place either through vacancies or interstitials. Diffusion coefficient at temperature  $T$  is given by equation (7).

$$D = D_0 \exp(-Q_a / kT) \quad (7)$$

where  $Q_a$  is the activation energy for diffusion and  $D_0$  is Diffusivity.

The donor elements (Group V) show higher diffusion coefficients than do the acceptor elements (Group III) [Sharma, 1970]. Diffusivity for Ga is  $2.73 \times 10^{-54} m^2 / sec$  and for As is  $1.8 \times 10^{-60} m^2 / sec$ . Diffusion mechanisms are also discussed in terms of vacancy, interstitials and exchange mechanisms in the book of Tuck [1974]. Diffusion is usually an unwanted process because it leads to crystallographic defects. Surface reconstruction phenomena are also based on substrate diffusion.

### *Implantation*

Ion implantation takes place when ions of energies in the range 20 eV - 300 keV strike the target surface. Implanted ions stop in the bulk material, many atomic layers below the surface. Studies of this process is beyond the scope of this project.

Computer simulation of atomic collisions in solids is a widely used method of study. Many codes, based on Sigmund's linear cascade theory and thermodynamic approaches have been developed to predict chemical and physical evolution of the surface. TRIM code is one of them and it will be presented in the following section.

### 2.4.3 The stopping and range of ions in matter - the SRIM code

Up to date, many codes for simulation of ion - surface interaction have been developed. Each code has limitations due to the approximations used in collision theories and also in calculation of surface binding energy and target structure. Therefore, the results obtained using different codes are different [Swart et al, 2000], [Kwei, 1986], [Grappnerhaus, 1997].

With HYPERCHEM code, non-fixing of the atom coordinates in the GaAs lattice does not allow calculation of energy transfers after impact. Also, interaction of surfaces with polyatomic ions is difficult. MARLOWE code takes into account surface lattice, but the code is very complicated to use and interpret. SUSPRE is another code that may be used with relative success. SRIM code (2000) is the updated version of Transport of ions in matter (TRIM) and is presented in more detail later in this chapter. Full description of the code is found in the tutorial book of Ziegler [1985] and also in the instruction manual of SRIM available with the code. Ziegler presents the physics of ion penetration of solids and the source code for TRIM programs with full explanation of the physics involved.

SRIM consists of a group of programs for calculating the stopping and range of ions into matter using a quantum-mechanical treatment of ion-atom collisions. This simulation program consists of following a large number of particle "histories" in a target. The input parameters are: energy, position and direction of the incoming particle. The energy is reduced as a result of nuclear and electronic energy losses, and a history is terminated either when the energy drops below a certain value or when the particle's position is outside the target.

The incident energies can be varied from 0.1 eV to several MeV. The target is considered amorphous with atoms at random locations, and thus the directional properties of the crystal lattice are ignored. Therefore, selection of target atoms is performed by random numbers, assuming the probabilities of encounters being proportional to their stoichiometric abundance. The surface binding energy is difficult to estimate, especially for compound systems (details are given in Chapter 2.1). This code uses a default value of 2.35 eV.

The program can be used for all target - material combinations. It provides information on ion range and damage, as well as reflection and transmission properties of targets. The standard output of the program contains lateral and depth distribution of ions in the target, depth and number (per ion) of vacancies created, sputtering yields. The total stopping cross section of ions in solids is divided in two parts: the energy transferred by ion to the target electrons (called electronic stopping) and to the target nuclei (called nuclear stopping).

Computer simulation of the slowing down and scattering of energetic ions in materials can be used in studies of ion implantation, radiation damage, sputtering, reflection and transmission of ions.

A set of parameters are used in this code and their definitions are presented in the following:

*Range distribution* - distribution of stopped ions with depth. This quantity is useful in doping semiconductors by ion implantation [Smith, 1997].

*Projected range* - the distance along a direction perpendicular to the surface at which particles stop in the target material. This parameter is different from *range* which represents the mean distance the ion travels along its own path.

*Range straggling* - standard deviation of the range.

*Lateral spread* - lateral distribution of the range distribution. This parameter is very important in fabrication of integrated circuits.

Collision cascade is a process whereby primary recoil atoms can produce new recoils and so forth.

Using this program, a set of calculations using Full Damage Cascade for 10 000 ions were performed in this work. The results of calculations are presented in Chapter 4 and are compared with experimental data in Chapter 5.

## Chapter 3. Materials and instrumentation

The present work is devoted to the study of the interactions of capacitively coupled RF plasmas with the surface of GaAs. For this project, experiments were designed to accurately measure the BEs associated with the Ga 3d, Ga 2p<sub>3/2</sub> and LMM peaks using XPS analysis and propose identification in terms of the oxides of GaAs. GaAs wafers and some reference compounds (such as metallic Ga and Ga<sub>2</sub>O<sub>3</sub> powder) were used. Surface analyses were undertaken using XPS and AFM, and Langmuir probe and mass/energy analyser were used for plasma diagnosis. All materials and devices used for this work are described in this chapter.

### 3.1 GaAs wafer

This material was chosen not only because of its importance in the electronics industry (as shown in Chapter 2) but also for theoretical studies.

Mechanically polished (100) GaAs wafers (unmasked) and also patterned (PMMA mask) wafers were used. These samples were supplied by GEC Marconi in the form of discs of 9 cm diameter. Prior to plasma treatment, the samples were cut in small pieces of approx. 5 mm<sup>2</sup> and cleaned. The samples were cleaned for 15 minutes in acetone, rinsed for 15 minutes in isopropanol using a ultrasonic bath, then dried in flowing compressed air. This procedure is used in industry for fabrication of electronic devices with GaAs as a base material and no major surface changes are expected by using it. Also, removal of the mask after plasma treatment was undertaken using the same cleaning procedure. Surface composition analyses of virgin and cleaned GaAs were also conducted. XPS analyses of virgin GaAs will reveal the native oxidation of the surface whereas those of cleaned GaAs provide the starting point for the study of surface changes after plasma treatment.

Two small samples of unmasked wafers and another two of masked samples were used for each plasma treatment. It is advisable always to produce a reserve sample. The unmasked samples were analysed using XPS for determining surface composition whereas the masked ones were analysed using AFM for measuring etch depths (details of the analysis and procedures are given later in this chapter). The masked samples proved not to be useful. Etching them with argon and oxygen plasma did not give reproducible results. The mask was either removed, especially in the case of oxygen, or hardened during plasma treatment and could not be completely removed. Apart from the usual cleaning procedure (described earlier in this chapter), other chemical procedures using N-methyl pyrrolidone have been tried to solve the problem of mask hardening, but were unsuccessful. Another way to overcome mask hardening would have been to use a very "mild" oxygen plasma.

This procedure could be satisfactory if proper studies of best plasma parameters to be used are undertaken. This is because the masks subjected to different argon plasmas have differing hardness and choosing the best oxygen plasma to remove all of them is not an easy task. Thus, etch pit depth measurements were subject to large errors or unable to be realised. This problem was finally resolved by using a small, finely cut piece of GaAs as mask. This small piece was placed on top of a larger piece of GaAs wafer (complicated problems usually have simple solutions). The results obtained using this procedure proved to be reproducible thus very reliable and free from errors caused by type of gas, RF power or gas pressure.

Another experiment undertaken consisted of analysis of the influence of the background gas composition on the final surface chemical composition. For this purpose, an argon plasma was used with and without oxygen background. The oxygen background was produced by allowing oxygen into the chamber for 10 minutes at 90 mT and a flow of 10 sccm followed by pumping down to the usual background pressure.

### **3.2 Plasma treatment of GaAs**

One of the most commonly used method for etching of semiconductors for applications in industry is RIE. This method provides a combination of physical processes as well as chemical processes on the surface of semiconductors. For a better understanding of the phenomena taking place when the semiconductor is exposed to reactive etchants, a separation of the physics and chemistry involved is necessary. Therefore, plasmas of inert gases had to be firstly employed. Two gases, argon and neon, were chosen for this purpose.

In the following section, a description of the device used for plasma etching of GaAs wafers is presented.

#### **3.2.1 The etching chamber and experimental setup**

The experiments were carried out in an asymmetrical, capacitively coupled 13.56 MHz rf industrial Oxford Instruments Plasma Technology System 100 cell controlled from a PC. A schematic diagram of the etching chamber is shown in Figure 3.1.

In order to obtain a radially uniform plasma, the driven electrode (denoted cathode) was shielded by a grounded cylinder. The cathode had a diameter of 20.5 cm and consisted of a quartz plate on an Al base. The samples to be exposed were placed in the middle of the quartz plate of 19.5 cm diameter and 1.2 cm thickness. The grounded electrode (denoted anode) is a cylinder of 38 cm diameter formed by the grounded walls of the plasma chamber. The height of the cylinder was 45 cm. The plasma cell contained an automatic matching network, also.

In order to minimize the infiltration of impurities (including water vapour) from the ambient air, a sealed preparation chamber (glove box) vented with liquid nitrogen was also used.

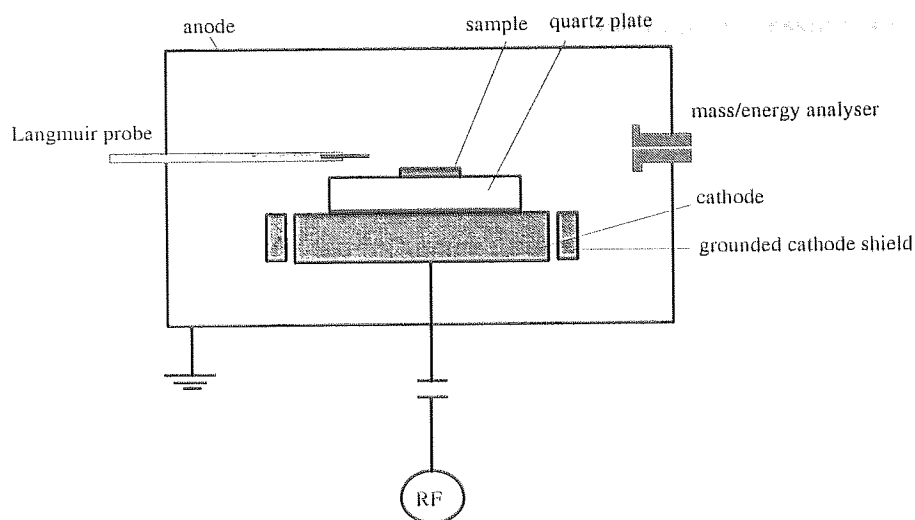


Figure 3.1 Schematic diagram of the etching chamber

Plasma treatment of GaAs surface was undertaken in different gases, as shown in Table 3.1. For easy comparisons of surface changes with plasma parameters the same ranges of power, pressure and gas concentration were used for all gases and gas mixtures. The oxygen and hydrogen content of the mixtures were calculated from the total amount of gas admitted to the cell.

Table 3.1 Gases used for plasma processing of GaAs

Gas	Power range [W]	Pressure range [mT]	Concentration [%]
Ar	5 - 200	10 - 90	100
Ne	5 - 200	10 - 90	100
O <sub>2</sub>	5 - 200	10 - 90	100
H <sub>2</sub>	5 - 200	10 - 90	100
Ar + O <sub>2</sub>	5 - 200	10 - 90	O <sub>2</sub> (0.2 - 70)
Ar + H <sub>2</sub>	5 - 200	10 - 90	H <sub>2</sub> (0.2 - 70)

For each power - pressure combination, four samples of which two were masked were introduced in the process chamber. The unmasked samples were analysed with XPS for determination of surface compositional changes and the masked samples were used to determine the etch rate using AFM. The other two samples were used to check reproducibility when required.

At each rf power, nine experiments with pressures increasing from 10 to 90 mT in increments of 10 mT were undertaken. The values of rf power used were 5, 25, 50, 100, 150 and 200 W. All samples were exposed to the plasma for 30 minutes and the base pressure was always better than  $2.0 \times 10^{-6}$  mT. Although the unit of pressure is not given in SI units here, it is custom and practice to use mT in this field.

Surface oxidation prior to the transfer into the surface analysis chamber was inevitable. For a very accurate study of surface oxides, a system with direct transfer would have been most useful. In order to understand the influence of air exposure while transferring the sample to the XPS chamber on the final results, a separate study of surface changing with time after plasma treatment was also undertaken here. For this experiment three samples were simultaneously etched with argon plasma at 150 W and 10 mT and analysed at time intervals ranging from 20 minutes to 13 months.

Correlated to the experiment above, another experiment on the influence of the quantity of ambient oxygen on surface oxidation was employed. Therefore, oxygen gas was admitted into the etching chamber immediately after plasma treatment. Different fluxes, pressures and times of exposure were chosen. Reproducibility checks were also conducted in a separate experiment and are described in the following section.

Another interesting experiment was to look at the changes in shape of the etch pit with pressure and power. To get comparable results, the samples had been scanned using the same AFM parameters: scanner rate 0.1 Hz, set point 15 and gain 1.6.

### **3.2.1.1 Experimental errors**

#### **3.2.1.1.1 Residual impurities and calculation of standard errors**

It is known that any surface contains a certain amount of water depending on the ambient pressure. Even at  $10^{-9}$  mbar surface water can consist of over 100 monolayers. During plasma processing, ions bombard the chamber walls and remove  $H_2O$  which is then dissociated by plasma constituents. Thus, the water adsorbed on the chamber walls becomes source of oxygen and hydrogen species.

A rough estimation of the partial pressure of impurity oxygen coming from dissociation of water can be easily obtained. The ionization coefficient of low temperature plasmas is  $10^{-3}$ . Suppose that the concentration of active species of oxygen (oxygen ions, ozone ions etc.) has a maximum value of 1 %. For a vacuum of  $10^{-6}$  mbar (used in this work), the partial pressure of oxygen impurity is  $10^{-3} \times 10^{-6}$  mbar which is  $0.75 \times 10^{-6}$  mT.

The amount of residual oxygen varies with type of gas used. For example, argon plasma is the most efficient for  $H_2O$  desorption, so a higher amount of oxygen and hydrogen species is expected to appear in this plasma compared to plasmas of other inert gases. Care had to

be taken while placing the samples in the treatment chamber due to the inherent insertion of water vapours from ambient air. Therefore, it was important to maintain the same procedure for sample insertion in the chamber so that the quantity of water introduced was approximately the same. Although the plasma equipment used had a preparation chamber with a constant nitrogen flow, water vapour was still present in appreciable quantities in the process chamber. The quantity of water vapour in the process chamber is indicated by the time required for pumping down. A direct relationship between the time the process chamber remained opened and the time taken for pumping down to background pressure was observed. Therefore, the time spent for placing the samples in the chamber had to be minimized as much as possible or maintained the same for all experiments. This would partially overcome the impurity problem by introducing systematic errors.

A set of experiments were carried out to assess the errors introduced by residual impurities. Thus, five samples were etched separately with argon plasma for 30 minutes at the same plasma parameters: 10 mT and 150 W. The samples were then analysed with XPS. Standard deviation of the relative concentration of the surface compounds was then calculated as follows.

$$S = \sqrt{\frac{\sum_{i=1}^N (X_i - X_{med})^2}{N - 1}}$$

where  $X_{med}$  is the average of all values  $X_i$  and  $N$  is the number of values for which the standard deviation is calculated (here,  $N = 5$ ). The standard deviation represents the statistical measure of the precision in a series of repetitive measurements.

### 3.2.1.1.2 Impurities introduced by gases

Argon, neon, oxygen and hydrogen were used in this work. The first three gases were high purity (99.999%) standard industrial grade and hydrogen was research grade (99.9995%). In standard industrial gases, the impurities do not exceed: 4 vpm O<sub>2</sub>, 15 vpm N<sub>2</sub> and 1 vpm H<sub>2</sub>. The partial pressure of oxygen at the extreme values used in this work, 10 mT and 90 mT is  $4 \times 10^{-4} \times 10$  mT and  $4 \times 10^{-4} \times 90$  mT, respectively. The partial pressure of active oxygen at these pressures is  $4 \times 10^{-6}$  mT and  $36 \times 10^{-6}$  mT, respectively. In research grade gases the impurity oxygen does not exceed 1 vpm. Thus, the partial pressure of active oxygen is  $10^{-6}$  mT and  $9 \times 10^{-6}$  mT, at 10 and 90 mT total gas pressure, respectively.

Comparison of the values above with those of partial pressure of residual oxygen (given in the previous section, second paragraph) shows that the quantity of oxygen introduced by process gases is more important. The sum of the two kinds of impurity can be important in surface processing by plasma.

Among all plasma constituents, ions play a key role in the plasma etching of

semiconducting materials and therefore determination of their identity, flux, and energy is very important. The plasma etcher used contained two plasma diagnostic tools, both controlled by specific software: a Langmuir probe and a mass/energy analyser and will be briefly described in the following section.

### **3.2.2 Langmuir probe**

The electrical probe is a Hiden Analytical Langmuir probe positioned as shown in Figure 3.1. This type of electrical probe is generally used for DC plasmas, where the plasma parameters are stationary over the duration of voltage sweep. Therefore, the most accurate diagnosis of RF plasmas is achieved by using a compensation electrode beside the probe which drives it with radio-frequency of, in this case, 13.6 MHz. Assuming that the plasma parameters are stationary over a period of the voltage change, the simple probe can give information on electron temperature, plasma potential and plasma density.

In our experimental arrangement, the Langmuir probe had a fixed vertical position near the cathode (about 10 mm from the cathode). Thus, careful observation of the relative position of the probe to the cathode sheath was necessary in order to gain reliable results.

For measuring the energy distribution of ions impinging on the cathode, Kuypers [1988] introduced an ion energy analyser into the cathode. However, it requires sophisticated techniques, since the potential of the whole analyser must follow the rf signal. Another method is the inversion of the electrode geometry, i.e., the connection of the rf generator to the larger electrode while the smaller electrode, is grounded, as presented by Wild [1991]. Also, this is not possible because of the geometry of the system as a whole.

### **3.2.3 Mass/energy analyser**

The plasma etcher contains also a Hal Hiden EQP mass/energy analyser positioned on the wall of the etching chamber, as shown in Figure 3.1. There are two modes in which the probe can be operated: residual gas analysis mode (RGA) for neutrals analysis and SIMS mode for analysis of ions extracted from the plasma. Four display modes of the RGA mode can be selected. The BAR mode, which outputs histograms of relative concentration of all types of ions extracted from the plasma having a certain energy; PROF mode, which gives the profile of the ion spectra); MID mode (where 16 different channels can be simultaneously used to detect changes of ion concentration with time). Finally, MAP mode, where the internal parameters of the analyser are set up by sweeping a certain range of atomic weights.

For this work, the only useful information given by this analyser concerned the determination of the type of species (ions and neutrals) existing in different plasmas.

Determination of ion energies at the sample surface (e.g. at the cathode) were not possible using the mass-energy analyser due to the fact that it was built in at the anode.

### 3.3 Surface analysis

#### 3.3.1 X-ray Photoelectron Spectroscopy (XPS)

XPS, also known as Electron Spectroscopy for Chemical Analysis (ESCA) is a widely-used technique for investigation of chemical composition of solid surfaces. The technique involves irradiation of solid surfaces in vacuum with soft x-rays and analysing the emitted photo and Auger electrons by energy.  $MgK\alpha$  x-rays (1253.6 eV) or  $AlK\alpha$  x-rays (1486.6 eV) are generally used. The photons emitted by the x-ray source interact with atoms in the surface region by photoelectric effect and electrons are emitted. Also, Auger electrons are emitted due to relaxation of the energetic ions left after photoemission. The Auger electrons are emitted roughly  $10^{-14}$  seconds after the photoelectric event [Wagner et al, 1979]. Figure 3.2 shows the emission diagram of the photoelectric and Auger processes.

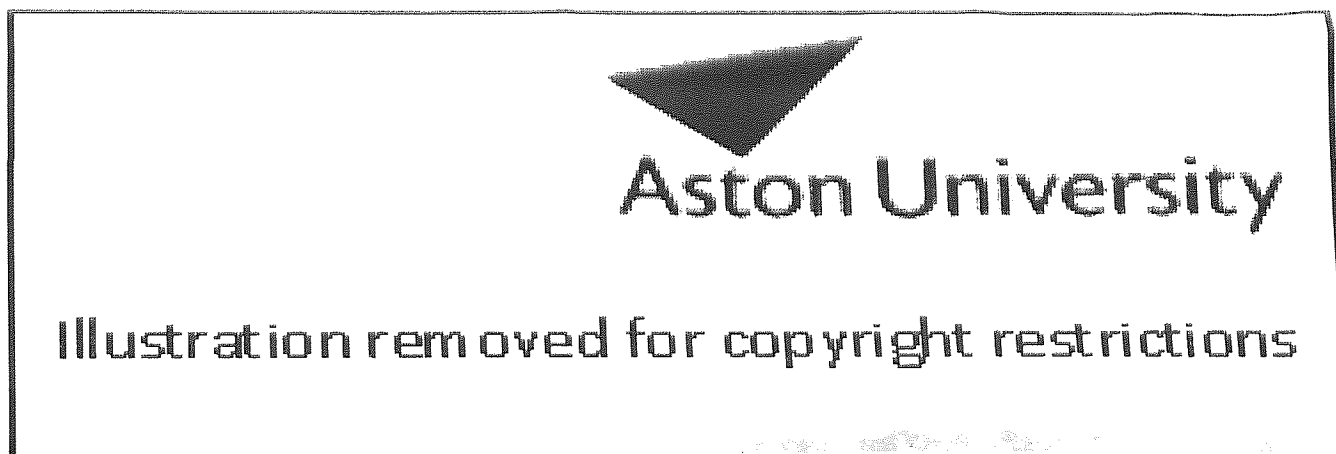


*Figure 3.2 Schematic emission diagram of photoelectric process (top) and the Auger process (bottom), (after Wagner [1979])*

Penetrating depths of photons emitted by Al sources are of the order 1 - 10  $\mu\text{m}$ . Since the mean free path of electrons through solids is very small (of the order of tens of angstroms), the detected electrons come from the top few atomic layers. The probability of an inelastic scattering event occurring is determined by both the electron energy and the material through which it is travelling. The number of electrons of energy  $E$  falls exponentially with depth into the surface. The inelastic mean free path ( $\lambda$ ) represents the depth at which photoelectrons have a probability of  $1/e$  of escaping without energy loss.

Numerous references to the theoretical and experimental determination of  $\lambda$  can be found in current literature [Seah, 1979], [Zommer et al, 1998], [Christie, 1980]. For GaAs, an electronic mean free path value of 26 Å was used [Wei, 1995], [Lu et al, 1993]. For metallic Ga, a value of 52 Å for the electronic mean free path was used [<http://physics.nist.gov/PhysRefData/XrayMassCoef/tab3.html>].

The electrons leaving the sample are detected by an electron spectrometer according to their kinetic energy. The analyser is set to accept electrons having an energy within a small range (referred to as the pass energy).

The XPS analysis for this work was carried out in a VGS ESCALAB 200D spectrometer using Al K-alpha unmonochromated radiation (1486.6 eV, FWHM = 0.8 eV) at an anode voltage of 15 kV. The analyser pass energy was 20 eV and the energy step size was 0.05 eV.

The spectra were acquired and processed using VG Eclipse software. Curve synthesis of individual peaks was required to identify the various chemical states and the elements examined as so to identify the compounds formed in each surface. The books of Seah and Dench [1979] and Seah [1990] give a comprehensive introduction to curve synthesis.

For the fitting procedure performed on Ga 3d and As 3d peaks, 30% Gaussian and 70% Lorentzian combinations of line shapes were used. Relative atomic concentrations were calculated from the intensities of the major photoelectron spectral lines (integrated peak areas) after subtracting a Shirley background.

Narrow-scan spectra were collected for Ga 2p<sub>3/2</sub> and 3d peaks, Ga LMM Auger lines, O 1s and C 1s peaks with all samples. Curve synthesis was employed to determine the binding energies and relative concentrations of surface species. A considerable amount of data was collected in order to properly determine the positions of all peak components and FWHM values.

The final procedure of 3d peak fitting was chosen after a wealth of trials for obtaining the best fit with the original data. Spectrum fitting was conducted in the following steps:

### ***1. Smoothing***

Smoothing is applied for partially removing the noise from the acquired data. Smoothing with 13 points and 30 passes was found to give reliable results for all spectra having a high number of counts (at least 2500 counts for the As 3d peak). Smoothing data having poor counts can give erroneous results.

### ***2. Charge shift adjustment of the whole spectrum***

In an "as acquired" XPS spectrum, the peaks are not at the expected positions mainly due to surface charging. This effect is the result of the balance between the electron loss from the surface (by x-ray induced emission) and electron gain by conduction or by the minor effect of acquisition of slow or thermal electrons from the vacuum space. This charge can be corrected by choosing a reference peak line and shifting the whole spectrum according to its known position. The use of general reference peaks taken from databases is however unreliable mainly due to the different values they provide.

The C 1s line at 284.6 eV cannot be used as reference in this system as confirmed by other workers [Schwartz et al, 1979], [Breeze et al, 1980]. This is due to the fact that adventitious carbon can be bound differently on different surfaces (e.g. different roughness or loose surface bounds). No reproducible results were obtained by using this line as reference. A large number of workers have used a reference other than C 1s [Massies, 1985], [Debiemme-Chouvy et al, 1993], [Ballutand et al, 1995]. For example, for C 1s there are authors using 285 eV or 284.6 eV; for Au 4f<sub>7/2</sub>, 84.0 eV or 84.25 eV; for Ar 2p<sub>3/2</sub>, 240.3 eV or 241.5 eV etc.

In this work, corrections of the charge shift were accomplished by taking As(GaAs) at 41.1 eV as reference [Surdu-Bob et al, 2001]. This value was chosen from extensive previous work within the group on GaAs [Sullivan et al, 1998], [Sullivan et al, 1995] and agrees with many entries in the NIST database. Typical values of the charge shift found in this work were around 5.5 eV.

### 3. As peak fitting

a) As(GaAs) was fixed at 41.1 eV (value chosen as shown above), then a convenient scanned energy range was chosen to include the major peak and any subsidiary peaks associated to it. The binding energies were connected as shown in Table 3.2. The chemical shifts for As<sub>2</sub>O<sub>3</sub> and As<sub>2</sub>O<sub>5</sub> were chosen from previous work in our lab. The values for FWHM were chosen only as a starting point for fitting and were automatically minimized by fitting. Then, fitting was performed. After fitting, values as low as 1.57 eV for the FWHM of As(GaAs) were obtained.

Table 3.2 As peak fitting

Element	Binding energy [eV]	FWHM [eV]
As(GaAs)	41.1	1.6
As <sub>2</sub> O <sub>3</sub>	As(GaAs) + 3.1	1.9
As <sub>2</sub> O <sub>5</sub>	As(GaAs) + 4.4	1.9

b) sometimes, the fit was not satisfactory and a  $\pm 0.05$  eV variation of FWHM

was allowed. A further adjustment of FWHM for As(GaAs) was very occasionally needed.

#### **4. Ga peak fitting**

a) a convenient scanned energy range was chosen, similar to step 3.

b) energies and FWHM fixed as shown in Table 3.3. These values were chosen after performing a large number of analyses of the reference compounds (metallic Ga, Ga<sub>2</sub>O<sub>3</sub> powder) and of boiled GaAs wafer (details of analysis of these samples are given later in this chapter). The fit was then performed.

Table 3.3 Ga peak fitting

Element	Binding energy [eV]	FWHM [eV]
O 2s	23.3	2
Ga(OH) <sub>3</sub>	21.7	1.6
Ga <sub>2</sub> O <sub>3</sub>	20.7	1.6
Ga <sub>2</sub> O	20.1	1.6
Ga(GaAs)	19.1	1.6
Metallic Ga	18.48	1.5

c) fitting was performed again with an allowance for the FWHM of  $\pm 0.05$  eV

d) further adjustment of FWHM for Ga(GaAs) to a lower value and fit was occasionally required.

This fitting procedure ensured complete consistency when analysing spectra from different samples. Sensitivity factors given by the manufacturer of the XPS device are either theoretically calculated or generally determined and do not refer to a particular instrument. Therefore, sensitivity factors for the Ga and As lines were previously determined in our lab [Wei, 1995] and these values were used in this work.

The difference in BE between the photoelectron and the Auger lines is called the Auger parameter  $\alpha$ :

$$\alpha = KE_A - KE_P = BE_P - BE_a \quad (1)$$

$$KE_P = \alpha KE_A - \alpha \quad (2)$$

$$KE_P = h\nu - BE_P \quad (3)$$

$$KE_A + BE_P = \alpha + h\nu \quad (4)$$

A plot of the Auger kinetic energy versus photoelectron binding energy is independent of the photon energy. This is very useful when comparing data reported by authors who used different photon energies. The use of Auger parameter can help also in finding the chemical states existent on the surface. Any chemical state is characterised by a unique photoelectronic peak and by a unique Auger peak. The Auger parameter was used in this work and is tabulated in Chapter 4 for different compounds found on the samples analysed here.

Chemical shifts of Auger lines may be more pronounced than those of photoelectron lines. This fact can be very useful for identification of chemical states. Accurate assignment of Auger lines was more difficult than for photoelectron lines since the Auger lines cannot be synthesized due to broadening, in mixed oxides. Therefore, samples with a single oxide

had to be used for Auger line identification.

The spectrum of wet-etched GaAs sample (previously acquired in our lab) was also used for identification of the LMM line of Ga<sub>2</sub>O<sub>3</sub>. This sample contained Ga<sub>2</sub>O<sub>3</sub> only. The Ga<sub>2</sub>O<sub>3</sub> powder sample in which the powder grains are fully enclosed by Ga<sub>2</sub>O oxide was used for identification of the LMM line in the latter oxide.

XPS can be used to investigate not only the surface composition but also the variation of composition with depth by different methods:

### *1. Analysis using different core levels of the same element:*

Since the photoelectrons coming from different core levels have different energies, their sampling depth is different. This fact may be used to determine, from a single spectrum acquired, whether a particular atom species is enriched or depleted in the surface, relative to the bulk. In this work, along with the 3d lines, 2p<sub>3/2</sub> lines were also used. For GaAs, the sampling depths (at 0 take-off angle) are 67 Å (for 3d lines) and 29 Å (for 2p<sub>3/2</sub> lines) [Wei, 1995]. Peak positions of the 2p<sub>3/2</sub> region are given in Chapter 4.

### *2. Analysis using different photoelectron emission angles:*

Sampling depth ( $d$ ) varies with cosine of the take-off angle ( $\theta$ ) as follows

$$d = \lambda \cos \theta$$

and may be controlled by varying  $\theta$ . A spectrum recorded at normal emission has three times sampling depth of a spectrum recorded at 70° to the surface normal. This technique is called angle resolved XPS (ARXPS).

In this work, the ARXPS data is presented versus sampling depth, not versus take-off angle.

The combination of the two techniques presented above gives a better view in structural analysis. The higher BE peaks are single peaks and different chemical states may be identified more easily. In this work, ARXPS analysis of virgin, clean and plasma etched GaAs wafers were undertaken. The etched samples were processed with argon plasma at 100 W, 10 mT and 90 mT.

### *3. Analysis using different X-ray energies*

Since the photoelectron kinetic energy ( $E_k$ ) is related to the X-ray energy ( $h\nu$ ) by the Einstein relation ( $E_k = h\nu - E_b$ ) then, the sampling depth of photoelectrons from any core level of any element will increase with increasing energy. Thus, XPS spectra excited

using different X-ray sources may be used to generate composition depth profiles. The differences in the energies emitted by Al and Mg x-ray sources available for this project is not great enough to make this technique useful here.

#### 4. Sputter-depth profiling

All the above techniques are non-destructive but their maximum sampling depth is approx. 100 Å. In order to probe greater depths, it is necessary to remove some of the sample surface and expose the underlying layers for analysis. The most popular method is in-situ inert gas ion etching. A major limitation of this technique is the destructive nature of the ion-beam which can lead to erroneous conclusions. When the surface is sputtered, reduction of surface oxides and damage of layers usually occur. A very good reference on this subject is [Choudhury, PhD, 1991].

##### 3.3.1.1 Calculation of oxide layer thickness

Etching of GaAs with plasmas has indicated oxide formation. The oxidation of GaAs surfaces has both a theoretical and a technological importance. The oxide films have an important role in the passivation of semiconductor surfaces, in mask diffusion and in preparation of wafers for epitaxy. Also, their electrical properties are a key feature of electronic device fabrication. Hence, studying the variation of composition and thickness with plasma parameters is of great importance. Following is a description of the method for calculation of oxide thickness using XPS data.

The calculation of oxide thickness was based on the model described by Briggs and Seah [1990]. The model is based on the assumption that the oxide layer is made of a homogeneous mixture of As and Ga oxides (as shown in Figure 3.3).

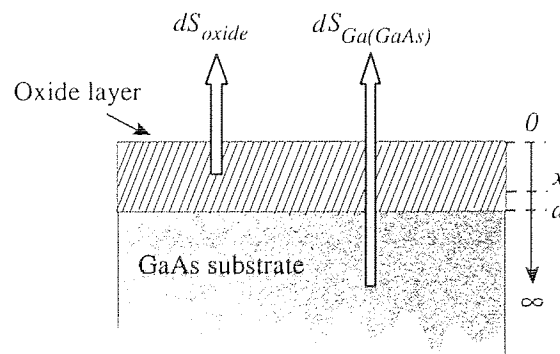


Figure 3.3. Simple model of the layered structure of GaAs

The photoelectron intensity signal is generally expressed as:

$$I = J\sigma(h\nu)L(\gamma)D(E_k)T(E_k) \int_0^\infty n(z) \exp\left(-\frac{z}{\lambda(E_k) \cos \theta}\right) dz \quad (1)$$

where  $J$  is the flux of the X-ray,  $\sigma$  is the cross section for emission of a photoelectron from a core level of an atom excited by a photon of energy  $h\nu$ ,  $L(\gamma)$  is the angular asymmetry of the intensity of the photo-emission of the core level electron of the atom.  $D(E_k)$  is the detection efficiency for an electron with a kinetic energy of  $E_k$  transmitted by the electron spectrometer;  $T(E_k)$  is the analyser transmission function;  $n(z)$  is the atomic density of the atom at a depth of  $z$ ;  $\lambda(E_k)$  is the attenuation length (values used in this work are given earlier in this section) and  $\theta$  is the electron take-off angle.

By integrating (5) from infinity to  $d$ , the XPS signal coming from the substrate can be written as:

$$S_{GaAs} \cong C_{GaAs} \lambda \exp(-d/\lambda \cos \theta) \quad (2)$$

Similarly, the signal  $S_{oxide}$  coming from an oxide (component of the oxide layer) is given by the integration of (1) between  $d$  and  $0$ :

$$S_{oxide} \cong C_{oxide} \lambda [1 - \exp(-d/\lambda \cos \theta)] \quad (3)$$

From equations (2) and (3), the thickness of the oxide layer  $d$  can be calculated using the equation:

$$d/\lambda \cos \theta = \ln(S_{GaAs}C_{oxide}/S_{oxide}C_{GaAs} + 1) \quad (4)$$

where  $C_{oxide}$  and  $C_{GaAs}$  can be simply calculated from the XPS data at the corresponding  $\theta$ . In this work, calculation of oxide thickness was performed at zero take-off angle because the values for XPS intensities are most reliable, but XPS data at any  $\theta$  should give similar results for  $d$ .

### 3.3.1.2 Sources of errors in data acquisition and processing

XPS analysis introduce errors due to both spectrum acquisition and spectrum processing. Poor statistics of spectrum acquisition is the most important factor and is mostly caused by using the channeltron at the end of its lifetime. An idea of the size of error that can be introduced by this factor is given in Chapter 5 where XPS data of a sample acquired in three different stages of the lifetime of the channeltron are given. An important source of errors is due to accuracy of spectrum fitting, also. This procedure did not introduce an error greater than 5%.

### 3.3.2 Atomic Force Microscopy (AFM)

Several techniques are available for magnifying the detailed features of a surface. Optical instruments are limited by the wavelength of visible light and resolve objects down to approximately 0.5 microns. Atomic force microscopy provides topographic information

down to the angstrom level.

In this work, for topography and measurement of etch depth, a Topometrix AFM was employed. The etch rate was determined by simply dividing the depth of the etch pit by the etch time.

The principle of operation is based on the interaction of the tip with the atoms of the sample under investigation. A physical probe is scanned across the sample using piezoelectric ceramics while a feedback loop is used to maintain a constant interaction between the probe and the sample. The force sensor measures the deflection of a cantilever on which a tip is mounted as it is shown in Figure 3.4. The amount of motion of the cantilever is calculated from the difference in light intensity (detected by a photodetector) of the laser beam deflected by the cantilever.

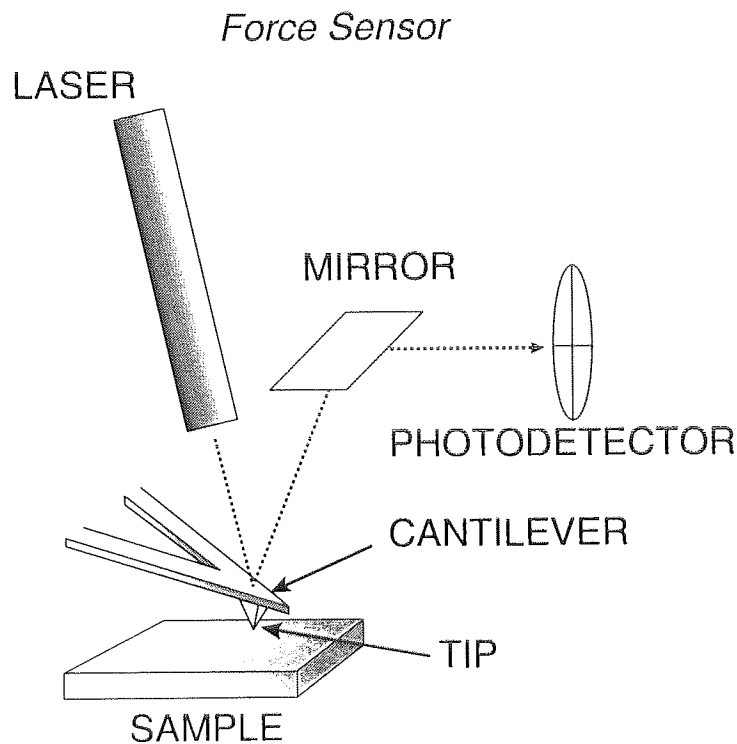


*Figure 3.4 The force sensor*

Hooke's law gives the relationship between the cantilever motion  $x$ , and the force required to generate the motion,  $F$ :

$$F = -kx \quad (9)$$

The position of the probe and the feedback signal are electronically recorded to produce a three dimensional map of the surface. Various measurements of surface roughness are also available. The feedback electronic circuit is combined with a probe and piezoelectric ceramics to create the positioning mechanism. With this positioning mechanism the sensor can be maintained at a fixed distance from the surface. When the sensor moves towards the surface, the output of the sensor electronics increases. The differential amplifier

compares the increased value to the reference value and outputs a correction voltage. The correction voltage excites the piezoelectric ceramic in such a way that the sensor is pulled away from the surface.

### 3.4 Reference compounds

When etching with inert gases, physical processes are not the only process taking place; surface oxidation process are also encountered. Therefore, before understanding the etching mechanisms with inert gases, a study of the oxides that can be encountered on GaAs surface proved to be essential. Reference samples were required to unequivocally identify the various oxides on the GaAs surface. Also, the appearance of unknown gallium compounds on the surface of GaAs has led to the necessity of a separate study aiming at their characterization. For this purpose, a set of XPS analyses of reference compounds (such as metallic Ga, Ga<sub>2</sub>O<sub>3</sub> powder and virgin and boiled GaAs wafer) subjected to different conditions has been also undertaken in this work.

#### 3.4.1 Ga<sub>2</sub>O<sub>3</sub> powder

The Ga<sub>2</sub>O<sub>3</sub> powder supplied by PI-KEM Ltd had been previously analysed by X-ray Powder Diffraction method to check its purity. It was found that it had the  $\beta$  modification (see Chapter 2) and it was free of other gallium oxides.

XPS and depth profile analysis were also performed. For depth profile analysis, the powder was exposed to 1  $\mu$ A, 3 keV Ar ion beam. The procedure consisted of etching 12 levels of the sample for different amounts of time and taking XPS analysis level by level as shown in Table 3.4. The chamber pressure was  $2 \times 10^{-7}$  torr. For XPS analysis, the powder was mounted by pressing it gently onto double-sided tape.

Table 3.4 Duration of etching for each level of argon ion bombardment of Ga<sub>2</sub>O<sub>3</sub> powder

Level	0	1	2	3	4	5	6	7	8	9	10	11	12
Etch time [s]	0	10	120	420	720	1320	1920	2520	3120	4320	5520	6720	7920

It should be mentioned that problems were encountered when studying Ga<sub>2</sub>O<sub>3</sub> powder samples using the XPS technique due to surface charging effects. X-ray photoelectron spectrum calibration is very difficult when analysing samples which do not contain reference peaks (e.g. As(41.1 eV) as in the case of GaAs). Introducing an external calibrant (Au) by mixing gold powder with Ga<sub>2</sub>O<sub>3</sub> powder did not prove to be useful probably due to the imperfection in obtaining homogeneous powder mixtures. Differential

charging of the material while exposed to X-rays for analysis most probably occurred. This is probably the explanation for the poor reproducibility of the results obtained. Therefore, Auger and  $2p_{3/2}$  lines of spectra of pure  $Ga_2O_3$  powder were used. These peaks are also useful for complete identification of components, even for surfaces containing reference peaks, as it will be discussed later.

### 3.4.2 Metallic Ga

Two samples of metallic Ga were also analysed using XPS. One of the metallic Ga samples was in the form of 5 mm pieces and was supplied by BDH Labs. and the other was prepared in our laboratory by thermal evaporation. These two different samples of metallic Ga were chosen in order to study gallium oxide formation immediately after making the sample and also after a long time of exposure to air. In order to avoid preferential charging of the sample when exposed to X-rays for analysis, a fine mesh of Ga on a conductive material had to be constructed. For this purpose, a fine, flat gold substrate was firstly prepared and a metallic Ga mesh was deposited on top of it. Following is a description of the technique used for preparing the "new" metallic gallium sample.

The system used is a standard thermal evaporation device shown in Figure 3.5. The material to be evaporated was placed in a high melting point crucible. The crucible was heated up till the melting point of the particular metal was reached. The vapours of the evaporated material filled the process chamber and deposited on the substrate placed 10 cm away from the crucible. After obtaining the gold substrate, the vacuum chamber was opened and a fine innox mesh was placed 2 cm above the substrate. Pieces of metallic Ga were then evaporated through the fine mesh and deposited on the gold substrate.

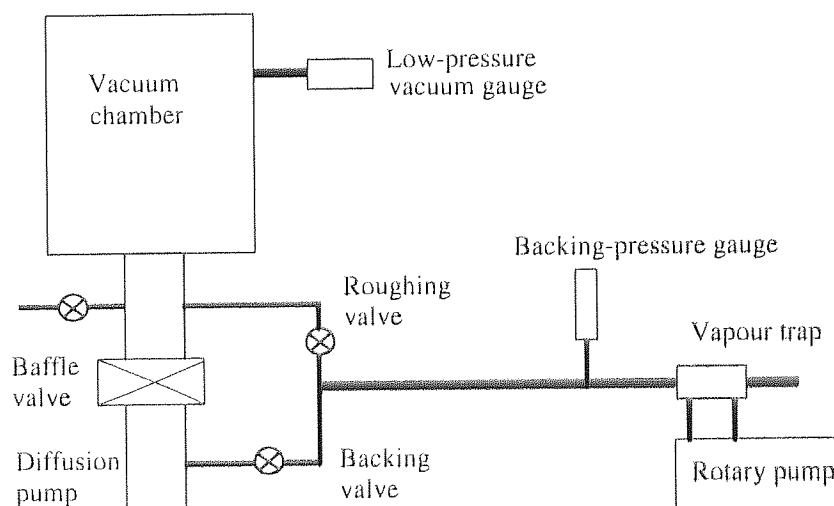


Figure 3.5 Device for thermal evaporation

The "old" sample was analysed after prolonged exposure to air (approx. 3 years) and the other one was analysed soon after fabrication (but also after air exposure). Caution had to be taken on the duration of analysis in the UHV chamber due to the low evaporation temperature of pure metallic Ga (30°C).

### 3.4.3 Boiled GaAs

Doubt exists concerning the assignment of a peak at 21.6 eV. As pointed out in Chapter 2, in current literature, either a hydroxide of Ga or GaAsO<sub>4</sub> are proposed to be found at this binding energy. Peak synthesis of O 1s peak cannot be used for accurate identification because this peak of oxygen is very complex.

A separate experiment was designed for obtaining a hydroxide on the surface of GaAs. A number of GaAs wafers were boiled in deionized water for four hours and analysed shortly after treatment. A simple lab-type electric heater was used for boiling the samples. Care had to be taken when boiling to top up the water so that the surface would not get into direct contact with ambient air before boiling process was finished. Immediately after boiling, the samples were transferred in the XPS analysis chamber.

## Chapter 4. Experimental results

Since this work is dedicated to the study of surface compositional changes of GaAs subjected to plasma treatments, a good knowledge of plasma constituents, energy and density is absolutely necessary. The first section of this chapter provides minimal characterization of the plasmas used here. A compilation of the knowledge of the RF plasma is constructed with the aid of current literature on plasma diagnosis and is presented in Chapter 6. Results of surface analyses are presented in the second section of this chapter. A separate study aiming the identification of the GaAs surface oxides was also undertaken and is presented in the first part of Section 4.2 dedicated to the results of the surface analysis. Finally, surface compositional changes of GaAs subjected to plasmas of inert gases, oxygen, hydrogen and mixtures are given.

### 4.1 RF plasma diagnosis

To understand the surface processes taking place when the surface is exposed to plasma, both the energies and densities of plasma constituents need to be known. A change in the plasma input parameters (gas pressure, power) causes a change in the type, amount and velocity of active species generated. In the following section typical values of plasma characteristics, including DC bias, sheath width, current density and ion energy distributions for all gases and mixtures used are given.

#### 4.1.1 Plasma of inert gases: Ar and Ne

##### *The DC bias*

Comparison of the variation of DC bias ( $V_{dc}$ ) at the cathode with pressure and power for argon and neon plasmas is given in Figure 4.1 and 4.2, respectively. Almost no change with pressure of  $V_{dc}$  was observed in these plasmas. The fact that the DC bias is proportional to the square root of applied RF power was reported by Layberry [PhD, 1999].

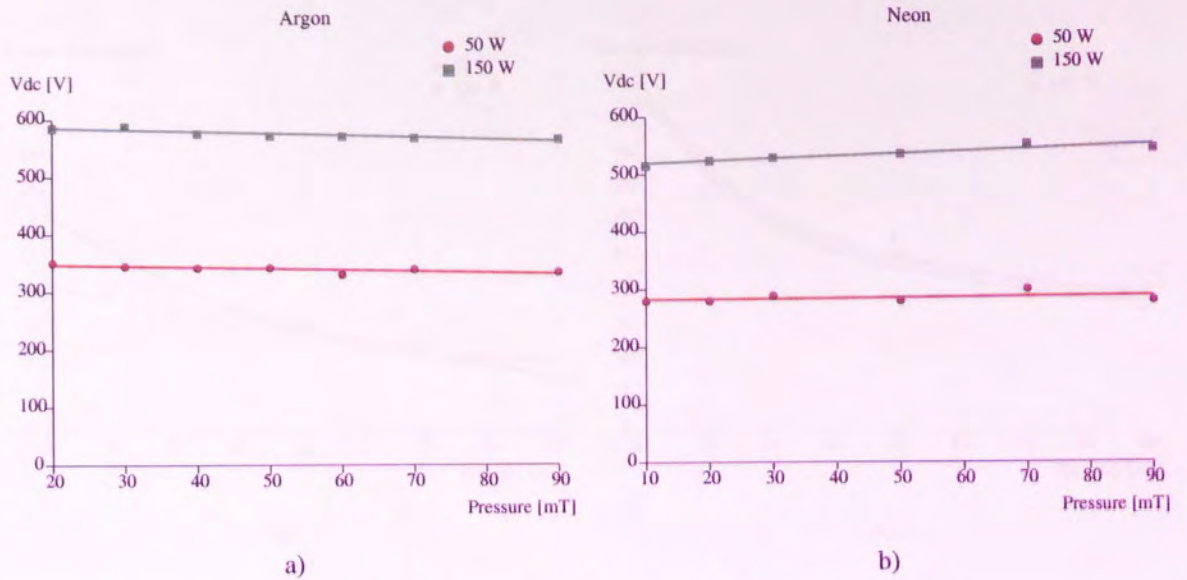


Figure 4.1 Variation of  $V_{dc}$  with pressure in a) Ar and b) Ne plasma

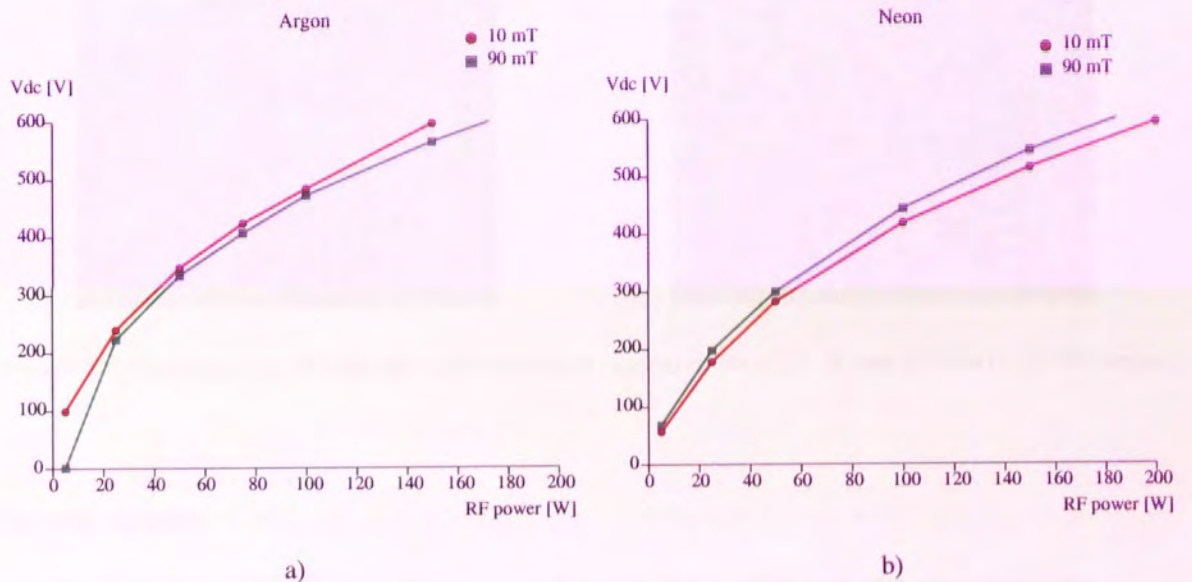


Figure 4.2 Variation of  $V_{dc}$  with power in a) Ar and b) Ne plasma

### The RF sheath

Changes in cathode sheath width (Figure 4.3) and sheath brightness (Figure 4.4) give an idea about the intensity of the processes taking place at the cathode. The boundary of the bulk plasma is brighter or darker depending on plasma parameters. The sheath of both plasmas turned gradually dark and became more diffuse with pressure. Both plasma bulk and sheath became brighter with increasing power.

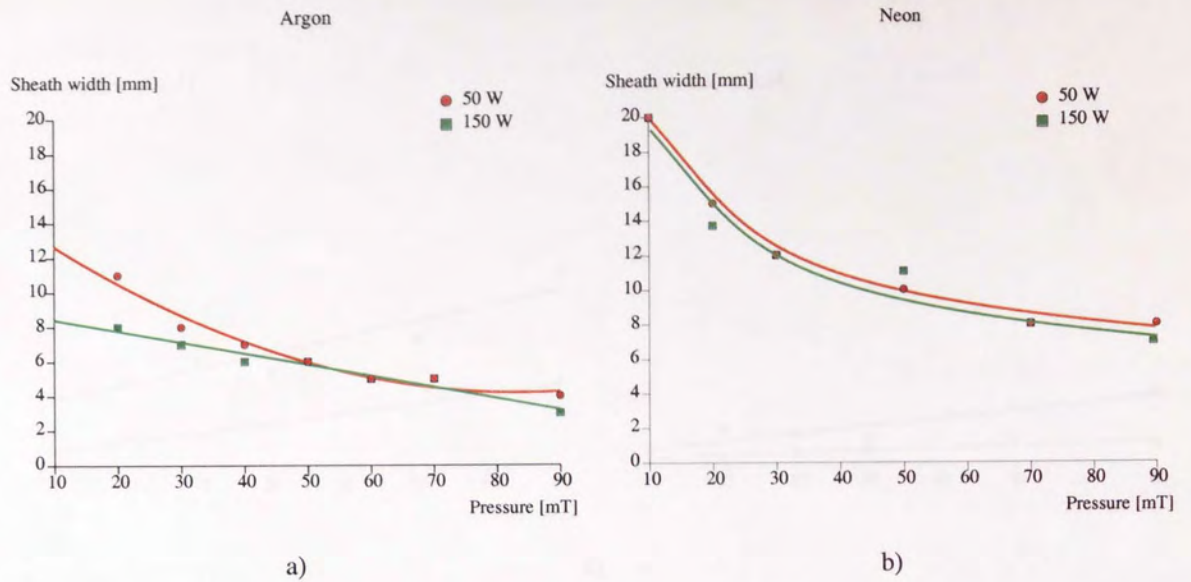


Figure 4.3 Variation of sheath width with pressure at 50 W and 150 W in a) Ar and b) Ne RF plasma



Figure 4.4 Photograph of the plasma - cathode sheath region; a) 90 mT, 5 W and b) 90 mT, 150 W (argon)

### Current density

Current density increased with pressure and power for both argon and neon plasmas (Figure 4.5). In the case of neon, current density was significantly smaller than for argon.

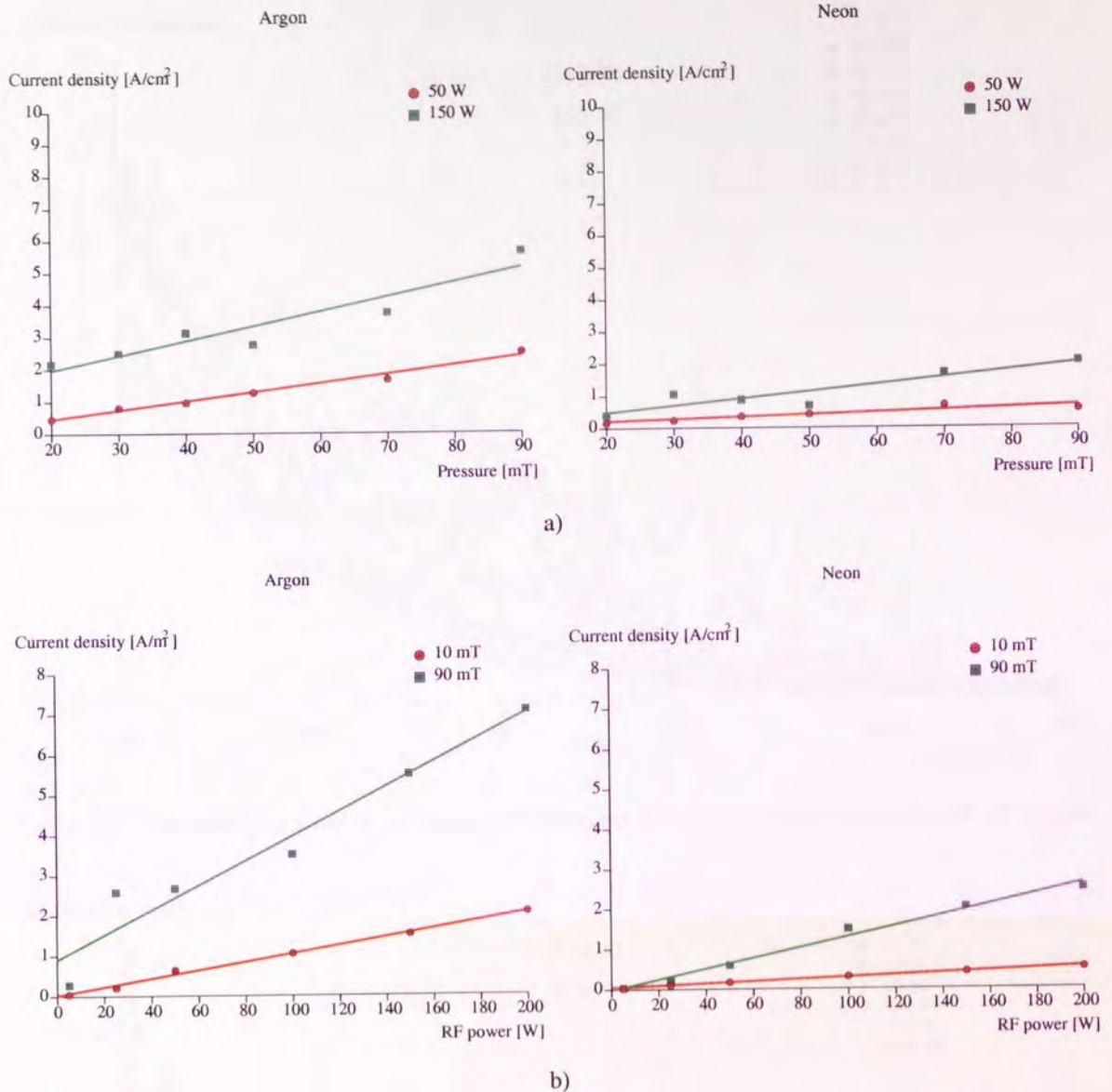


Figure 4.5 Variation of current density with a) pressure and b) power for Ar and Ne plasmas, respectively

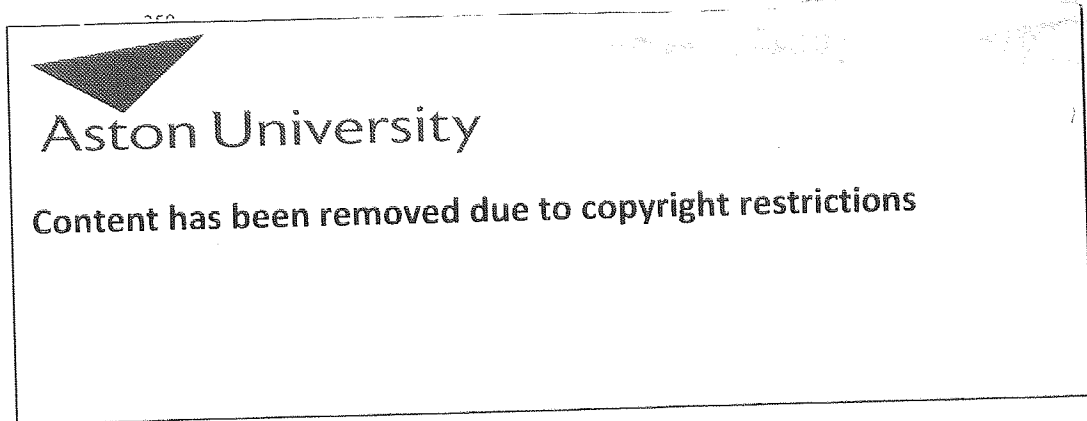
### Ion energy distribution

At low pressures ( $<1$  mT), the ions pass through the sheath without colliding. Their energy can be determined by the difference between the plasma potential and the electrode potential. For pressures used in this work (over 10 mT) this approach would not give accurate ion energies because collisions within the sheath scatter ions and change their energy. In this case, one must take into account the cross sections of the processes in the plasma by modelling. A model has been developed [Layberry, PhD, 1999] which follows electrons and ions through time varying potentials using experimentally determined  $V_{dc}$ ,  $V_f$  and sheath width as input parameters. The major specie formed in argon plasma is  $Ar^+$  [Rusu, PhD, 2001].

The variation of  $Ar^+$  ion energy distribution (IED) with power and pressure is given in Figure 4.6 a), b), respectively. As expected, ion energies are higher at high powers and are

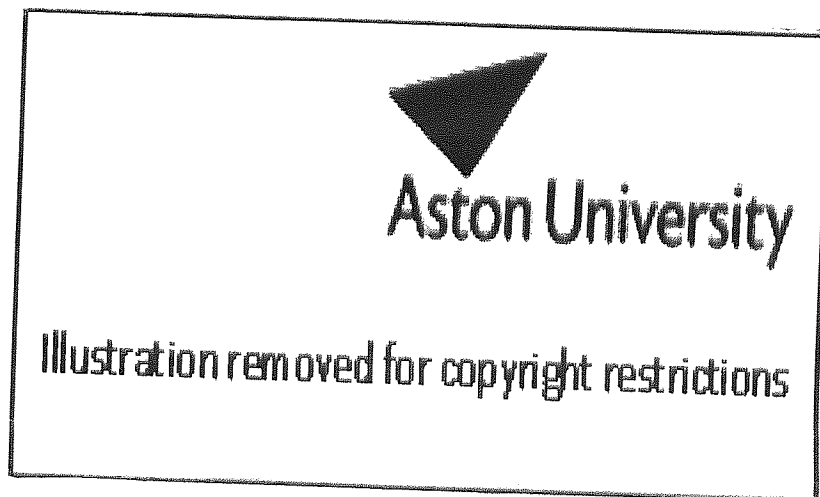
lower with increasing pressure. This result was also found by other workers [Wild, 1991].

Relative ion count [a.u.]



200 300 400 500 600 700  
Ion energy [eV]

Figure 4.6 a) Number of ions versus ion energy for a number of pressures in the range 20 + 90 mT (argon).



0 100 150 200 250 300 350 400  
Ion energy [eV]

Figure 4.6 b) Number of ions versus ion energy for a number of powers in the range 5 + 200 W (argon).

### 4.1.2 O<sub>2</sub> plasma

Due to its property of removing carbon from the chamber walls, oxygen plasma is used for *seasoning* of the process chamber.

The only positive oxygen ions found in a pure oxygen plasma are O<sub>2</sub><sup>+</sup> and O<sup>+</sup> [Rusu, PhD, 2001]. As shown in Chapter 2, the charge transfer cross sections for the collisions between these two ions and molecular oxygen in the energy ranges 100 - 200 eV are of the same order of magnitude. Therefore, calculation of mean free path and current density for these two ions give similar results.

#### *The DC bias and the sheath width*

Variation of V<sub>dc</sub> with power and pressure (Figure 4.7) was similar with that of argon, but the sheath width (Figure 4.8) showed an increase with power, in contrast to the case of argon.

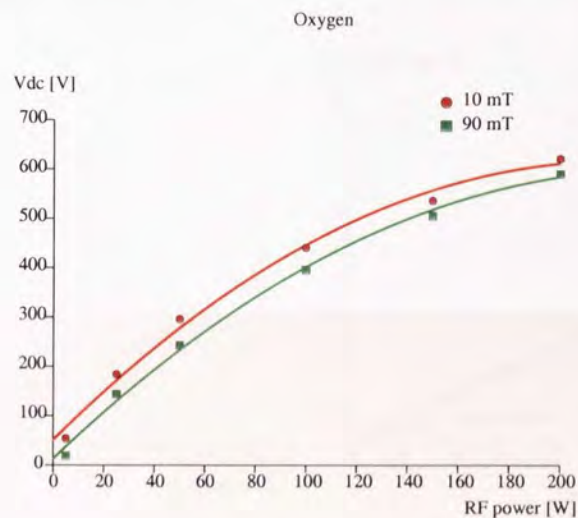


Figure 4.7 Variation of V<sub>dc</sub> with power for pressures of 10 and 90 mT (oxygen plasma)

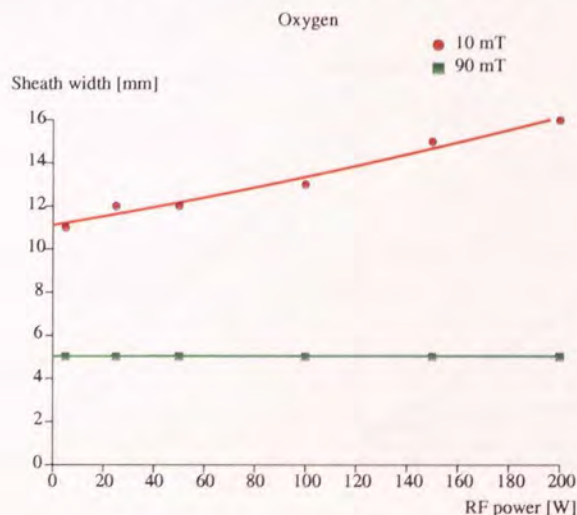


Figure 4.8 Variation of sheath width with power at pressures of 10 mT and 90 mT (oxygen plasma)



Figure 4.9 Photograph of the plasma - cathode sheath region, 90 mT, 150 W (oxygen plasma)

### Current density

Current density was calculated from experimental data as shown in Chapter 2.

Variation of current density showed very similar behaviour for  $O_2^+$  and  $O^+$  with pressure and RF power (Figure 4.10).

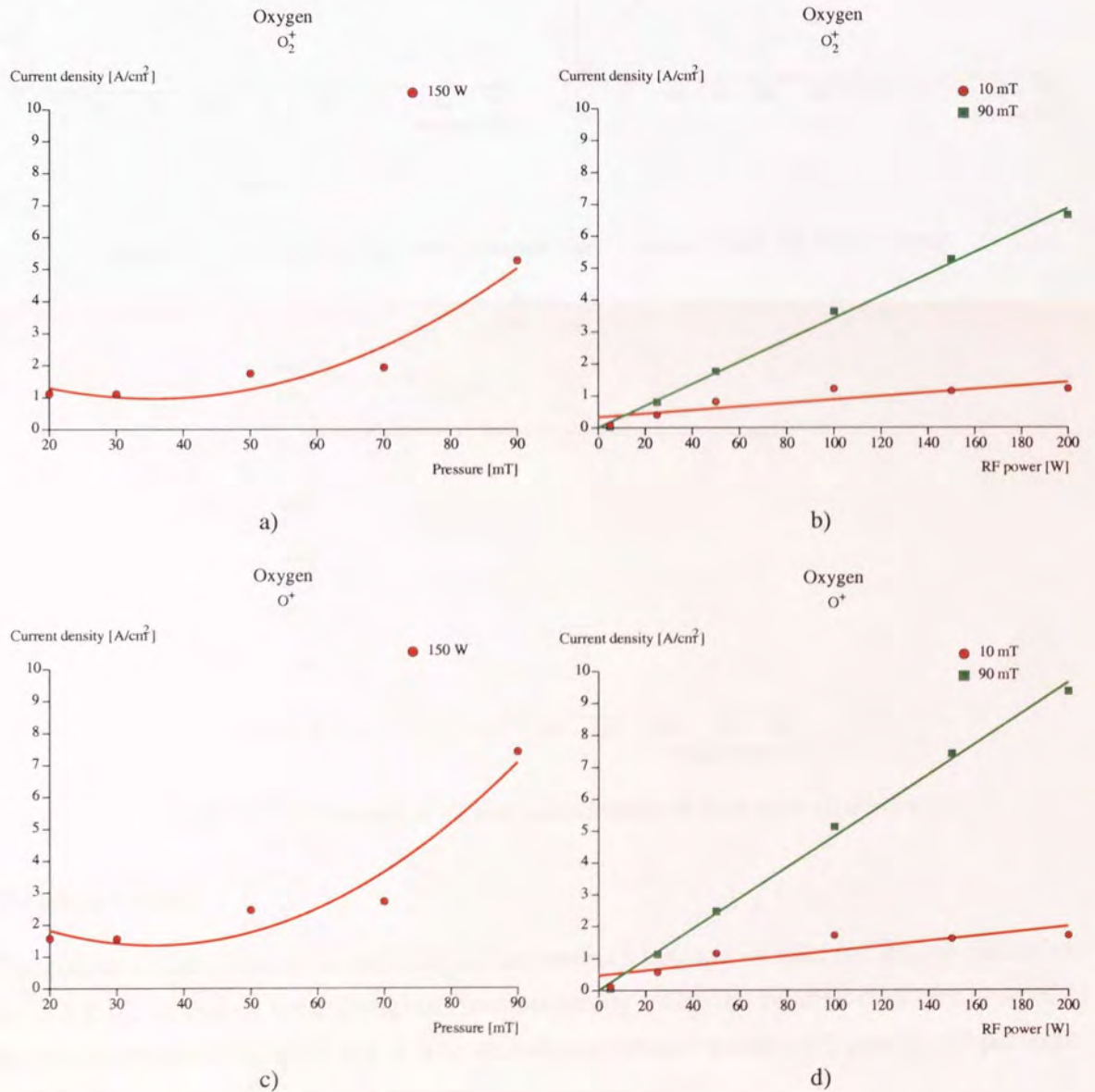


Figure 4.10 Variation of current density with pressure a) and c) for  $O_2^+$ ; with power b) and d) for  $O^+$

### 4.1.3 Ar + O<sub>2</sub> plasma

#### The DC bias

The same trend of  $V_{dc}$  with power and pressure was observed in the mixture (Figure 4.11 a) and b)), as in the case of argon and oxygen plasmas separately. No variation with oxygen concentration was observed (Figure 4.11 c)).

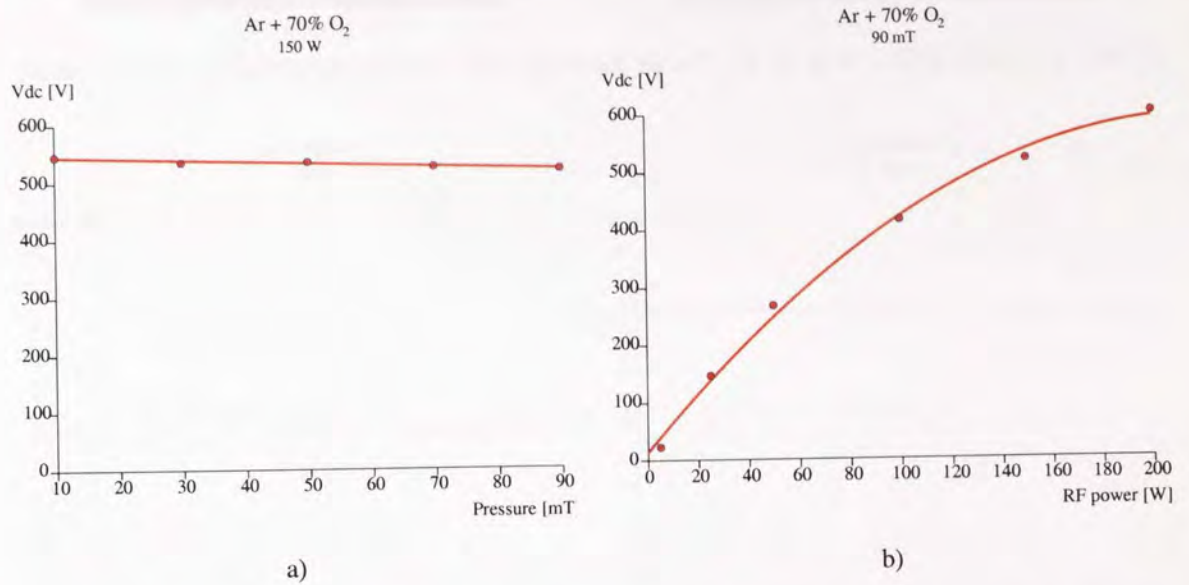


Figure 4.11 Variation of  $V_{dc}$  with a) pressure and b) power (Ar + 70% O<sub>2</sub> plasma)

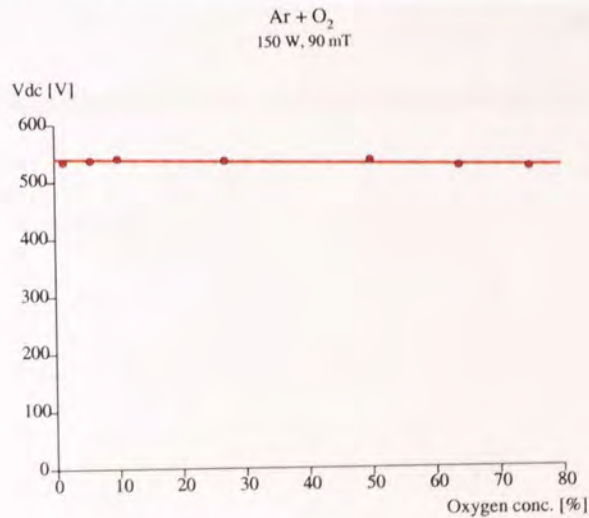


Figure 4.11 c) Variation of  $V_{dc}$  with concentration of O<sub>2</sub> in Ar + O<sub>2</sub> mixture

#### The sheath width

The colour of this plasma is a mixture of the separate colours - violet (of argon) and green (of oxygen), its colour tone changing "proportionally" with the relative concentration of the two components (Figure 4.12). The variation of sheath width with power and pressure at 70% O<sub>2</sub> was similar to that of pure oxygen (Figure 4.13).



Figure 4.12 Photograph of the plasma - cathode sheath, 90 mT, 150 W, a) Ar + 50% O<sub>2</sub> b) Ar + 75% O<sub>2</sub>

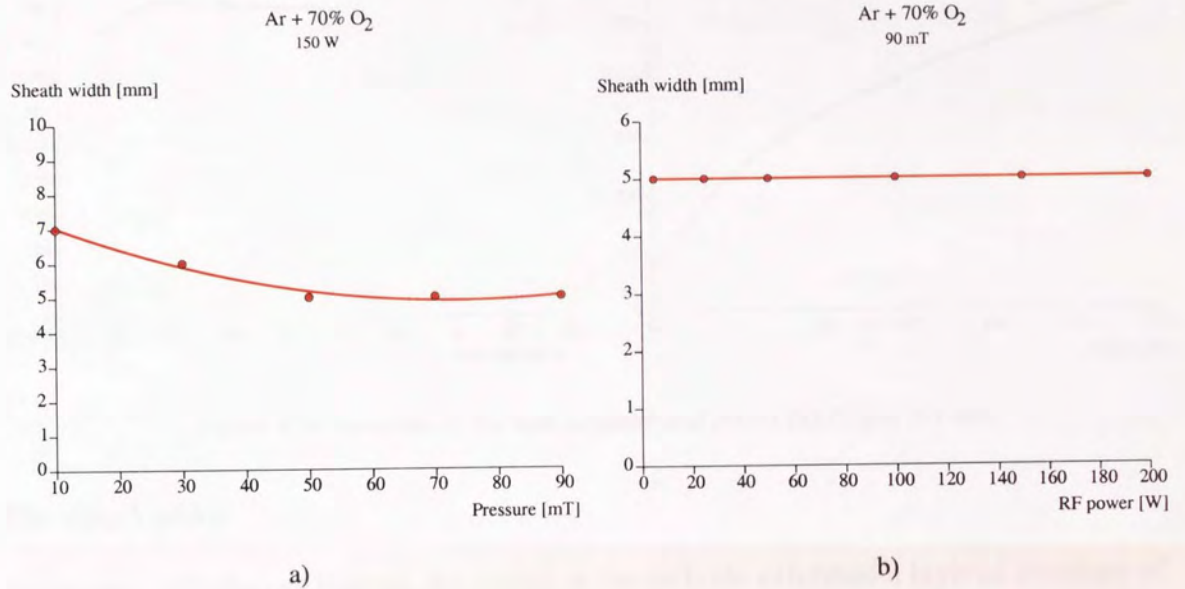


Figure 4.13 Variation of sheath width with a) pressure and b) power in Ar + 70% O<sub>2</sub> mixture

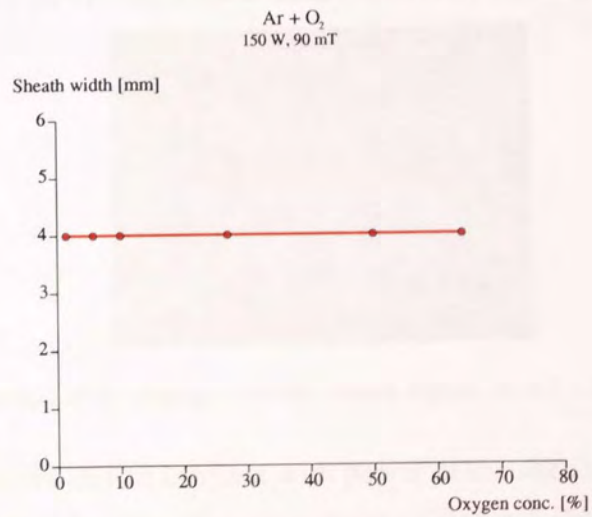


Figure 4.13 c) Variation of sheath width with O<sub>2</sub> concentration in Ar + O<sub>2</sub> mixture

#### 4.1.4 H<sub>2</sub> plasma

##### *The DC bias*

Variation of  $V_{dc}$  with power in hydrogen plasma (Figure 4.14) had the same trend as for the other gases, e.g. proportional to the square root of applied RF power.  $V_{dc}$  was unchanged with pressure.

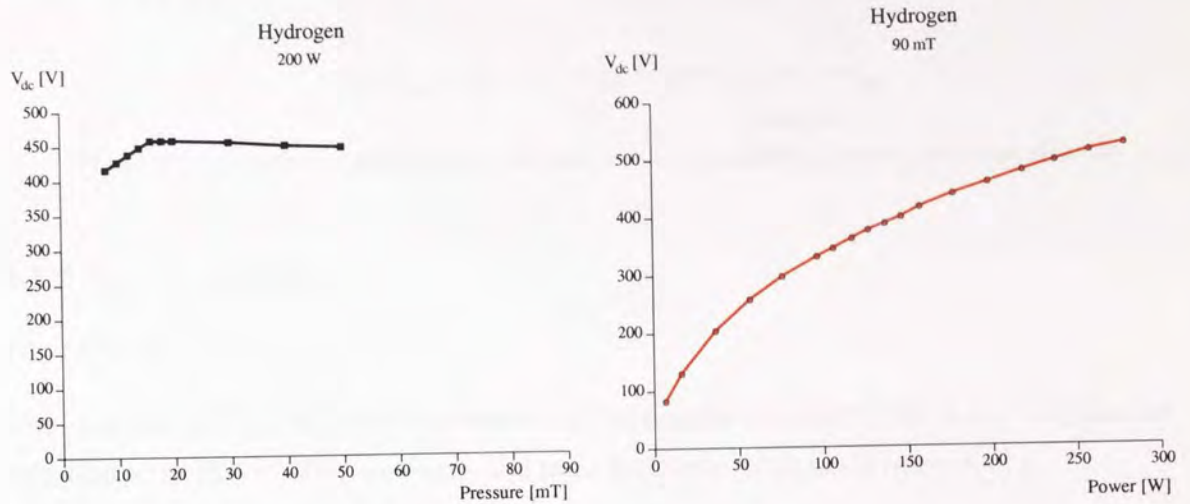


Figure 4.14 Variation of  $V_{dc}$  with pressure and power (hydrogen plasma)

##### *The sheath width*

In the case of hydrogen plasma, the sheath at the cathode exhibited a layered structure of bright and dark spaces, as can be observed in Figure 4.15. Hydrogen plasma is bright violet. With increasing power the plasma sheath boundary became brighter.



Figure 4.15 Photograph of the plasma - cathode sheath region, 90 mT, 150 W (hydrogen plasma)

A decrease with pressure and an increase with power of the sheath width in hydrogen plasma were found, as in the case of oxygen plasma (Figure 4.16).

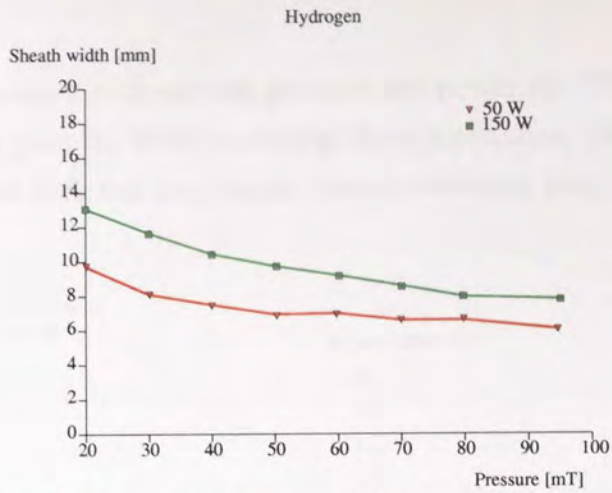


Figure 4.16 Variation of sheath width with pressure at two different powers (hydrogen plasma)

### 4.1.5 Ar + H<sub>2</sub> plasma

#### The DC bias

The variation of  $V_{dc}$  with power, pressure and hydrogen concentration of Ar + H<sub>2</sub> plasma was similar to that of the pure argon and pure hydrogen plasmas (Figure 4.17).

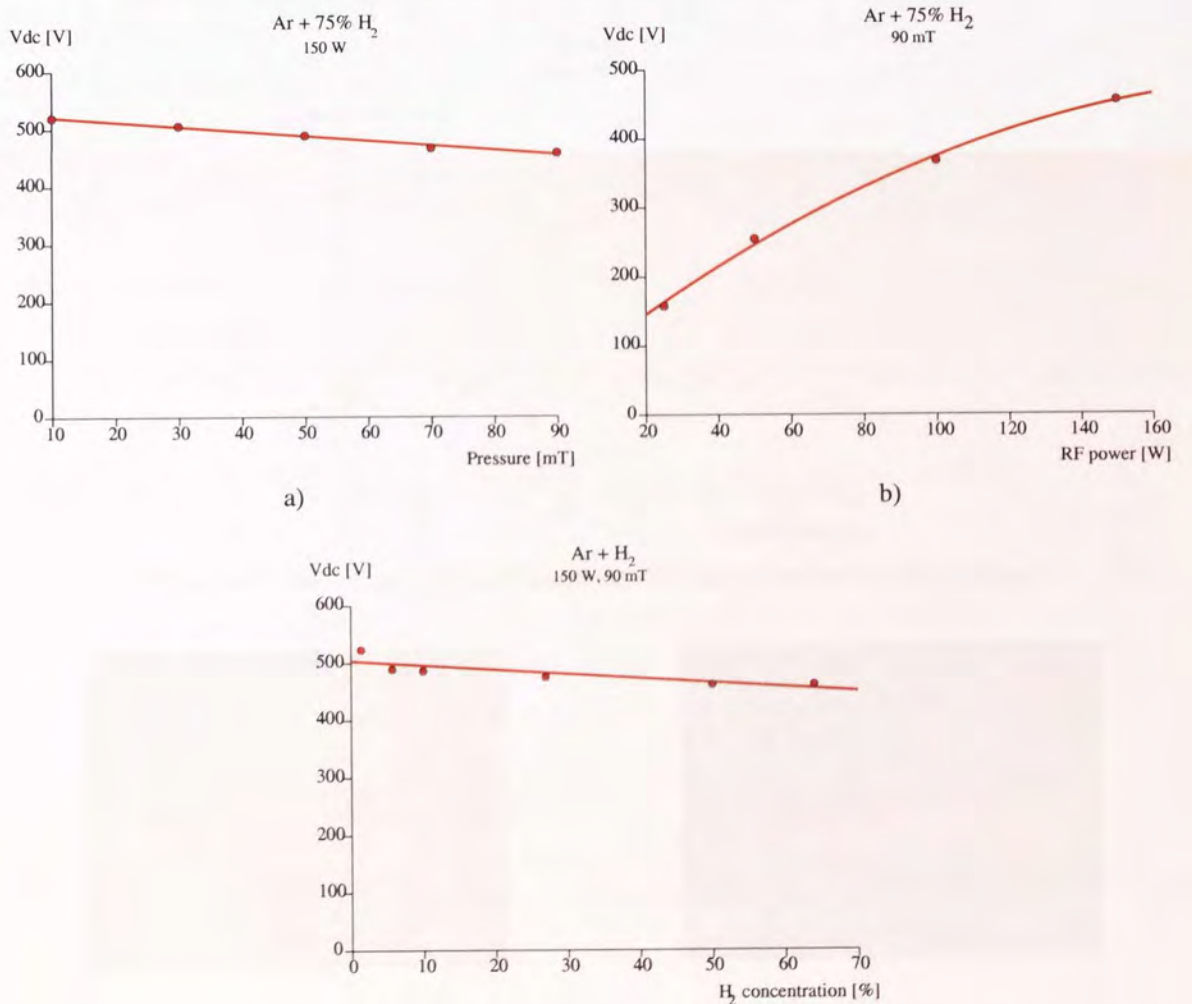


Figure 4.17 Variation of  $V_{dc}$  with a) pressure, b) power and c) concentration of H<sub>2</sub> in Ar + H<sub>2</sub> mixture

### The sheath width

The sheath width behaviour with varying pressure and power for 75% H<sub>2</sub> (Figure 4.18) was similar to that for pure H<sub>2</sub>. With increasing H<sub>2</sub> concentration, the sheath width increased but remained dark and the plasma - sheath boundary became bright (Figure 4.19).

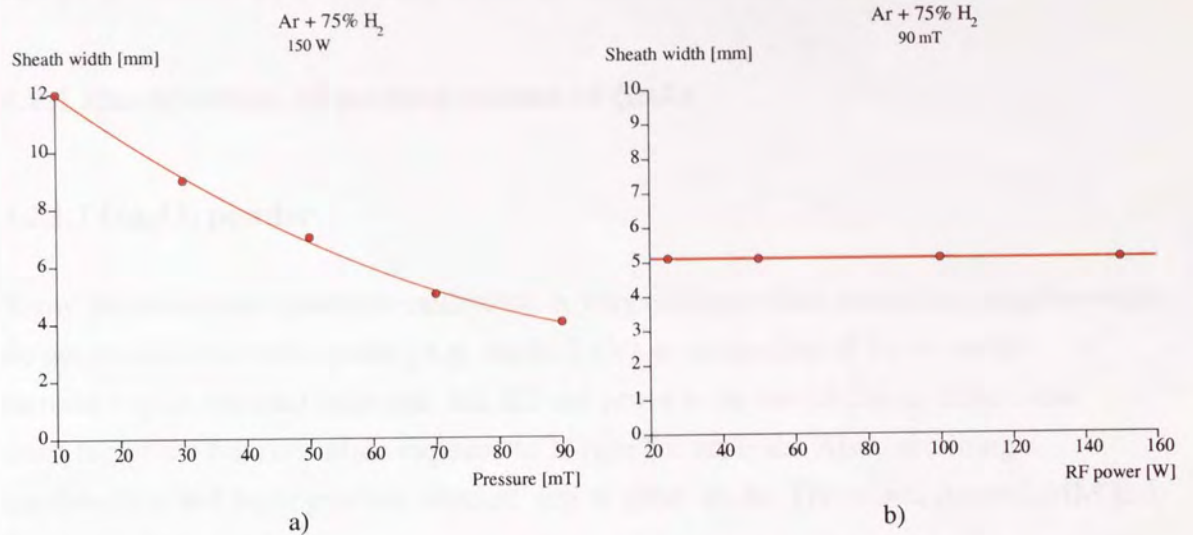


Figure 4.18 Variation of sheath width with a) pressure and b) power (Ar + H<sub>2</sub> plasma)

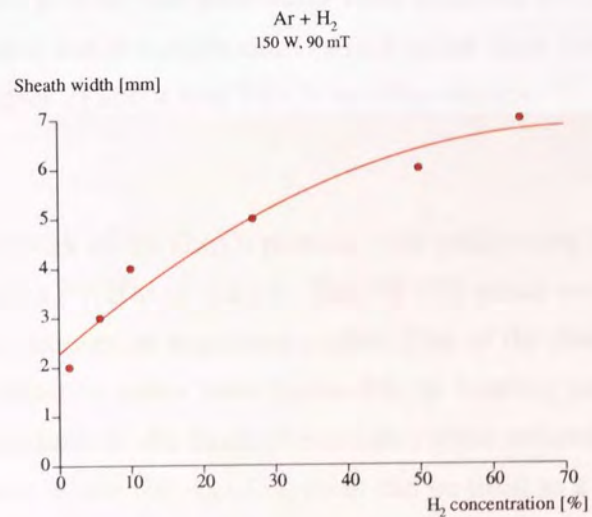


Figure 4.18 c) Variation of sheath width with H<sub>2</sub> concentration (Ar + H<sub>2</sub> plasma)



Figure 4.19 Photograph of the plasma-cathode sheath, 90 mT, 150 W, a) Ar + 50% H<sub>2</sub>, b) Ar + 75% H<sub>2</sub>

## 4.2 XPS analysis

In order to understand surface-plasma interactions in GaAs, surface oxides had to unequivocally be identified. For this purpose, reference compounds of pure materials such as Ga<sub>2</sub>O<sub>3</sub> powder and metallic Ga were analysed. GaAs wafers subjected to different surface treatments were also used to further characterization of surface oxides.

### 4.2.1 Identification of surface oxides of GaAs

#### 4.2.1.1 Ga<sub>2</sub>O<sub>3</sub> powder

X-ray photoelectron spectrum calibration is very difficult when analysing samples which do not contain reference peaks {e.g. As(41.1 eV) as in the case of GaAs wafer}. Introducing an external calibrant, Au, did not prove to be useful due to differential charging of the mixture while exposed to X-rays for analysis. Also, obtaining a reproducible and homogeneous mixture was in great doubt. Therefore, Auger LMM and 2p<sub>3/2</sub> lines were used.

The "as received" Ga<sub>2</sub>O<sub>3</sub> powder had previously been analysed by XRD to check its purity. It was found that it had  $\beta$  modification (which is the most stable of all Ga<sub>2</sub>O<sub>3</sub> modifications, see Chapter 2) and it was free from other oxides.

#### *XPS analysis*

Synthesizing the Ga 3d peak of the Ga<sub>2</sub>O<sub>3</sub> powder, two peaks were found with an energy separation of 0.6 eV and a FWHM of 1.6 eV. The FWHM value was deduced by iteration over a large number of samples, as explained earlier. One of the peaks must be Ga<sub>2</sub>O<sub>3</sub>. Knowing that higher oxidation states have higher BE, its binding energy was assigned at  $20.7 \pm 0.1$  eV. This was done on the basis of extensive cross referencing of oxide peaks formed on GaAs samples where the As (-Ga) peak can be used as a calibrant. For this identification, Auger parameters were also used. All Auger parameters found in this work are shown in Table 4.1. This assignment also agrees with other measurements [Bresse, 1994], [Pan et al, 1997], [Alnot et al, 1985].

Table 4.1 BE of the 3d peaks of Ga and As, the Ga and As Auger parameters (AP) and the FWHM intensity for the indicated compounds

Element	BE [eV]	AP [eV]	FWHM [eV]
metallic Ga	18.48	400.2	$1.6 \pm 0.1$
Ga(GaAs)	19.1	401.2	$1.55 \pm 0.1$
As(GaAs)	41.1	220.6	$1.8 \pm 0.1$
Ga(OH) <sub>3</sub>	21.6	-----	$1.7 \pm 0.1$
Ga <sub>2</sub> O <sub>3</sub>	20.7	405	$1.7 \pm 0.1$
Ga <sub>2</sub> O	20.1	403.8	$1.7 \pm 0.1$
As <sub>2</sub> O <sub>3</sub>	44.3	223.4	$1.9 \pm 0.1$
As <sub>2</sub> O <sub>5</sub>	45.3	-----	$1.9 \pm 0.1$

As shown in Chapter 2, the only lower stable oxidation state of Ga is Ga<sub>2</sub>O. Hence the peak 0.6 eV below the Ga3d peak of the Ga<sub>2</sub>O<sub>3</sub> (at 20.1 eV) must be assigned to Ga<sub>2</sub>O.

Figure 4.20 a) with 3d peaks of Ga<sub>2</sub>O<sub>3</sub> powder shows that the majority of the oxide (89%) is Ga<sub>2</sub>O. Calculations using the 2p<sub>3/2</sub> peaks (which give more surface-specific information) indicate almost 100% Ga<sub>2</sub>O. This is somewhat surprising since the powder is specified as Ga<sub>2</sub>O<sub>3</sub> (determined from XRD characterization); therefore, this result must be due to the fact that the Ga<sub>2</sub>O<sub>3</sub> grains are covered with a layer of Ga<sub>2</sub>O (greater than 6 nm). The calculated relative concentrations are given in Table 4.2. Thus, as was mentioned earlier, this material is an ideal sample for confident identification of the position of the Ga<sub>2</sub>O LMM line at 424 eV.

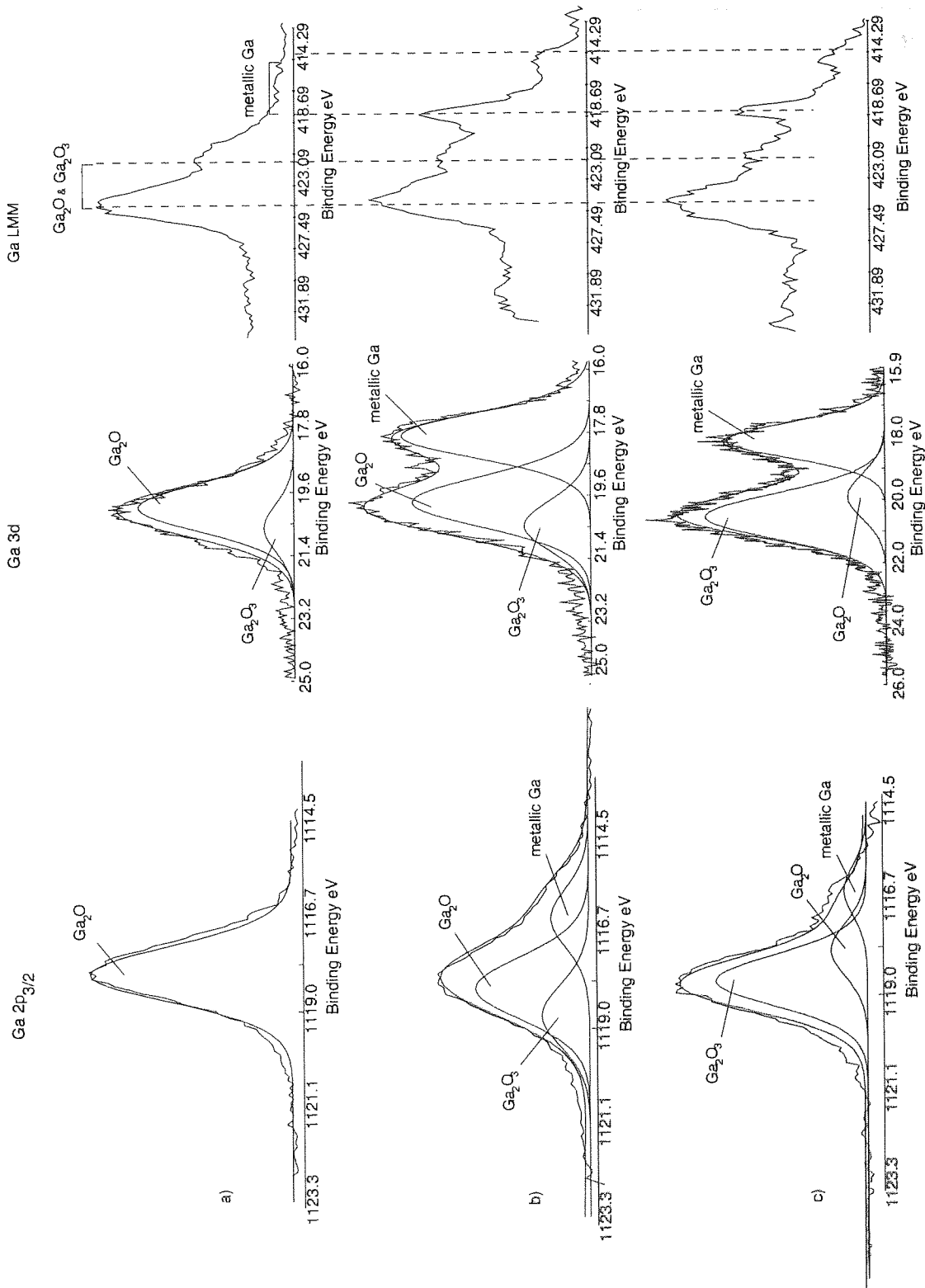


Figure 4.20 Ga  $2p_{3/2}$ , Ga 3d and Ga LMM spectra of: a)  $\text{Ga}_2\text{O}_3$  powder; b) thermally evaporated metallic Ga; c) as-received metallic Ga

Table 4.2 Surface composition of the reference compounds

Sample \ chemical compound	Ga(-Ga)		Ga <sub>2</sub> O		Ga <sub>2</sub> O <sub>3</sub>	
	3d	2p <sub>3/2</sub>	3d	2p <sub>3/2</sub>	3d	2p <sub>3/2</sub>
Ga <sub>2</sub> O <sub>3</sub> powder [%]	-----	-----	89	100	11	-----
Air exp. met. Ga [%]	31.7	13.5	14.2	24	54.1	62.5
Thermal. evap. met. Ga [%]	35.9	15	45.6	65.4	18.5	19.6

The Ga 2p<sub>3/2</sub> lines for these powder samples showed peaks at 1118.8 eV and 1118.0 eV corresponding to Ga<sub>2</sub>O<sub>3</sub> and Ga<sub>2</sub>O, respectively. These results are used in the later analysis.

#### *Argon ion bombardment of Ga<sub>2</sub>O<sub>3</sub> powder*

The study of the argon ion bombardment of Ga<sub>2</sub>O<sub>3</sub> powder was intended to reveal the reduction of the oxidation state of Ga<sub>2</sub>O<sub>3</sub>. In Table 4.3, relative concentration of the surface compounds at different stages of ion bombardment is presented. As can be observed, surface changes have taken place with increasing time of ion bombardment and processes like Ga<sub>2</sub>O formation by reduction of Ga<sub>2</sub>O<sub>3</sub>, Ga<sub>2</sub>O reduction and appearance of metallic Ga are believed to have contributed to these results.

Table 4.3 Surface composition of argon-bombarded Ga<sub>2</sub>O<sub>3</sub> powder at different stages of bombardment.

level/compound	metallic Ga [%]	Ga <sub>2</sub> O [%]	Ga <sub>2</sub> O <sub>3</sub> [%]
level 0	0	89	11
level 1	2	80	18
level 6	8	81	11
level 9	7	81	12
level 12	15	81	4

Of interest here is the surface composition obtained after level 12 of ion bombardment. The amount of Ga<sub>2</sub>O<sub>3</sub> is negligible here and the Auger spectrum gives the profile of GaLMM for Ga<sub>2</sub>O which can be used for further studies. The GaLMM spectra for the levels mentioned above are shown in Figure 4.21.

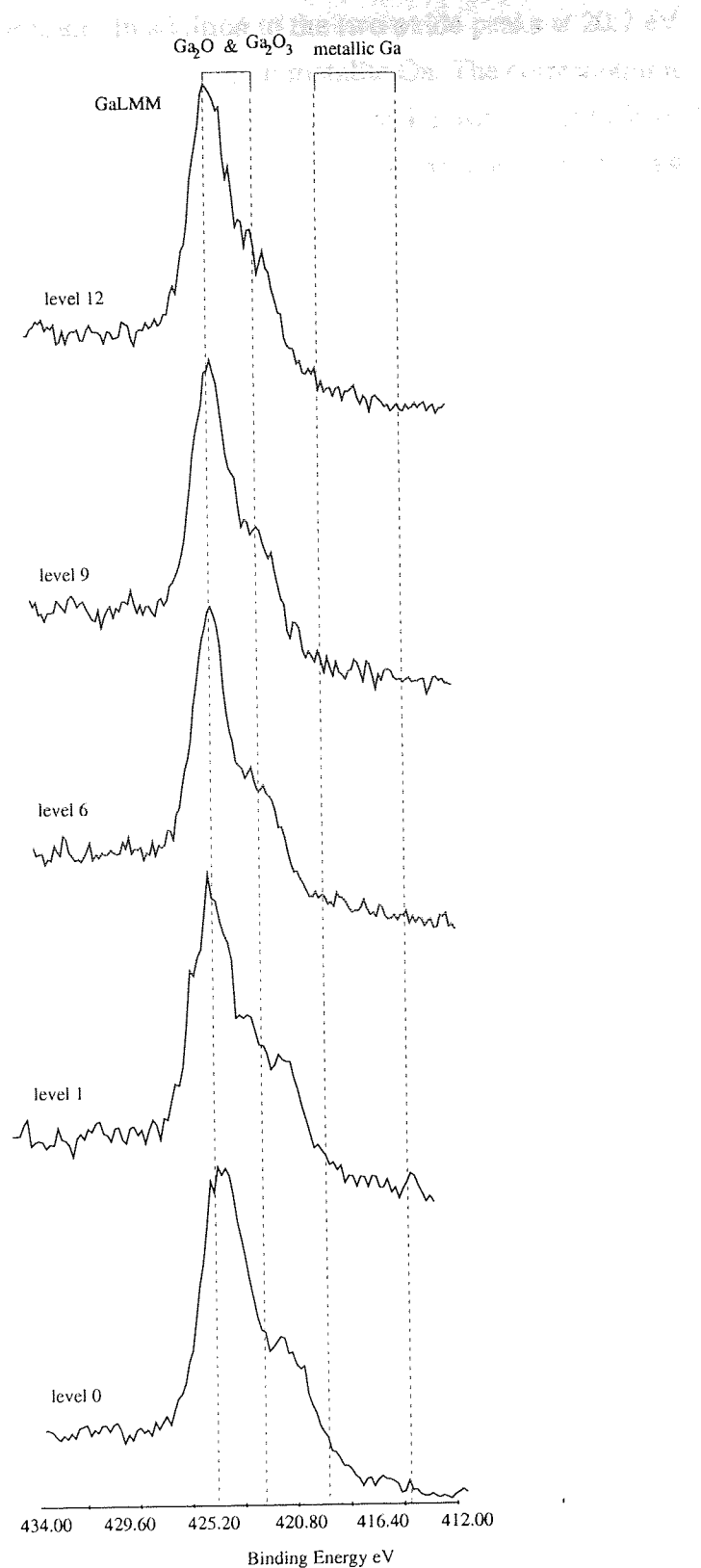


Figure 4.21 Argon ion bombardment of Ga<sub>2</sub>O<sub>3</sub> powder

#### 4.2.1.2 Metallic Ga

*Thermally evaporated metallic Ga*

Analysis of the thermally evaporated metallic Ga sample revealed the existence of three

peaks in the Ga 3d region of the spectrum. In addition to the two oxide peaks at 20.7 eV and 20.1 eV, there is a peak at 18.3 eV corresponding to metallic Ga. The corresponding peaks in the 2p<sub>3/2</sub> spectrum were 1118.8, 1118 and 1116.4 eV. Peak positions and FWHM are shown in Table 4.4. The Ga LMM spectrum also contained an extra doublet at 418.4 eV and 414 eV attributed to metallic Ga.

The calculated oxide layer thickness was 54 Å (the method of calculation is presented in Chapter 3 and the XPS data is given in Table 4.5) and it is clear from Figure 4.20 b) that the majority oxide is Ga<sub>2</sub>O at a concentration of about 45.6% whereas the concentration of Ga<sub>2</sub>O<sub>3</sub> was only 18.5% (calculated using the 3d peaks). The relative concentrations of Ga<sub>2</sub>O and Ga<sub>2</sub>O<sub>3</sub> calculated from the 2p<sub>3/2</sub> peaks were about 65.4% and 19.6%, respectively.

Table 4.4 Peak positions and FWHM of the thermally evaporated metallic Ga.

Chemical compound	Ga(-Ga)		Ga <sub>2</sub> O		Ga <sub>2</sub> O <sub>3</sub>	
	3d	2p <sub>3/2</sub>	3d	2p <sub>3/2</sub>	3d	2p <sub>3/2</sub>
BE [eV]	18.3	1116.4	20.1	1118	20.7	1118.8
FWHM [eV]	1.5	1.7	1.6	1.8	1.6	1.8

Table 4.5 XPS data used for calculation of oxide thickness of the metallic Ga samples. The calculated oxide thickness (d) is also given.

Sample\parameter	C <sub>metGa</sub> [%]	S <sub>metGa</sub> [a.u.]	C <sub>Ga<sub>2</sub>O<sub>3</sub></sub> [%]	S <sub>Ga<sub>2</sub>O<sub>3</sub></sub> [a.u.]	d [Å]
Thermal. evap. met. Ga	100	953	28.9	493	54
Air exp. met. Ga	100	365	79.3	623	60

#### *Prolonged air exposure of metallic Ga*

As a further reference, an "as received" solid metallic Ga sample was also examined. This was exposed much longer to the ambient air than the thermally evaporated sample. The 3d and 2p<sub>3/2</sub> photoelectron and Auger LMM lines are shown in Figure 4.20 c). In this sample very similar peak positions were observed to those found for the evaporated Ga sample, but the relative concentrations of the oxides was much different. In the case of the sample exposed longer to air, the total oxide film thickness was 60 Å. The majority oxide was Ga<sub>2</sub>O<sub>3</sub> (54%) with the Ga<sub>2</sub>O concentration (derived from the 3d peaks) here representing

only 14.2% while the relative Ga<sub>2</sub>O concentration calculated from the 2p<sub>3/2</sub> peaks was about 24%. We attribute the difference in the oxide composition and thickness of the two samples to the extended exposure to air. Comparison of the surface composition calculated using 2p<sub>3/2</sub> and also 3d peaks (Table 4.2) showed a faster increase of Ga<sub>2</sub>O than of Ga<sub>2</sub>O<sub>3</sub> which indicates that in this layer of mixed oxides, Ga<sub>2</sub>O concentration is higher at the outermost surface than near the substrate.

Angle resolved XPS analysis would have given more information on the layered structure of the oxides present on the metallic Ga samples but a prolonged analysis of the sample in the UHV chamber would have caused unwanted evaporation of the material on the chamber walls since Ga can be liquid at 30°C.

#### 4.2.1.3 Virgin and clean GaAs wafer

The Ga 3d spectra of a cleaned GaAs wafer (shown in Figure 4.22) contained three major components with BEs of 19.1 eV, 20.1 eV, 20.7 eV corresponding to Ga(-As), Ga<sub>2</sub>O and Ga<sub>2</sub>O<sub>3</sub>. The corresponding BEs of the 2p<sub>3/2</sub> lines were 1117.0, 1118.0 and 1118.8 eV. A very small concentration of a compound with associated binding energy of Ga 3d at 21.6 eV was also observed with a corresponding 2p<sub>3/2</sub> peak at 1119.8 eV. A further peak was detected in the 3d spectra at 23.2 eV in some samples. The As 3d spectrum consisted of three components at 41.1 (used as a calibrant), 44.2 and 45.2 eV, corresponding to As(-Ga), As<sub>2</sub>O<sub>3</sub> and As<sub>2</sub>O<sub>5</sub>, respectively and the corresponding As 2p<sub>3/2</sub> peaks were found at energies of 1322.9, 1325.9 and 1327.0 eV. The positions of the Ga LMM line are similar to those found in previous experiments with some variation in the positions of the Ga<sub>2</sub>O<sub>3</sub>/Ga<sub>2</sub>O LMM lines due to broadening effects for mixed oxides. The LMM lines of As(GaAs) is at 261.6 eV on the BE scale while the position for As<sub>2</sub>O<sub>3</sub> is 267.4 eV. Table 4.1 shows the binding energies, Auger parameter and the full width at half maximum of the important peaks.

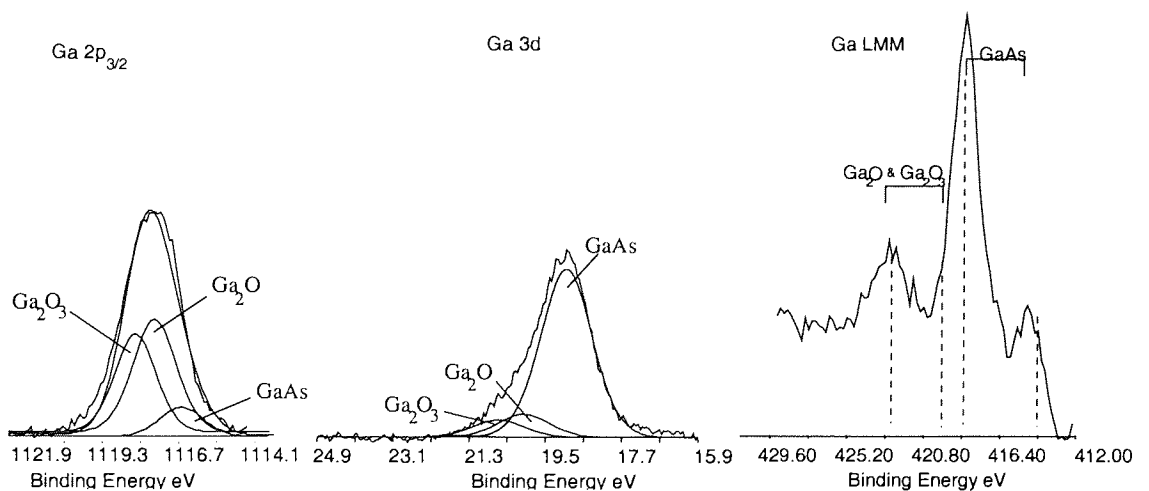


Figure 4.22 Ga 2p<sub>3/2</sub>, Ga 3d and Ga LMM spectra of cleaned GaAs wafer

ARXPS analysis of virgin and clean (Figure 4.23 a) and b), respectively) GaAs wafers revealed a layered structure of the surface oxide. In this figure, the relative concentration of surface components is plotted against depth. As can be observed, the concentrations of Ga(GaAs) and As(GaAs) are equal. Also, the total As oxide is equal to the total Ga oxide. No important changes of surface composition after ex-situ cleaning in acetone and isopropile (the cleaning procedure is presented in Section 3.1) were observed. The thickness of the surface oxide remained constant after cleaning. The calculated oxide thickness for these samples was 9 Å; similar values for virgin and clean GaAs wafers had been reported by other authors [Bresse, 1994], [Barrett et al, 1990]. Another important result of the ARXPS analysis is that the lower oxidation states of Ga and As are nearer to the substrate than the higher oxidation states. Also, the higher oxidation states form a shallower oxide than the others in both virgin and cleaned GaAs.

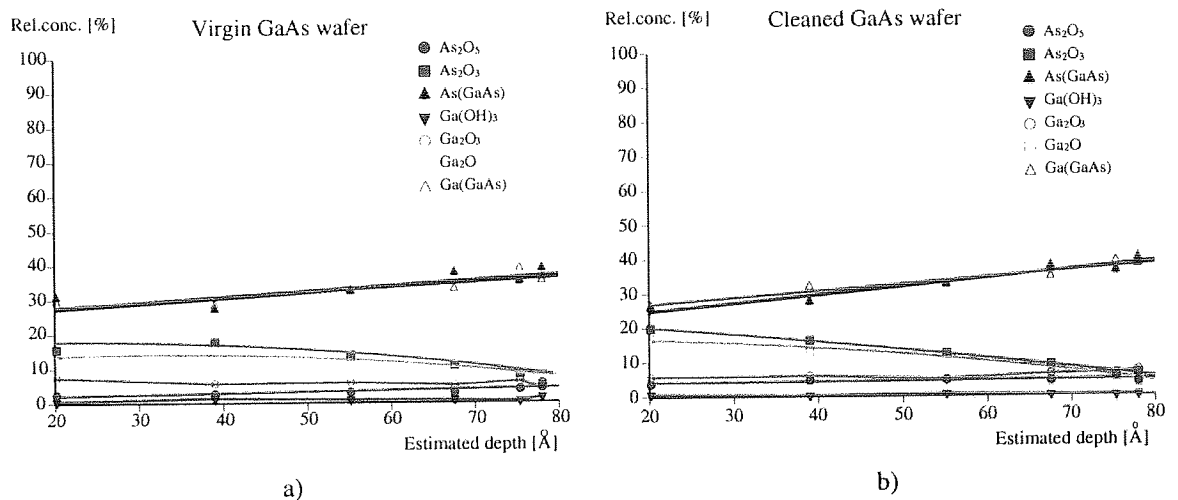


Figure 4.23 ARXPS analysis of a) virgin and b) wet cleaned samples. Estimated depth was calculated with:  $d = \lambda \cos\theta$ , where  $\lambda = 26 \text{ \AA}$

#### 4.2.1.4 Boiled GaAs in water

Doubts exist concerning the assignment of the peak at 21.6 eV binding energy. Therefore, it was decided to deliberately promote formation of the hydroxide by boiling a sample of GaAs in water. The XPS analysis showed a large increase in the amount of the component having a binding energy of 21.6 eV, from 3% to 27% on the boiled sample (Figure 4.24).

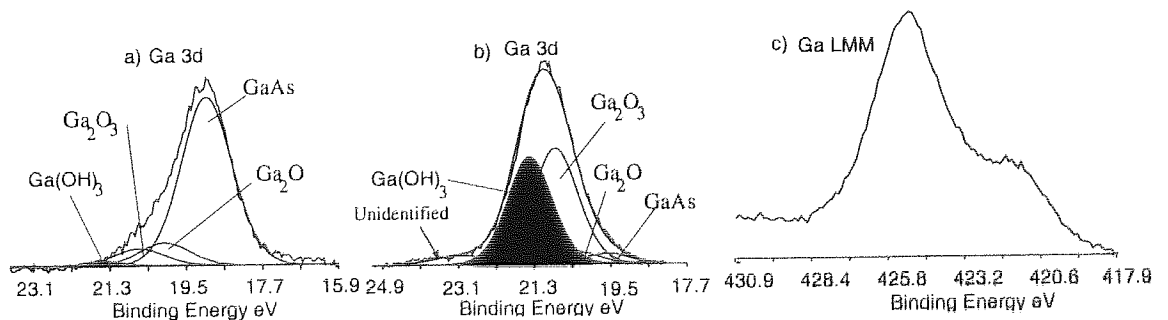


Figure 4.24 The 3d fit of GaAs a) before boiling; b) after boiling; c) Ga LMM of boiled wafer.

#### 4.2.1.5 The O 2s peak

In the current literature, a peak appearing in the spectrum of certain samples with a BE of  $23.2 \pm 0.4$  eV is given different assignments, but no explanation of its origin is given [Bresse, 1994], [Lu et al, 1993].

Ga and O 1s spectra for argon plasma etched samples, normalized to As(-Ga) at 41.1 eV, are given in Figure 4.25. A correlation between the O 1s peak height and the appearance of the peak at 23.2 eV is easily observable and it is discussed in Chapter 5. The amount of the surface oxide (shown in the figure) is calculated relative to the total amount of surface species (Ga, As and oxides).

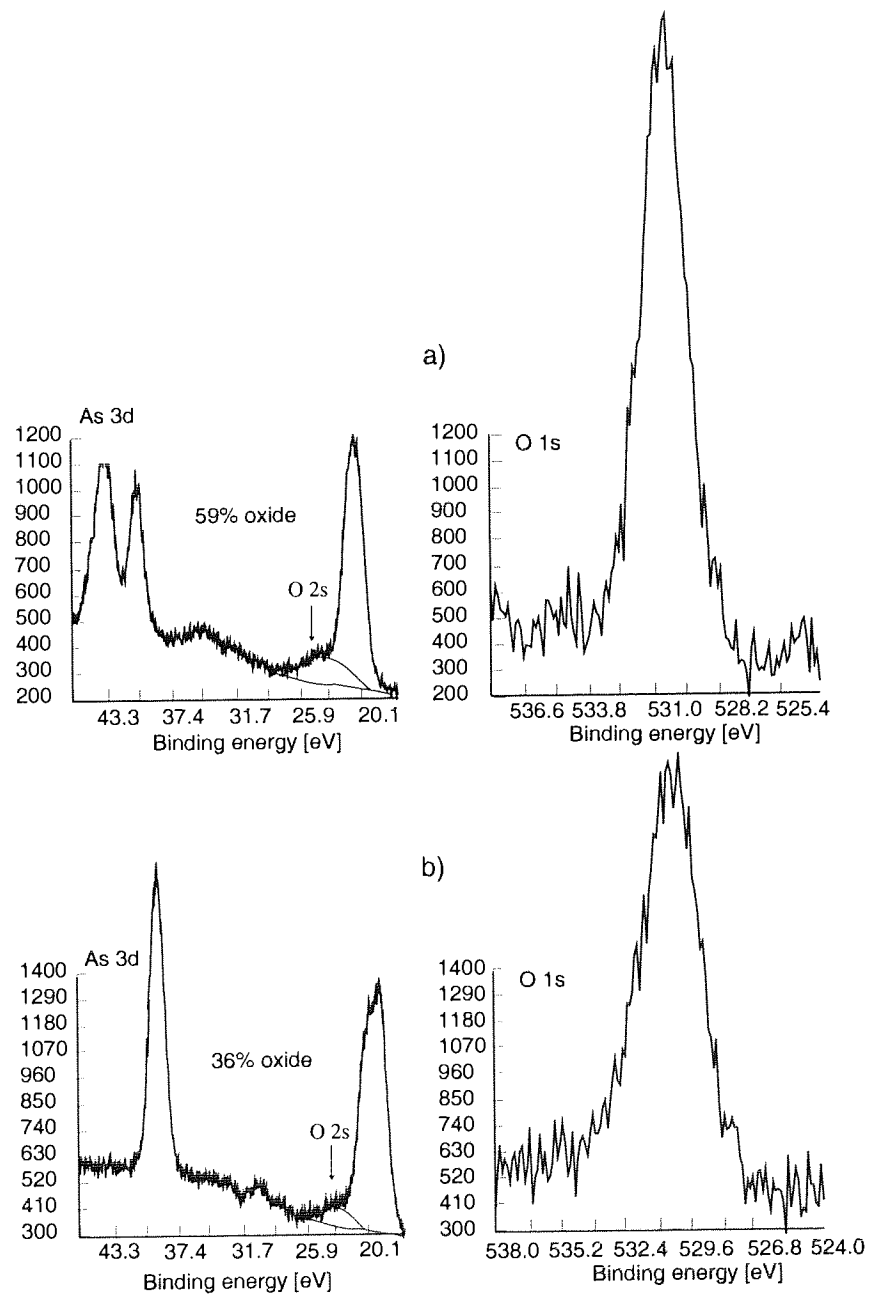


Figure 4.25 Normalized spectra of Ga 3d and O 1s for: a) GaAs wafer etched in Ar plasma 5W, 90 mT; b) GaAs wafer etched in Ar plasma 200 W, 90 mT.

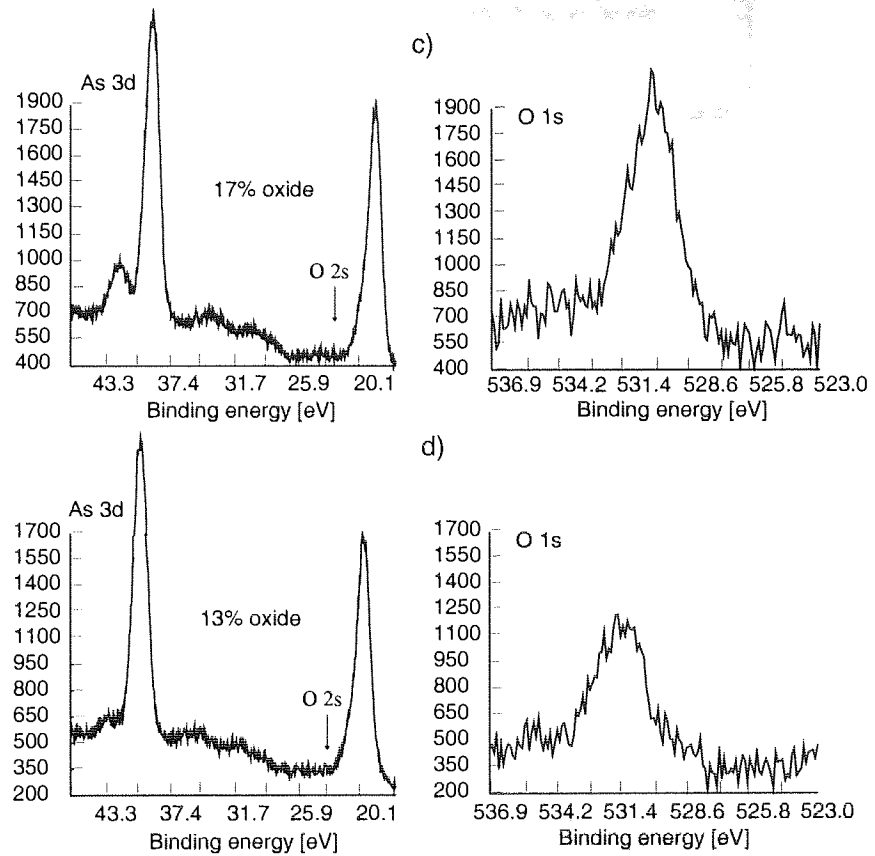


Figure 4.25 (continued) Normalized spectra of Ga 3d and O 1s for: c) clean GaAs wafer; d) GaAs wafer etched in Ar plasma 150 W, 10 mT

## 4.2.2 Plasma-treated GaAs wafer surfaces

### 4.2.2.1 Inert gas plasmas

#### 4.2.2.1.1 Argon plasma

##### *XPS spectra and example of curve synthesis*

In the following, the procedure for spectrum fitting described in Section 3.3.1 will be applied on the XPS spectra acquired for argon etching - pressure dependence at 50 W.

#### **10 mT, 50 W**

The spectrum acquired for the argon plasma treated GaAs at 10 mT, 50 W, 30 min is presented in Figure 4.26.

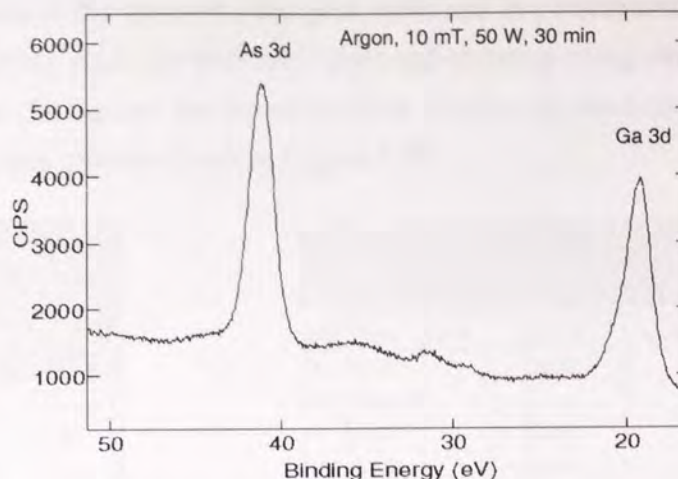


Figure 4.26 XPS spectrum for GaAs exposed to Ar plasma, 10 mT, 50 W, duration of etching 30 min

Smoothing with 13 points and 30 passes was applied for this spectrum. Shirley background subtraction was performed. Then, the peak table shown in Figure 4.27 was used as a starting point for fitting of the As 3d region of the spectrum. The binding energies were connected and the values for FWHM were allowed to vary 0.1 eV as shown in the constraints table below. Also, 30% Gaussian and 70% Lorentzian combinations of line shapes were used and maintained constant during iteration.

Peak Table			Constraints Table						
Remove Add			Fix Print						
Adjust Fit			Ref	Peak	Area	Centre	Height %	FWHM	G/L %
Fold Print									
Peak	Centre	FWHM	A	As2O5		C+4.44		<>0.10	fixed
As2O5	45.54	1.90	B	As2O3		C+3.10		<>0.10	fixed
As2O3	44.22	1.90	C	AsGa				<>0.10	fixed
AsGa	41.10	1.70	FWHM limits for peak C		1.65	1.75			

Figure 4.27 Peak Table and Constraints Table for the As 3d region of all the XPS spectra acquired in this work

Two iterations using the Constraints table above were performed and the best fit presented in Figure 4.28 was obtained with a Chi Square of 0.973.

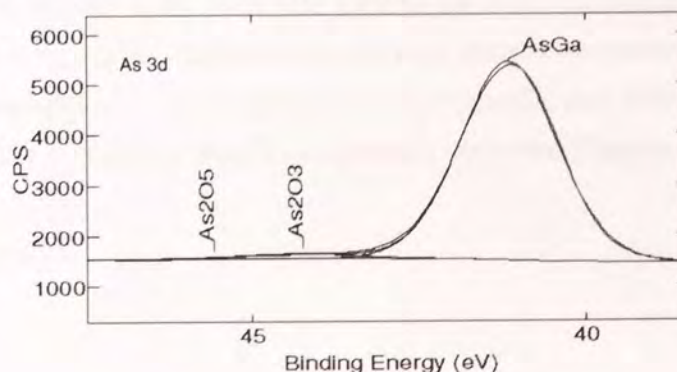


Figure 4.28 Best fit obtained for the As 3d region for the sample etched in Ar plasma, 10 mT, 50 W, 30 min

For the Ga3d region of the spectrum, the peak table and the constraints table shown below were used as a starting point for iteration. A second iteration using similar constraints was performed and the Chi Square decreased to 0.859. Further iteration did not improve the fitting. The fitted spectrum is shown in Figure 4.30.

Peak Table			Constraints Table						
Remove	Add		Fix Print						
Adjust	Fit		Ref	Peak	Area	Centre	Height %	FWHM	G/L %
<b>Fold</b>	<b>Print</b>		Peak	Centre	FWHM				
O 2s	23.33	2.00	A	O 2s		fixed		<>0.10	fixed
Ga(OH) <sub>3</sub>	21.72	1.56	B	Ga(OH) <sub>3</sub>				<>0.10	fixed
Ga <sub>2</sub> O <sub>3</sub>	20.70	1.56	C	Ga <sub>2</sub> O <sub>3</sub>		fixed		<>0.10	fixed
Ga <sub>2</sub> O	20.12	1.56	D	Ga <sub>2</sub> O		fixed		<>0.10	fixed
GaGAs	19.10	1.56	E	GaGAs		fixed		<>0.10	fixed
			FWHM limits for peak E				1.51	1.61	

Figure 4.29 Peak Table and Constraints Table for the Ga 3d region of all the XPS spectra acquired in this work

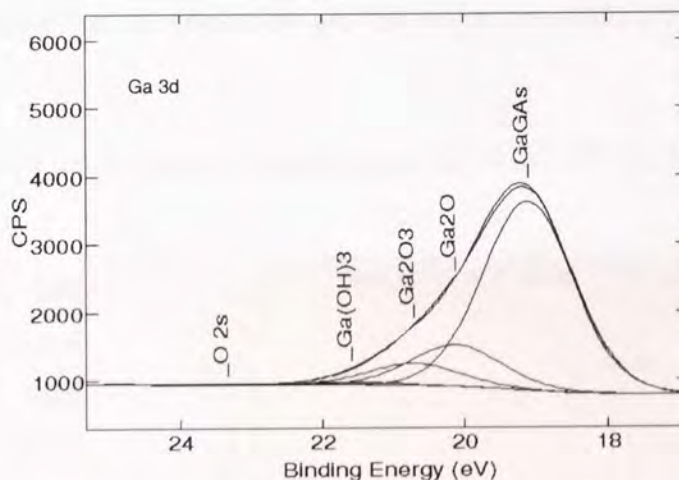


Figure 4.30 Best fit obtained for the Ga 3d region for the sample etched in Ar plasma, 10 mT, 50 W, 30 min

The areas under the peaks were used for the calculation of the relative concentration of surface compounds from their total and also from the As 3d and Ga 3d regions separately, as shown in Table 4.6. A relative sensitivity factor previously determined in our lab of 1.52 for the Ga with respect to As lines was used in the third column in Table 4.6. Using the data calculated in this table, surface changes with plasma parameters (pressure, power and type of gas) were put in evidence by plotting two graphs, one containing all surface compounds, the other containing the Ga compounds only (see Figures 4. a) and b), respectively).

Table 4.6 Calculation of the relative concentration of surface compounds from the total (the fourth column) and from As and Ga regions (the fifth column), respectively for Ar etching, 10 mT, 50 W, 30 min.

Compound	Area	Real area	% all compounds	% from As, Ga
As <sub>2</sub> O <sub>5</sub>	28	28	0.17	0.40
As <sub>2</sub> O <sub>3</sub>	99	99	1.62	1.40
As(GaAs)	6927	6927	43.13	98.20
Ga(OH) <sub>3</sub>	134	204	1.27	2.26
Ga <sub>2</sub> O <sub>3</sub>	396	602	3.75	6.68
Ga <sub>2</sub> O	1121	1704	10.61	18.92
Ga(GaAs)	4275	6498	40.46	72.14

Similar procedure was used for all XPS data and only slight adjustments were needed for some spectra, as will be shown in the following paragraphs. For all XPS spectra, the starting point for fitting was the peak table and the constraints table presented above.

### 30 mT, 50 W

The XPS spectrum for the Ar plasma treated sample at 30 mT, 50 W, 30 min is presented in Figure 4.31.

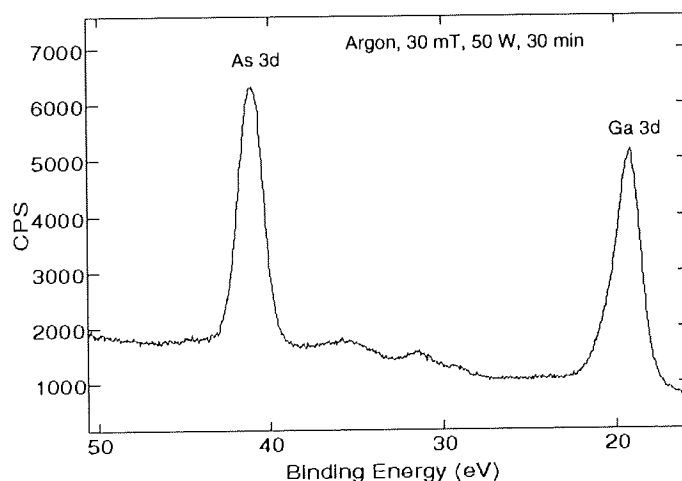


Figure 4.31 XPS spectrum for Ar etching of GaAs at 30 mT, 50 W, 30 min

Smoothing with 13 points and 30 passes was also applied for this spectrum. A Shirley background subtraction was performed. Then, the peak table and the constraints table shown in Figure 4.27 were used as a starting point for fitting. Also, 30% Gaussian and 70% Lorentzian combinations of line shapes were used and maintained constant during iteration. For fitting the As peak, the constraints table in Figure 4.29 was applied twice and a Chi Square of 0.966 was obtained.

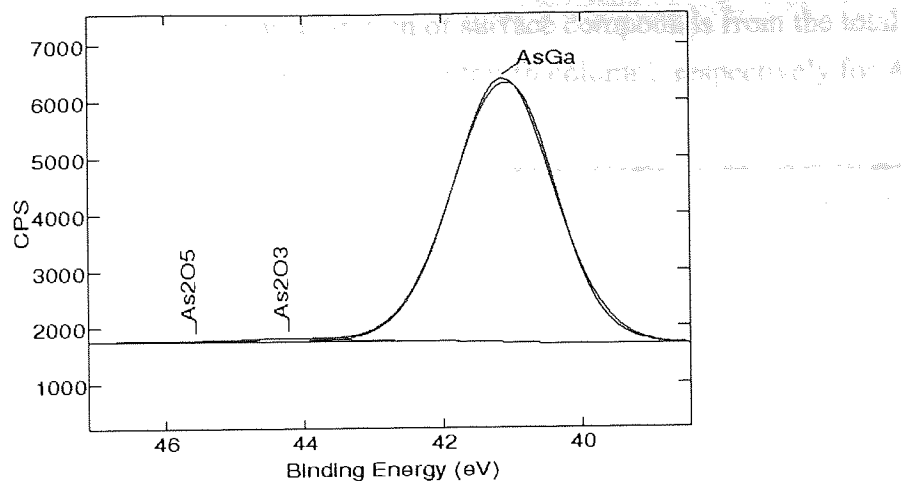


Figure 4.32 Best fit obtained for the As 3d region for the sample etched in Ar plasma, 30 mT, 50 W, 30 min

For the Ga3d region of the spectrum, the peak table and the constraints table shown in Figure 4.29 were used as a starting point for iteration. A second iteration using similar constraints was performed and the Chi Square decreased to 1.332. Further manual adjustment was needed for a better fit. The fitted spectrum is shown in Figure 4.33.

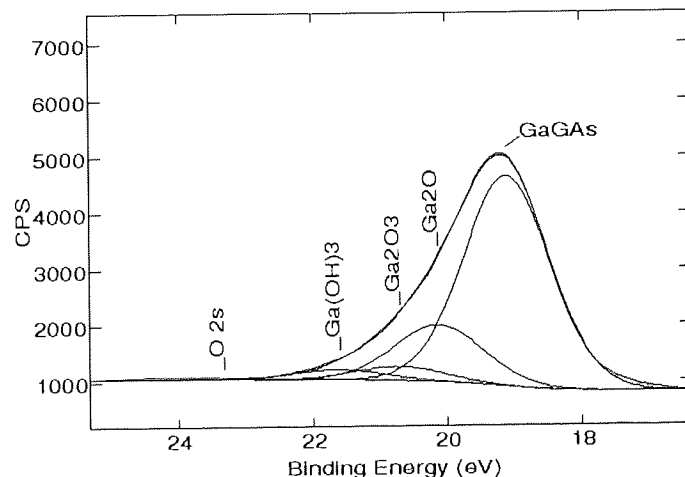


Figure 4.33 Best fit obtained for the Ga 3d region for the sample etched in Ar plasma, 30 mT, 50 W, 30 min

The areas under the peaks were used for the calculation of the relative concentration of surface compounds from their total and also from the As 3d and Ga 3d regions separately, as shown in Table 4.7.

Table 4.7 Calculation of the relative concentration of surface compounds from the total (the fourth column) and from As and Ga regions (the fourth column), respectively for Ar etching, 30 mT, 50 W, 30 min.

Compound	Area	Real area	% all compounds	% from As, Ga
As <sub>2</sub> O <sub>5</sub>	1	1	0	0.01
As <sub>2</sub> O <sub>3</sub>	1	1	0	0.01
As(GaAs)	8109	8109	40.06	99.98
Ga(OH) <sub>3</sub>	208	316.16	1.56	2.61
Ga <sub>2</sub> O <sub>3</sub>	348	528.96	2.61	4.36
Ga <sub>2</sub> O	1848	2808.96	13.88	23.16
Ga(GaAs)	5576	8475.52	41.87	69.87

The data calculated in the above table were plotted in Figure 4...

### 50 mT, 50 W

The XPS spectrum for the Ar plasma treated GaAs at 50 mT, 50 W, 30 min is presented in Figure 4.34.

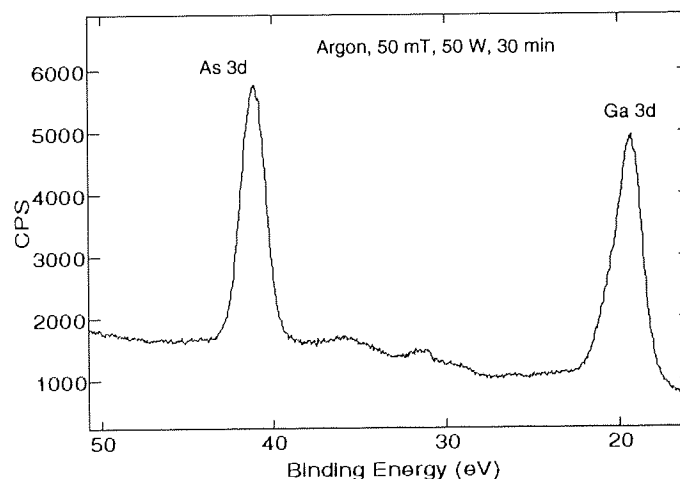


Figure 4.34 XPS spectrum for Ar etching of GaAs at 50 mT, 50 W, 30 min

Smoothing with 13 points and 30 passes was also applied for this spectrum. A Shirley background subtraction was performed. Then, the peak table and the constraints table shown in Figure 4.27 were used as a starting point for fitting. Also, 30% Gaussian and 70% Lorentzian combinations of line shapes were used and maintained constant during iteration.

For fitting the As peak, the constraints table in Figure 4.27 was applied once and a Chi Square of 0.692 was obtained. The fitted peak is shown in Figure 4.35.

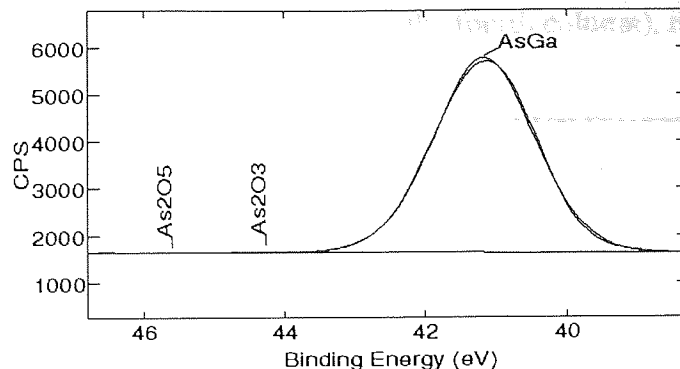


Figure 4.35 Best fit obtained for the As 3d region for the sample etched in Ar plasma, 50 mT, 50 W, 30 min

For the Ga3d region of the spectrum, the peak table and the constraints table shown in Figure 4.29 were used as a starting point for iteration. A second iteration using similar constraints did not improve the fitting. Further manual adjustment of the FWHM was needed for a better fit. The fitted spectrum is shown in Figure 4.36.

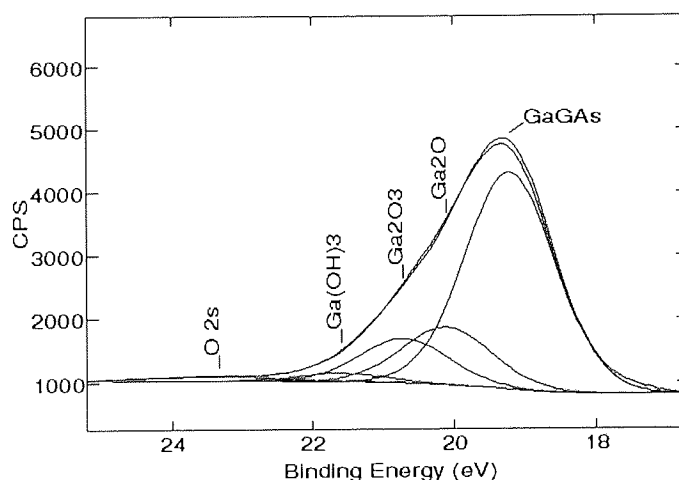


Figure 4.36 Best fit obtained for the Ga 3d region for the sample etched in Ar plasma, 50 mT, 50 W, 30 min

The areas under the peaks were used for the calculation of the relative concentration of surface compounds from their total and also from the As 3d and Ga 3d regions separately, as shown in Table 4.8.

Table 4.8 Calculation of the relative concentration of surface compounds from the total (the fourth column) and from As and Ga regions (the fourth column), respectively for Ar etching, 50 mT, 50 W, 30 min.

Compound	Area	Real area	% all compounds	% from As, Ga
As <sub>2</sub> O <sub>5</sub>	1	1	0.01	0.01
As <sub>2</sub> O <sub>3</sub>	1	1	0.01	0.01
As(GaAs)	7192	7192	38.81	99.98
Ga(OH) <sub>3</sub>	144	2188.88	1.18	1.93
Ga <sub>2</sub> O <sub>3</sub>	987	1500.24	8.09	13.23
Ga <sub>2</sub> O	1351	2053.52	11.08	18.11
Ga(GaAs)	4978	7566.56	40.83	66.73

The data calculated in the table above were also plotted in Figure 4.

### 70 mT, 50 W

The XPS spectrum for the Ar plasma treated GaAs at 70 mT, 50 W, 30 min is presented in Figure 4.37. Smoothing with 13 points and 30 passes was also applied for this spectrum. A Shirley background subtraction was performed. Then, the peak table and the constraints table shown in Figure 4.27 were used as a starting point for fitting. Also, 30% Gaussian and 70% Lorentzian combinations of line shapes were used and maintained constant during iteration.

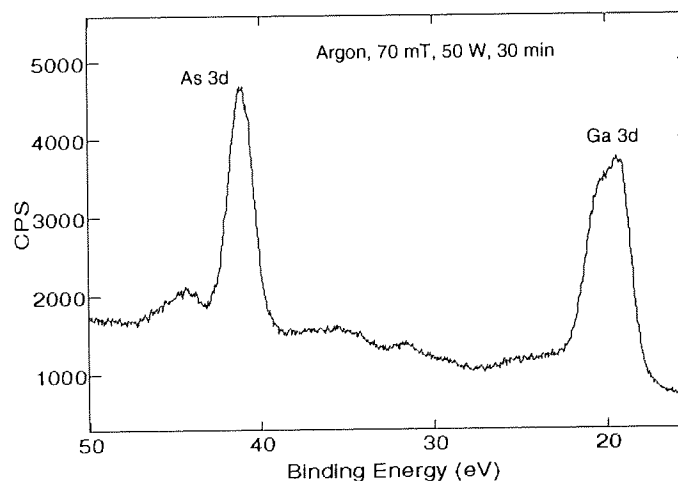


Figure 4.37 XPS spectrum for Ar etching of GaAs at 70 mT, 50 W, 30 min

For fitting the As peak, the constraints table in Figure 4.27 was applied twice and a Chi Square of 0.561 was obtained. The fitted peak is shown in Figure 4.38. For the Ga3d region of the spectrum, the peak table and the constraints table shown in Figure 4.29 were used as a starting point for iteration. After iterating for three times, the Chi Square decreased to 0.532. The fit obtained is presented in Figure 4.39.

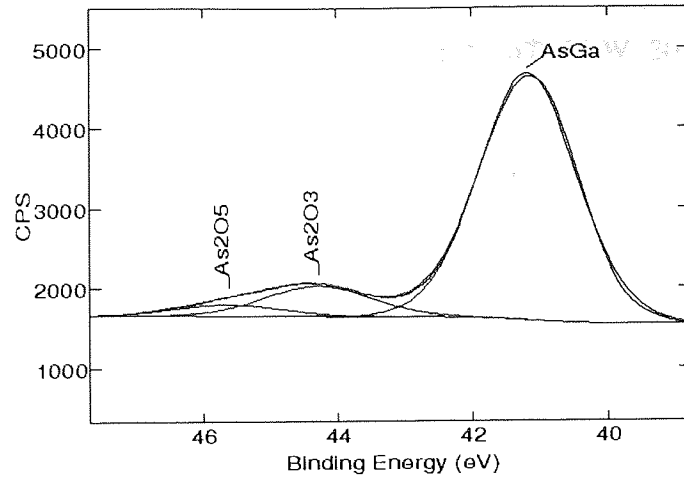


Figure 4.38 Best fit obtained for the As 3d region for the sample etched in Ar plasma, 70 mT, 50 W, 30 min

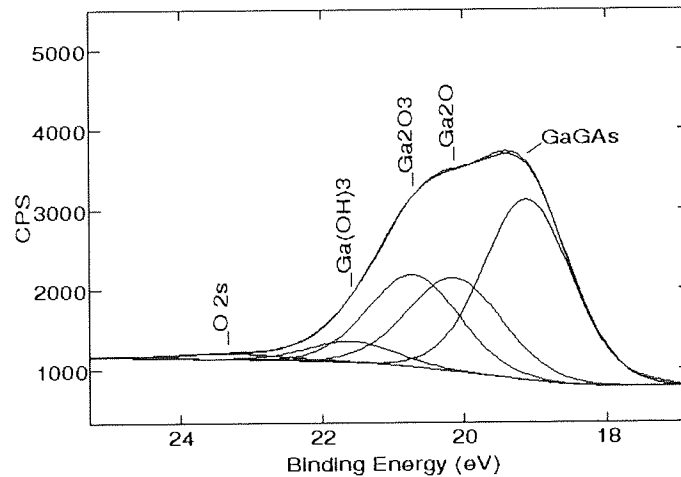


Figure 4.39 Best fit obtained for the Ga 3d region for the sample etched in Ar plasma, 70 mT, 50 W, 30 min

The areas under the peaks were used for the calculation of the relative concentration of surface compounds from their total and also from the As 3d and Ga 3d regions separately, as shown in Table 4.9.

Table 4.9 Calculation of the relative concentration of surface compounds from the total and from As and Ga regions, respectively for Ar etching, 70 mT, 50 W, 30 min.

Compound	Area	Real area	% all compounds	% from As, Ga
As <sub>2</sub> O <sub>5</sub>	247	247	1.38	3.84
As <sub>2</sub> O <sub>3</sub>	748	748	4.18	11.64
As(GaAs)	5433	5433	30.36	84.52
Ga(OH) <sub>3</sub>	322	489.44	2.73	4.27
Ga <sub>2</sub> O <sub>3</sub>	1931	2935.12	16.40	25.59
Ga <sub>2</sub> O	1606	2441.12	13.64	21.29
Ga(GaAs)	3686	5602.72	31.31	48.85

The data calculated in the above table were also plotted in Figure 4.

## 90 mT, 50 W

The XPS spectrum for the Ar plasma treated GaAs at 90 mT, 50 W, 30 min is presented in Figure 4.40.

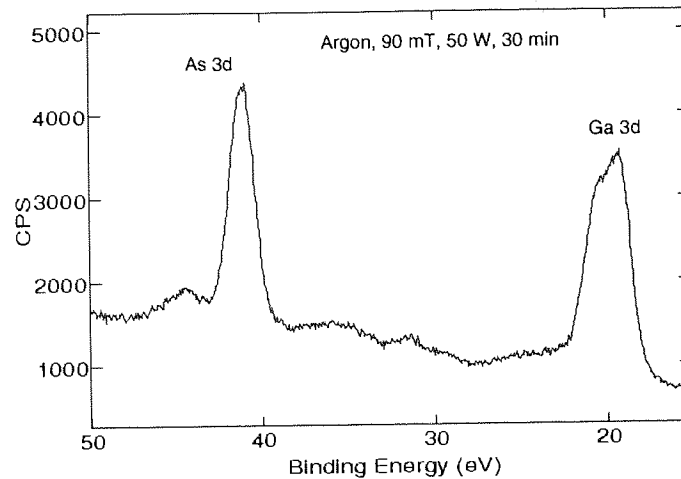


Figure 4.40 XPS spectrum for Ar etching of GaAs at 90 mT, 50 W, 30 min

Smoothing with 13 points and 30 passes was also applied for this spectrum. A Shirley background subtraction was performed. Then, the peak table and the constraints table shown in Figure 4.27 were used as a starting point for fitting. Also, 30% Gaussian and 70% Lorentzian combinations of line shapes were used and maintained constant during iteration.

For fitting the As peak, the constraints table in Figure 4.27 was applied twice and a Chi Square of 0.07 was obtained. The fitted peak is shown in Figure 4.41.

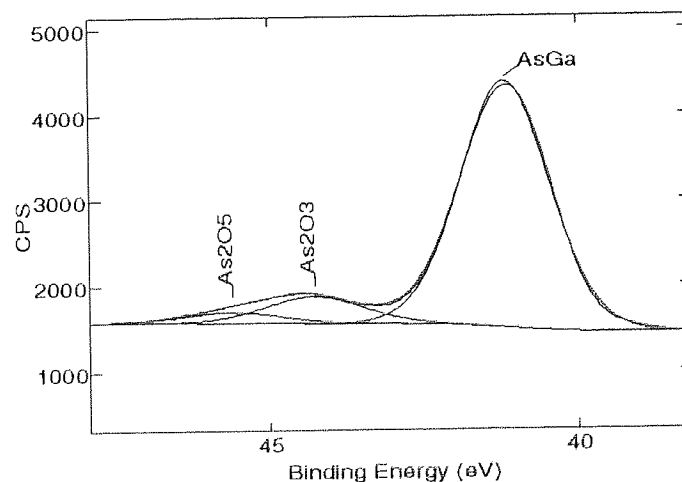


Figure 4.41 Best fit obtained for the As 3d region for the sample etched in Ar plasma, 90 mT, 50 W, 30 min

For the Ga3d region of the spectrum, the peak table and the constraints table shown in Figure 4.29 were used as a starting point for iteration. After iterating for three times, the Chi Square decreased to 1.532. Further manual adjustment by slightly changing the FWHM was needed for a better fit. The final fit is presented in Figure 4.42.

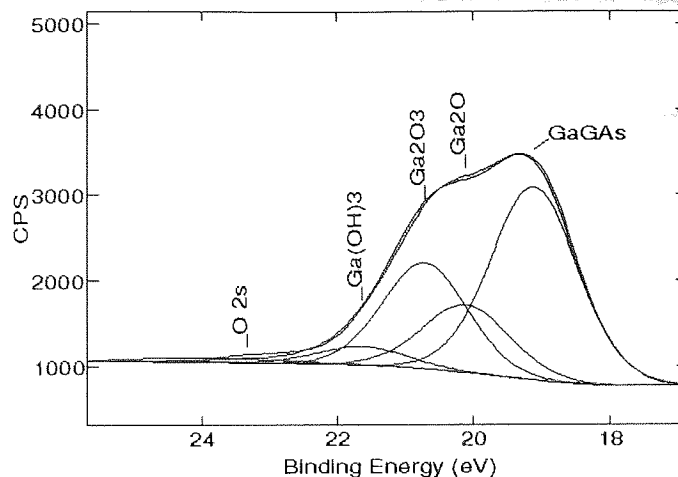


Figure 4.42 Best fit obtained for the Ga 3d region for the sample etched in Ar plasma, 90 mT, 50 W, 30 min

The areas under the peaks were used for the calculation of the relative concentration of surface compounds from their total and also from the As 3d and Ga 3d regions separately, as shown in Table 4.10.

Table 4.10 Calculation of the relative concentration of surface compounds from the total (the fourth column) and from As and Ga regions (the fourth column), respectively for Ar etching, 90 mT, 50 W, 30 min.

Compound	Area	Real area	% all compounds	% from As, Ga
As <sub>2</sub> O <sub>5</sub>	180	180	1.09	3.11
As <sub>2</sub> O <sub>3</sub>	573	573	3.47	9.91
As(GaAs)	5031	5031	30.50	86.98
Ga(OH) <sub>3</sub>	390	592.80	3.59	5.53
Ga <sub>2</sub> O <sub>3</sub>	2065	3138.80	19.03	29.30
Ga <sub>2</sub> O	1283	1950.16	11.82	18.21
Ga(GaAs)	3309	5029.68	30.49	46.96

The data calculated in Table 4.10 were also plotted in Figure 4.

#### Surface compositional changes

The variation of surface composition for all pressure - power combinations can be deduced from two sets of graphs; a dependence with power at two different pressures and another dependence with pressure at two different powers. Here, 50 and 150 W and also 10 and 90 mT were chosen.

Variation of the relative concentration of the surface components in argon plasma with changing gas pressure is given in Figure 4.43. The instrumental errors shown in the graph are estimated to be less than 10% and they apply to all similar plots presented in this

chapter. These errors are difficult to evaluate due to a multitude of factors (as presented in Chapter 3) but are estimated to be less than 5%.

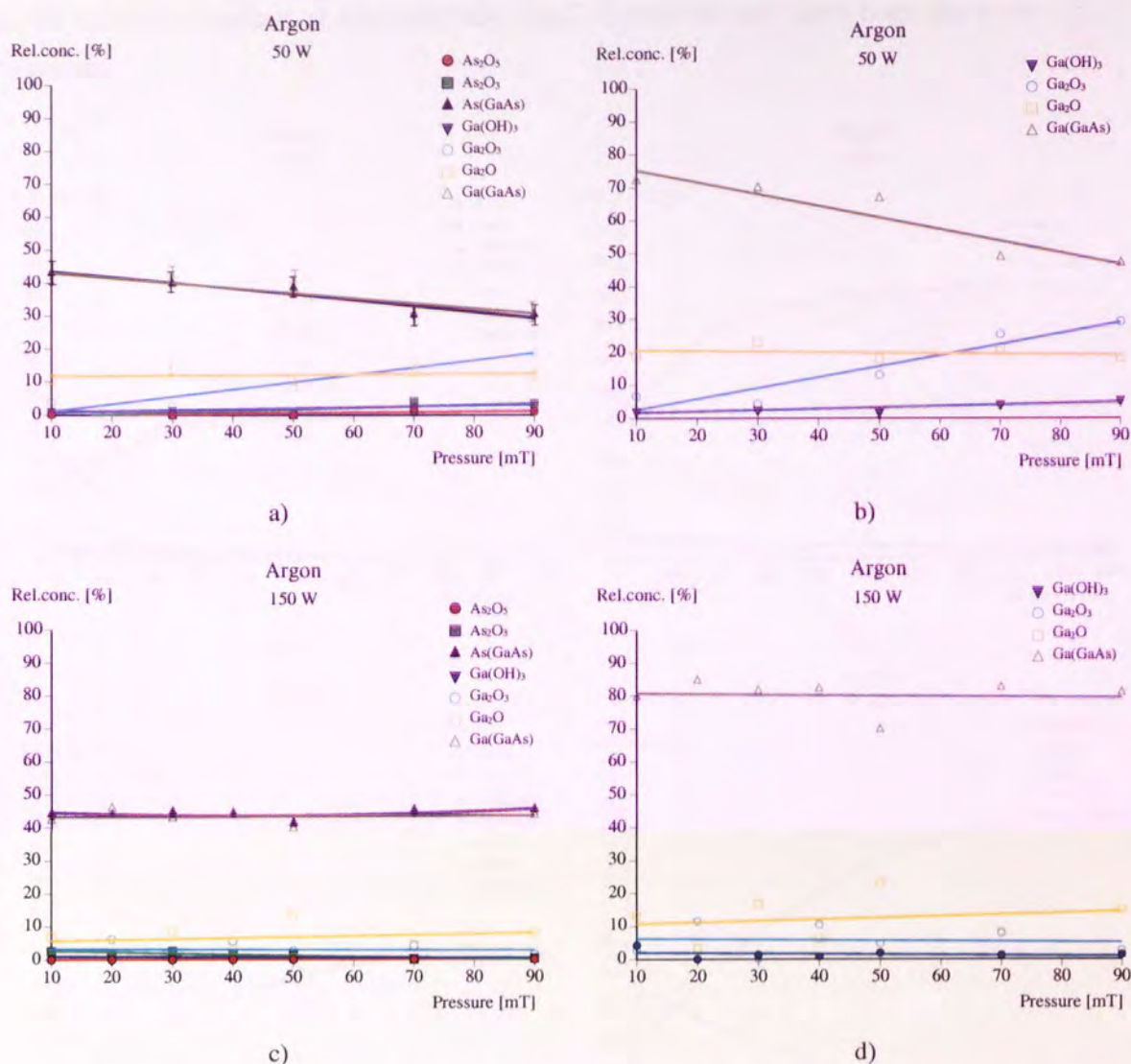


Figure 4.43 Variation with pressure of the relative percentages of: a), c) all the GaAs surface components and b), d) Ga components only (argon plasma, each time: 30 min, at indicated powers)

The only oxide whose concentration increased with increasing pressure at 50 W was  $\text{Ga}_2\text{O}_3$ . It is also interesting to note that at 150 W and 10 mT practically the only oxide present on the surface was  $\text{Ga}_2\text{O}$ .  $\text{As}_2\text{O}_5$  was not present on the surface of any of the argon-treated samples, not even in the outermost layer. Concentration of  $\text{Ga}(\text{OH})_3$  was less than 5% in all samples. Similar trends of concentration of surface compounds with pressure at 50 and 150 W were observed. The main difference was in the amounts of  $\text{Ga}_2\text{O}$  and  $\text{Ga}_2\text{O}_3$  which were higher at 50 W. This is an important result which will be discussed later in the work.

In the variation of surface composition with power (Figure 4.44 a) and b)), two regions can be distinguished. At 10 mT, the first region - with powers below 50 W - showed a fast decrease of the oxide. The As enrichment observed in Figure 4.44 a) is small, within the error bars. Above 50 W, no surface compositional changes were observed. At 5 W the ion

energies are so low that most probably the native oxide was not completely etched. It is also interesting to note that at 200 W and 10 mT the only oxide present on the surface was Ga<sub>2</sub>O. Knowing that some surface oxidation of the sample may occur during transfer in air to the analysis chamber, at least partially, Ga<sub>2</sub>O formation may have been due to air exposure.

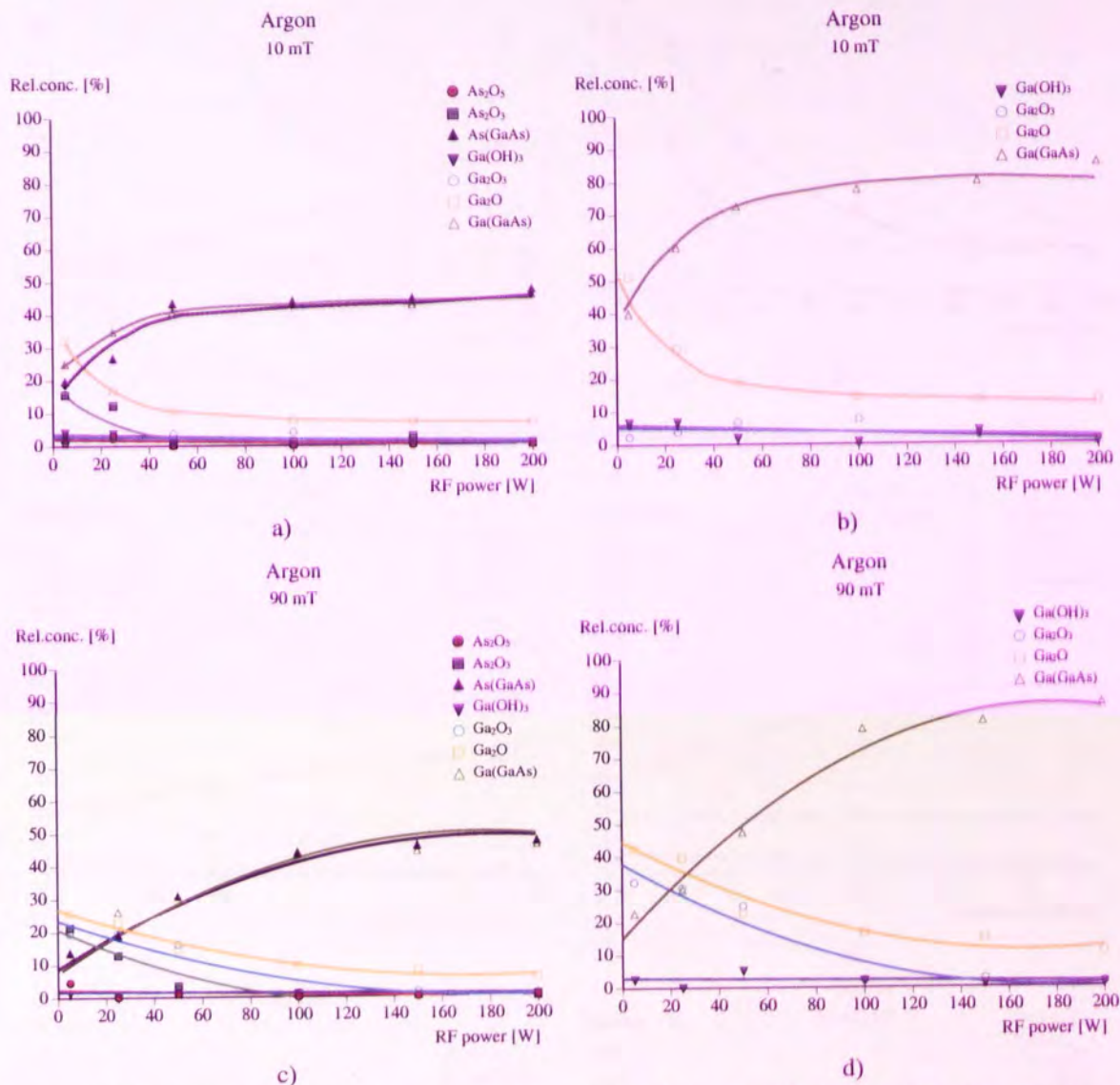


Figure 4.44 Variation with power of the relative percentages of: a), c) all the GaAs surface components and b), d) Ga components only (argon plasma, each time: 30 min, at indicated pressures)

The plots of the oxide layer thickness versus pressure and power are presented in Figure 4.45 a) and b), respectively. With increasing pressure, the oxide thickness increased and was higher at lower pressure. With power, after an abrupt decrease up to about 50 W, the oxide thickness remained constant at both highest and lowest pressure studied.

#### Layered structure of the surface

ARXPS analysis for the sample etched at 100 W and 10 mT (Figure 4.46 a)) showed a fast decrease of Ga<sub>2</sub>O concentration with depth. This result suggests that Ga<sub>2</sub>O forms the outermost layer of the surface. A small concentration of As<sub>2</sub>O<sub>3</sub> closer to the surface was

also observed. At 90 mT and 100 W (Figure 4.46 b)), more  $\text{As}_2\text{O}_3$  was formed on the surface. Also,  $\text{Ga}_2\text{O}_3$  was formed nearer the surface than at 10 mT.

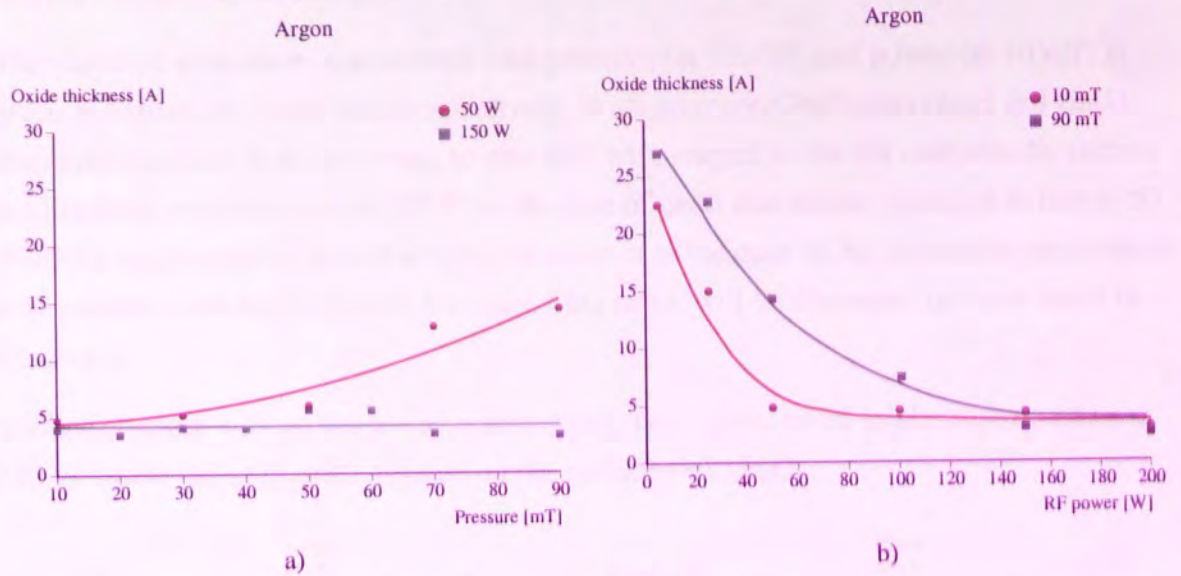


Figure 4.45 Variation of oxide layer thickness with a) pressure and b) power (argon plasma, 30 min)

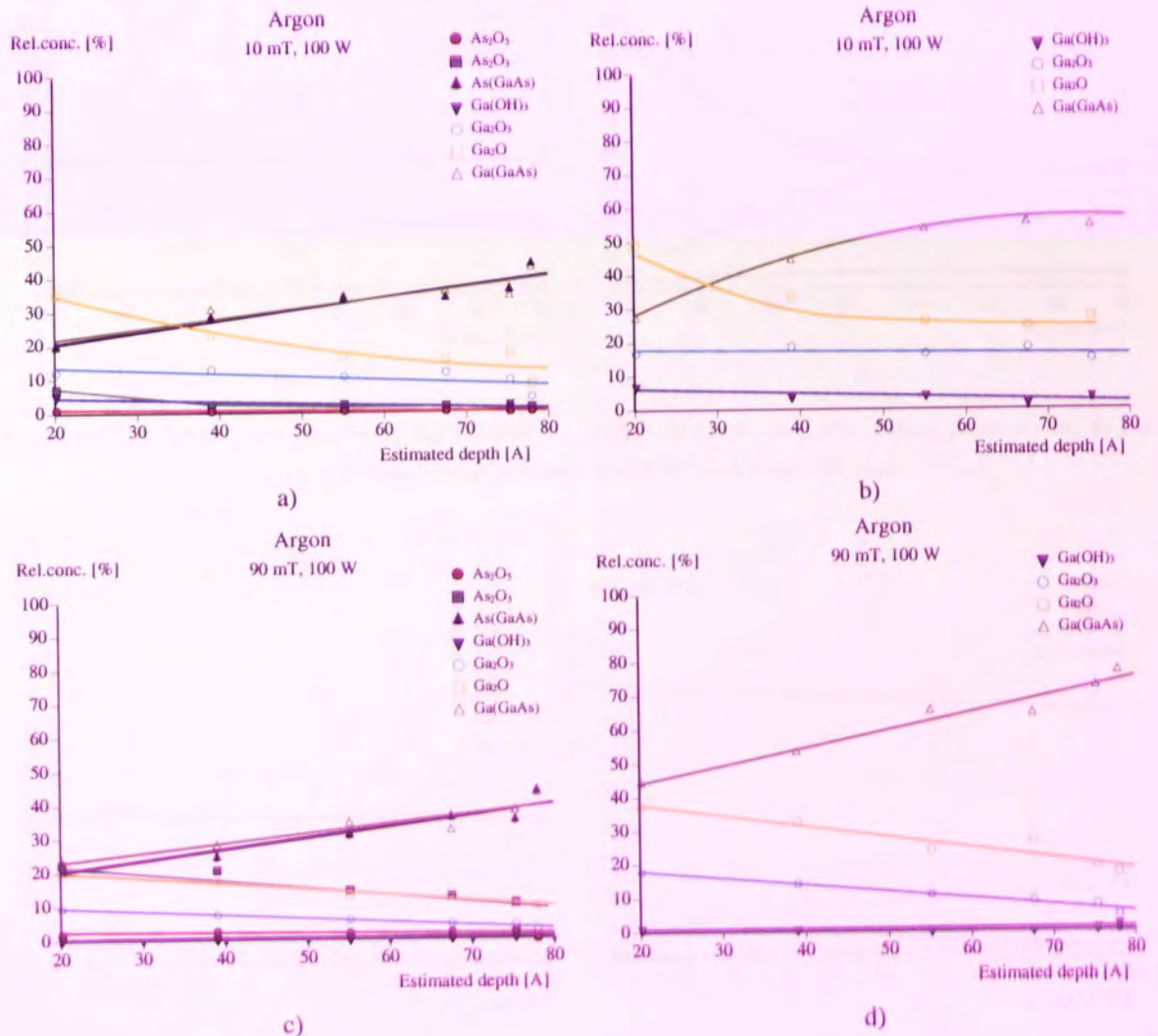


Figure 4.46 Variation with depth of the relative percentages of: a), c) all the GaAs surface components and b), d) Ga components only (argon plasma, etch time: 30 min, at indicated pressures and powers). Estimated depth was calculated with:  $d = \lambda \cos \theta$ , where  $\lambda = 26 \text{ \AA}$

#### 4.2.2.1.2 Neon plasma

##### Surface compositional changes

The variation of surface composition with pressure (at 150 W) and power (at 10 mT) is given in Figures 4.47 and 4.48, respectively. With pressure,  $\text{Ga}_2\text{O}_3$  increased and  $\text{Ga}_2\text{O}$  remained constant. It is interesting to note that with respect to the Ga compounds, surface modification with pressure at 150 W in the case of neon was almost identical to that at 50 W of the argon-plasma treated surface. In contrast to the case of Ar, an arsenic enrichment with pressure was also observed for neon. This result will be discussed in more detail in Chapter 5.

Surface changes with power are also interesting.  $\text{Ga}_2\text{O}_3$  decreased to almost extinction at 150 W where the only oxide formed on the surface was  $\text{Ga}_2\text{O}$ .

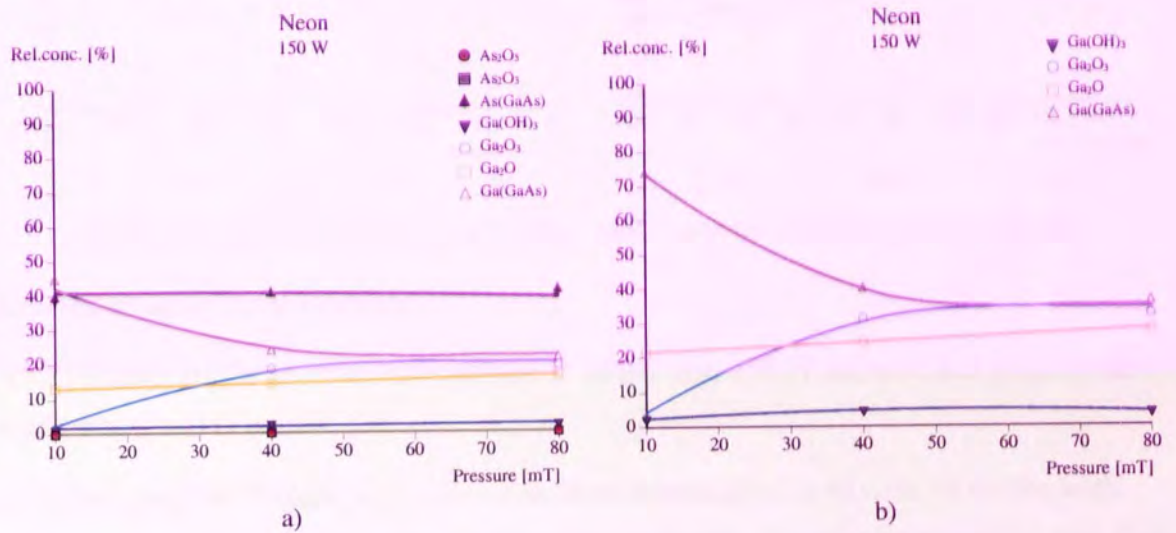


Figure 4.47 Variation with pressure of the relative percentage of a) all the GaAs surface components; b) Ga components only (neon plasma at 150 W, etch time: 30 min)

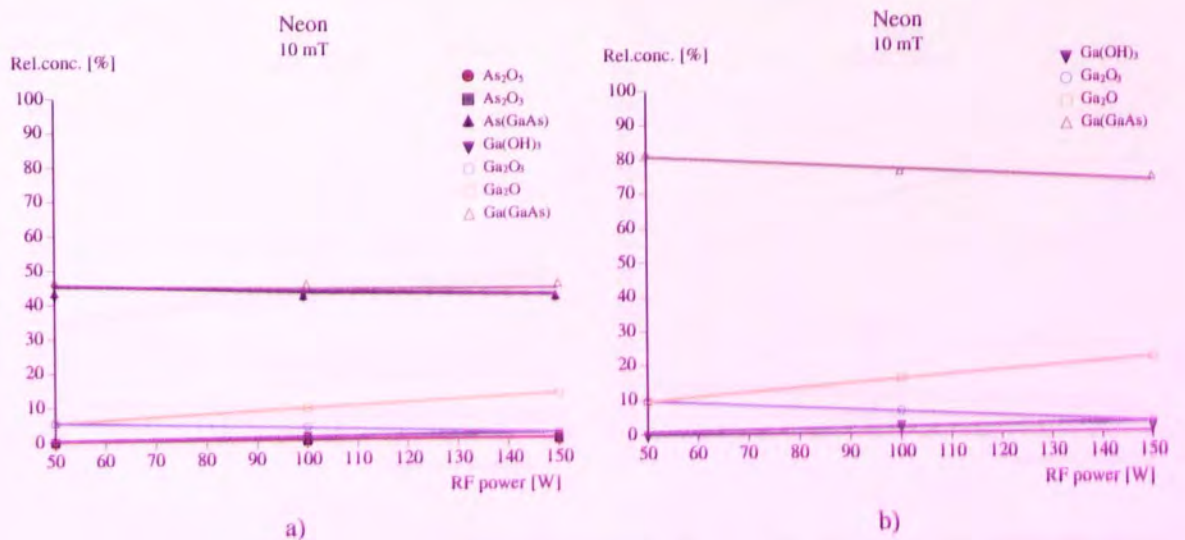


Figure 4.48 Variation with power of the relative percentage of a) all the GaAs surface components; b) Ga components only (neon plasma at 150 W, etch time: 30 min)

Because no As oxides were detected and Ga<sub>2</sub>O remained the same with increasing pressure, the growth with pressure of the oxide thickness observed in Figure 4.49 a) is due to Ga<sub>2</sub>O<sub>3</sub> only, as in the case of argon. With increasing power Figure 4.49 b), no significant changes of oxide thickness were observed. Generally, the oxide thickness was lower for the neon-treated samples than for the argon-treated samples. This will be discussed later in terms of energy transferred to the surface by the ions in the plasma.

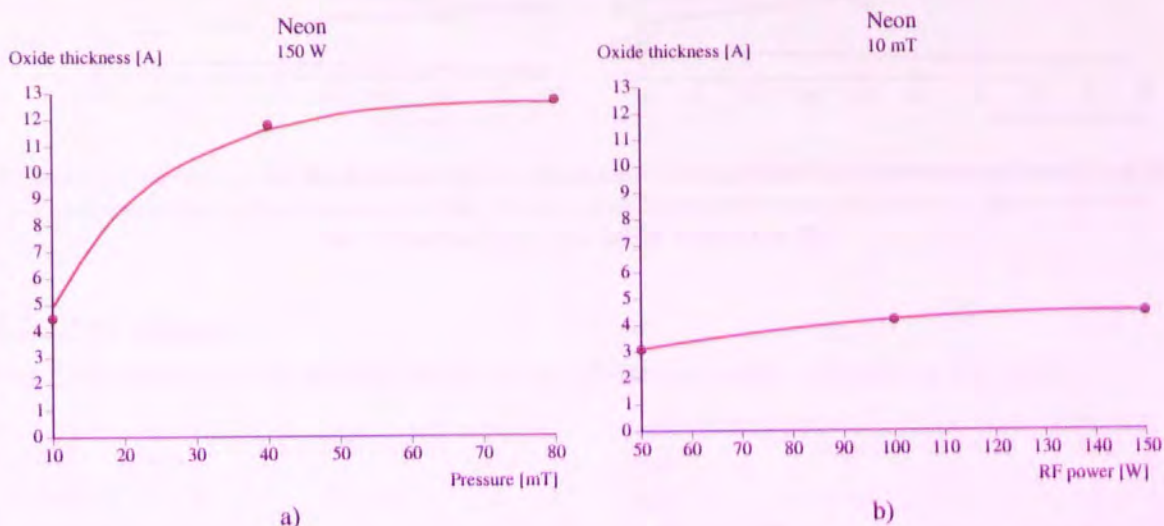


Figure 4.49 Variation of oxide layer thickness with a) pressure and b) power (neon plasma)

#### Layered structure of the surface

ARXPS analysis for neon treated samples at 10 mT and 150 W showed that most of the oxide was Ga<sub>2</sub>O (Figure 4.50).

At higher pressure (Figure 4.51), the oxide layer consisted of a mixture of oxides with more Ga<sub>2</sub>O<sub>3</sub> at the outermost layer than near the substrate. It is also important to note that at 10 mT the XPS signals of As and Ga were equal whereas at 80 mT more As than Ga was observed even at 80 Å.

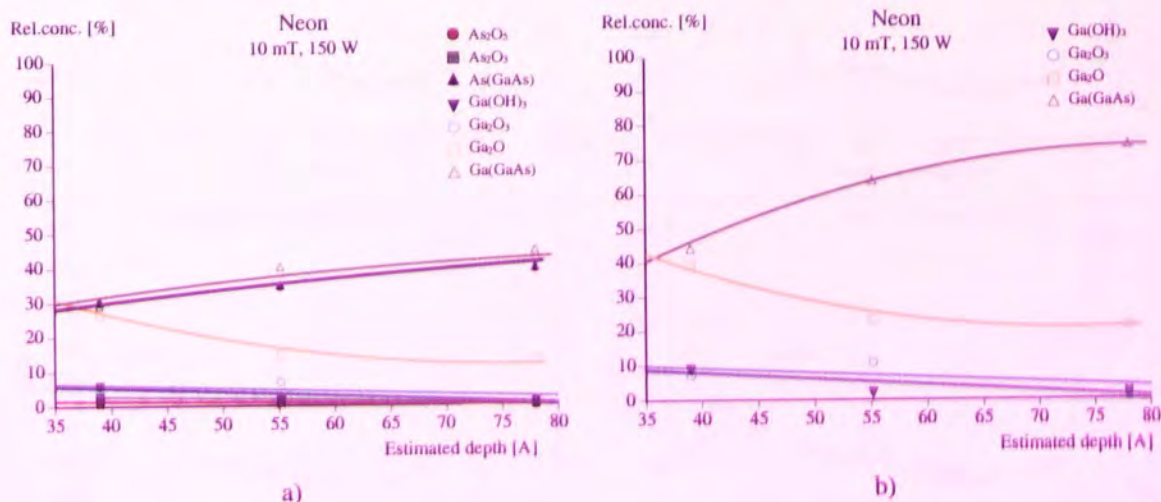


Figure 4.50 Variation with depth of the relative percentages of: a) all the GaAs surface components and b) Ga components only (neon plasma, etch time: 30 min, at indicated pressures and powers). Estimated depth was calculated with:  $d = \lambda \cos \theta$ , where  $\lambda = 26 \text{ \AA}$

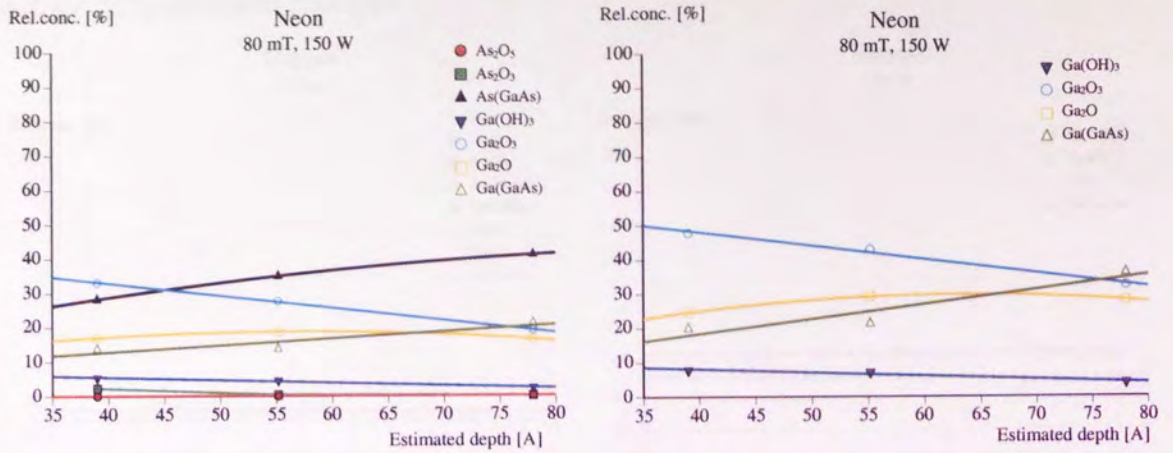


Figure 4.51 Variation with depth of the relative percentages of: a) all the GaAs surface components and b) Ga components only (Ne plasma, each time: 30 min, at indicated pressures and powers). Estimated depth was calculated with:  $d = \lambda \cos \theta$ , where  $\lambda = 26 \text{ \AA}$

#### 4.2.2.2 O<sub>2</sub> plasma

The XPS spectra for O<sub>2</sub> etching at 10 mT at different powers is shown in Fig. 4.52.

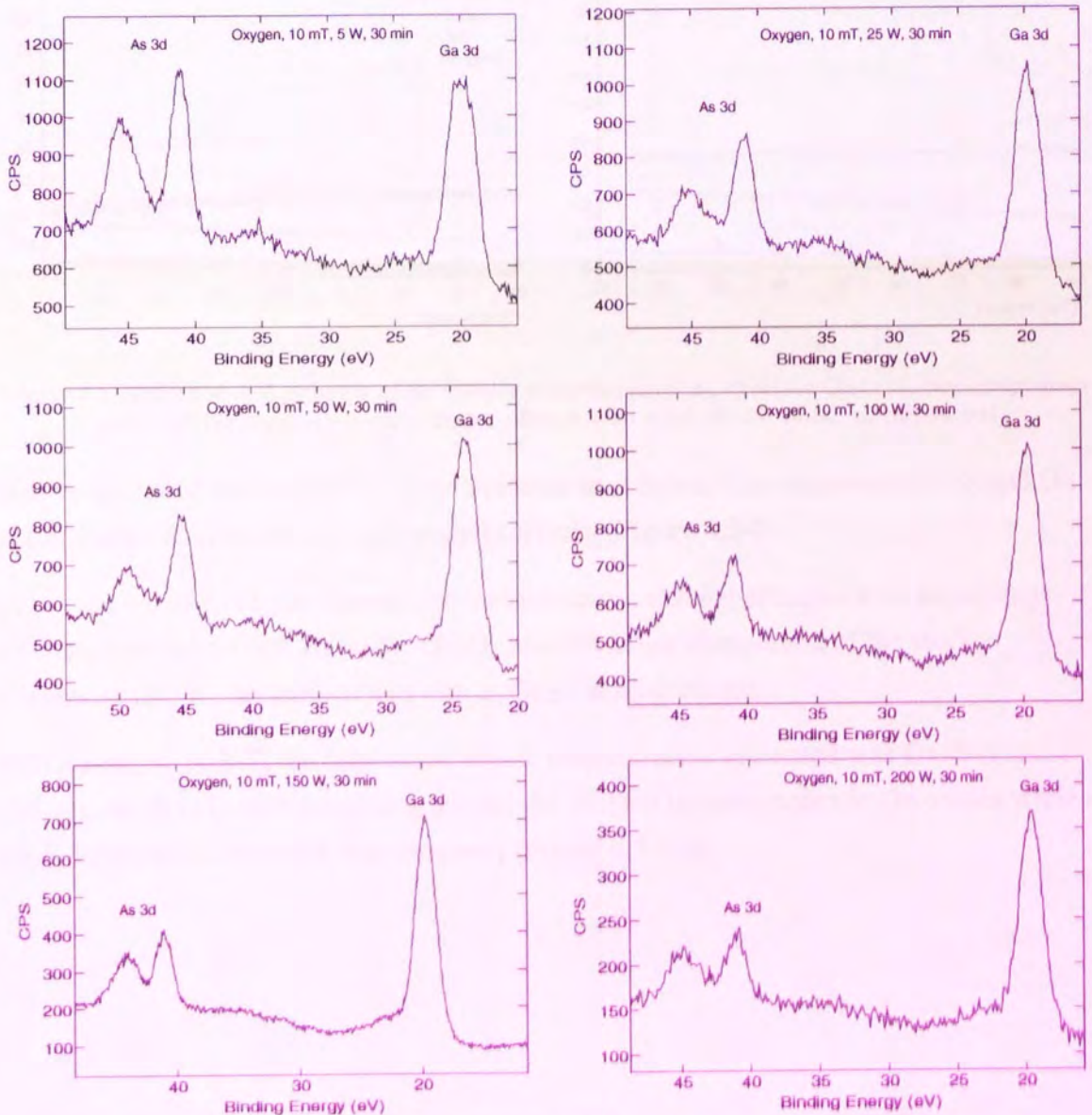


Figure 4.52 XPS spectra for oxygen etching of GaAs at 10 mT, 30 min at different powers

## Surface compositional changes

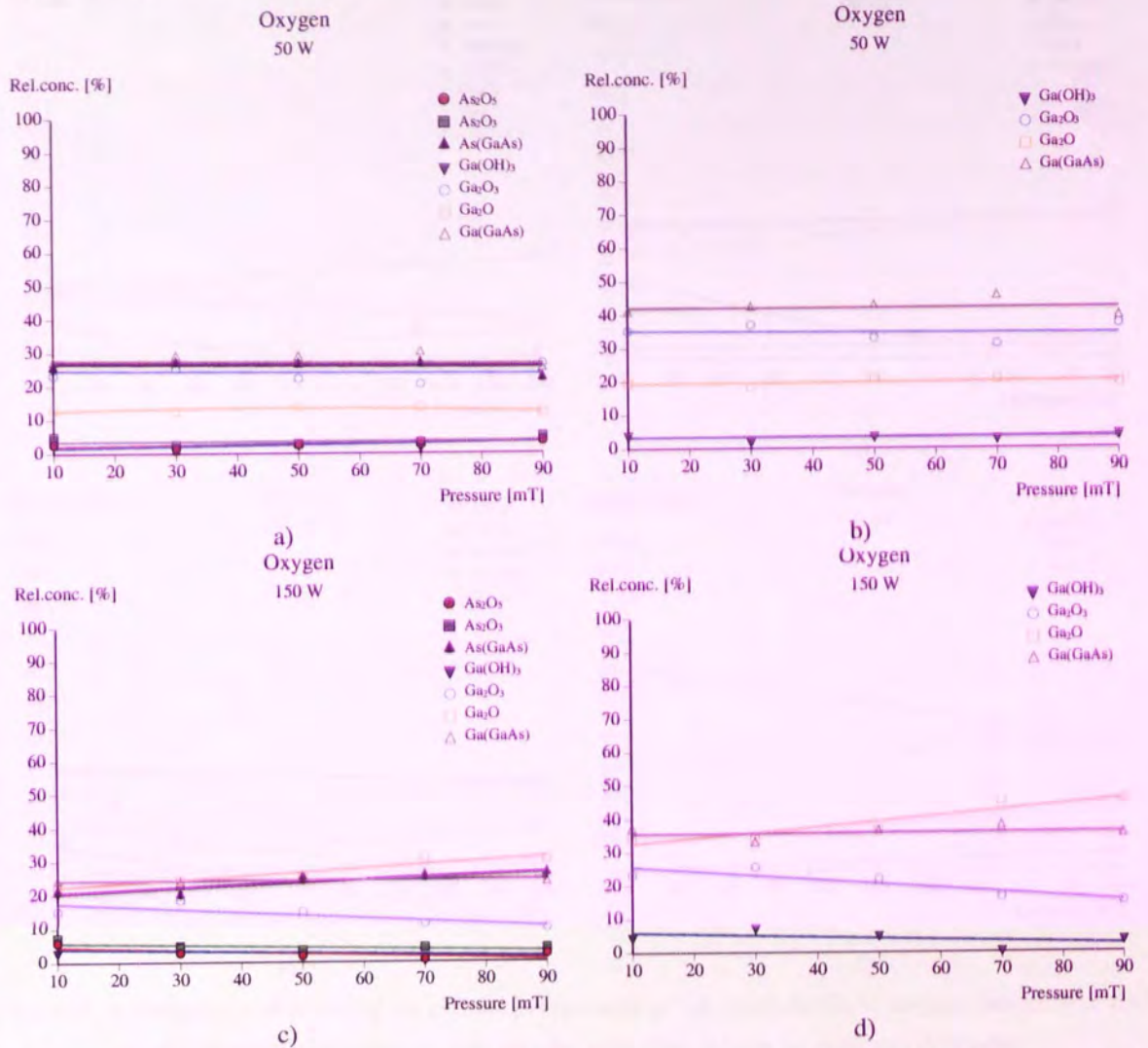


Figure 4.53 Variation with pressure of the relative percentages of: a), c) all the GaAs surface components and b), d) Ga components only (oxygen plasma, etch time: 30 min, at indicated powers)

Surface oxidation was higher in oxygen plasma than in inert gas plasmas. All As and Ga oxides were found on the oxygen-treated surfaces (Figure 4.54).

As in the case of inert gas plasmas, no surface compositional changes with increasing pressure, were observed. At 50 W,  $\text{Ga}_2\text{O}_3$  was the major component of the surface whereas at 150 W, the surface was rich in  $\text{Ga}_2\text{O}$  at all pressures.

With power, at 10 mT, the only oxide whose concentration increased was  $\text{Ga}_2\text{O}$  (Figure 4.54 a)). At 90 mT, with increasing power, the surface became richer in Ga oxides while a small decrease in As oxides was observed (Figure 4.54 c)).

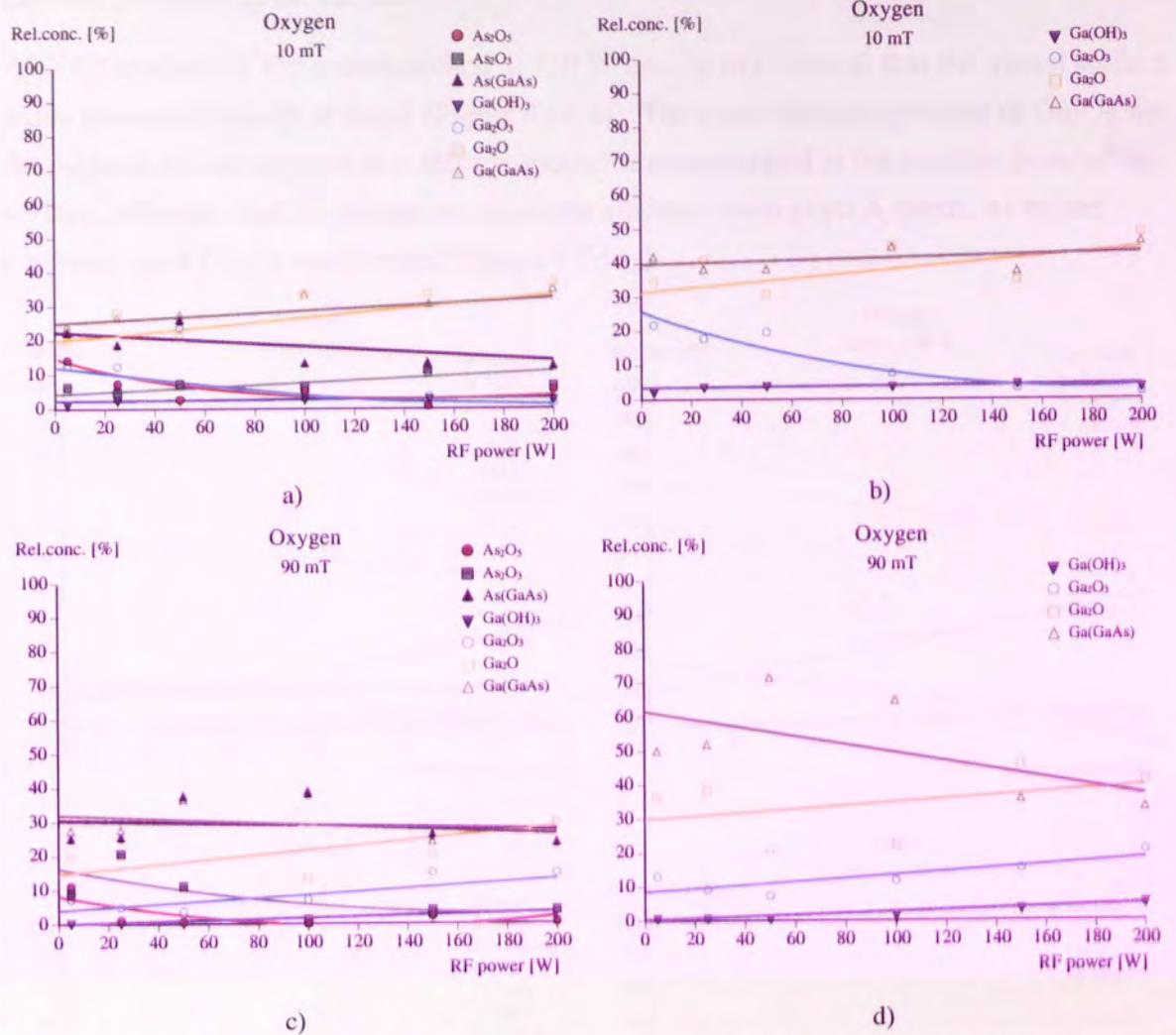


Figure 4.54 Variation with power of the relative percentages of: a), c) all the GaAs surface components and b), d) Ga components only (oxygen plasma, etch time: 30 min, at indicated pressures)

As expected, the oxide thickness was higher for oxygen than for inert gas plasmas (Figure 4.55). In the case of argon plasma, at the lowest power only the oxide thickness was higher than that obtained with oxygen. No significant variation of oxide thickness with power was observed for oxygen.

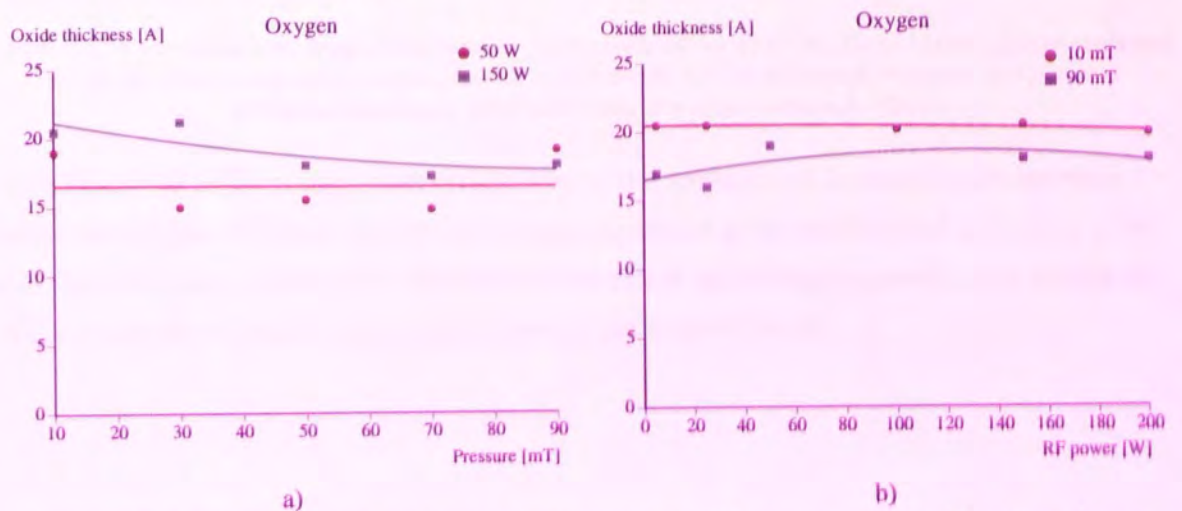


Figure 4.55 Variation of oxide thickness with a) pressure and b) power - etching with oxygen plasma

### Layered structure of the surface

ARXPS analysis of the sample etched at 150 W and 10 mT showed that the mixed surface oxide consisted mainly of Ga<sub>2</sub>O (Figure 4.56 a)). The concentration gradient of Ga<sub>2</sub>O<sub>3</sub> was the highest, which suggests that this compound is concentrated at the topmost layer of the surface, whereas Ga<sub>2</sub>O is present in important amounts even at 80 Å depth. At higher pressure, more Ga<sub>2</sub>O<sub>3</sub> was formed (Figure 4.56 c)).

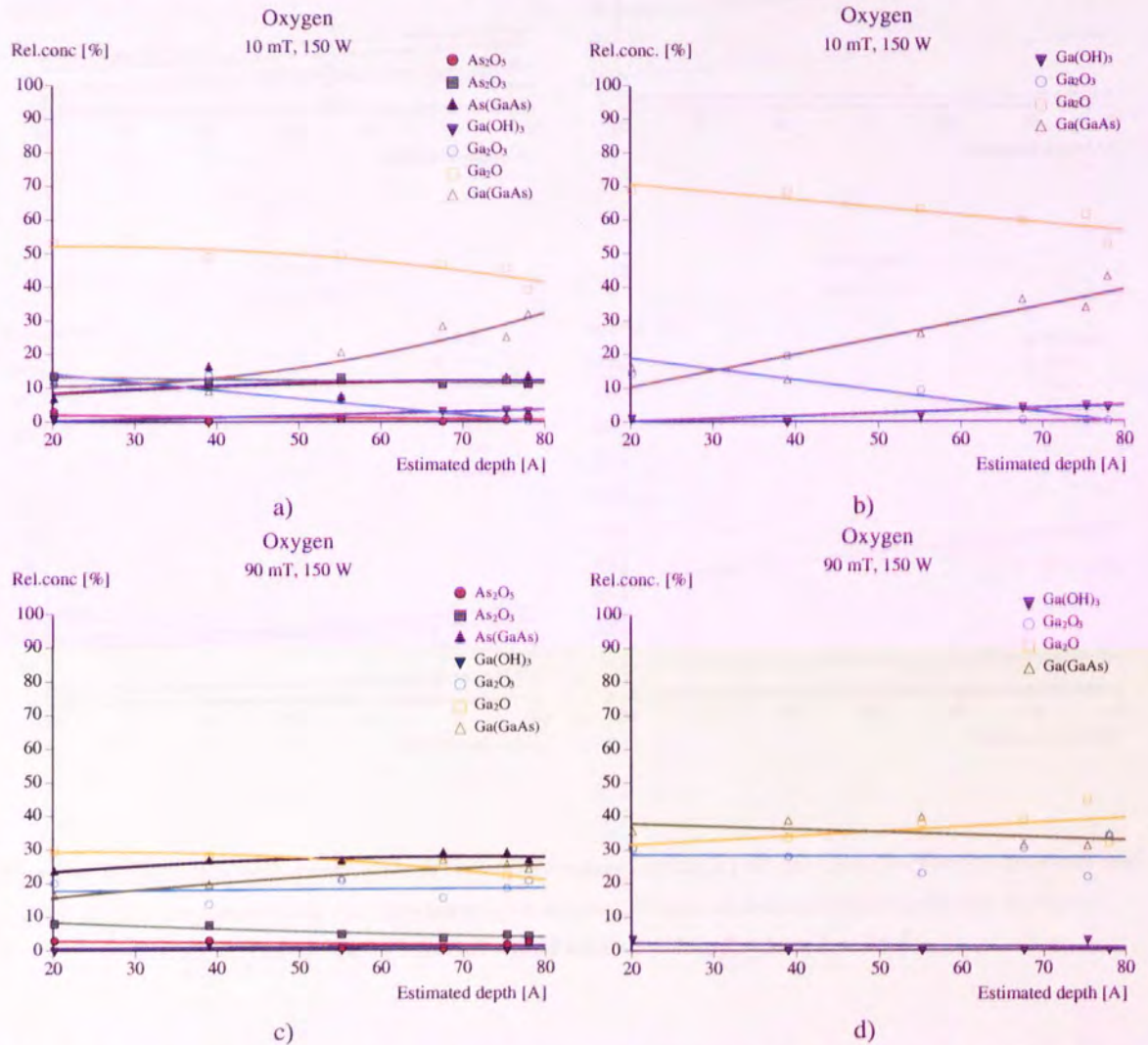


Figure 4.56 Variation with depth of the relative percentages of: a), c) all the GaAs surface components and b), d) Ga components only (oxygen plasma, etch time: 30 min, at indicated pressures and powers). Estimated depth was calculated with:  $d = \lambda \cos\theta$ , where  $\lambda = 26 \text{ \AA}$ .

At 5 W and 90 mT, no important differences in the amounts of As and Ga oxides were observed (Figure 4.57 c)). This result is very important as no preferential oxidation of As and Ga took place. In this case, probably no physical sputtering occurred. At 5 W and 10 mT, the amount of As<sub>2</sub>O<sub>3</sub> was slightly lower than that of Ga<sub>2</sub>O<sub>3</sub>.

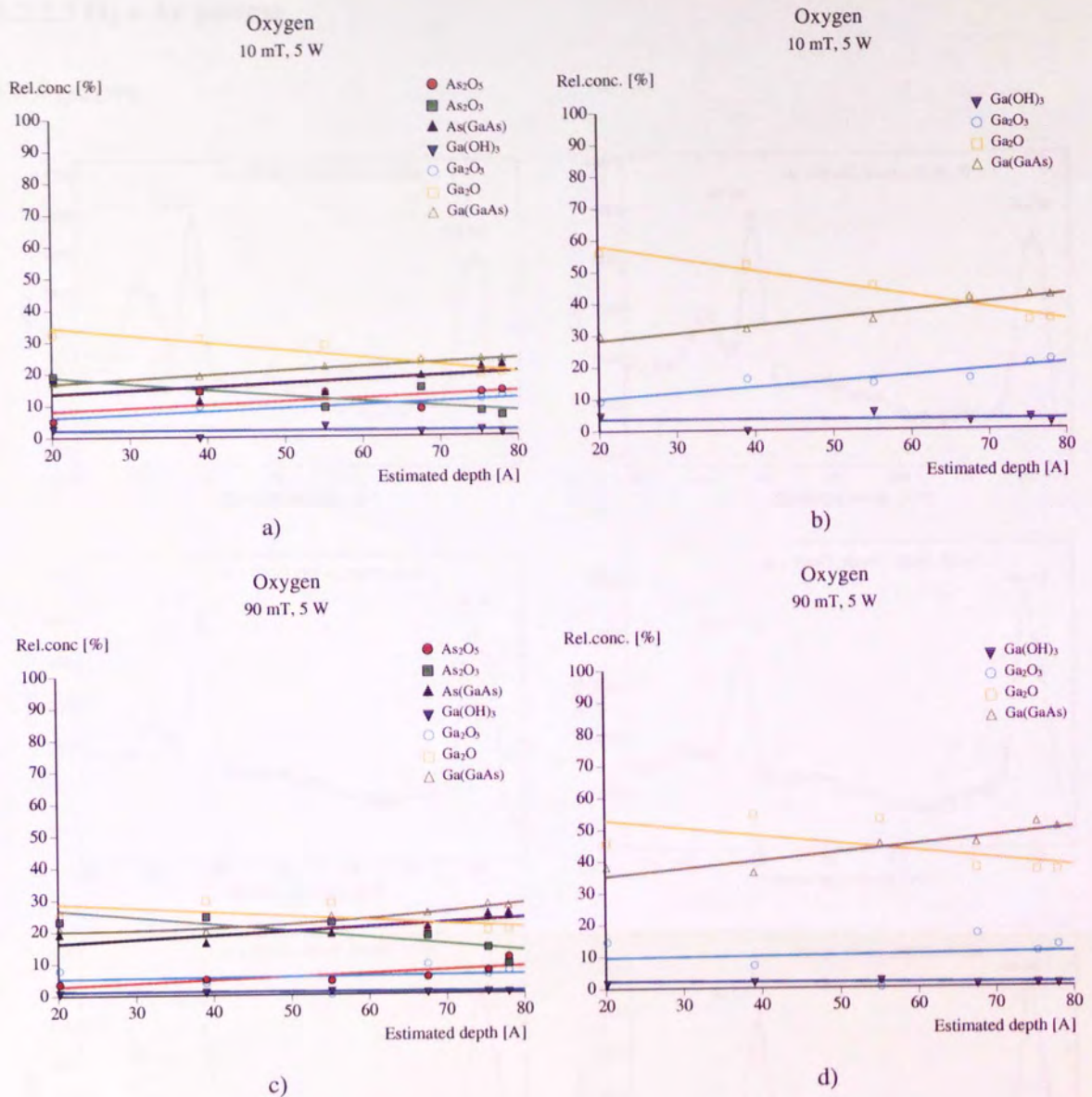


Figure 4.57 Variation with depth of the relative percentages of: a), c) all the GaAs surface components and b), d) Ga components only (oxygen plasma, etch time: 30 min, at indicated pressures and powers). Estimated depth was calculated with:  $d = \lambda \cos \theta$ , where  $\lambda = 26 \text{ \AA}$ .

### 4.2.2.3 O<sub>2</sub> + Ar plasma

#### XPS spectra

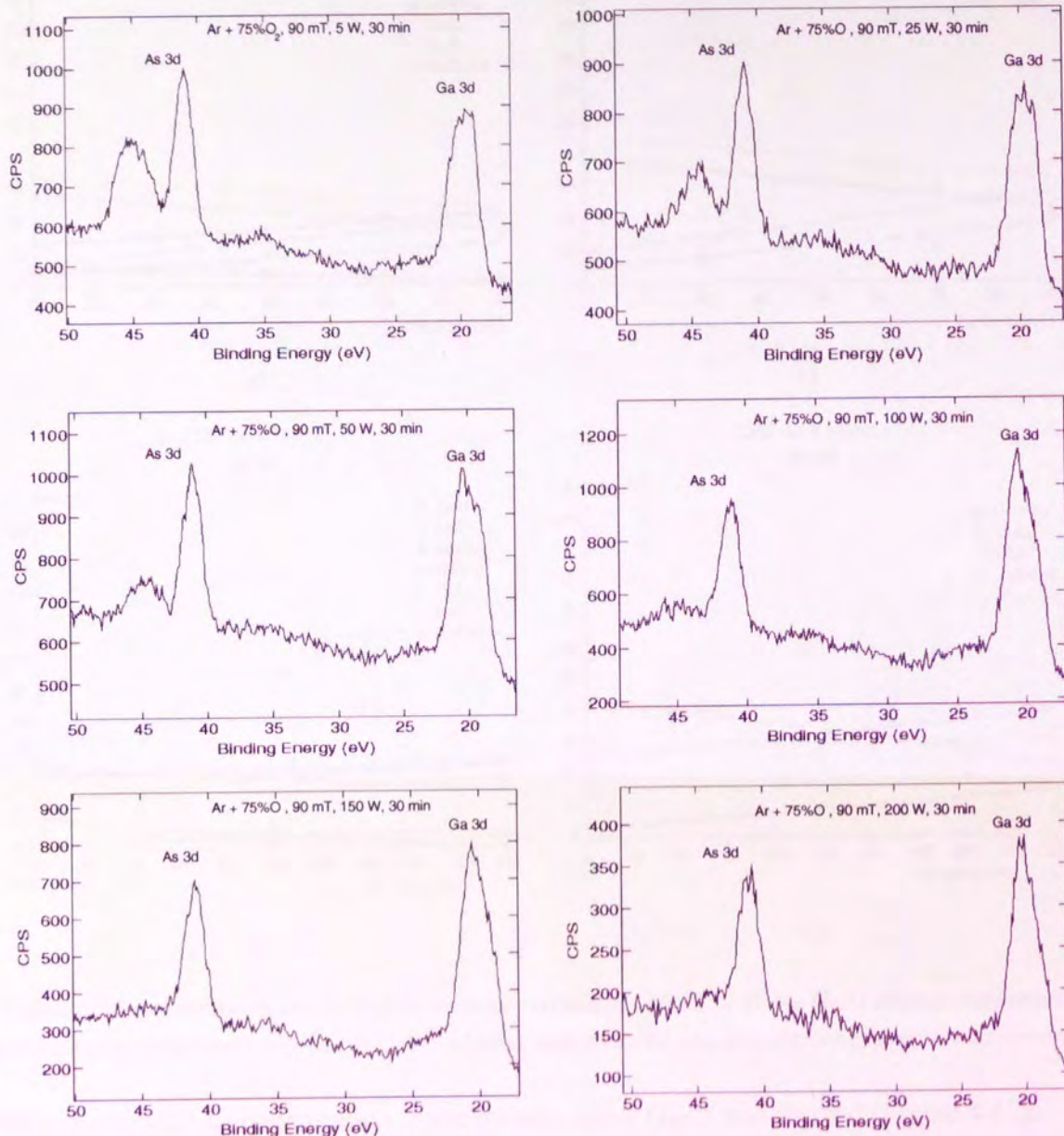


Figure 4.58 XPS spectra for Ar + 75%O<sub>2</sub> etching of GaAs at 90 mT, 30 min at different powers

#### Surface compositional changes

As expected, the oxidation was higher than in the case of argon, with most of the oxide as gallium oxide.

An interesting result of the XPS analysis of the GaAs surface treated in the oxygen-argon mixture was that a high concentration of Ga(OH)<sub>3</sub> was obtained especially at high pressures (see Figure 4.59), in contrast with previous results.

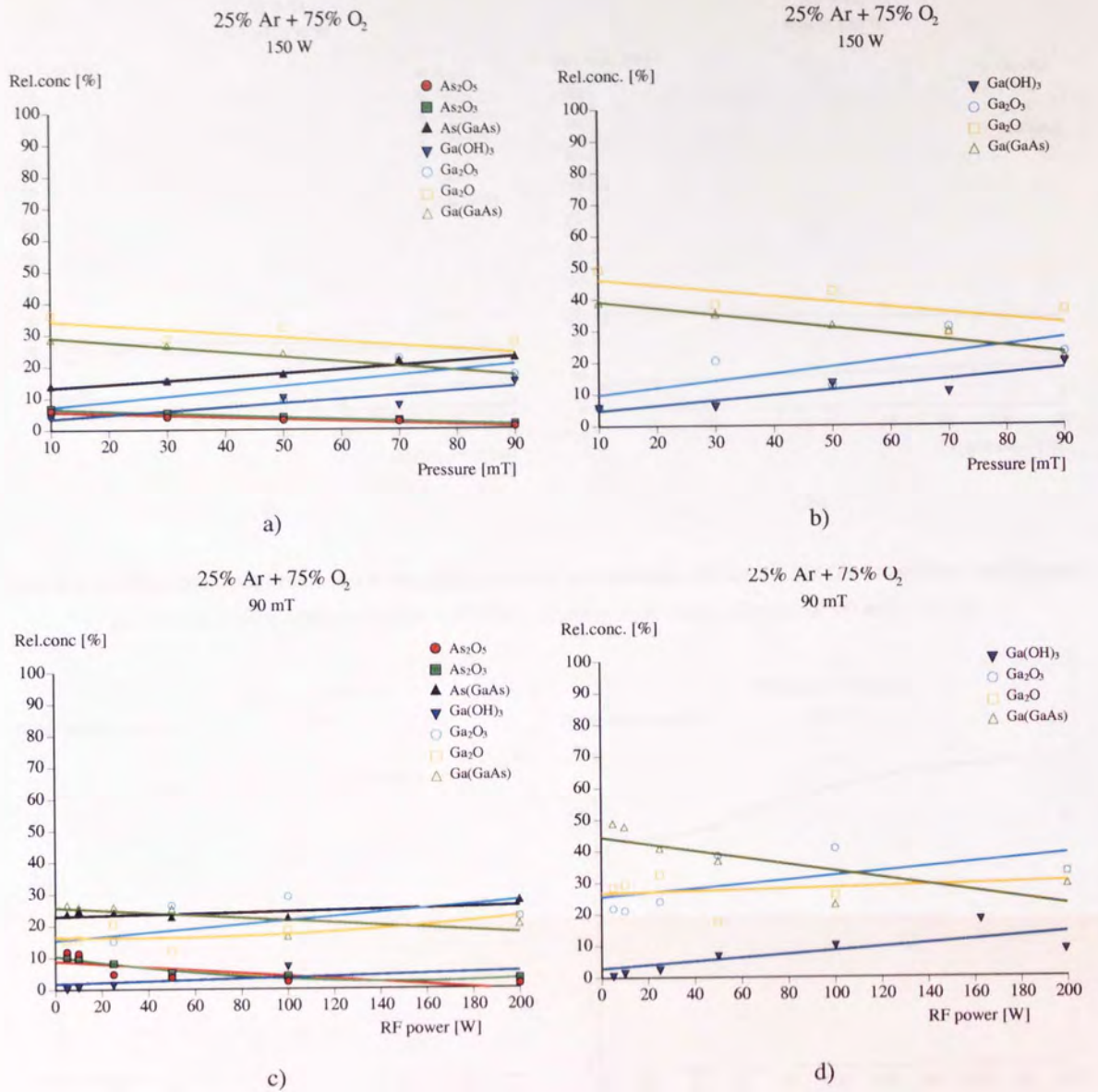


Figure 4.59 Variation with pressure of the relative percentages of: a), c) all the GaAs surface components and b), d) Ga components only (Ar + 75%O<sub>2</sub> plasma, etch time: 30 min, at indicated pressures and powers).

With increasing O<sub>2</sub> concentration in the plasma, more Ga<sub>2</sub>O was formed (Figure 4.61).

Another interesting result is that the oxide thickness was higher in the case of argon-oxygen mixtures than when using pure oxygen plasma (see Figure 4.61). With increasing oxygen content above 2%, no increase in surface oxidation was observed.

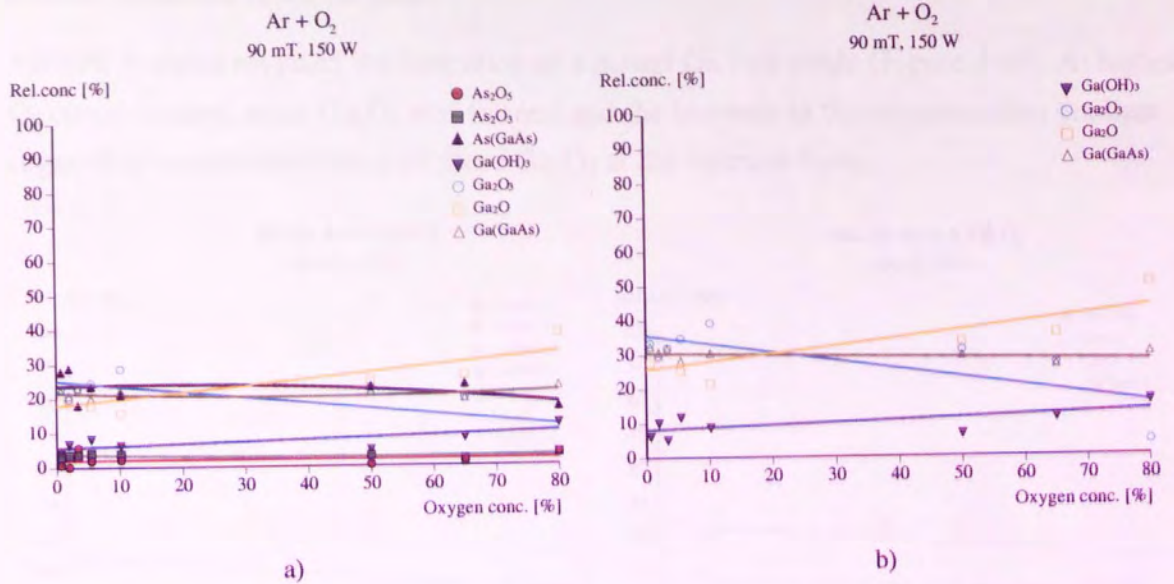


Figure 4.61 Variation with concentration of the relative percentages of: a) all the GaAs surface components and b) Ga components only (Ar + 75%O<sub>2</sub> plasma, etch time: 30 min, at 90 mT, 150 W)

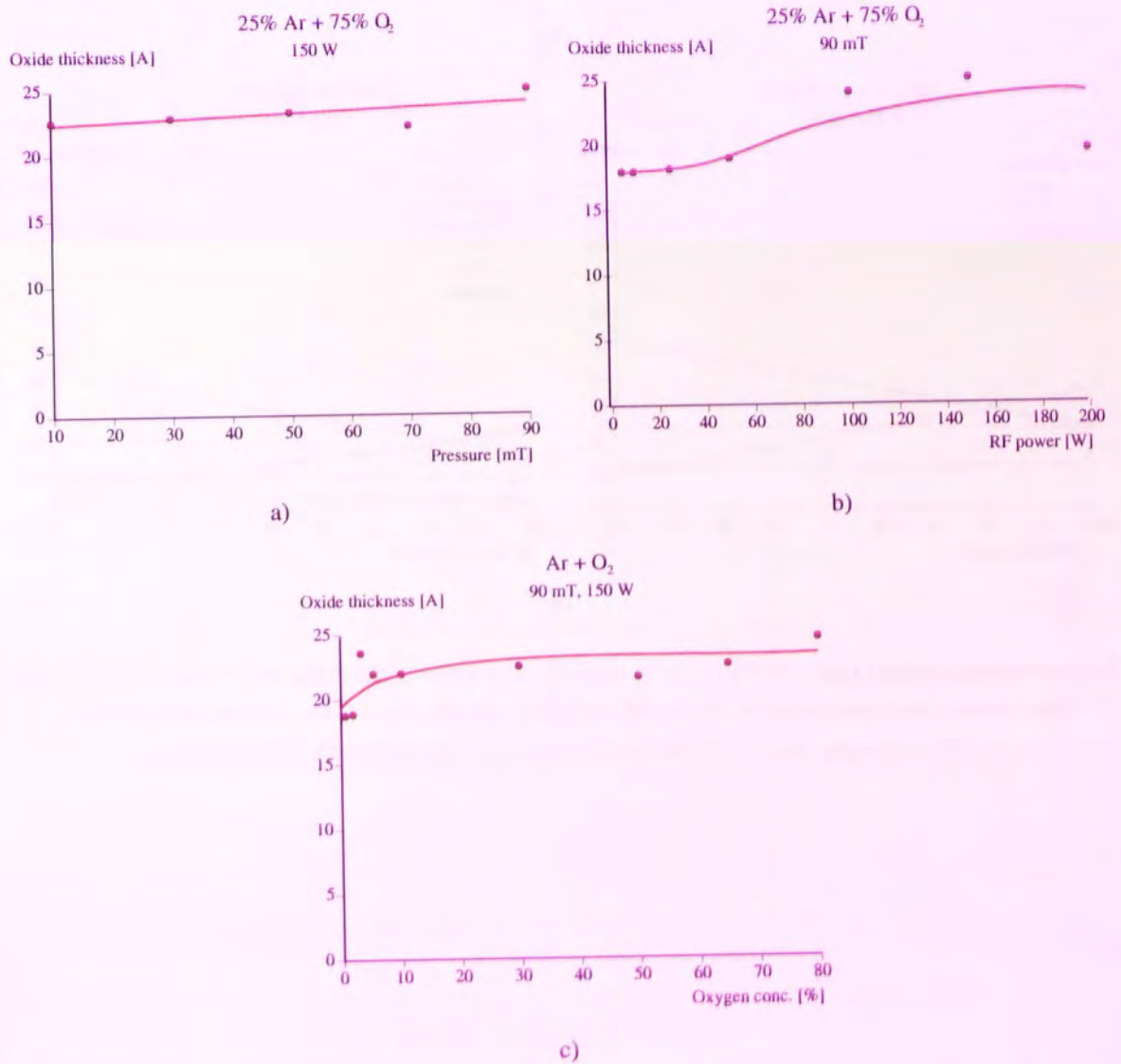


Figure 4.62 Variation of oxide thickness with a) pressure, b) power and c) O<sub>2</sub> concentration

### Layered structure of the surface

ARXPS analysis revealed the formation of a mixed Ga rich oxide (Figure 4.63). At higher O<sub>2</sub> concentration, more Ga<sub>2</sub>O<sub>3</sub> was formed and the increase in the concentration gradient suggests a layered structure with more Ga<sub>2</sub>O<sub>3</sub> at the topmost layer.

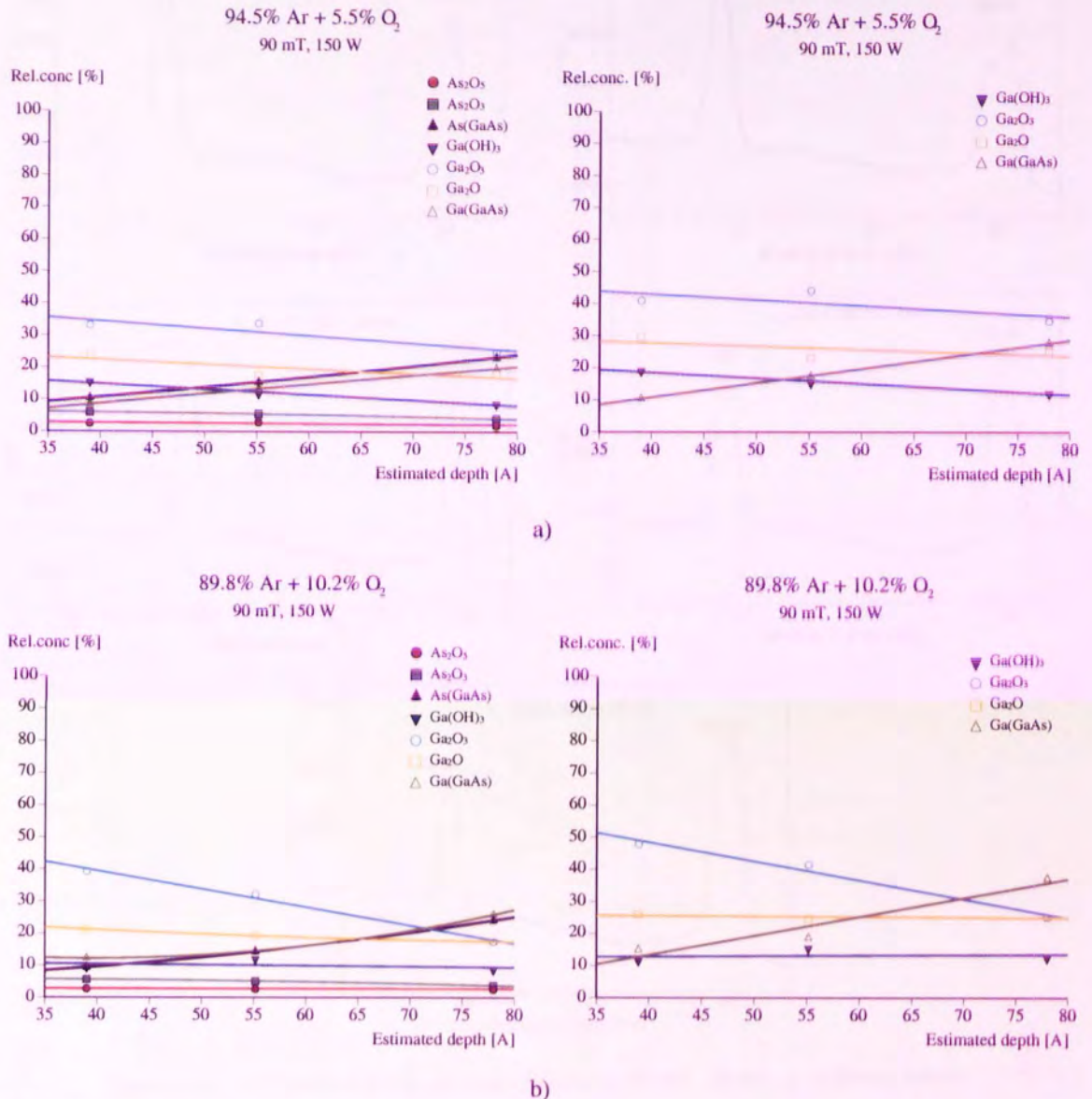


Figure 4.63 Variation with depth of the relative percentages of: a), c) all the GaAs surface components and b), d) Ga components only (oxygen plasma, etch time: 30 min, at indicated pressures, powers and concentrations). Estimated depth was calculated with:  $d = \lambda \cos \theta$ , where  $\lambda = 26 \text{ \AA}$ .

#### 4.2.2.4 H<sub>2</sub> plasma

##### XPS spectra

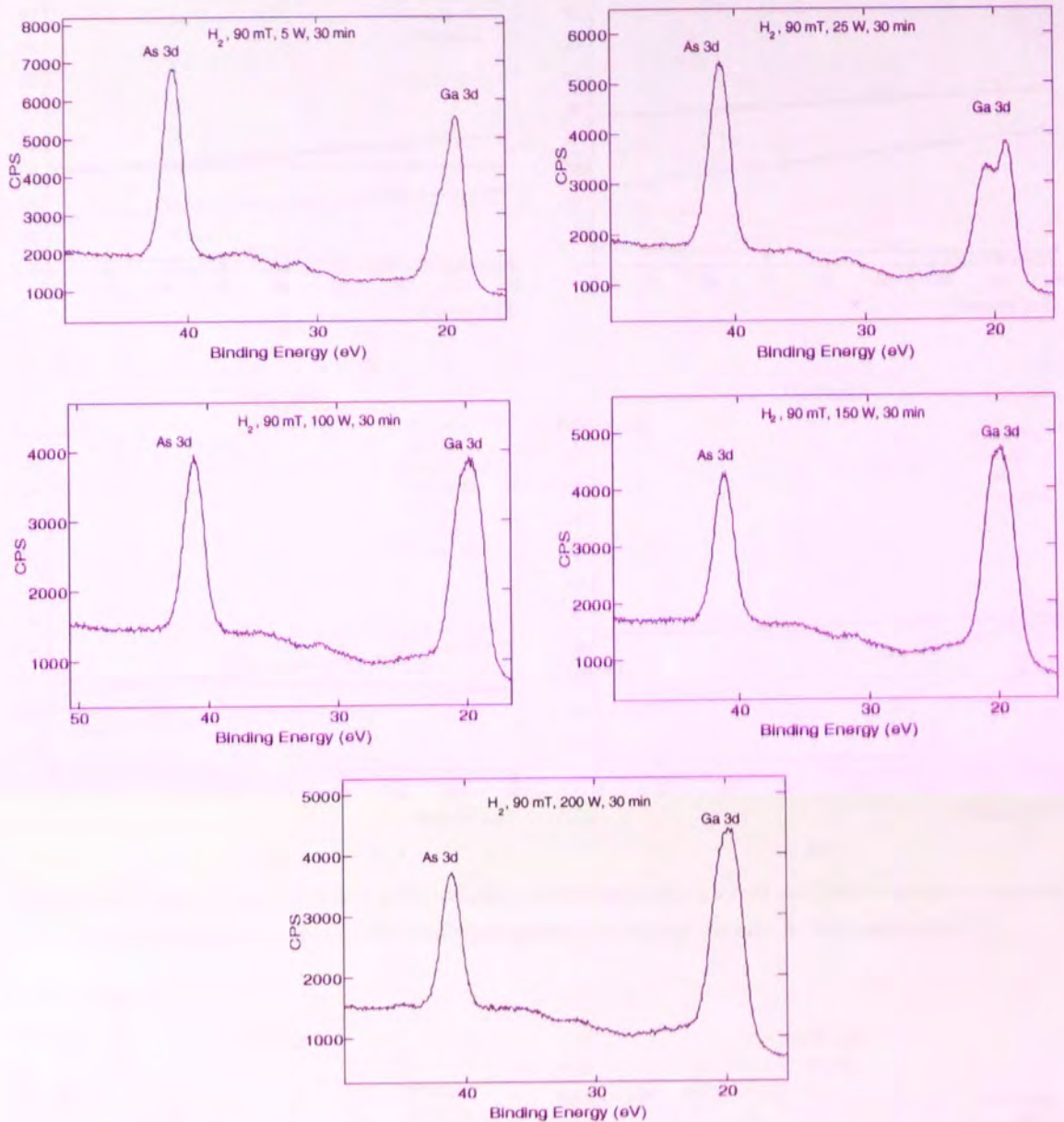


Figure 4.64 XPS spectra for H<sub>2</sub> etching of GaAs at 90 mT, 30 min at different powers

##### Surface compositional changes

In the case of hydrogen plasma treatment, the native oxide plays an important role on the final surface composition because no physical sputtering can occur.

As can be observed in Figure 4.65, the As oxides completely disappeared after treatment. Some gallium hydroxide was formed.

With power, Ga<sub>2</sub>O concentration increased and Ga<sub>2</sub>O<sub>3</sub> remained constant (Figure 4.66).

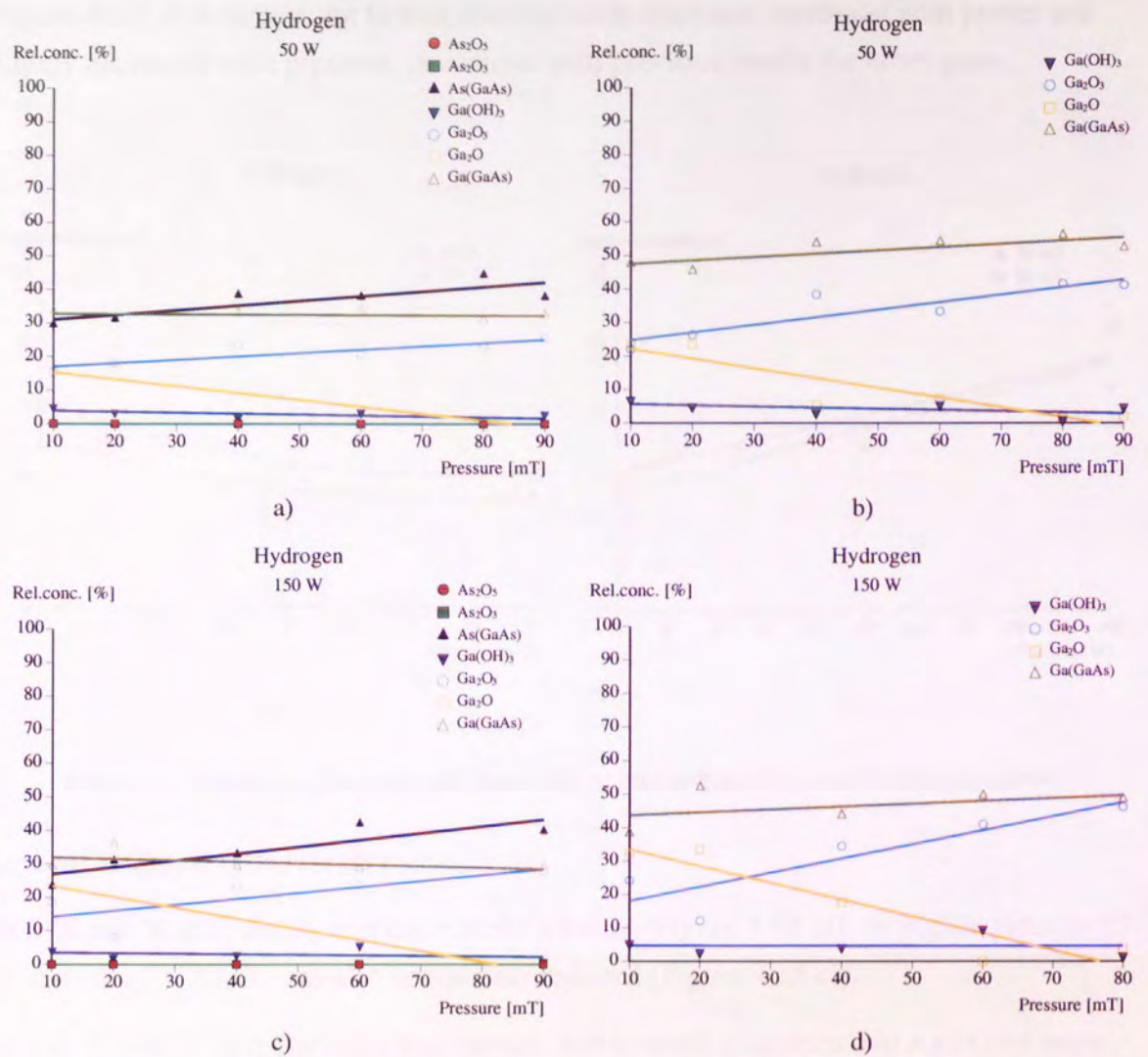


Figure 4.65 Variation with pressure of the relative percentages of: a), c) all the GaAs surface components and b), d) Ga components only (hydrogen plasma, etch time: 30 min, at indicated powers).

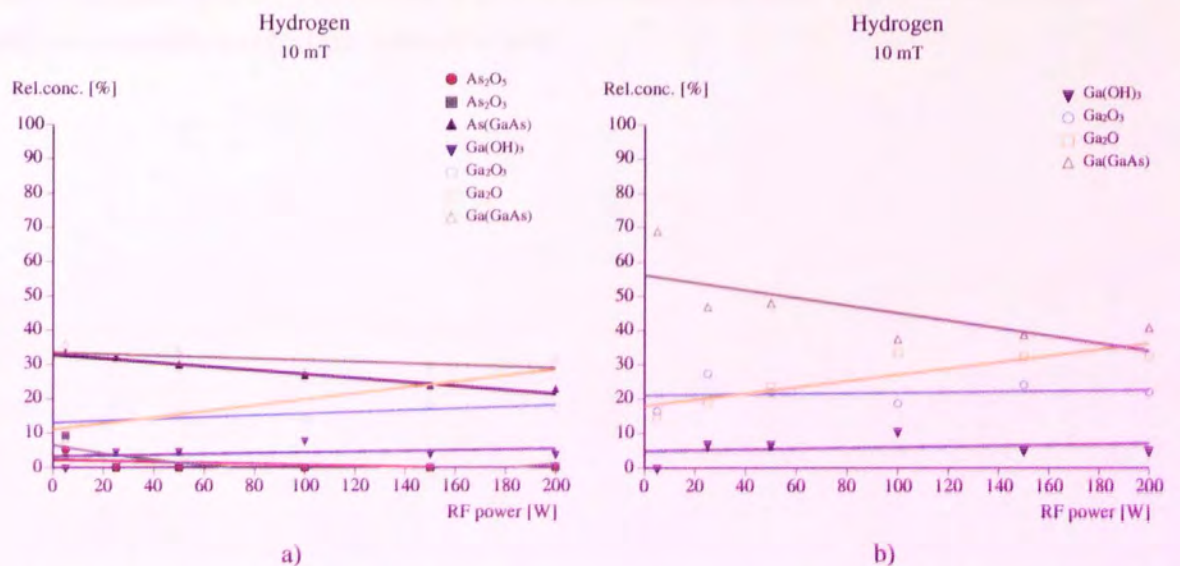


Figure 4.66 Variation with power of the relative percentages of: a) all the GaAs surface components and b) Ga components only (hydrogen plasma, etch time: 30 min, at 10 mT).

At low power and high pressures the oxide thickness was close to that of the native oxide (Figure 4.67). It is interesting to note that the oxide thickness increased with power and slightly decreased with pressure, in contrast with previous results for other gases.

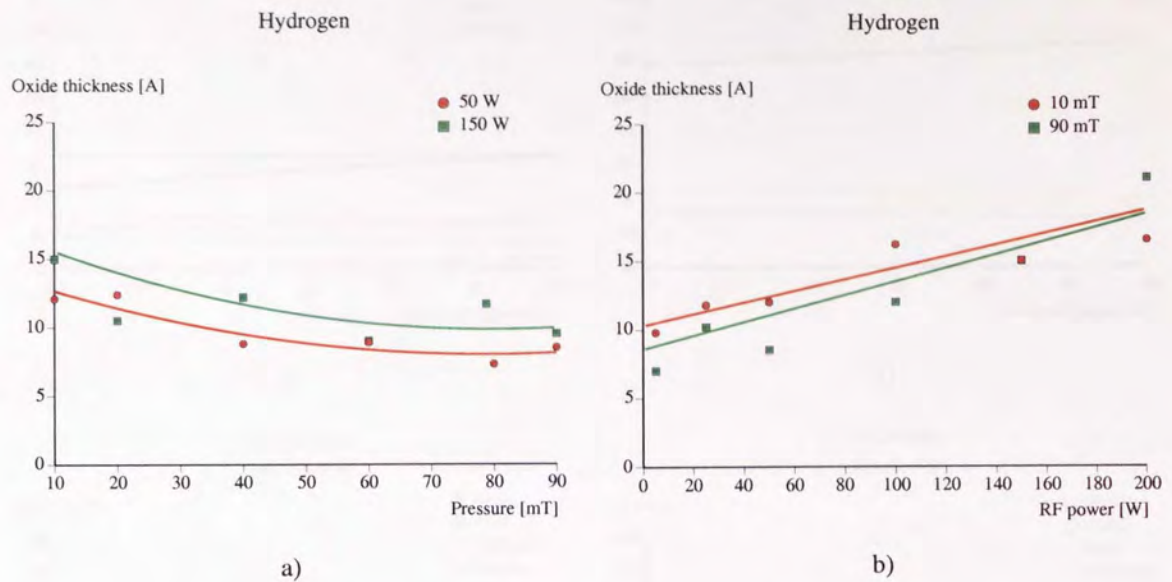


Figure 4.67 Variation of the oxide thickness with a) pressure and b) power (hydrogen plasma)

#### Layered structure of the surface

At 5 W and 10 mT,  $\text{As}_2\text{O}_5$  was completely reduced (Figure 4.68 a). At higher pressure (5 W and 90 mT),  $\text{As}_2\text{O}_3$  was also completely reduced (Figure 4.68 c)).

At 200 W and 10 mT,  $\text{Ga}(\text{OH})_3$  was formed, but in small quantities. No As oxides were detected and the major Ga oxide was  $\text{Ga}_2\text{O}$ .

At 200 W and higher pressure, the fast increase of  $\text{Ga}(\text{OH})_3$  concentration with take-off angle suggests that this compound is part of the outermost layer (together with  $\text{Ga}_2\text{O}_3$  whose concentration had the same gradient).

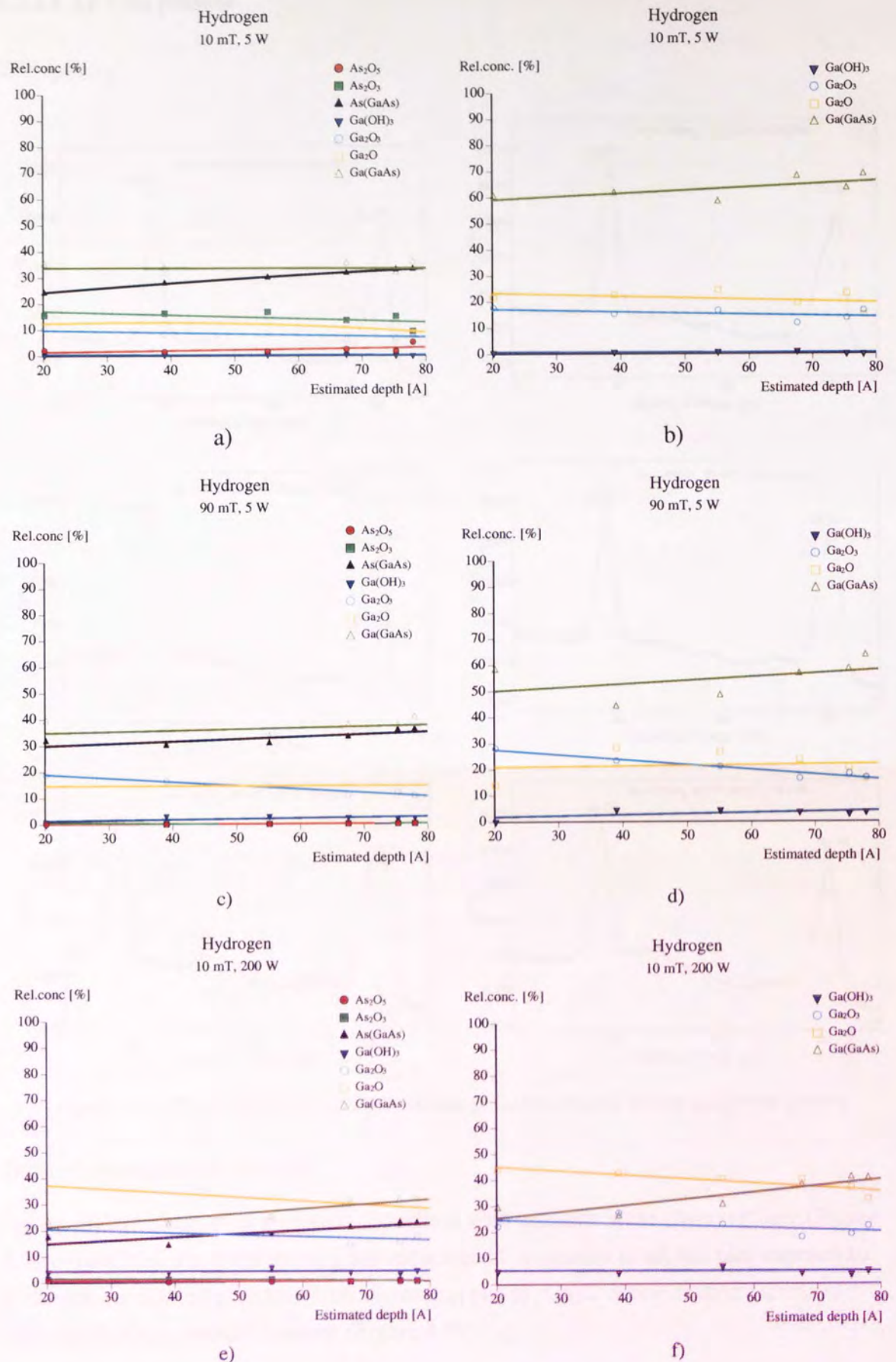


Figure 4.68 Variation with depth of the relative percentages of: a), c), e) all the GaAs surface components and b), d), f) Ga components only (hydrogen plasma, etch time: 30 min, at indicated pressures and powers). Estimated depth was calculated with:  $d = \lambda \cos \theta$ , where  $\lambda = 26 \text{ \AA}$ .

### 4.2.2.5 Ar + H<sub>2</sub> plasma

#### XPS spectra

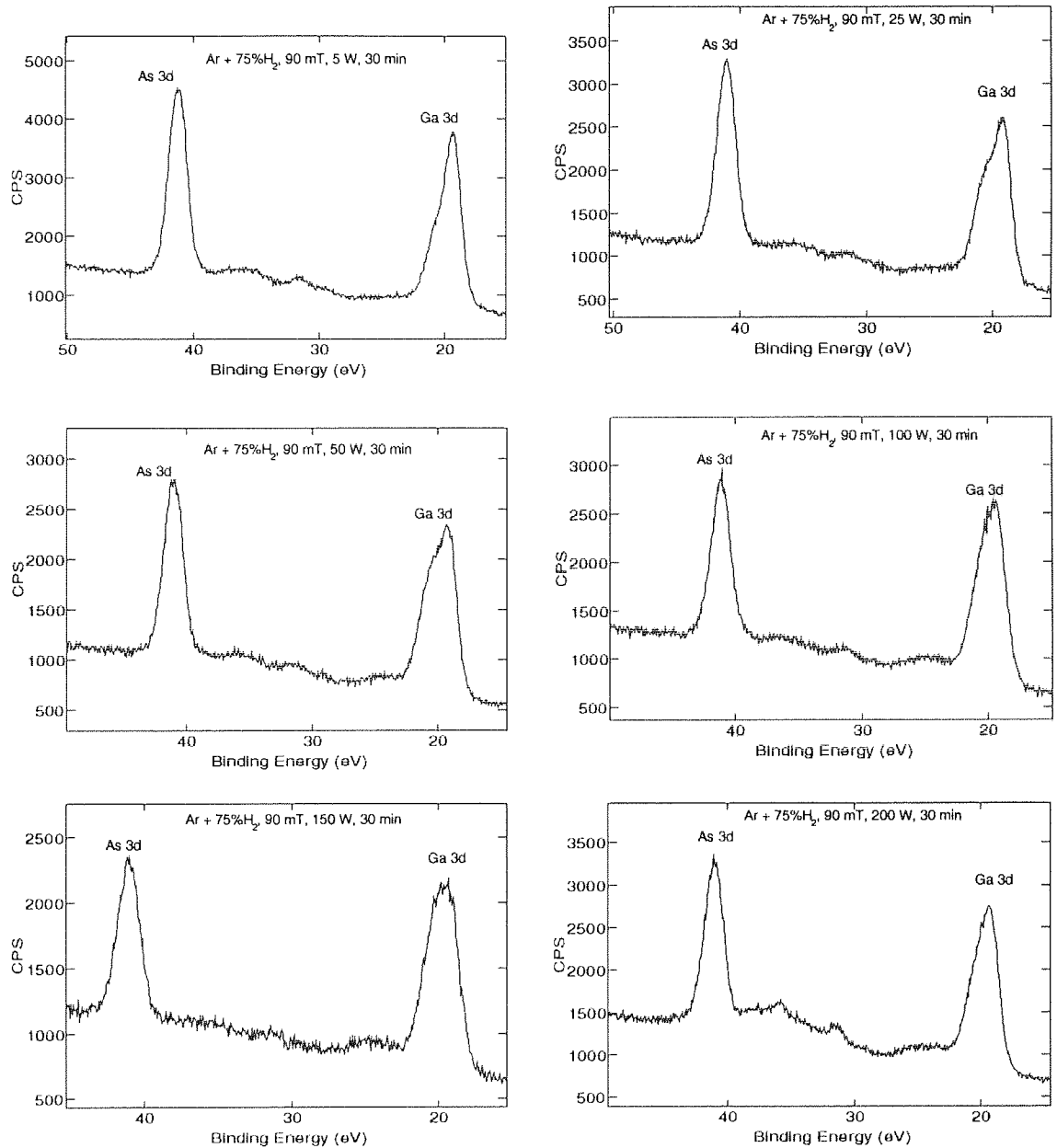


Figure 4.69 XPS spectra for Ar + 75% H<sub>2</sub> etching of GaAs at 90 mT, 30 min at different powers

#### Surface compositional changes

No significant changes of surface composition with pressure were observed here (Figure 4.70). Also, it is worth mentioning the reduction of As oxides in all samples exposed to hydrogen-containing plasmas. With increasing power, Ga<sub>2</sub>O concentration increased whereas Ga<sub>2</sub>O<sub>3</sub> remained constant (Figure 4.71).

With increasing H<sub>2</sub> concentration, the concentration of both Ga<sub>2</sub>O and Ga<sub>2</sub>O<sub>3</sub> increased (Figure 4.72).

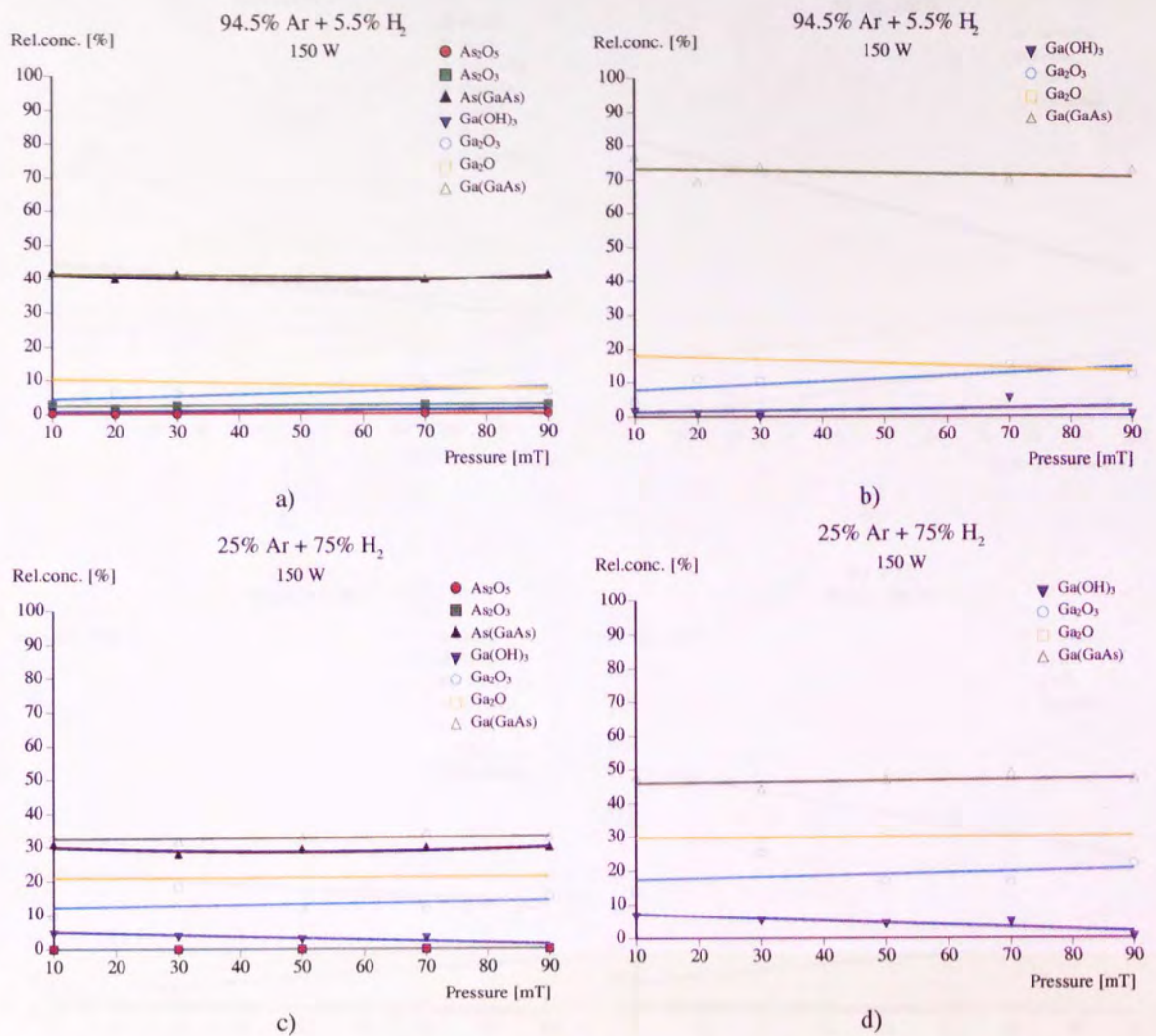


Figure 4.70 Variation with pressure of the relative percentages of: a), c) all the GaAs surface components and b), d) Ga components only (Ar + 75%H<sub>2</sub> plasma, etch time: 30 min, at indicated powers)

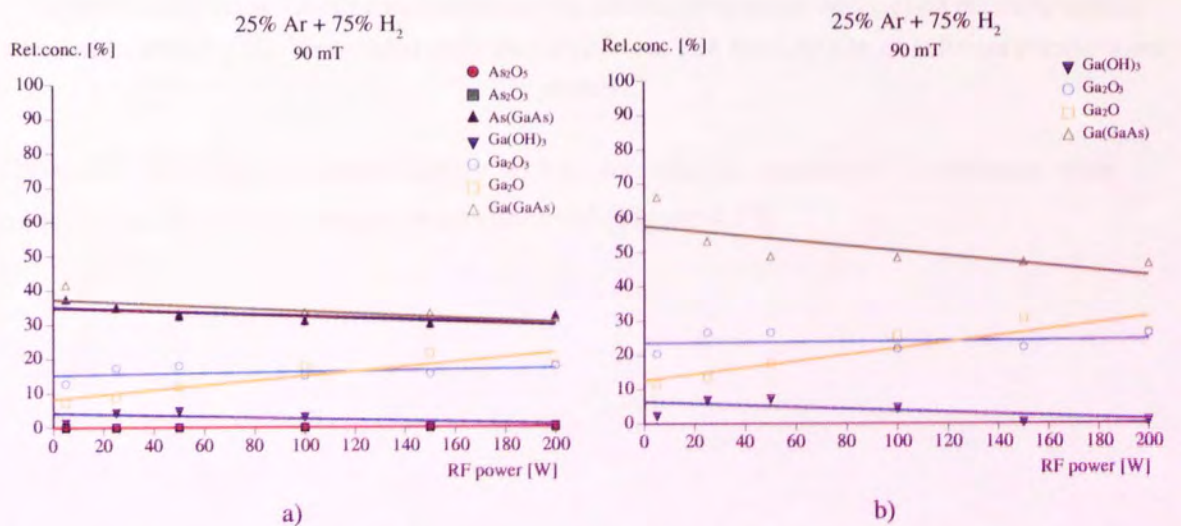


Figure 4.71 Variation with power of the relative percentages of: a) all the GaAs surface components and b) Ga components only (Ar + 75%H<sub>2</sub> plasma, etch time: 30 min, at indicated pressures)

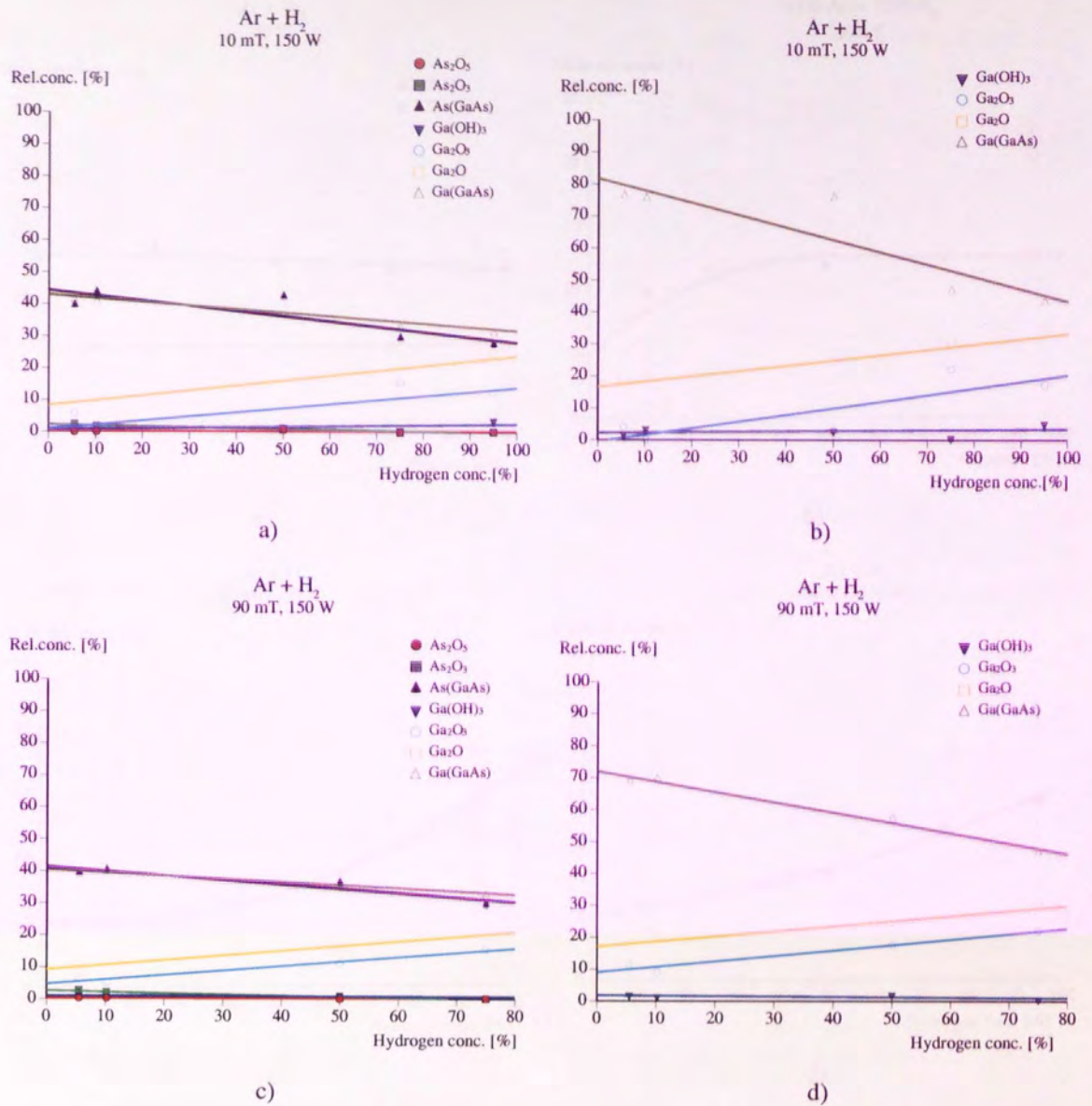


Figure 4.72 Variation with H<sub>2</sub> concentration of the relative percentages of: a), c) all the GaAs surface components and b), d) Ga components only (Ar + H<sub>2</sub> plasma, etch time: 30 min, at indicated pressures and powers)

The oxide thickness increased slightly with power and H<sub>2</sub> concentration whereas with pressure no significant changes were observed (Figure 4.73).

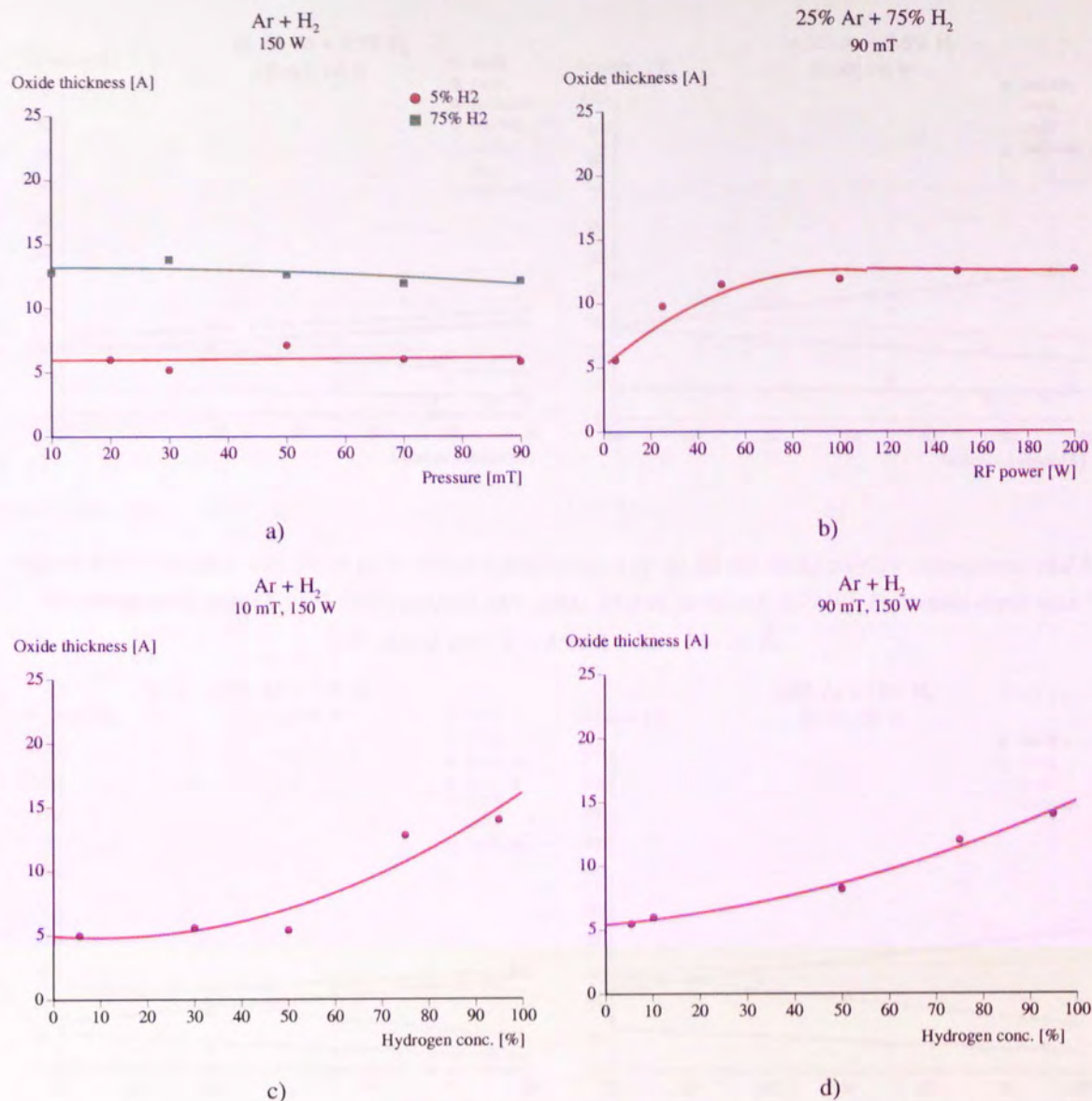


Figure 4.73 Variation of oxide thickness with a) pressure, b) power and c), d) H<sub>2</sub> concentration

#### Layered structure of the surface

ARXPS analysis showed that the composition and structure of the oxide was different at 10 mT and 90 mT (Figure 4.74 a)).

At 75% H<sub>2</sub>, Ga(OH)<sub>3</sub> concentration was higher at low pressure than at high pressure.

Arsenic depleted surfaces were found at high ion energies, as observed in Figure 4.75.

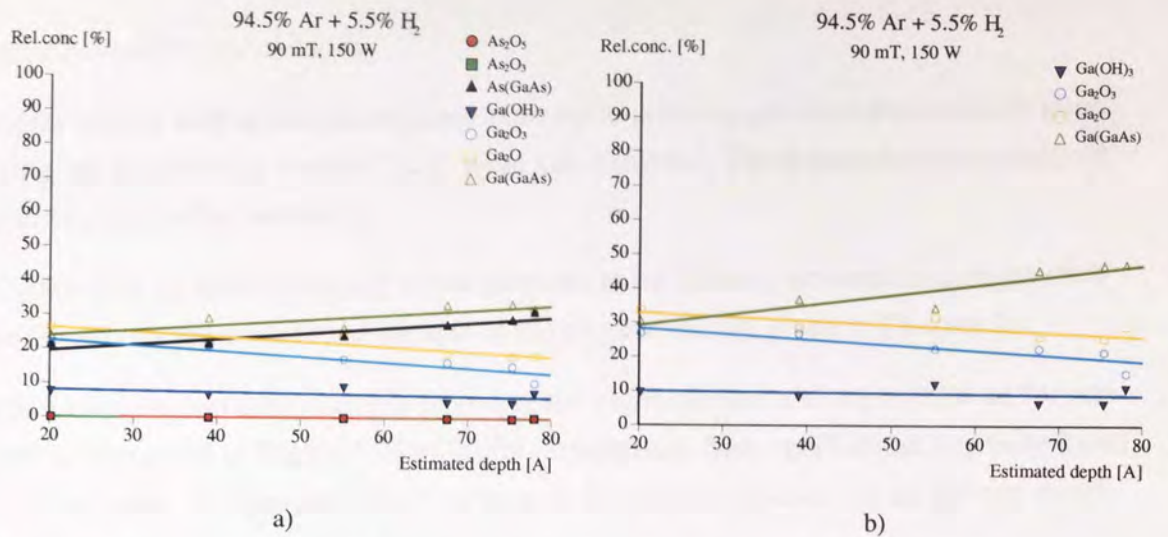


Figure 4.74 Variation with depth of the relative percentages of: a) all the GaAs surface components and b) Ga components only (Ar + 5.5% $H_2$  plasma, etch time: 30 min, at 90 mT, 150 W). Estimated depth was calculated with:  $d = \lambda \cos\theta$ , where  $\lambda = 26 \text{ \AA}$ .

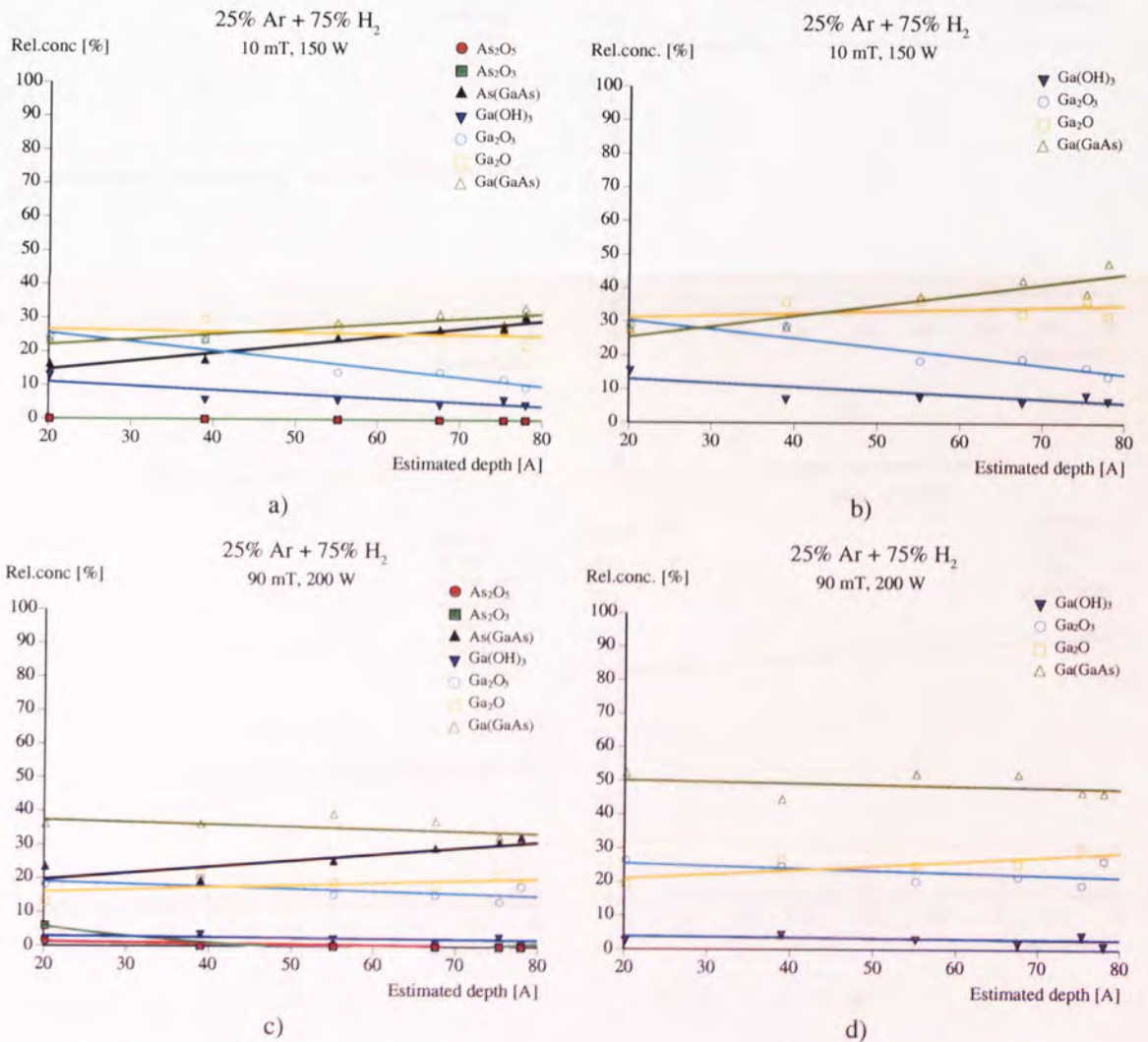


Figure 4.75 Variation with depth of the relative percentages of: a), c) all the GaAs surface components and b), d) Ga components only (Ar + 75% $H_2$  plasma, etch time: 30 min, at indicated pressures and powers). Estimated depth was calculated with:  $d = \lambda \cos\theta$ , where  $\lambda = 26 \text{ \AA}$ .

#### 4.2.2.6 O<sub>2</sub> flow

##### Surface compositional changes

Samples treated with argon plasma then exposed to pure oxygen flow immediately after etching (as described in Section 3.2.1) were also analysed. These samples were analysed within two days after treatment.

In Figure 4.76 c), with increasing argon pressure in the plasma, no surface changes after exposure to oxygen were found (details of the experiment are given in Chapter 3).

Surface composition of the sample etched in the argon plasma and exposed in air for one month is also given in Figure 4.76 a), b) for comparison. More gallium oxides were found after 20 minutes of exposure to O<sub>2</sub> flow than in the case of exposure to air for one month.

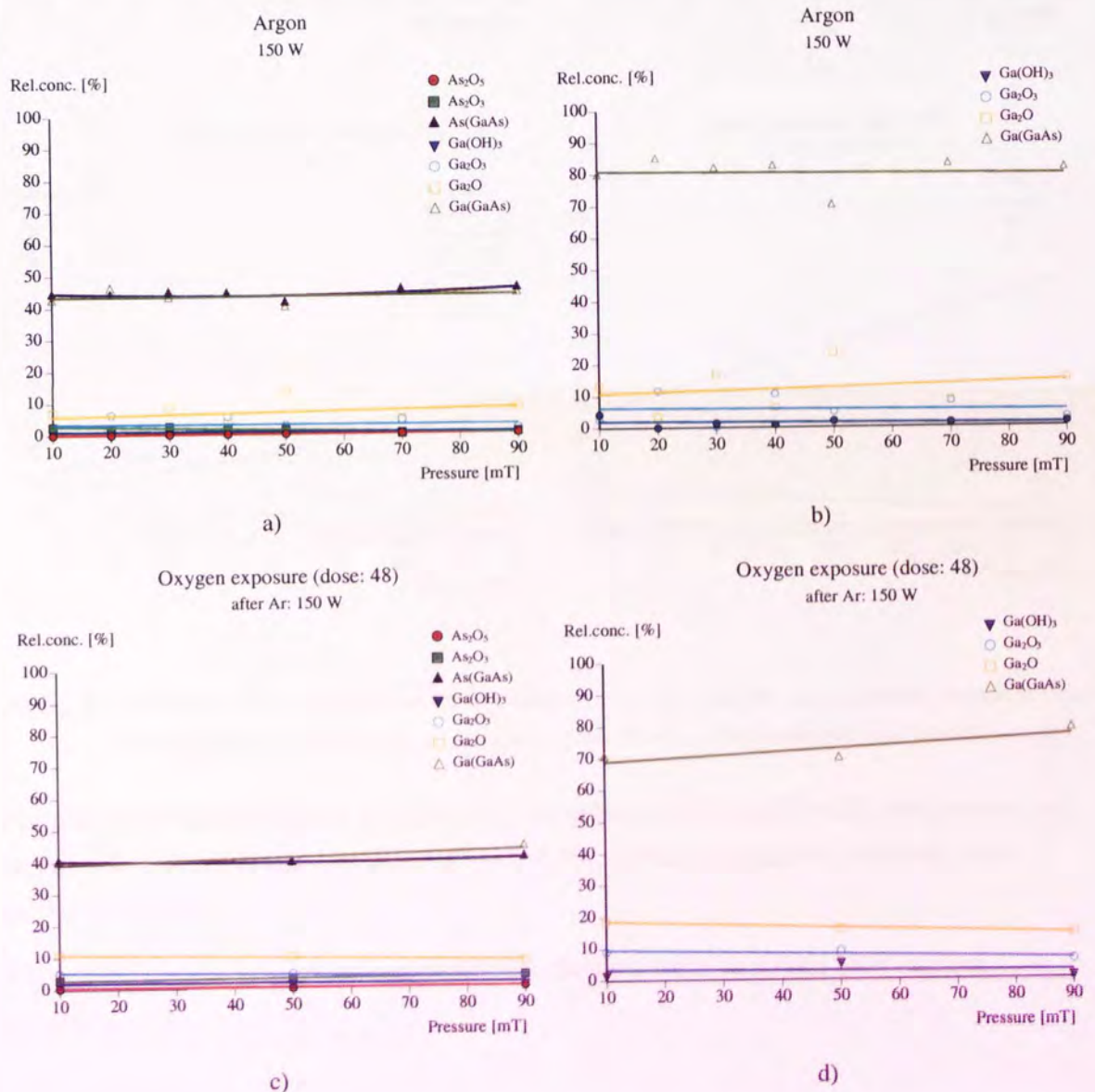


Figure 4.76 Variation with pressure of the relative percentages of: a), c) all the GaAs surface components and b), d) Ga components only (Ar plasma, etch time: 30 min, under indicated conditions).

Surface changes with RF power after oxygen exposure (Figure 4.77 c)) showed the appearance of  $\text{As}_2\text{O}_5$  at low powers but no changes at higher powers were observed.

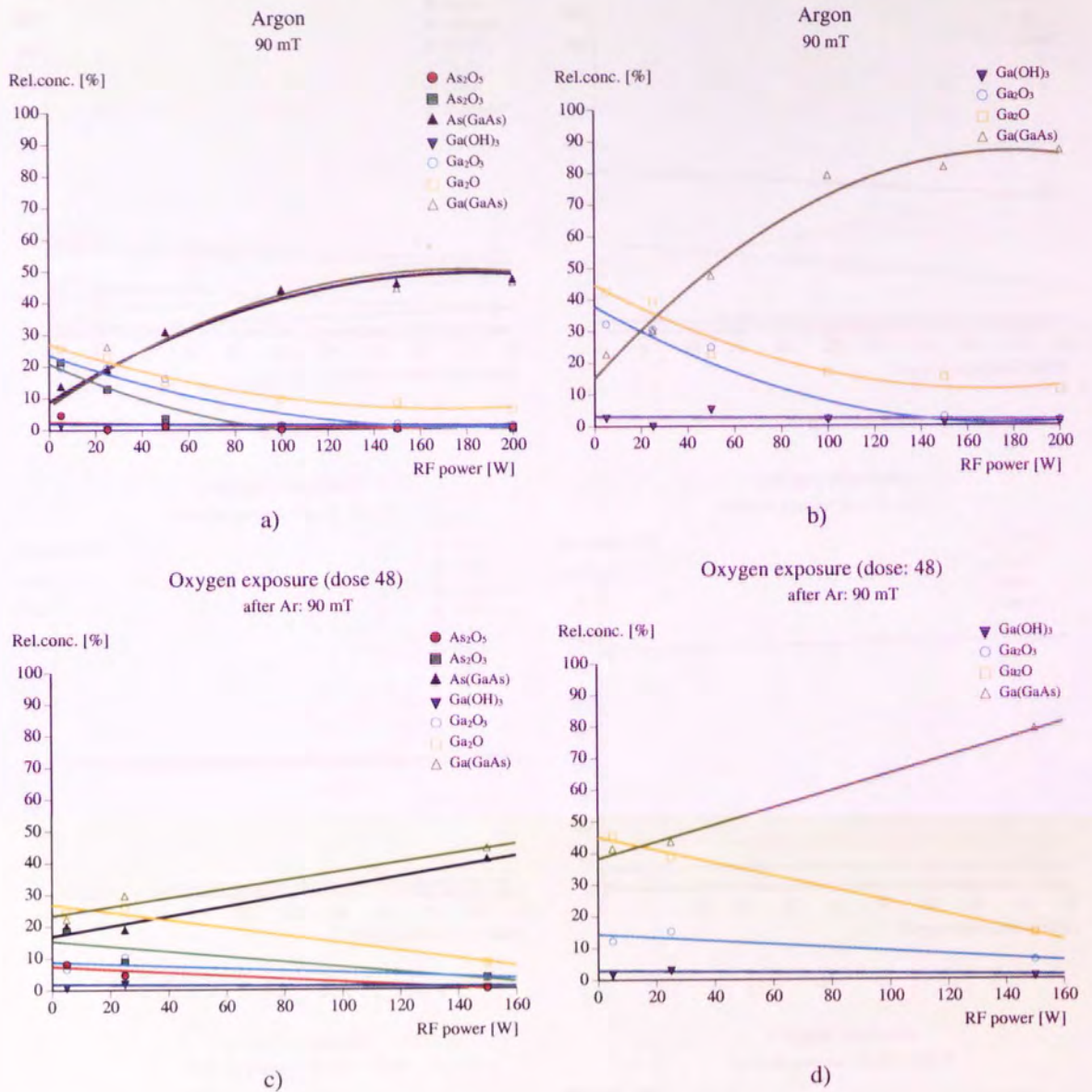


Figure 4.77 Variation with power of the relative percentages of: a), c) all the GaAs surface components and b), d) Ga components only (Ar plasma, etch time: 30 min, under indicated conditions).

For plasma conditions where no sputtering occurred (at 5W and 90 mT), with increasing oxygen dose after plasma treatment (Figure 4.78), surface oxidation increased in As oxides and  $\text{Ga}_2\text{O}$ .

At high RF power, no surface compositional changes were observed after oxygen exposure.

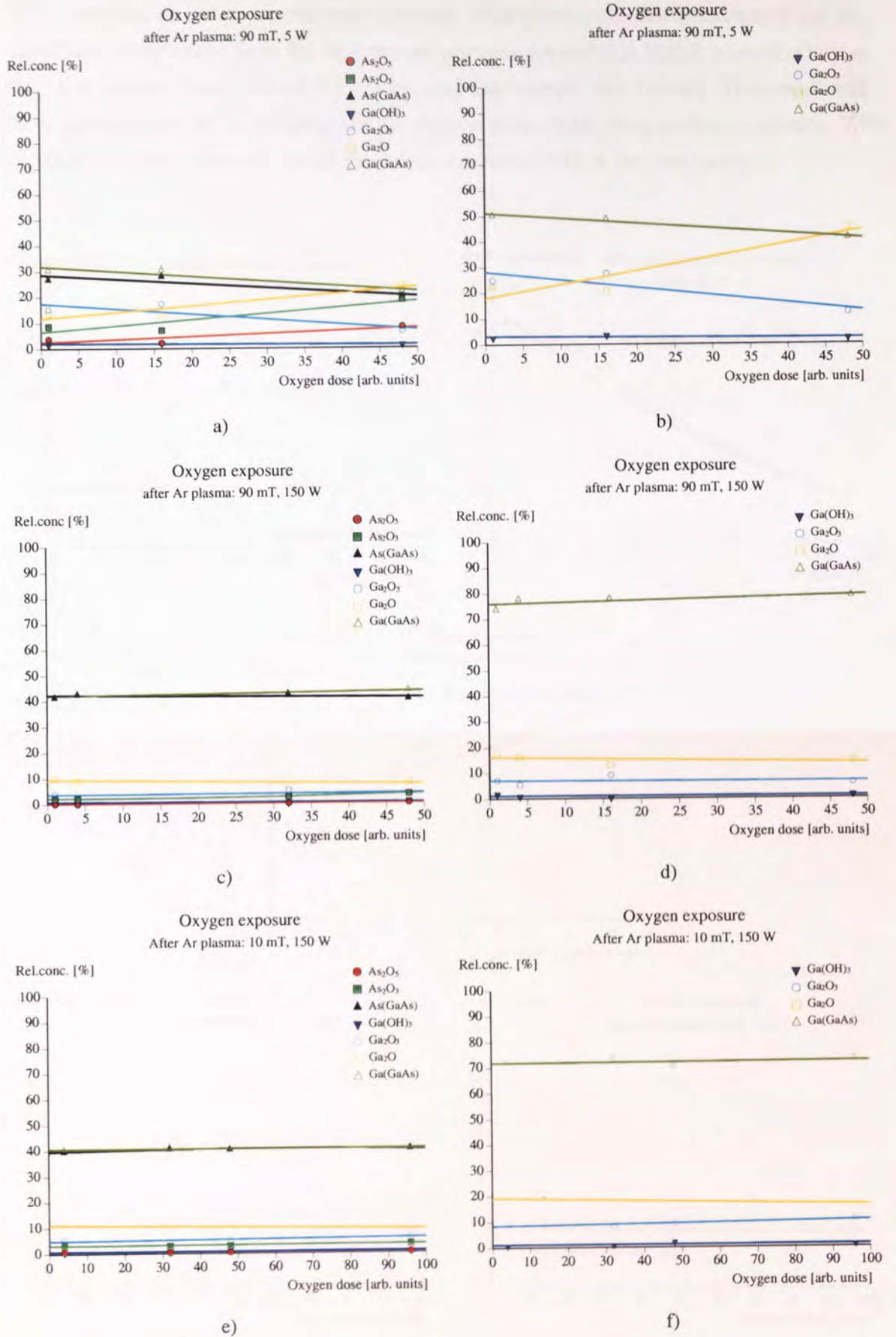


Figure 4.78 Variation with  $O_2$  dose of the relative percentages of: a), c), e) all the GaAs surface components and b), d), f) Ga components only (Ar plasma, etch time: 30 min, under indicated conditions).

Variation of oxide thickness with pressure, power and dose is presented in Figure 4.79. With pressure, no oxide growth was observed. With power, oxidation decreased and no significant differences from the air-exposed samples appeared at higher powers. Only at very low powers, less oxide on the oxygen-exposed sample was formed. This result will be explained later by the influence of the oxygen dose on the final surface oxidation. With increasing oxygen dose, the oxide thickness increased only at low ion energies.

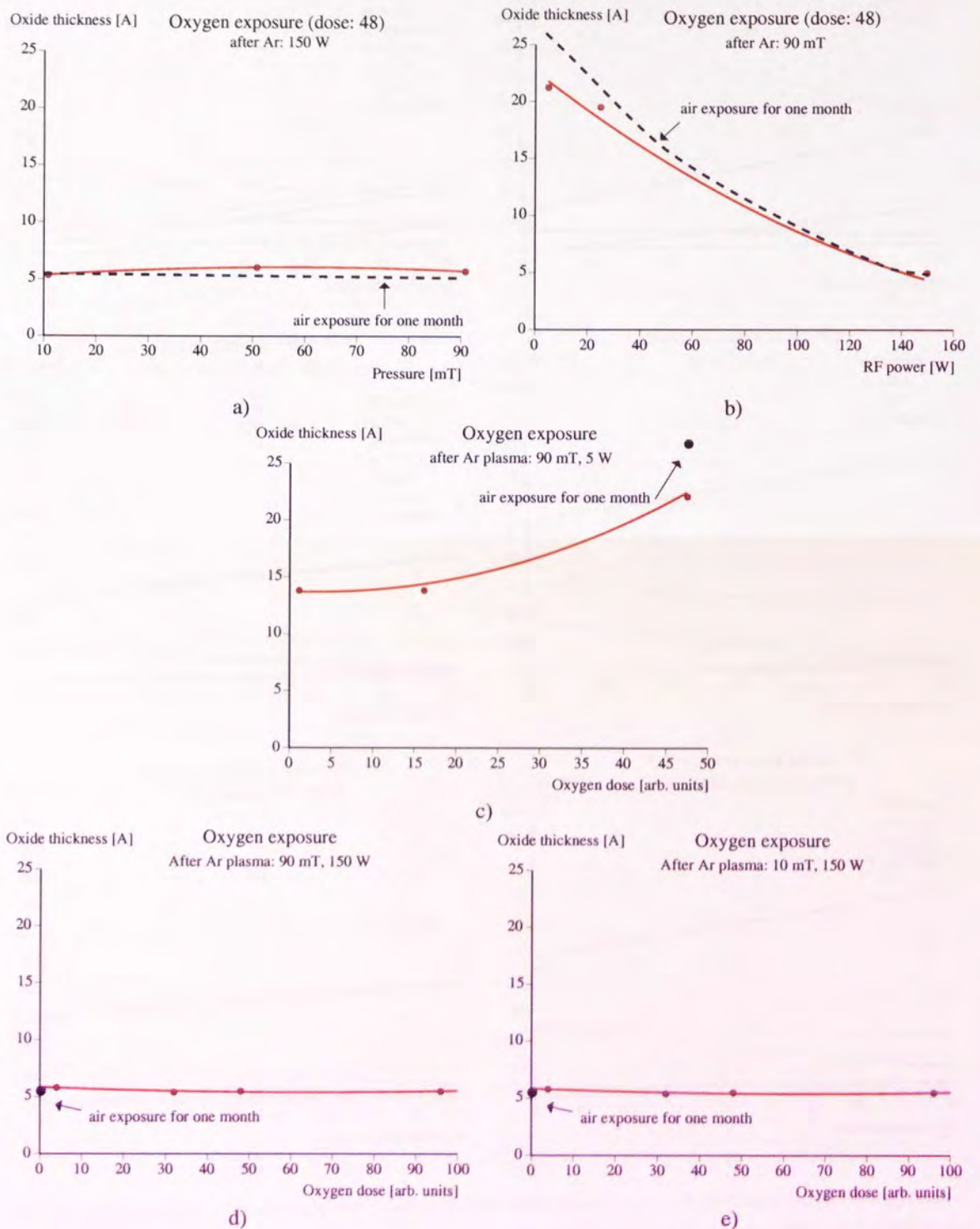


Figure 4.79 Variation of oxide thickness with a) pressure, b) power and oxygen dose at c) 90 mT, 5 W; d) 90 mT, 150 W; e) 10 mT, 5 W

## Layered structure of the surface

ARXPS analysis of the samples exposed to oxygen immediately after different Ar plasma treatments are shown in Figure 4.80. As can be observed in these figures, at very low ion energies, the surface is rich in Ga and As oxides. A significant amount of  $\text{As}_2\text{O}_5$  was found. At higher ion energies, a decrease of the concentration of As oxides was observed.

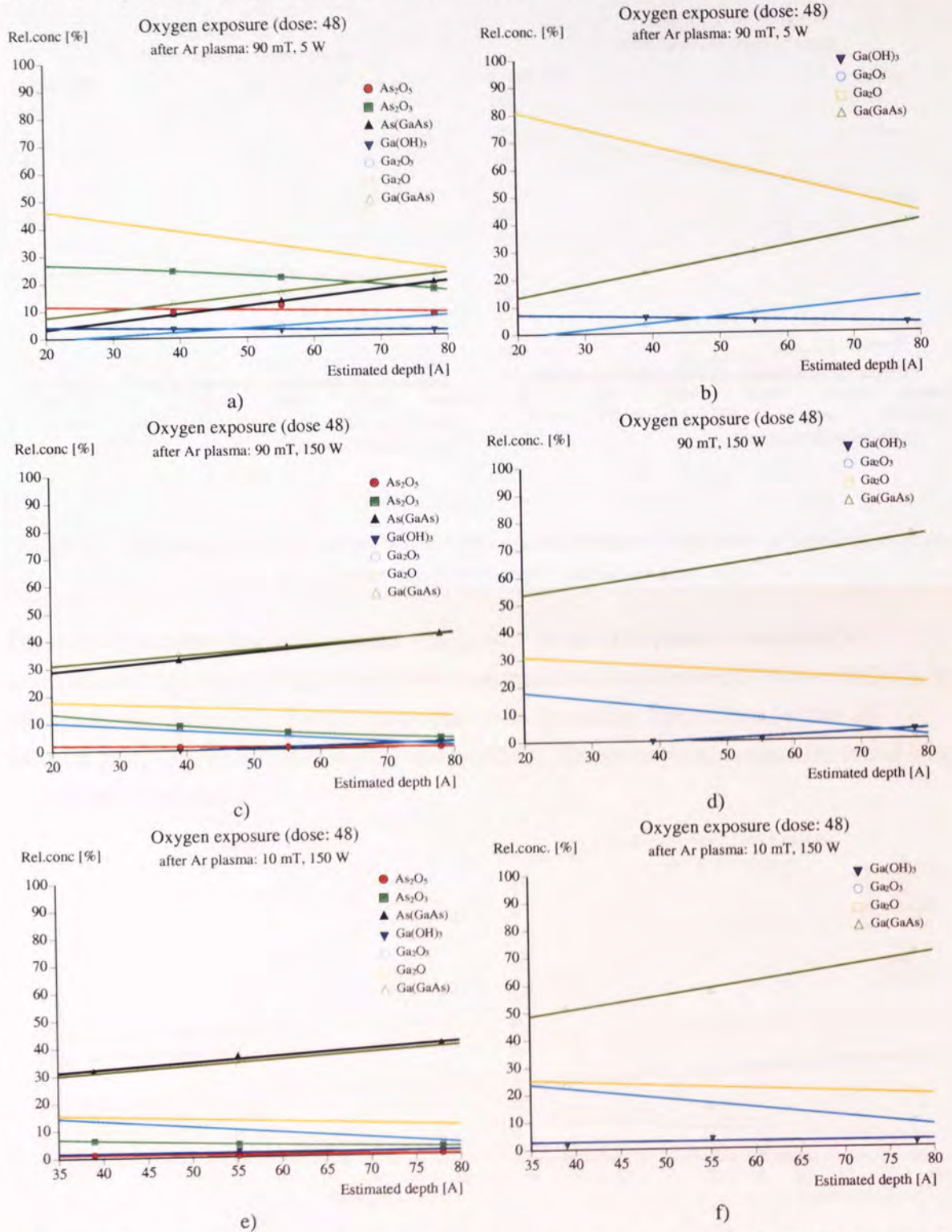


Figure 4.80 Variation with depth of the relative percentages of: a), c), e) all the GaAs surface components and b), d), f) Ga components only (argon plasma, etch time: 30 min then  $\text{O}_2$  exposure dose 48, at indicated pressures and powers). Estimated depth was calculated with:  $d = \lambda \cos\theta$ , where  $\lambda = 26 \text{ \AA}$ .

#### 4.2.2.7 Prolonged exposure to air

Air-exposed argon plasma-treated GaAs surfaces (at 150 W, 10 mT) showed a logarithmical increase of Ga<sub>2</sub>O and Ga<sub>2</sub>O<sub>3</sub> concentration within 13 months of exposure (Figure 4.81). It is interesting to note that during this time, no As oxides were formed.

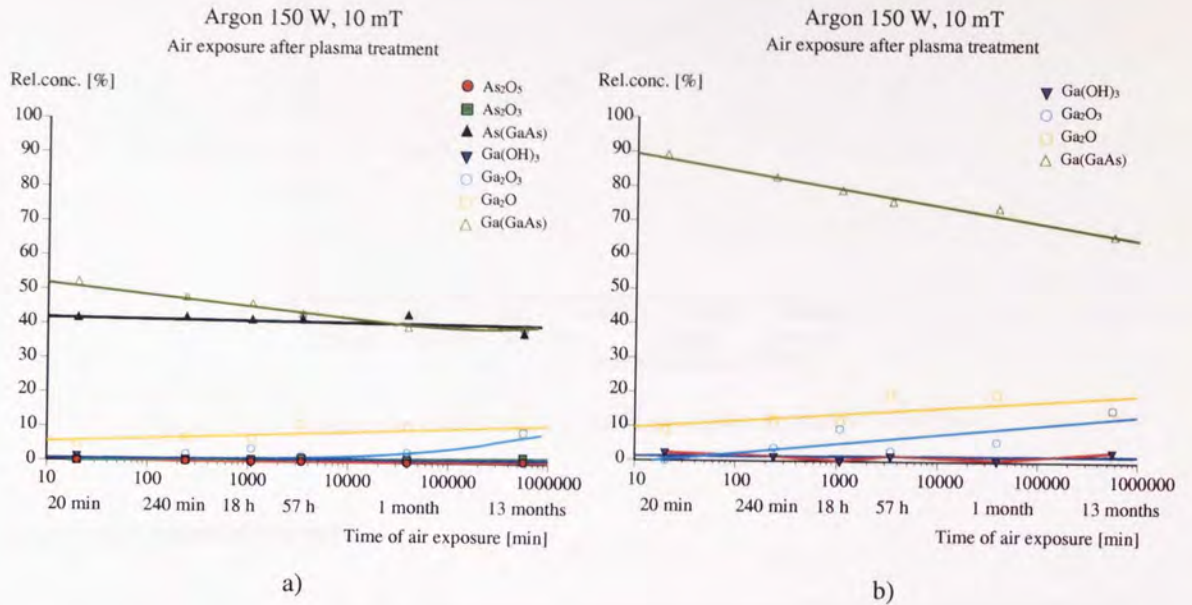


Figure 4.81 Variation with time of exposure to air after plasma treatment of the relative percentages of: a) all the GaAs surface components and b) Ga components only

Figure 4.82 showed that in 13 months of exposure to air after plasma treatment, a simultaneous increase of Ga<sub>2</sub>O<sub>3</sub> and Ga<sub>2</sub>O concentration was observed (Figure 4.82 b)). It should also be mentioned that the first oxide to be formed on the surface (within 20 minutes of air exposure) was Ga<sub>2</sub>O (Figure 4.82 a)). Traces of As<sub>2</sub>O<sub>3</sub> were also found after 13 months of exposure.

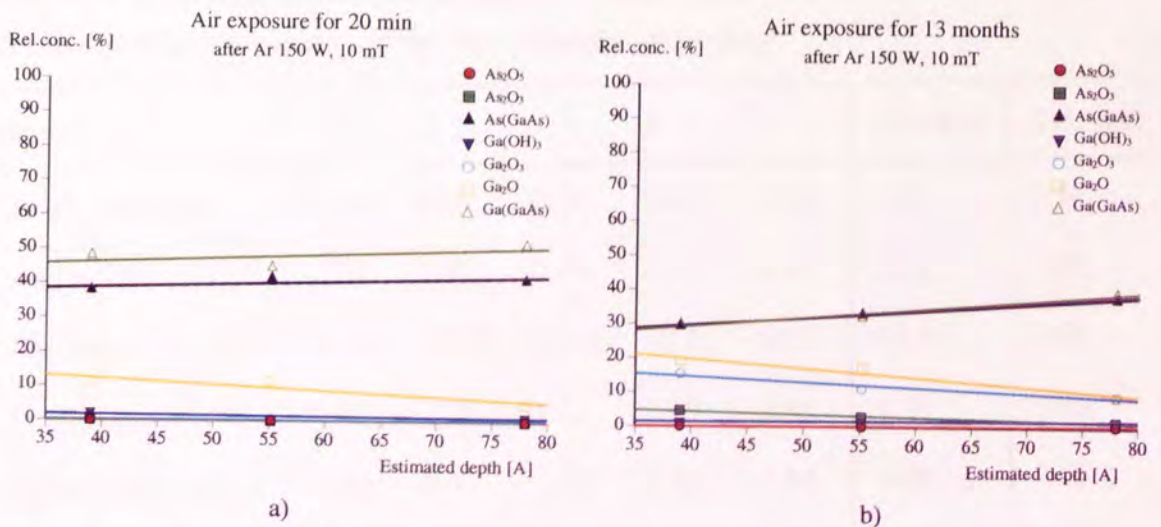


Figure 4.82 Variation with depth of the relative percentages of all the GaAs surface components. Argon plasma, etch time: 30 min then air exposure for a) 20 min b) 13 months. Estimated depth was calculated with:  $d = \lambda \cos\theta$ , where  $\lambda = 26 \text{ \AA}$ .

The thickness of the air-grown oxide increased by about three monolayers during this time, as can be observed in Figure 4.83.

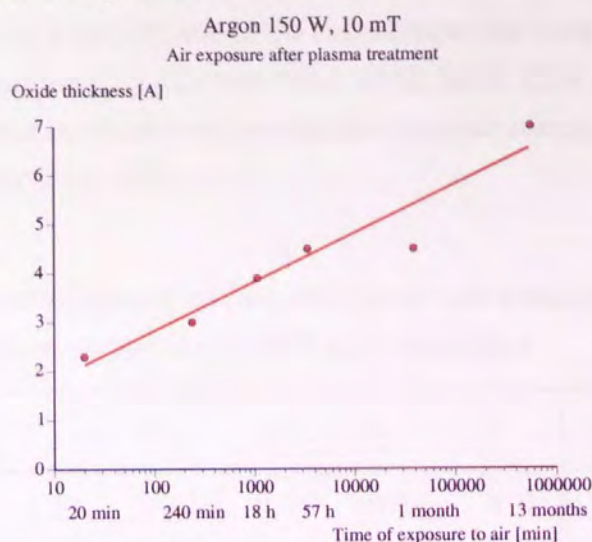


Figure 4.83 Variation of oxide thickness with time after Ar plasma treatment

#### 4.2.2.8 Experimental errors

The experimental error consists of the sum of the errors caused by plasma processing and XPS data processing. The instrumental error refers to the error introduced by the XPS device.

The errors due to plasma processing were put in evidence by etching separately five samples under the same conditions. The relative concentration of the species found is presented in Table 4.11. Standard deviation was calculated as described in Chapter 3 and is also given in the table for each surface component.

Table 4.11 Relative concentration of surface compounds and standard deviation calculated for each surface component - errors due to plasma processing

Sample no.	1	2	3	4	5	Average	Std. dev.
As <sub>2</sub> O <sub>5</sub> conc. [%]	0.34	0.07	0.07	0.07	0.32	0.17	0.14
As <sub>2</sub> O <sub>3</sub> conc. [%]	2.50	1.57	0.18	0.17	2.13	1.31	1.09
As(GaAs) conc. [%]	46.96	43.42	43.96	42.96	40.35	43.53	2.37
Ga(OH) <sub>3</sub> conc. [%]	0.95	1.29	1.56	0.79	2.45	1.41	0.65
Ga <sub>2</sub> O <sub>3</sub> conc. [%]	4.20	4.07	2.75	8.45	5.32	4.96	2.16
Ga <sub>2</sub> O conc. [%]	8.21	8.49	9.99	4.11	4.03	6.95	2.73
Ga(GaAs) conc. [%]	36.8	40.96	41.27	42.46	44.97	41.29	2.96

Poor statistics in XPS analysis (e.g. due to low lifetime of the channeltron) can sometimes result in important differences in the results. To measure the amount of error that can be introduced by this effect, XPS measurements of the same (etched with Ar, 10 mT, 150 W) sample at different stages of the lifetime of the channeltron had been undertaken. For the five experiments, the number of counts was 5453, 2910, 2820, 2509 and 605 for As(GaAs). The difference in relative concentration of surface components caused by the channeltron can be observed in Table 4.12.

Table 4.12 Relative concentration of surface compounds and standard deviation calculated for each surface component - errors due to XPS data acquisition

Event no.	1	2	3	4	5	Average	Std. dev.
As <sub>2</sub> O <sub>5</sub> conc.[%]	0.19	0.02	0.07	0.06	0.06	0.08	0.06
As <sub>2</sub> O <sub>3</sub> conc.[%]	1.64	1.72	0.18	0.90	1.2	1.13	0.83
As(GaAs) conc.[%]	46.56	47.62	42.96	44.6	43.5	45.05	3.77
Ga(OH) <sub>3</sub> conc.[%]	0.36	0.53	0.76	0.63	0.63	0.65	0.43
Ga <sub>2</sub> O <sub>3</sub> conc.[%]	6.11	2.85	8.46	5.20	5.80	5.68	2.34
Ga <sub>2</sub> O conc.[%]	6.69	12.17	6.5	8.34	7.71	8.28	3.24
Ga(GaAs) conc.[%]	38.43	35.87	42.46	40.25	41.1	39.62	4.22

### 4.3 AFM analysis

For studying topography changes of the surface with different plasma conditions and determination of etch depths, AFM analysis were employed.

#### 4.3.1 Topography

On exposure to different plasmas, no important changes of surface topography were found, as can be observed in the following figures. Roughness measurements are also shown in the figures. This behaviour was typical for the plasma treated samples and the figures shown below are representative for all the topographical images acquired. The features observed on some of the images are not spread uniformly and therefore are believed to represent contamination of the surface.

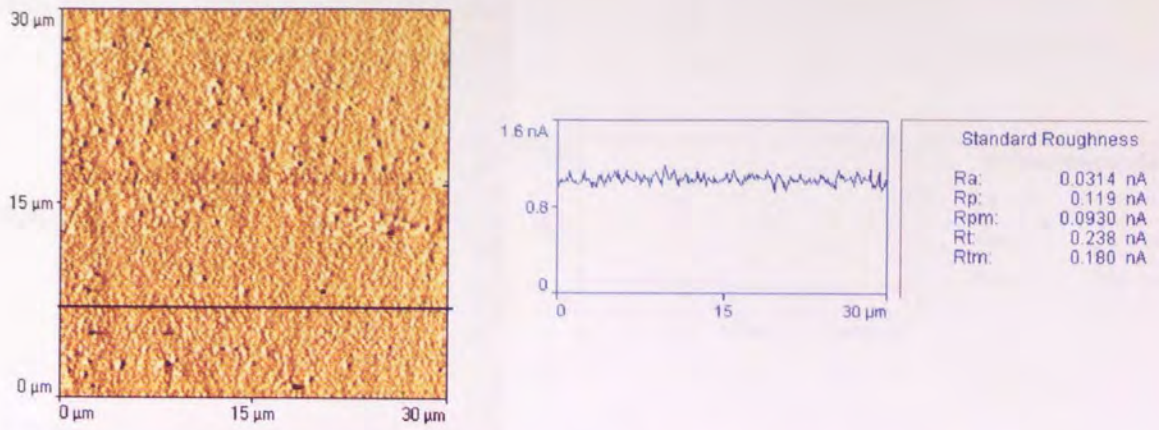


Figure 4.84 Topography and roughness for the virgin GaAs sample

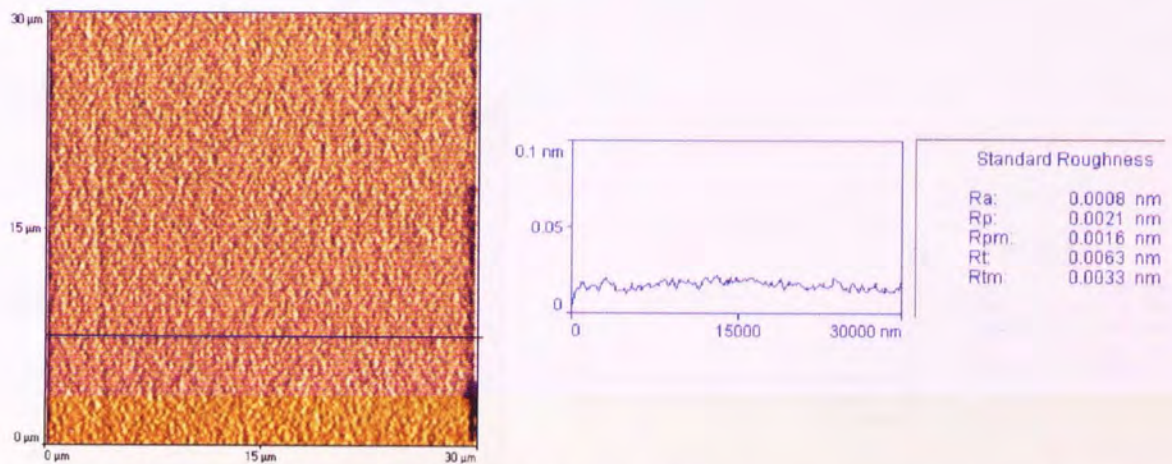


Figure 4.85 Topography and roughness for the 75% Ar + 25% H<sub>2</sub> plasma treated GaAs at 90 mT, 150 W, 30 min

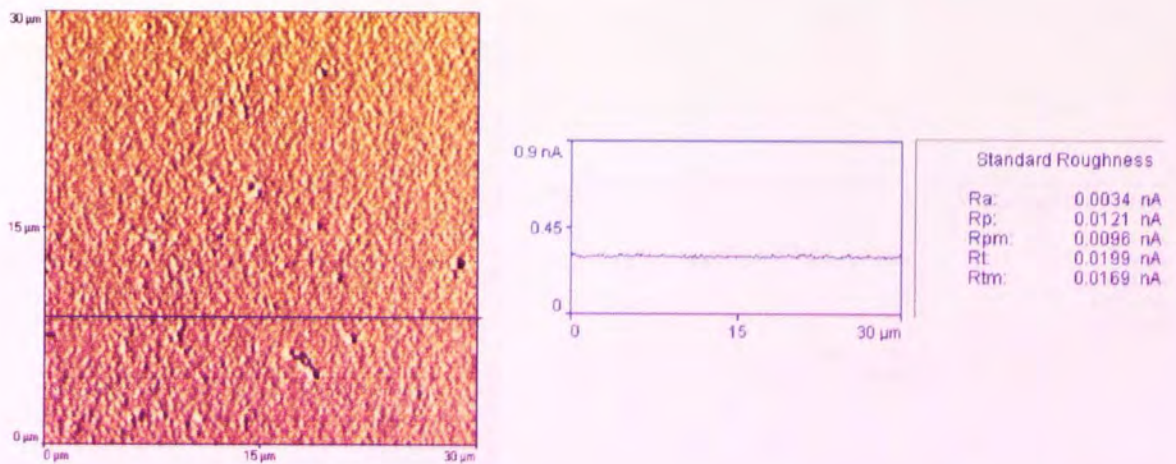


Figure 4.86 Topography and roughness for the 50% Ar + 50% H<sub>2</sub> plasma treated GaAs at 90 mT, 150 W, 30 min

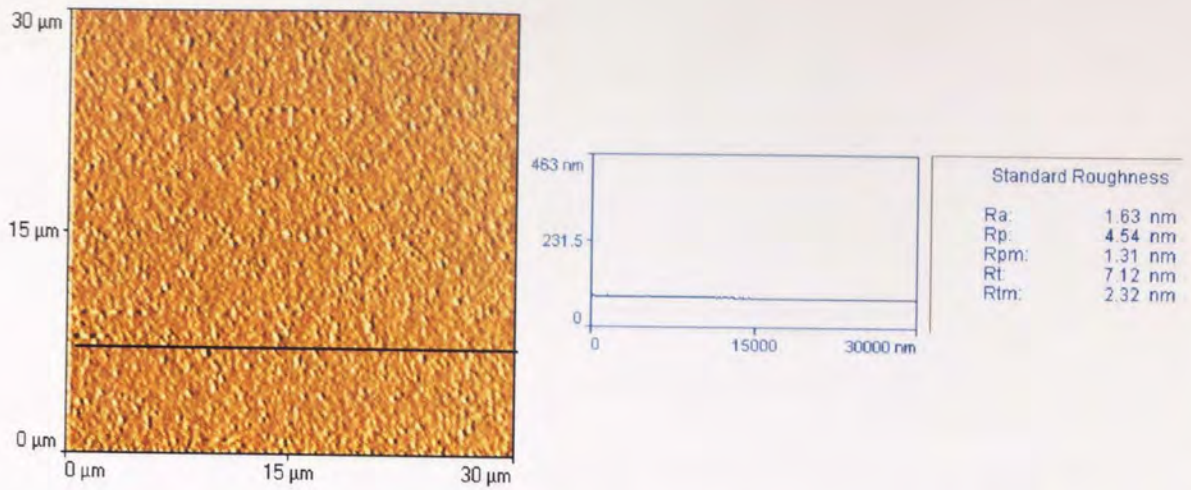


Figure 4.87 Topography and roughness for the 25% Ar + 75% H<sub>2</sub> plasma treated GaAs at 90 mT, 150 W, 30 min

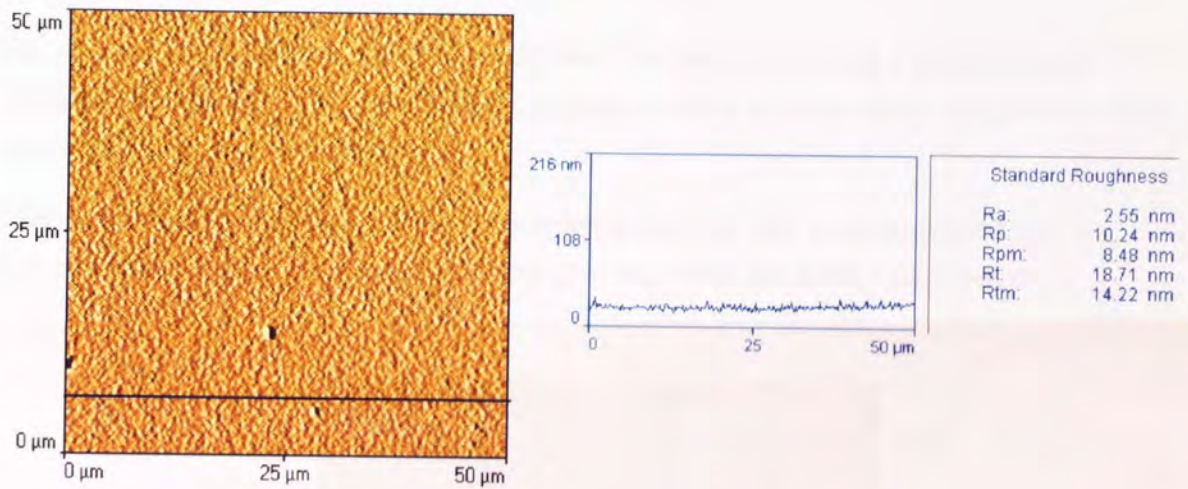


Figure 4.88 Topography and roughness for the 25% Ar + 75% H<sub>2</sub> plasma treated GaAs at 30 mT, 150 W, 30 min

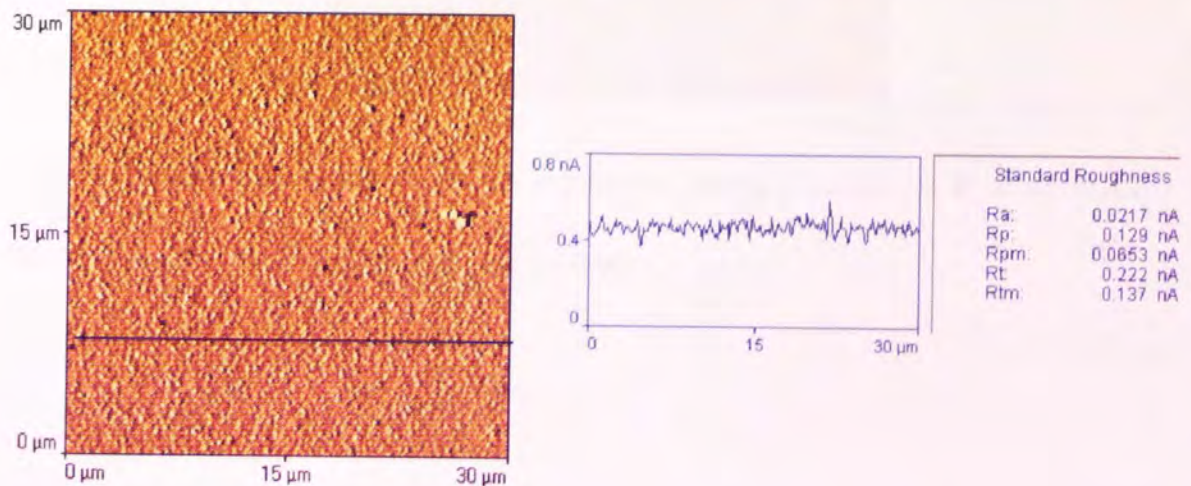


Figure 4.89 Topography and roughness for the H<sub>2</sub> plasma treated GaAs at 10 mT, 150 W, 30 min

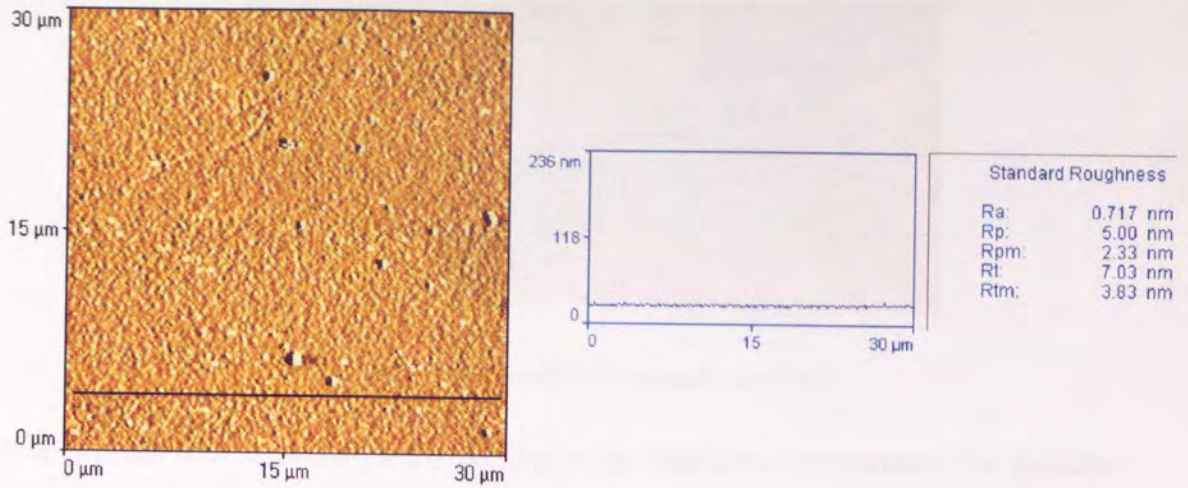


Figure 4.90 Topography and roughness for the  $H_2$  plasma treated GaAs at 90 mT, 200 W, 30 min

### 4.3.2 Shape of the etch pit

As explained in Chapter 3, the etch profile was obtained by treating a masked GaAs sample in the plasma. The mask was obtained by placing a small, finely cut piece of GaAs on top of the sample to be analysed.

The etch pit had a step-like profile. Line scans across the step were employed for determination of etch profile and etch depth, as shown in the AFM image below.

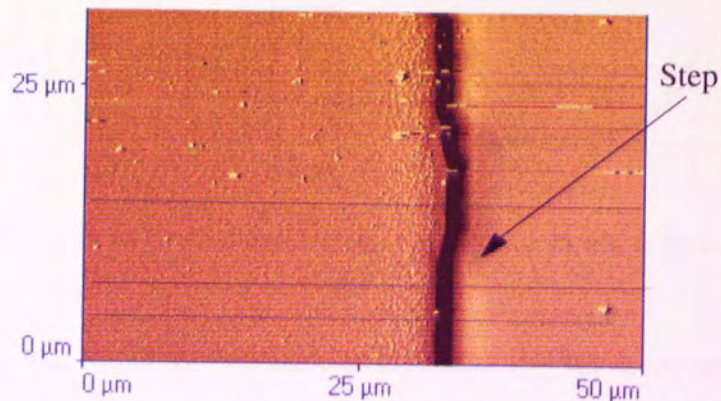


Figure 4.91 AFM image for determination of etch depth (Ar etching of GaAs at 150 W, 90 mT, 30 min)

The 3D image of the step is given in Figure 4.92.

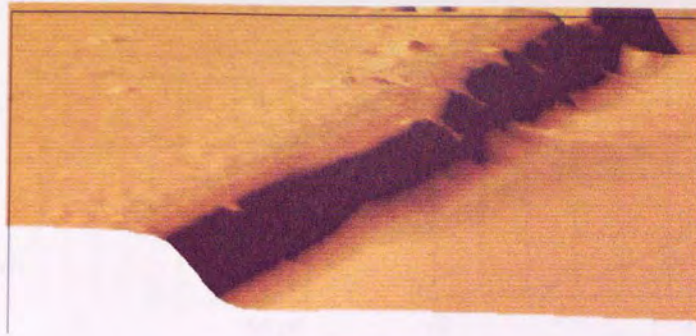


Figure 4.92 Zoomed 3D view of Figure 4.91.

Etch profiles were also analysed using line scans. For direct comparisons, the profiles were divided into cells of  $3\ \mu\text{m}/\text{div}$  and  $60\ \text{nm}/\text{div}$ .

At higher pressures, the etch profile is expected to be closer to a spherical shape than in the case of low pressures. This is because with increasing pressure the number of collisions increases and the ions are scattered. Thus, the ions are expected to arrive at different angles at the surface.

In Figure 4.93 a), it can be observed that the side wall of the etch profile stretches over a longer distance than in the other case (b)). This shows that the etch profile at  $10\ \text{mT}$  is closer to a spherical shape than that at  $30\ \text{mT}$ .

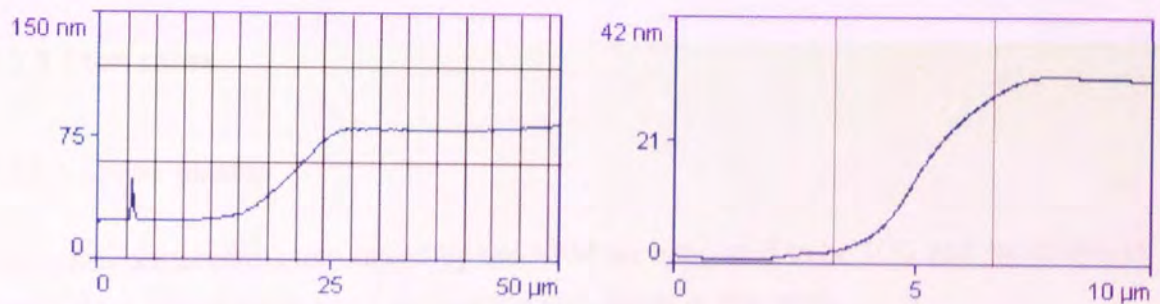


Figure 4.93 Profile of the etch pit for Ar plasma treatment of GaAs for 30 min, at 50 W and a)  $10\ \text{mT}$ ; b)  $30\ \text{mT}$

The opposite result was found for two samples etched at  $100\ \text{W}$ , as can be seen in Figure 4.94.

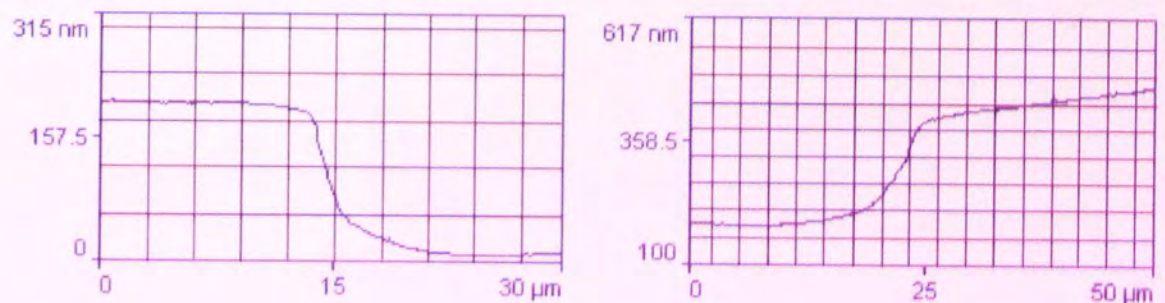


Figure 4.94 Profile of the etch pit for Ar plasma treatment of GaAs for 30 min, at  $100\ \text{W}$  and a)  $10\ \text{mT}$ ; b)  $90\ \text{mT}$

At 150 W, the etch profiles at 30 mT and 90 mT were about the same (see Figure 4.95).

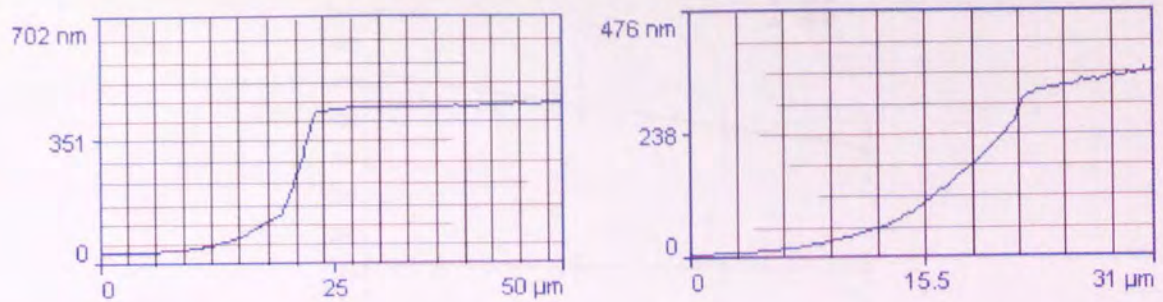


Figure 4.95 Profile of the etch pit for Ar plasma treatment of GaAs for 30 min, at 150 W and a) 30 mT; b) 90 mT

The results above show that no particular behaviour of the etch profile with increasing pressure can be found using this technique. This is probably due to the added interaction of the atoms of the side wall with the tip of the AFM, as the tip approaches the wall. Another explanation may be that the mask used to obtain the etch profile had irregularities at the edges which affected the plasma around them.

As etch profiles for argon etching of GaAs did not provide useful results, studies of etch profiles having depths lower than these found for the other gases used in this work are not expected to be more useful.

### 4.3.3 Etch rates

#### 4.3.3.1 Argon plasma

The instrumental errors introduced by the AFM are estimated to be 10% and are shown in Figure 4.96. This applies to all plots of the etch depth in this work.

At low power, with increasing pressure no significant change of etch depth was observed. Only at 150 W the etch depth was affected by increasing pressure. The decrease of the etch depth with pressure was not expected. This trend will be discussed in Chapter 5 using information on ion energies and fluxes given earlier in this chapter.

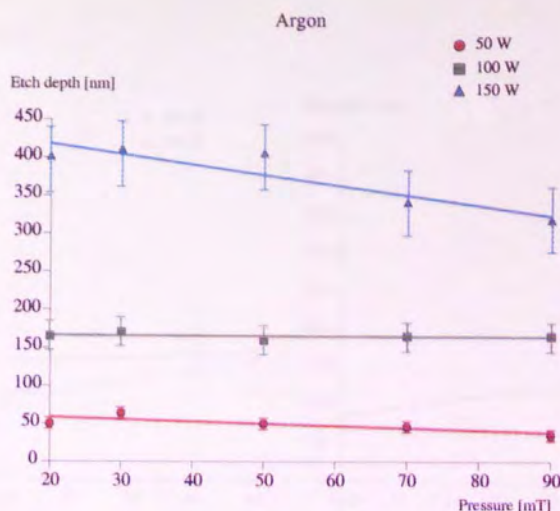


Figure 4.97 Variation of the etch rate with pressure at different powers (argon plasma)

Sputtering yield was calculated from experimental data as shown in Chapter 2 and its variation with pressure and power is presented in 4.98. Although ion flux density at the cathode increased with pressure, sputtering yield showed a decrease. This result confirms the assumption above that ion energies are more important than ion densities for the etch rates. The sputtering yield was below 1 for almost all pressure power combinations studied. Only for powers over 150 W and low pressures the sputtering yield was above 1.

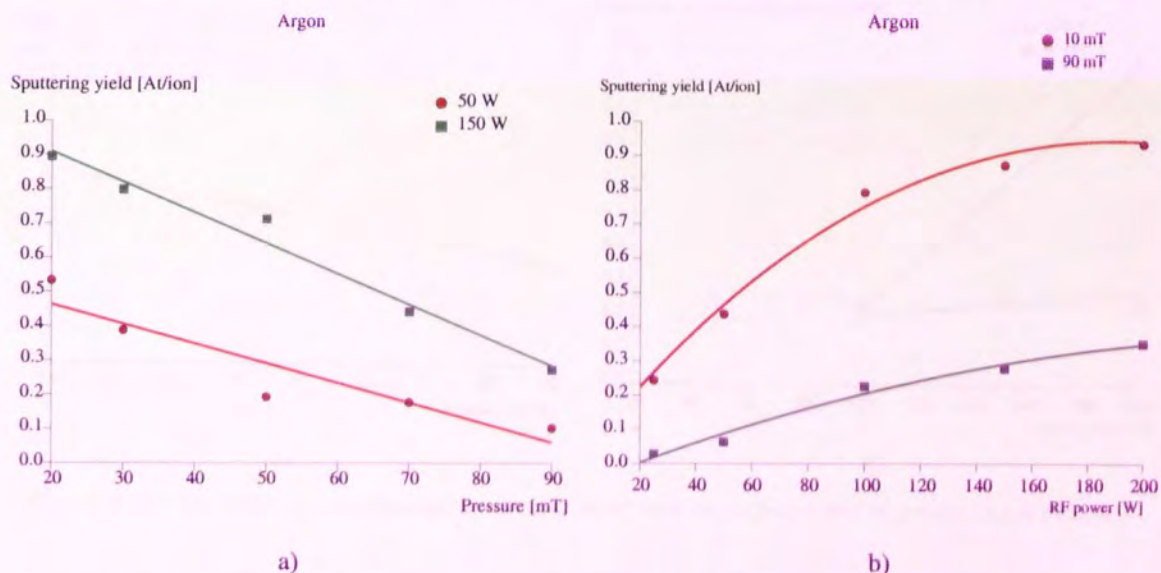


Figure 4.98 Variation of sputtering yield with a) pressure and b) power (argon plasma)

### 4.3.3.2 Neon plasma

The etch rates were much lower for neon than for argon (Figure 4.99 a) and b)). This result was to be expected, as their atomic weight is considerably different. For powers lower than 100 W, the etch depths for neon could not be measured.

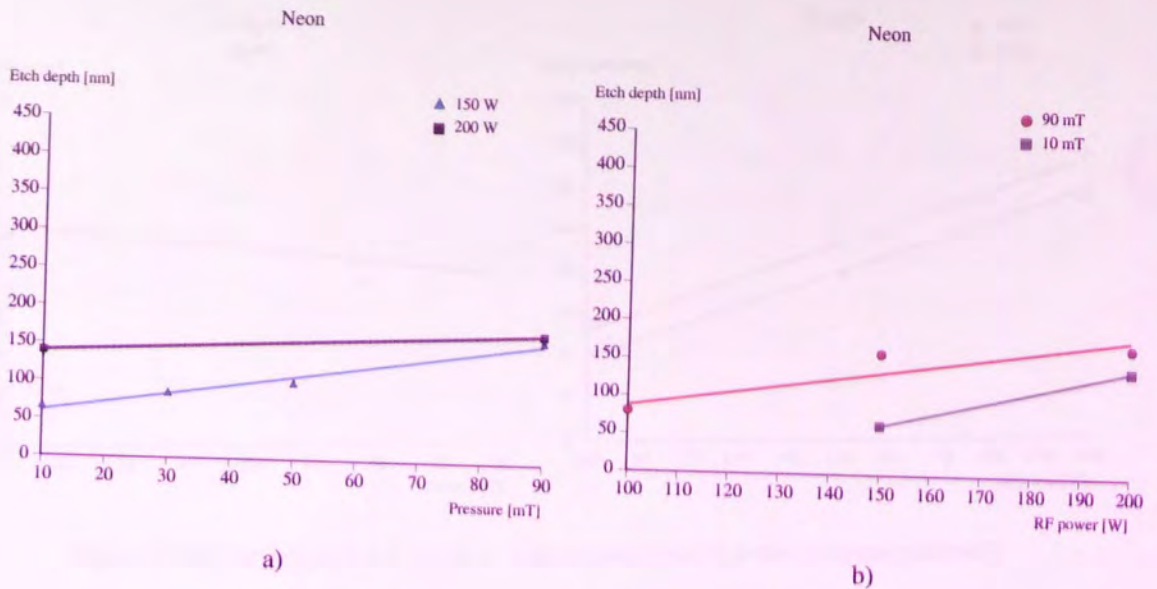


Figure 4.99 Variation of etch depth with a) pressure and b) power (neon plasma)

Sputtering yield showed a little decrease with pressure and a fast increase with power, as can be observed in Figure 4.100 a) and b). Overall, sputtering yield for neon was lower than that of argon.

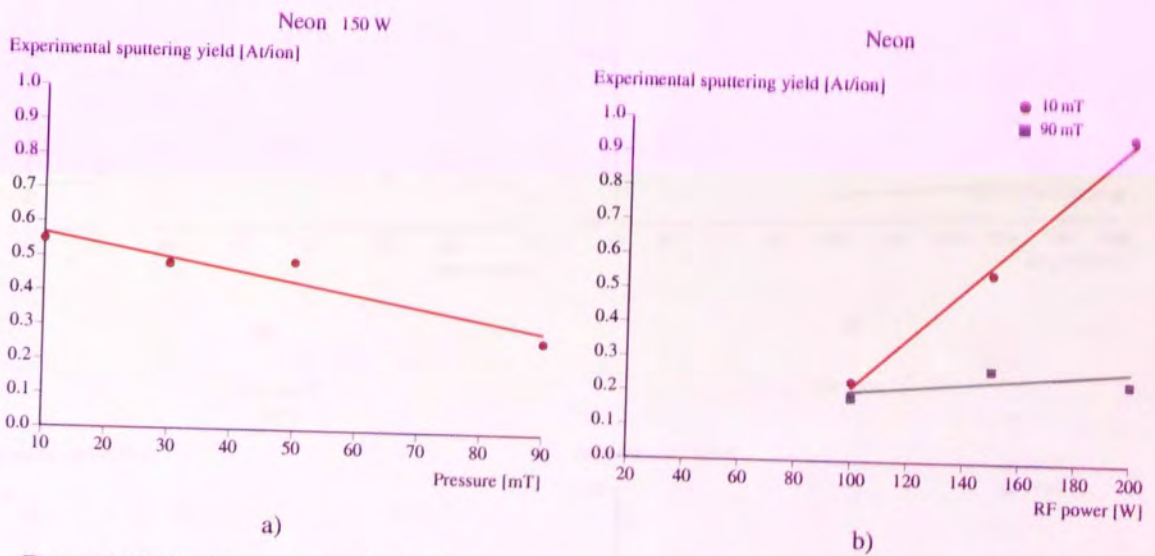


Figure 4.100 Variation of experimental sputtering yield with a) pressure and b) power (neon plasma)

### 4.3.3.3 Oxygen plasma

When etching with oxygen, etch depths comparable with neon were obtained (Figure 4.101). The total sputtering yield obtained with the oxygen plasma was lower than that of neon for all plasma conditions except for 150 W and low pressures, although the etch depths were comparable (Figure 4.102).

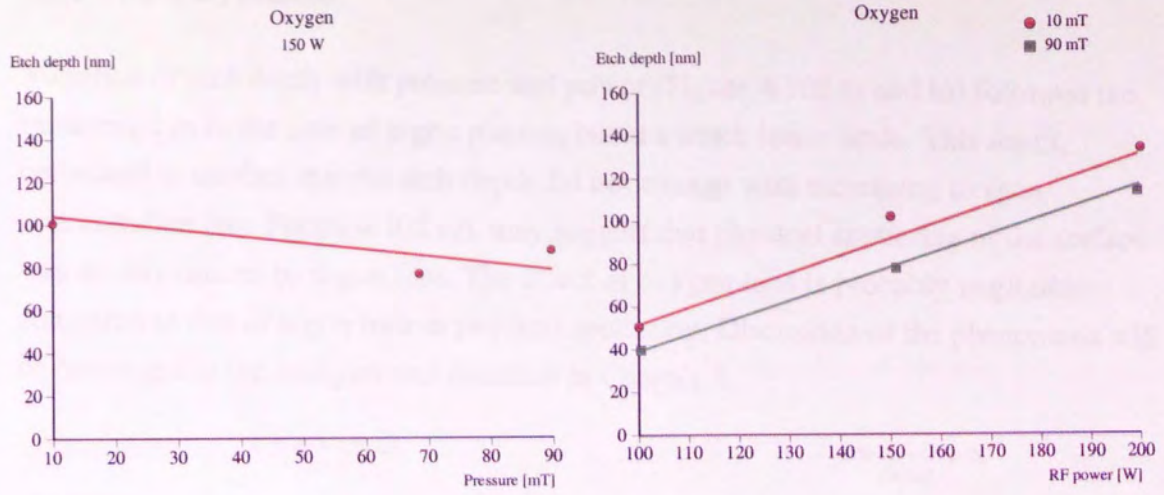


Figure 4.100 Variation of etch depth with a) pressure and b) power (oxygen plasma)

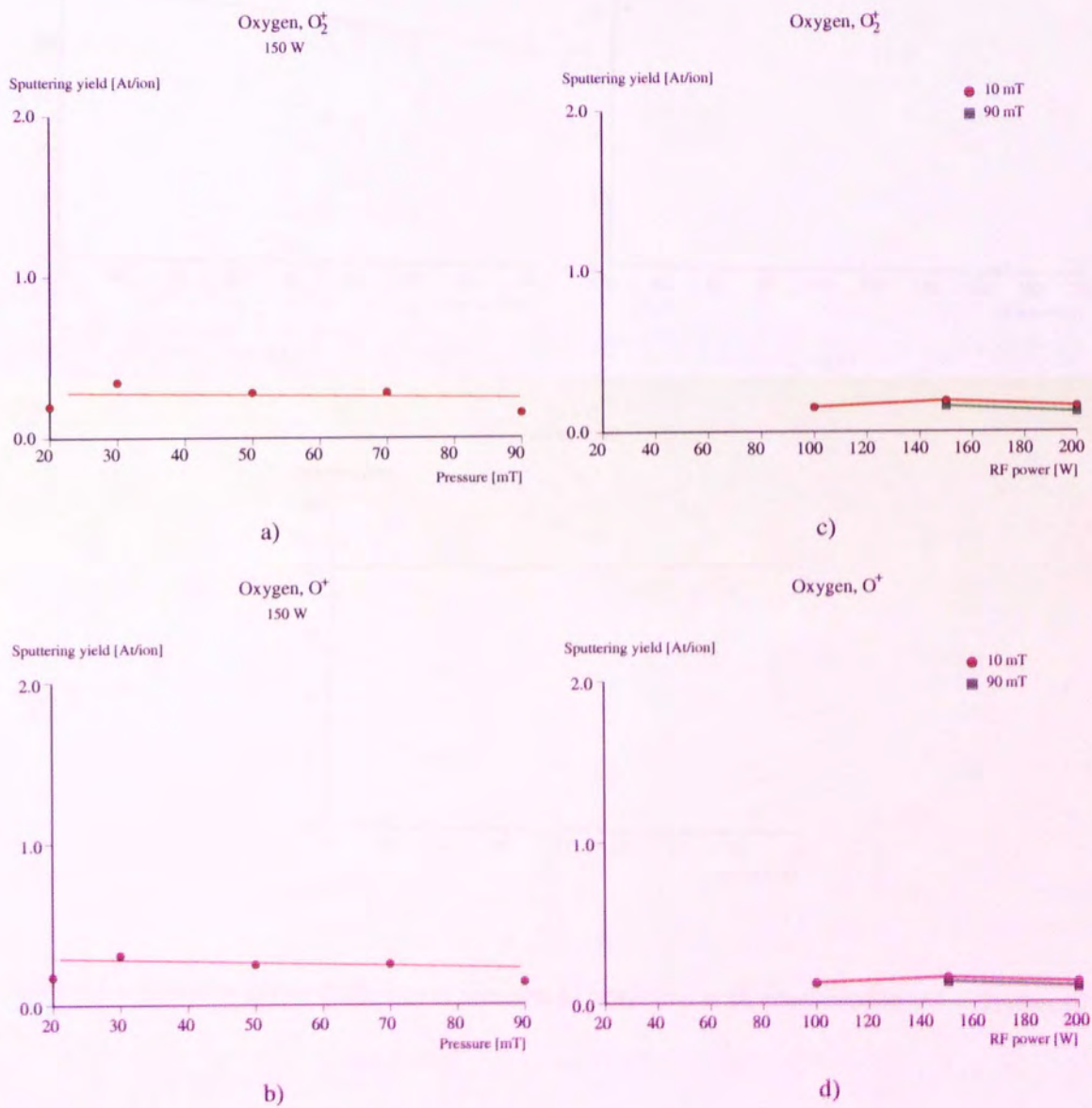


Figure 4.101 Variation of sputtering yield for O<sub>2</sub><sup>+</sup> and O<sup>+</sup> with a), b) pressure and c), d) power (O<sub>2</sub> plasma)

#### 4.3.3.4 Ar + O<sub>2</sub> plasma

Variation of etch depth with pressure and power (Figure 4.102 a) and b)) followed the same trend as in the case of argon plasma, but at a much lower scale. This result, correlated to the fact that the etch depth did not change with increasing oxygen concentration (see Figure 4.102 c)), may suggest that physical sputtering of the surface was mainly caused by argon ions. The effect of oxygen ions is probably negligible compared to that of argon ions in physical sputtering. Discussion of the phenomena will be correlated to ion energies and densities in Chapter 5.

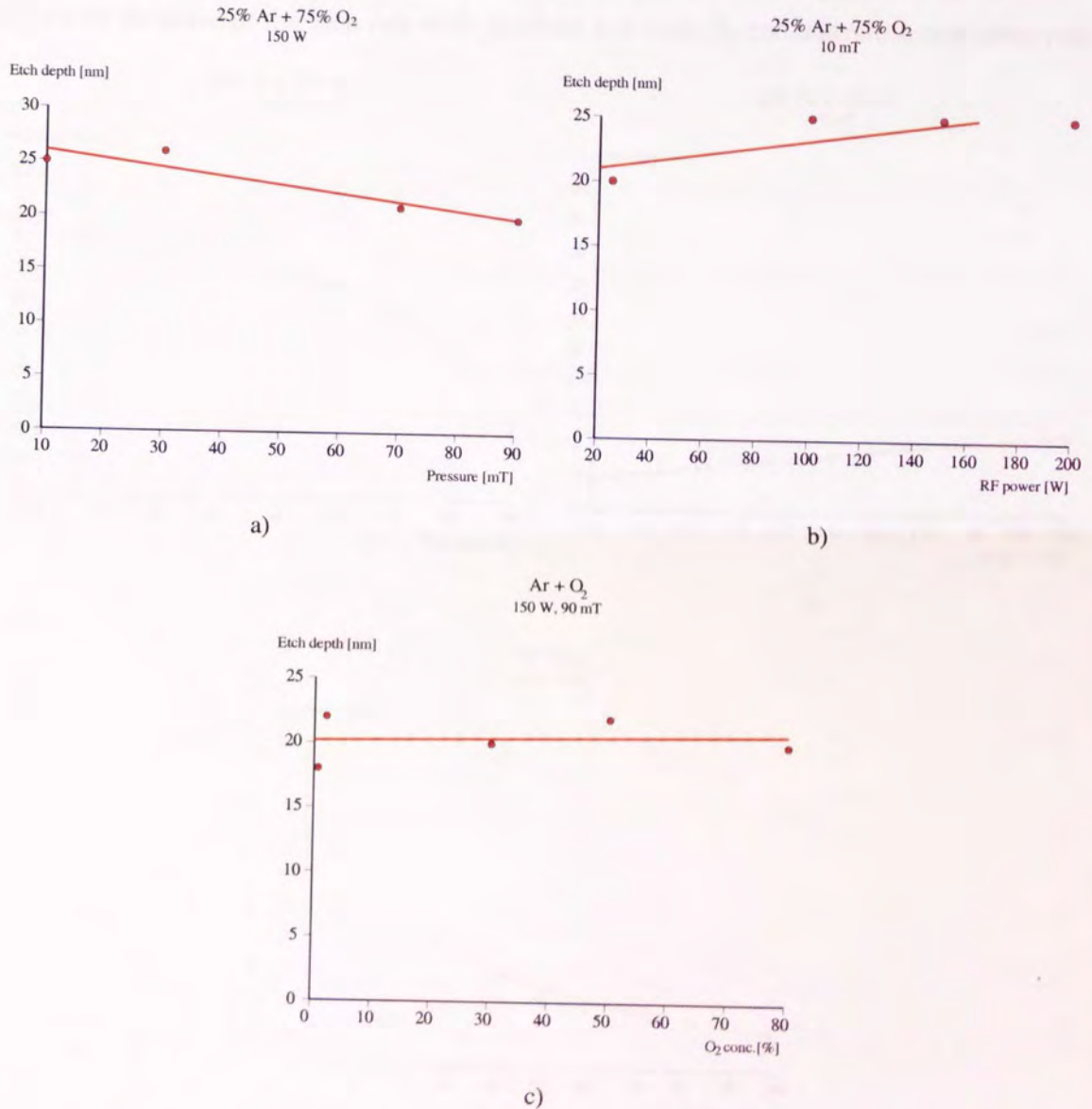


Figure 4.102 Variation of etch depth with a) pressure, b) power and c) O<sub>2</sub> concentration (Ar + O<sub>2</sub> plasma)

### 4.3.3.5 Hydrogen plasma

Hydrogen plasma treatment of GaAs showed mainly compositional changes on the surface. The highest etch pit found was 4 nm when etching at 10 mT and 150 W. This result will be discussed in Chapter 5.

### 4.3.3.6 Ar + H<sub>2</sub> plasma

Measurable etch pits were obtained due to the argon - ion content of the plasma but their values were much smaller than in the case of pure argon plasma (Figure 4.103). An important decrease of the etch rate with pressure and with H<sub>2</sub> concentration was observed.

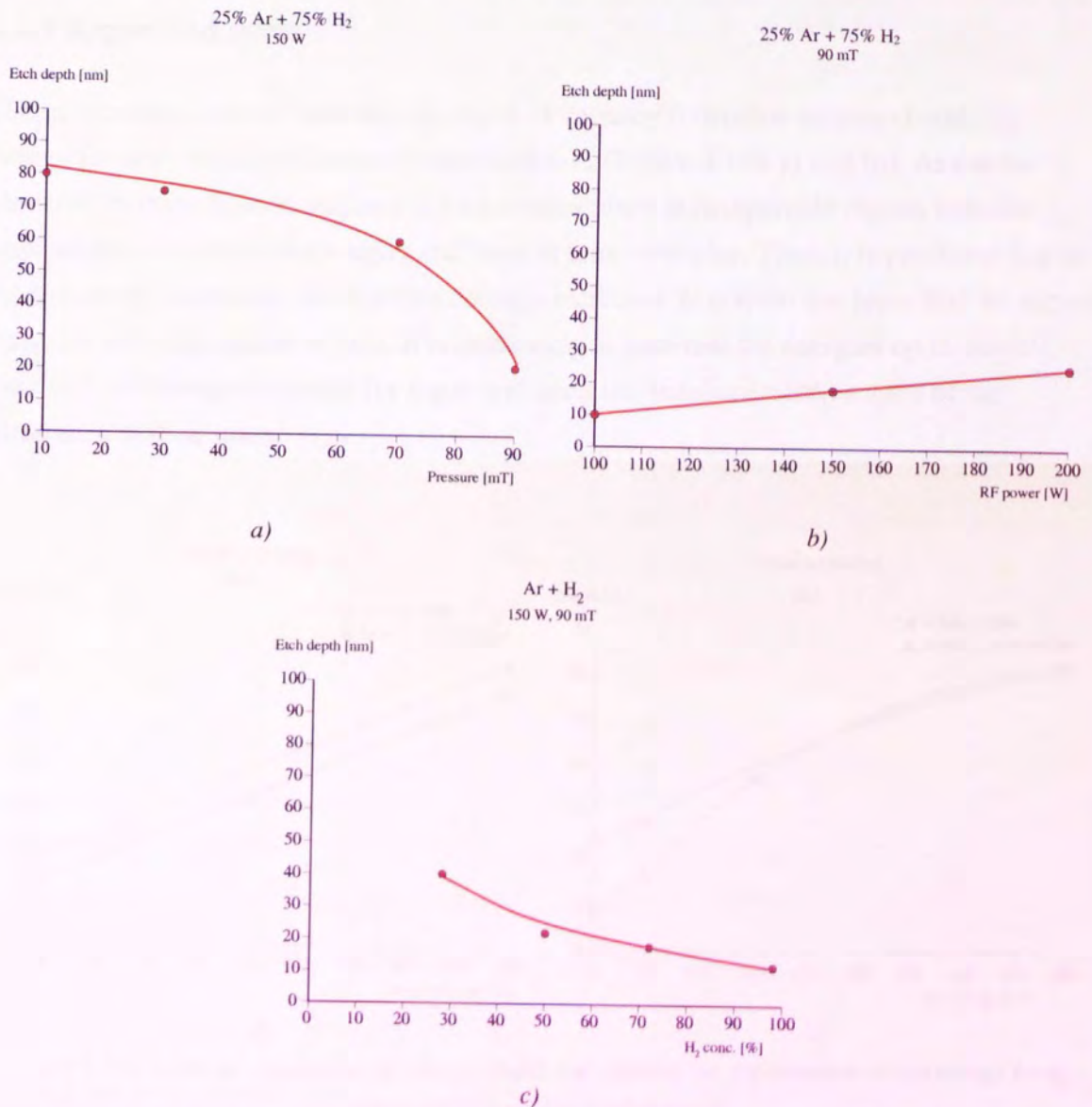


Figure 4.103 Variation of etch depth with a) pressure, b) power and c) concentration (Ar + H<sub>2</sub>)

## 4.4 Modelling of surface-plasma interactions

The SRIM code generally gives more reliable results for incident ion energies above 1 keV. At energies below this, the approximations used in the code are not particularly accurate. In these cases the incident particle interacts with the local lattice, not only with one atom and this is more accurately modelled as a many body problem. Nevertheless, some useful information can be obtained using this code by studying processes relatively, not necessarily taking the absolute values. Thus, variation of vacancy depth, ion penetration and sputtering yield with ion energy for different bombarding ions can be qualitatively studied.

### 4.4.1 Argon and neon

The penetration depth of ions and the depth of vacancy formation increased with ion energy for both argon and neon ion bombardment (Figure 4.104 a) and b)). As can be observed in these figures, vacancy creation takes place at comparable depths with ion implantation depths for both argon and neon at these energies. Thus, it is predicted that as the ion energy increases, the depth of damage increases. It is from this layer that we expect diffusion and segregation effects. It is interesting to note that for energies up to 500 eV, the depth of damage is similar for argon and neon ion bombardment, in spite of the difference in their mass.

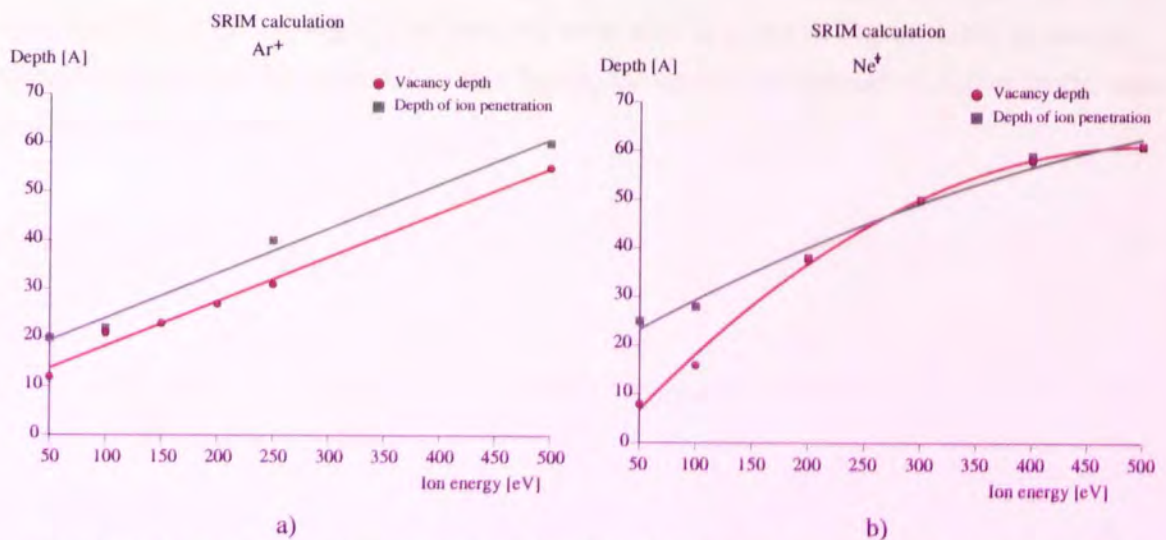


Figure 4.104 Predicted dependence of vacancy depth and depth of ion implantation on ion energy for a) argon and b) neon ion bombardment

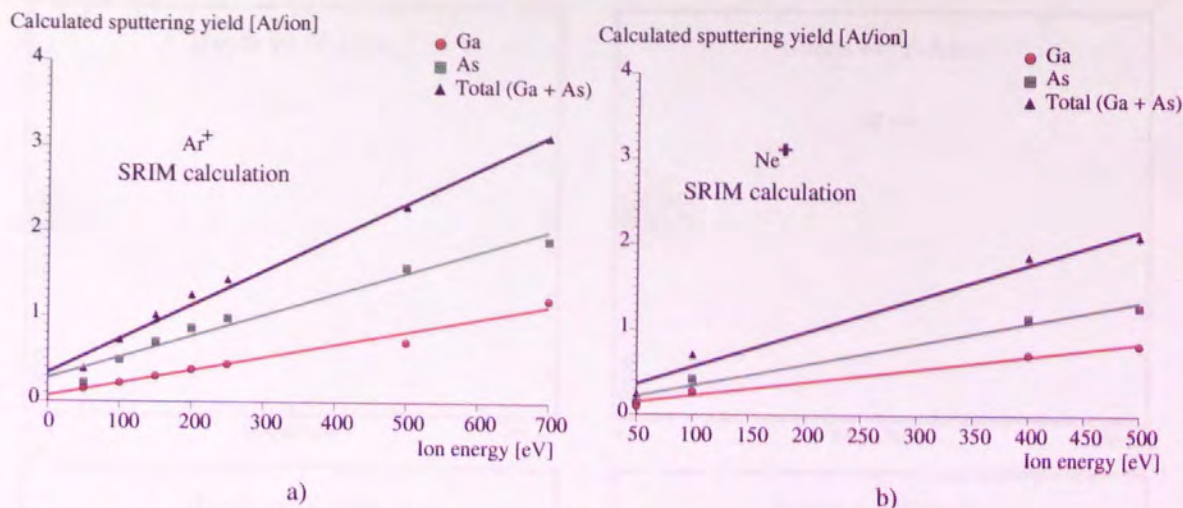


Figure 4.105 Calculated variation of sputtering yield versus ion energy for a) Ar and b) Ne bombardment

The calculated total sputtering yield (Y) for Ar and Ne ion bombardment for energies in the range (50 - 500) eV is given in Figure 4.105. By increasing the mass of the primary ion an increase in the sputtering yield is predicted to take place. This fact was also found by other authors [Smentkowski, 2000]. Also, similar results were presented by Malherbe [1994] in a comprehensive review. According to this author, the SRIM code gives an over estimate of sputtering yield especially at low ion energies (< 1 keV). Nevertheless, the important point in a simulation experiment is not to obtain exact values but to determine general trends.

Also, the sputtering yield for As is higher than for Ga.

A visual representation of the spatial distribution of ions and atoms in the target after bombardment with 100 argon ions and 100 neon ions is given in Figure 4.106 a) and b), respectively. As can be observed in this figure, the density of damage is higher in the case of argon than for neon.

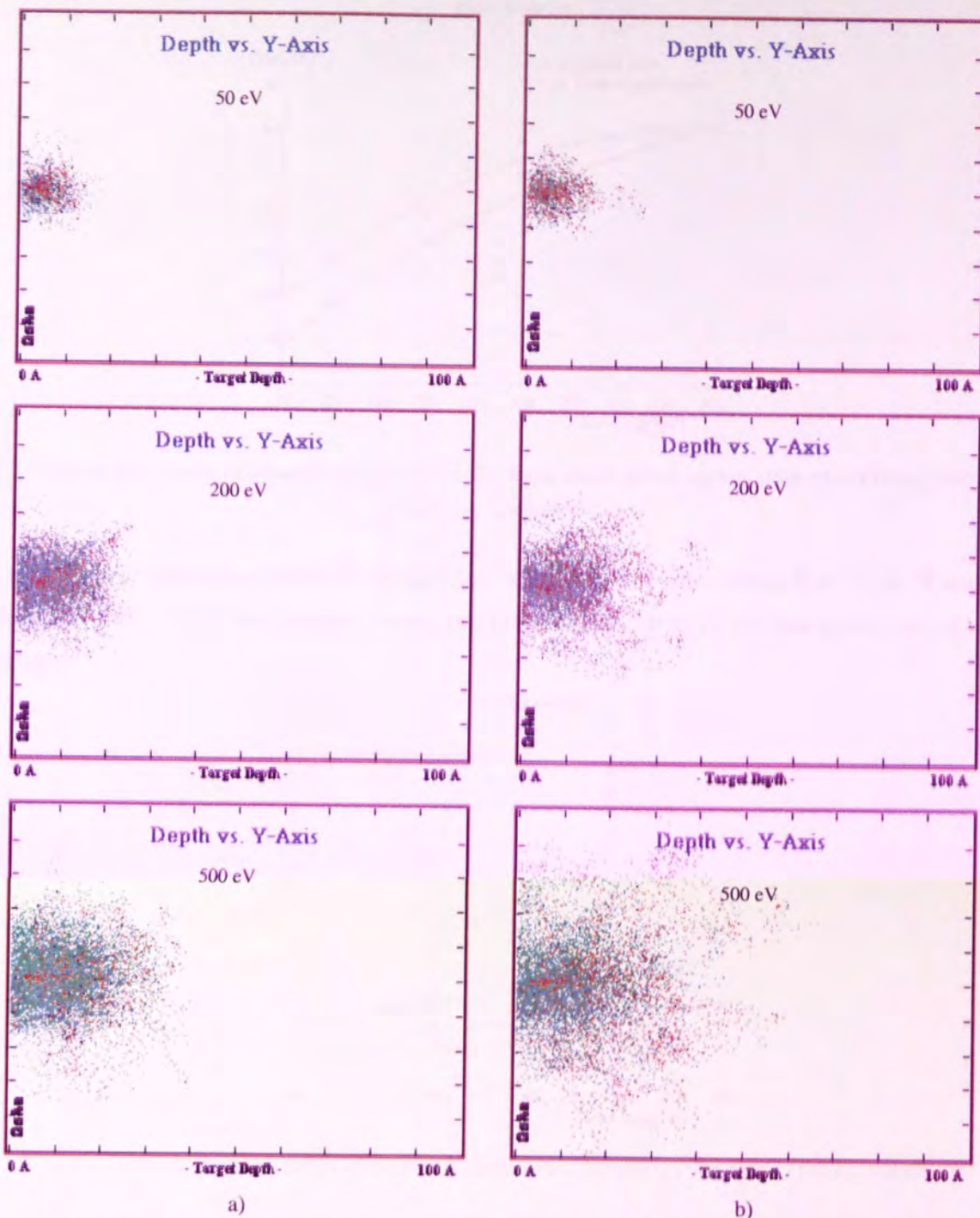


Figure 4.106 Predicted spatial distribution of ions and atoms in the target after collision for a) argon and b) neon for 100 bombarding ions (red dots represent penetrated ions, green dots show displaced target atoms)

#### 4.4.2 O<sub>2</sub>

In the case of oxygen ion bombardment, variation of vacancy depth and ion penetration depth with ion energy was similar to that found for Ar and Ne ion bombardment (see Figure 4.108).

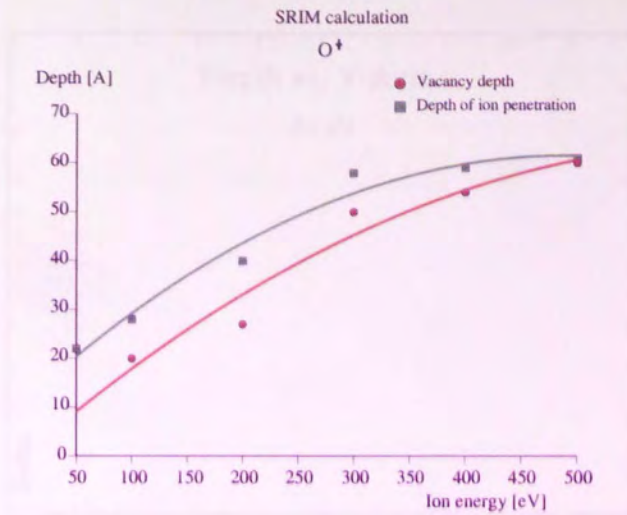


Figure 4.108 Predicted dependence of vacancy depth and depth of ion implantation on ion energy for oxygen ion bombardment

The values of sputtering yield for oxygen ion bombardment were lower than those of neon (Figure 4.109). As in the previous cases, preferential sputtering of As was predicted for oxygen.

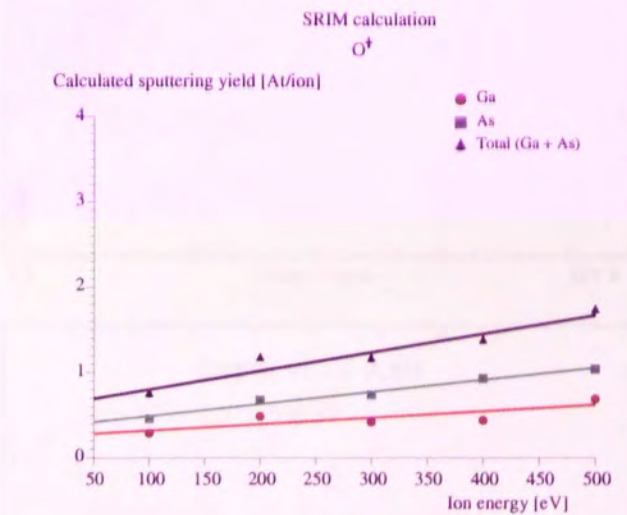


Figure 4.109 Calculated variation of sputtering yield versus ion energy for oxygen ion bombardment

The predicted spatial distribution of ion damage showed that at similar depths of damage, oxygen bombardment causes a lower density of the damage than neon does (Figure 4.111).

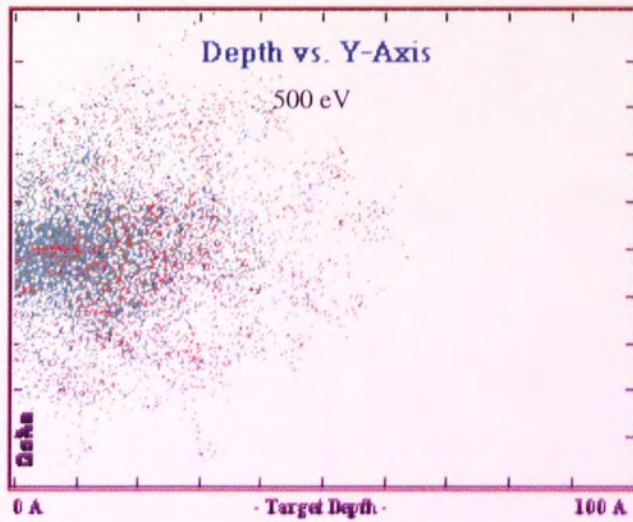
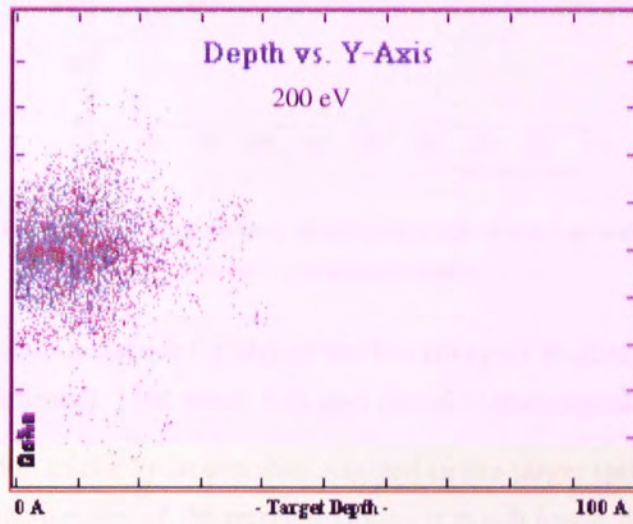
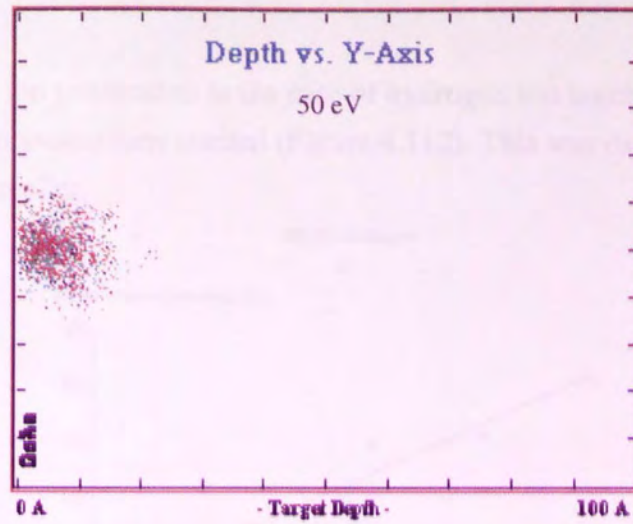


Figure 4.111 Predicted spatial distribution of ions and atoms in the target after collision for 100 oxygen bombarding ions

#### 4.4.3 H<sub>2</sub>

Predicted depths of ion penetration in the case of hydrogen ion bombardment were much higher than for the previous ions studied (Figure 4.112). This was expected, as the mass of hydrogen is much smaller.

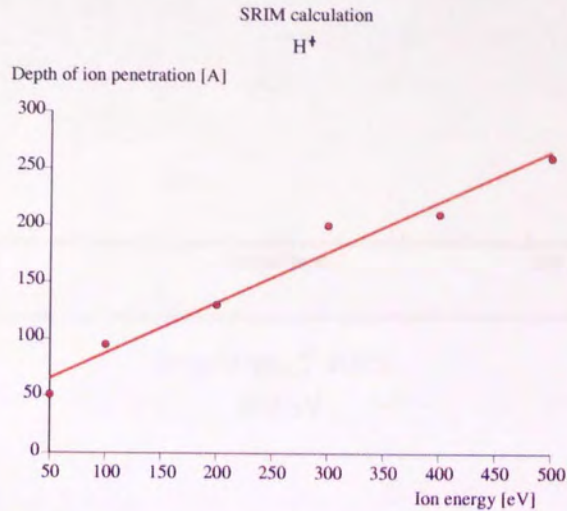


Figure 4.112 Predicted dependence of vacancy depth and depth of ion implantation on ion energy for hydrogen ion bombardment

No sputtering of the GaAs surface for any of the ion energies studied was predicted for hydrogen ion bombardment. This result was also found experimentally.

The spatial distribution of the hydrogen ions stopped in the target (presented in Figure 4.113) showed that the density of the implanted ions is much lower than that of oxygen.

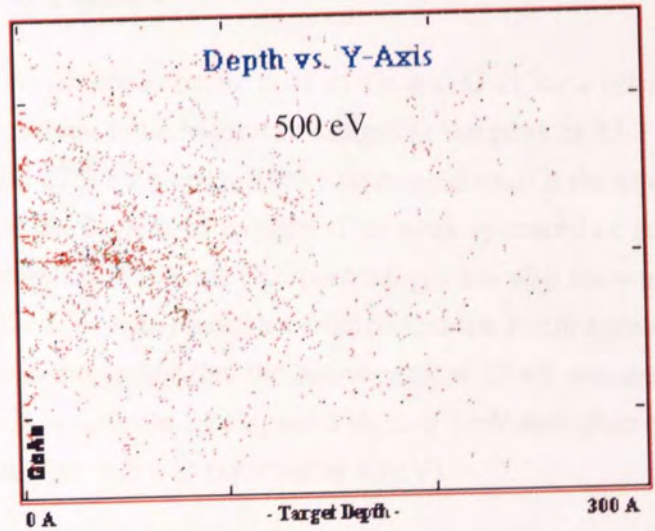
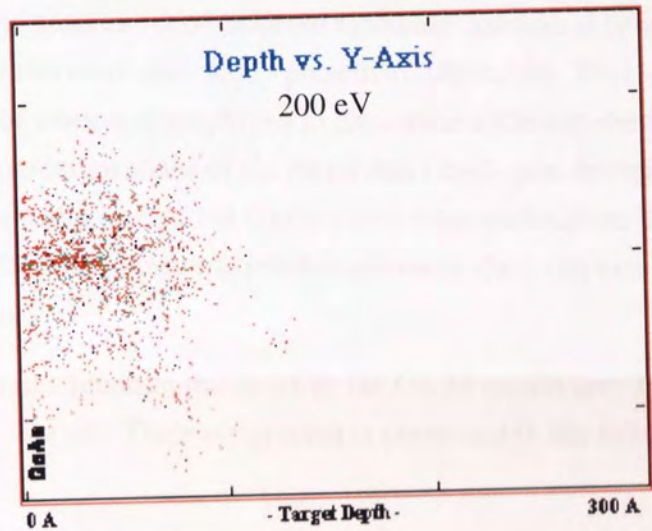
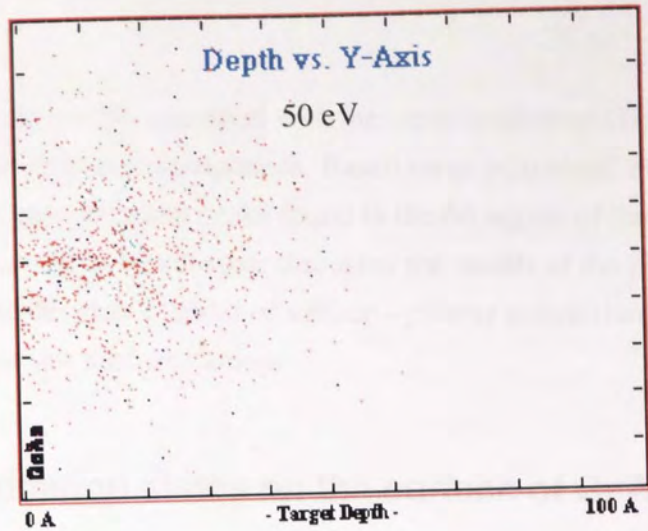


Figure 4.113 Predicted spatial distribution of ions and atoms in the target after collision for 100 hydrogen bombarding ions

## Chapter 5. Discussion of results

The first part of this chapter is concerned with the identification of GaAs surface oxides using XPS analysis of reference compounds. Based on experimental evidence, an assignment of all the photoelectron peaks found in the 3d region of the XPS spectra is proposed. The second part of this chapter discusses the results of the plasma - treated GaAs wafer aiming to develop a model of surface - plasma interaction and to determine optimal conditions for low surface damage.

### 5.1 Possible oxidation states on the surface of GaAs wafer

In the XPS spectra, chemical shifts of oxidized Ga3d are considerably smaller than those of oxidized As 3d and therefore their study presented difficulties. This is why a considerable amount of work was employed to determine different chemical states of Ga. Thus, analysis of the oxidation states of Ga metal and Ga<sub>2</sub>O<sub>3</sub> powder reference samples virgin and clean GaAs wafer and boiled GaAs wafer were undertaken. These measurements were intended to provide reliable reference data, not available from other sources, for further work.

The XPS binding energies found in this work in the Ga 3d region are: 23.2 eV, 21.6 eV, 20.7 eV, 20.1 eV and 19.1 eV. Their assignment is presented in the following.

#### 5.1.1 The peak at $23.2 \pm 0.2$ eV

Normalized spectra of the photoelectronic peak of Ga and O 1s for a selection of samples (shown in Figure 4.25) proved to be helpful in assigning the peak at 23.2 eV. As the O 1s peak became smaller, the 23.2 eV peak intensity decreased until it disappeared. It is believed that this peak is the 2s peak of oxygen. This peak appeared on surfaces containing more than approx. 20% oxide (the percentages are also shown in Figure 4.25). This approach was verified for many samples studied and the result agrees with the findings of Lu [1993] who suggested that the broad peak at 23 eV was due to O 2s. In the work of Shin [1991] O 2s is taken at 24 eV, but a shift of 1 eV to higher energies of all their spectra is observed (As(-As) was reported at 42 eV).

It is interesting that the O 2s peak has often been missed in previous work probably due to the fact that a narrow energy range was used for the Ga 3d core levels.

### 5.1.2 The peak at $21.6 \pm 0.2$ eV

The assignment of this peak is very much disputed in current literature, as shown in Chapter 2. The main chemical states proposed are: a hydroxide,  $\text{Ga}(\text{OH})_3$  and  $\text{GaAsO}_4$ . Boiling a GaAs virgin sample in deionized water showed a very large increase of the compound at 21.6 eV, from 3% to 27% suggesting that it is formed in the presence of water. As the OH compounds are more likely to be found in boiled water than the multiple oxygen molecules, the peak at 21.6 eV almost certainly belongs to the hydroxide  $\text{Ga}(\text{OH})_3$ . This conclusion is also confirmed by the fact that no peak corresponding to  $\text{GaAsO}_4$  (at 45.2 eV) was observed in the As 3d spectrum. In the Ga LMM spectrum (Figure 4.24 c)), movement of the larger peak of the doublet to higher binding energy suggests also the appearance of this new compound (see Figure 4.22 for comparison).

### 5.1.3 The peak at $20.7 \pm 0.2$ eV

This peak is widely agreed to be assigned to  $\text{Ga}_2\text{O}_3$ .

### 5.1.4 The peak at $20.1 \pm 0.2$ eV

The first and maybe the easiest assignment was for the peak at 20.1 eV. This peak was assigned to  $\text{Ga}_2\text{O}$  due to the fact that, according to Sheka [1966], the lowest oxidation state of Ga stable long enough to be detected is  $\text{Ga}_2\text{O}$ . The other lower oxidation state,  $\text{GaO}$ , is not stable and has only been detected by spectroscopic means.

The study of argon - bombarded pure  $\text{Ga}_2\text{O}_3$  powder was intended to reveal the reduction of the oxidation state to  $\text{Ga}_2\text{O}$ . No useful results have been obtained from this study due to the uncontrolled occurrence of two competitive processes: removal of atoms and reduction of the oxides due to ion bombardment. Thus, the argon ions firstly reduced the oxidation state of the first few  $\text{Ga}_2\text{O}_3$  monolayers to  $\text{Ga}_2\text{O}$ . The  $\text{Ga}_2\text{O}$  overlayer was then removed and another oxide reduction followed. The results did not show any correlation of the surface composition with the period of time the sample was bombarded.

The above peaks were used for discussion of all XPS data for the plasma-treated samples.

## 5.2 Virgin and clean GaAs wafer

The surface of a virgin GaAs wafer had the following composition:

Table 5.1 Surface composition - virgin GaAs

Compound	Approx. concentration [%]
As <sub>2</sub> O <sub>5</sub>	4
As <sub>2</sub> O <sub>3</sub>	10
As(GaAs)	35
Ga(OH) <sub>3</sub>	1
Ga <sub>2</sub> O <sub>3</sub>	4
Ga <sub>2</sub> O	10
Ga(GaAs)	35

The fact that the surface of virgin GaAs contained equal amounts of As and Ga oxides is an important result of the analysis. This clearly shows that the process of mechanical polishing of the surface used to obtain the "as received" sample did not introduce preferential oxidation of As or Ga. This implies that Ga and As oxidize simultaneously if no preferential treatment is given.

No significant changes of the surface composition of a virgin GaAs wafer after cleaning with izopropile and deionized water were observed. The thickness of the native oxide was found to be 0.9 nm, which represents about 5 monolayers.

The ARXPS analysis of GaAs wafer presented in Figure 4.23 showed that the concentration gradients of As<sub>2</sub>O<sub>3</sub> and Ga<sub>2</sub>O were higher than those of As<sub>2</sub>O<sub>5</sub> and Ga<sub>2</sub>O<sub>3</sub>. This result shows that the lower oxidation states of As and Ga are nearer to the surface than the higher oxidation states. Also, As<sub>2</sub>O<sub>3</sub> and Ga<sub>2</sub>O formed in higher amounts than the other two. The layered structure of the virgin sample is presented in Figure 5.1.

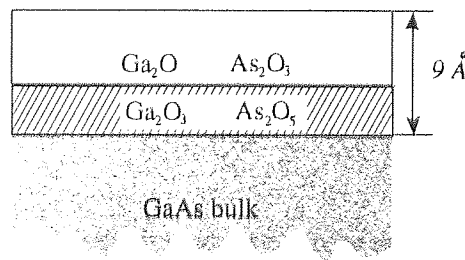


Figure 5.1 Layered structure of the surface of a virgin sample

A complete picture of surface oxidation in the case of virgin sample cannot be given at

this stage due to the fact that no experimental results of the air exposure with time after surface polishing are available. Nevertheless, the experiment where surface changes during air exposure (after argon plasma treatment) with time presented later in this chapter helped complete the oxidation model. It will be shown there that the lower oxidation states are firstly formed on the surface. With increasing time of exposure to air, more oxygen arrives at the activated surface and the surface is completely covered with a layer of oxide in the lower oxidation state. Then, the higher oxidation state starts to be formed by a further oxidation of the lower oxidation state.

For the virgin sample, surface activation was obtained by mechanical polishing.

### **5.3 Surface-plasma interactions in GaAs**

In this section, based on the correlation between plasma diagnosis and surface analysis, a model for the surface-plasma interactions in GaAs subjected to RF plasmas is proposed.

As will be shown in the following, under certain conditions, impurities in the plasma and surface modification in air prior to analysis play an important role in the final surface composition.

#### **5.3.1 Contamination, sources of oxygen and hydrogen species in the plasma**

During plasma processing, the ions bombard the chamber walls and remove H<sub>2</sub>O which then suffers dissociation in the active plasma. Thus, the water adsorbed on the chamber walls becomes source of oxygen and hydrogen species in the plasma. Another important source of impurities is the feed gas.

A rough estimation of the partial pressure of impurity oxygen originating from these sources is presented in Chapter 3. It is shown there that the partial pressure of impurity oxygen contained in the feed gas is more important than that introduced by adsorbed water on the process chamber walls. This implies that, with increasing pressure, the amount of impurities in the process chamber increases proportionally. Care was taken to ensure that the cell condition was similar for all experiments. However, sample to sample variations did occur due to variation in the cell condition and this is evident in any commercial plasma cell.

As shown in Chapter 3, XPS analysis introduced errors due to both spectrum acquisition and spectrum processing. Poor statistics of spectrum acquisition and accuracy of spectrum fitting are also important. These errors were minimized by rigorous application of the same procedure for spectrum fitting. According to our evaluation, in this work, this procedure did not introduce an error greater than  $\pm 5\%$ . To account for the experimental

errors, discussion of the results presented in Chapter 4 will be made only for variations of the relative concentration greater than 5%. As shown at the end of Chapter 4, low values of the relative concentrations carry a smaller error than the high concentrations.

### **5.3.2 Non-reactive etching of GaAs**

In order to separate the physical and chemical surface processes induced by reactive plasma treatment (e.g. methane- hydrogen), inert plasmas had to be used. For this purpose, argon and neon plasmas were chosen. In the following, discussion of the surface changes subjected to argon and neon plasma treatment is given.

#### **5.3.2.1 Argon etching**

##### **5.3.2.1.1 Air exposure after plasma treatment**

It is known that a virgin GaAs surface consists of a layer of roughly equal amounts of As and Ga oxides [Passeggi et al, 1999], [Surdu-Bob et al, 2001]. This shows that if no preferential treatment is given to As or Ga (e.g. mechanic polishing of the surface), these two components oxidize simultaneously. In the case of argon plasma treatment, some preferential treatment must have taken place to account for the differences found in the oxidation and stoichiometry of As and Ga.

Arsenic depletion has been reported in the case of  $\text{Ar}^+$  ion bombardment at energies of the order of a few hundreds eV by many authors [Wolan et al, 1998], [Ching-Hui et al, 1995], [Malherbe et al, 1992], [Singer et al, 1981]. The XPS analyses of these samples was undertaken soon after ion bombardment when surface relaxation was far from being completed, and also without air exposure after ion bombardment.

As depletion due to argon bombardment at energies below 500 eV is also supported by our SRIM results which will be discussed later in this section. Thus, there is a high probability that As segregation has also taken place on the surfaces exposed to argon plasmas.

The sample exposed for a long period of time to the ambient air after argon plasma treatment was key to the understanding of our results. The data showed that at least at high power and low pressure (high ion energies), 20 minutes after extinguishing the plasma, the surface did not reach thermodynamic equilibrium. After a month of exposure to air, the Ga rich GaAs surface contained equal amounts of Ga and As, due to surface relaxation and/or oxidation (Figure 4.81). As observed in Figure 4.83, some surface oxidation has taken place in the air, immediately after plasma treatment.

At this stage, it is impossible to say unequivocally whether the initial oxidation has taken place during plasma processing or on exposure to air. A typical time interval between etching and XPS analysis for the samples studied in this work was of about one month. In

this time interval, at least when using high power and low pressure plasmas, most of the surface changes had taken place prior to surface analysis. As a result, no surface compositional changes with pressure or power were found at high ion energies (Figures 4.26 b) and 4.27). Also, no changes in the thickness of the oxide with plasma conditions were observed at high ion energies (Figure 4.45).

To overcome the fact that the experimental setup did not allow surface analysis without prior exposure to air and also to understand surface modification during plasma processing for all plasma conditions, other experiments had to be undertaken, as will be discussed later in this section.

In Figure 4.45 b), a decrease of the oxide thickness with increasing power at 10 mT for powers up to about 50 W can be observed. A similar situation was found at 90 mT and powers below 150 W. These results show that under these plasma conditions, at least partially, surface oxidation has probably taken place during plasma processing.

Two different plasma conditions will be discussed separately. Their separation point will be the value of the power where, at a certain pressure, surface oxidation remained constant with further increase of the power. These two different plasma conditions will be referred to (in this thesis) as *weak* and *strong* plasmas. In other words, *weak* plasmas are those where sputtering rate is lower than oxidation during plasma treatment. Their separation point is different for different pressures. The above definitions refer to the surface effect induced by the plasma on the target material, not to the plasma itself.

Although surface changes with increasing power were observed only at 10 mT and 90 mT in this work, there is a strong belief that surface changes at pressures between the two values follow the same trends. Thus, the separation points at those pressures (given by the RF power) will have a monotonic increase with power in the range (50 - 150) W. Since the ions in the plasma have a distribution of energies, this separation cannot be sharp and precise. Based on experimental results, a qualitative representation of this phenomenon is proposed in Figure 5.2, where the brighter colour represents a *stronger* plasma.

	5 W	25 W	50 W	100 W	150 W	200 W
10 mT						
20 mT						
30 mT						
50 mT						
80 mT						
90 mT						

Figure 5.2 Qualitative representation of the variation of the plasma strength with power and pressure for argon plasma. The brighter areas represent a stronger plasma

### *Weak plasmas*

Because of the fact that the mass of the incident ion is lower than that of surface atoms, for ion energies lower than the binding energy of the surface atom, it is expected [Kaminsky, 1976] that the incident ion is backscattered, transferring only a fraction of its energy to the surface atoms as thermal energy. Also, the surface atom in this collision may be driven towards the bulk and the oxide - substrate interface becomes less sharp. This phenomenon is called *mixing* [Smith, 1997] or *recoil implantation*. As the ion energy increases, bombarding ions become implanted. A further increase of ion energy (which is equivalent to an increase in RF power in the case of plasma) above the binding energy may result in sputtering of target atoms.

For *weak* plasmas, surface oxidation varied with plasma conditions. This suggests that either the plasma has oxidized the surface directly or the oxidation occurred entirely in air on the activated surface. This issue will be clarified later with the aid of the experiments where the just treated surface was exposed to pure oxygen.

There is also a high possibility that an important role in surface compositional changes during *weak*-plasma processing was played by impurities in the plasma. As previously found [Layberry, PhD, 1999], hydrogen can form volatile compounds with As. This may partially explain the depletion in As oxides observed in the case of *weak* plasmas. Also, the active impurity oxygen present in the plasma may penetrate the surface and create oxides. As will be later shown, this phenomenon is believed to explain the formation of Ga<sub>2</sub>O<sub>3</sub> during *weak* argon plasma treatment.

### *Strong plasmas*

At energies just above the sputtering threshold the surface atoms are directly sputtered by the incoming ions as a result of knock-on collisions. At higher ion energies (e.g. at least above 50 W at 10 mT and above 150 W at 90 mT), the surface composition did not change with increasing power (Figures 4.27 c) and d)). Also, the distribution of ion energies moved towards higher values (Figure 4.6 b)), etching increased (see Figure 4.97) while surface oxidation remained constant (Figure 4.45 b)).

The only oxide found on the samples exposed to *strong* plasmas was Ga<sub>2</sub>O with a thickness of about 0.5 nm (Figure 4.45 b)). Due to the fact that the first oxide formed on the surface in the first 20 minutes after plasma treatment was Ga<sub>2</sub>O (Figure 4.81), it is believed that the subsequent formation of Ga<sub>2</sub>O<sub>3</sub> after a certain time of exposure to air was realised by further oxidation of Ga<sub>2</sub>O. Similar phenomena is expected to have taken place in the case of the thermally evaporated samples. Ga<sub>2</sub>O at the outermost surface was found on both thermally evaporated metallic Ga samples (see comparison of surface composition given by 3d and 2p<sub>3/2</sub> regions in Table 4.2). The oxide formed on the metallic Ga sample exposed to the air for a long time increased due to formation of Ga<sub>2</sub>O<sub>3</sub> but again Ga<sub>2</sub>O had

a higher concentration at the surface. This is an important point in the discussion of results and will be used later in this chapter for understanding the appearance of these oxides on the surface exposed to different conditions.

The approx. 0.3 nm increase in the oxide thickness in the time interval between 20 minutes and a month of air exposure after plasma treatment (Figure 4.83) clearly shows that at least partially, the surface oxide was formed on the activated surface after the plasma had been extinguished. The rest of the oxide up to the total of 0.7 nm thickness was either formed in the plasma or in the air immediately after treatment (within the 20 minutes prior to XPS analysis). Although, at this stage, there are no means to directly obtain this information, it is believed that this oxide was formed in the air, as well. This is based on the fact that surface oxidation after plasma treatment had a logarithmic growth with time, which implies that most of the oxidation has taken place at the beginning of the air exposure.

The experimental arrangement used here did not allow surface analysis immediately after extinguishing the plasma. Although the final surface composition of a plasma - treated sample is given by the plasma and also by the air exposure prior to analysis, the sum of these two environments will be referred to as "condition after plasma treatment".

Surface changes induced by plasma only can be inferred by employing other experiments, as will be presented in the following section.

#### **5.3.2.1.2 Controlled neutral oxygen exposure after plasma treatment**

Further experiments where controlled oxygen flow was introduced in the process chamber immediately after plasma treatment helped complete the model for surface modification during argon plasma treatment. The discussion of the results will also be made separately for *weak* and *strong* plasmas.

##### *Weak* plasmas

At 5 W and 90 mT, a significant increase of the oxide layer thickness with oxygen dose from 1.4 nm to 2.2 nm was observed. Thus, the just-etched surface allowed formation of a relatively high-thickness oxide on exposure to neutral oxygen flow. This fact suggests that the surface remained significantly activated after this plasma treatment and the initial oxide (formed during plasma treatment) had a thickness lower than 1.4 nm.

Also, a high surface activation and a slow process of surface neutralisation after plasma processing at 5 W and 90 mT is suggested by the following result. The oxide thickness in the case of one month exposure to ambient air was higher than for the oxygen-exposed sample at dose 48 (see Figure 4.79 c)). A higher oxygen dose should have been used for obtaining an oxide thickness equal to that found on exposure to air for the same plasma treatment.

The oxide composition for the oxygen-exposed sample after Ar plasma treatment (at 5 W,

90 mT) changed with oxygen dose (Figure 4.78 a)). Only the concentration of  $\text{Ga}_2\text{O}$ ,  $\text{As}_2\text{O}_3$  and  $\text{As}_2\text{O}_5$  increased with dose. The decrease of  $\text{Ga}_2\text{O}_3$  with dose is not real. It is only due to the fact that the graph shows relative concentrations. The fact that  $\text{Ga}_2\text{O}_3$  was not formed during pure oxygen exposure implies that its formation has taken place in the plasma. This fact is also confirmed by the ARXPS analysis presented in Figure 4.80 a) which show that exactly the concentrations of  $\text{Ga}_2\text{O}$ ,  $\text{As}_2\text{O}_3$  and  $\text{As}_2\text{O}_5$  were closer to the surface than  $\text{Ga}_2\text{O}_3$ . Also, at a certain depth, the XPS signal from  $\text{Ga}_2\text{O}_3$  has completely disappeared which clearly shows that formation of  $\text{Ga}_2\text{O}_3$  has taken place prior to the formation of the other oxides, e.g. in the plasma. As the appearance of oxygen species in argon plasma can only be due to impurities, it results that formation of  $\text{Ga}_2\text{O}_3$  in the plasma is only due to their presence.

The fact that this higher oxidation state of Ga is preferentially formed during argon plasma treatment is most probably related to a minimum energy required for its formation, which can only be provided by energetic oxygen species created in the plasma. This is in accordance with the fact that  $\text{Ga}_2\text{O}_3$  can be obtained only at high temperatures (of  $650^\circ\text{C}$ ) [Sheka et al, 1966]. The kinetic energy of these species is expected to be higher than that of the oxygen molecules present in ambient air. Impurity oxygen species are ionised in the plasma and gain energy which is then used at the GaAs surface for formation of  $\text{Ga}_2\text{O}_3$ . This is the most likely process responsible for preferential  $\text{Ga}_2\text{O}_3$  formation during argon plasma treatment. This model is confirmed by the fact that concentration of  $\text{Ga}_2\text{O}_3$  increased with pressure, e.g. with increasing amount of oxygen impurities introduced by the feed gas. Also, as shown in Chapter 3, these impurities are more important than those introduced by water adsorbed on the process chamber walls.

Another interesting aspect found at 5 W and 90 mT is that the stoichiometry of the surface did not vary with oxygen dose (Figure 4.78 a)). Thus, minimization of free energy was achieved by a simultaneous oxidation of Ga and As, not by preferential oxidation of the excess substrate compound.

At this stage, the thickness of the oxide formed during plasma treatment at 5 W and 90 mT is still not known. It is only known that it contains only  $\text{Ga}_2\text{O}_3$ . Nevertheless, it can be calculated roughly using the XPS data acquired after exposure to oxygen (for the same plasma 5W and 90 mT) considering a sharp separation between the oxide layer formed in the plasma and the layer above formed on exposure to oxygen (see Figure 5.3). This layer can be regarded as an impurity layer on top of the  $\text{Ga}_2\text{O}_3$ -only surface oxide. The most accurate result for this calculation is expected to be obtained for dose 1 when the oxide formed during oxygen exposure was smaller than for the higher doses and this layer is expected to be the thinnest. This "impurity layer" will equally attenuate the XPS signals coming from the GaAs substrate and from the  $\text{Ga}_2\text{O}_3$  oxide layer. An approximate value of 0.6 nm for the  $\text{Ga}_2\text{O}_3$  oxide layer representing the oxide formed during plasma processing was found. As the total oxide thickness in the case of air exposure was 2.7 nm, the

thickness of the oxide formed in the air after plasma treatment at 5 W and 90 mT was about 2.1 nm.

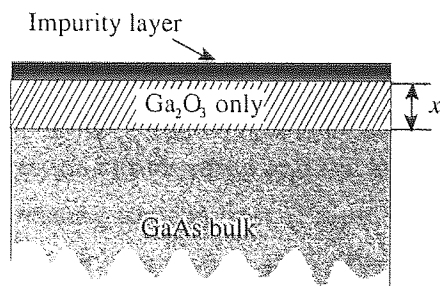


Figure 5.3 Model of surface layered structure at dose 1, for calculation of oxide thickness during plasma processing (denoted by  $x$  in the figure)

As suggested by the values of the oxide thickness after one month of air-exposure for all argon-plasma conditions studied in this work (Figure 4.45), the 5 W and 90 mT plasma represents the condition where the highest oxide thickness can be obtained.

The simultaneous increase of the concentration of As and Ga oxides with increasing oxygen dose found in the case of *weak* plasmas (Figure 4.78 a)) shows that no significant preferential activation of Ga compared to As takes place during *weak* plasma treatment. The preferential formation of a Ga oxide rather than an As oxide obtained during *weak* argon plasma treatment can be explained as follows. The impurity hydrogen ions present in the plasma (especially  $\text{ArH}^+$ , see Chapter 2) reacted with As forming volatile As-H compounds whereas the impurity oxygen reacted with the excess Ga forming  $\text{Ga}_2\text{O}_3$ . All the other target atoms of the surface were probably activated (ionized, etc.) only. Some preferential segregation and sputtering of arsenic has probably taken place, also. Thus, for *weak* plasmas, a difference in stoichiometry will mainly be the result of the following concurrent processes: Ga depletion due to formation of  $\text{Ga}_2\text{O}_3$  and As depletion due to both formation of volatile As-H compounds or preferential sputtering. The reason for preferential formation of the higher oxidation state of Ga during plasma processing is given earlier in this Section.

Information on surface oxide density may also be obtained for certain samples using XPS. This information is interesting due to the fact that in reality the surface oxide is not "pure", it contains atoms from the substrate. The method applied for determination of oxide thickness uses the approximation that the surface oxide is homogeneous, although in most of the real cases the oxide has a density gradient with depth (with respect to the amount of substrate atoms). The calculated value of oxide thickness is proportional to the total number of oxide molecules present in the oxide and is not sensitive to their spatial distribution within the oxide layer. Nevertheless, the density of the oxide can be qualitatively determined for surface oxides greater than 2 nm using sampling depths lower than this value (e.g. at 75 take-off angle). The total amount of As and Ga found at shallow angles is an indication of the oxide density/"purity".

At higher ion energies, e.g. at 90 mT and 150 W, no changes in surface oxidation with increasing dose were observed. This power-pressure combination represents the upper limit of *weak* plasmas.

#### *Strong* plasmas

At 10 mT and 150 W also, the oxide composition and thickness remained constant at a value of about 0.5 nm with increasing oxygen dose (Figure 4.79 e)). Similar oxide thickness was found after one month exposure to air for the sample exposed to the same plasma.

It is interesting to observe that, in the case of exposure to air for 20 minutes after the same plasma treatment, the oxide thickness was about 0.2 nm, which represents about one monolayer. Due to the fact that the oxide thickness had a logarithmic increase with time, most of the oxidation in air has taken place immediately after plasma treatment. Thus, at least one monolayer oxide must have formed before the 20 minutes of exposure to air. This implies that no oxidation has taken place during this plasma treatment. It can be concluded that, in the case of *strong* plasmas, the stoichiometry changes cannot be related to the presence of impurities in the plasma. Here, the preferential processes observed in the GaAs surface had been induced by argon ions. These processes will be discussed later in the section on SRIM.

The Ga rich surface observed 20 minutes after plasma treatment became stoichiometric after one month of exposure to air probably due to both oxidation and restructuring.

Returning to the sample exposed to oxygen flow after the same plasma treatment, it is now known that the 0.5 nm oxide was formed entirely after plasma treatment. Its composition was slightly different from the air-exposed one, but due to low values of the relative concentrations, no conclusions can be drawn on this matter.

In the case of *weak* plasmas, the depth of damage was higher than for *strong* plasmas and minimization of surface free energy after plasma treatment has mostly taken place by oxidation. For *strong* plasmas, removal of the damaged layer was high and the thin Ga rich layer remained after plasma treatment has oxidized in air forming low oxidation states of Ga and As. The layered structure resulting from the ARXPS analyses for the Ar plasma treatment at 100 W at low pressure and also at high pressure is presented in Figure 5.4.

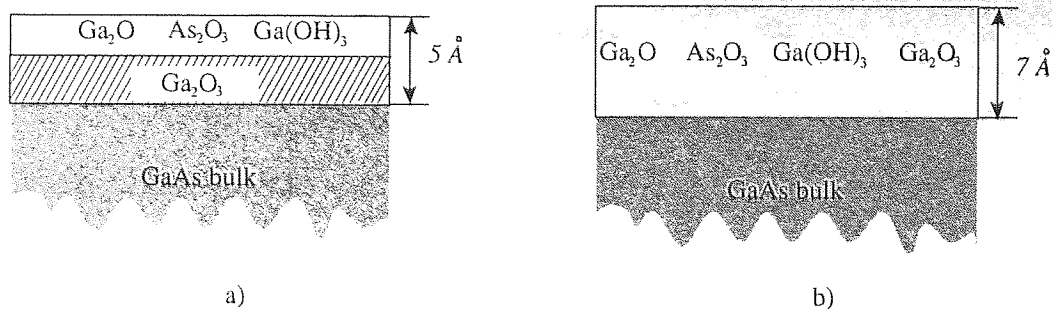


Figure 5.4 Layered structure for Ar plasma treated GaAs at 100 W for 30 min and a) 10mT, b) 90 mT

As a final observation, increasing arsenic depletion due to preferential sputtering can be only encountered with increasing ion energy, e.g. in the case of *strong* plasmas. At a certain point, a further increase in ion energy will increase the etch rate resulting in a decrease of arsenic depletion.

One of the limitations of the x-ray photoelectron spectroscopy is that the XPS signal acquired is an integration of the signal originating from all the layers above the sampling depth. As will be seen in the following, SRIM results helped to further understand the phenomena that had taken place during argon plasma treatment of the surface of GaAs.

### 5.3.2.1.3 SRIM results

Accurate evaluation of the absolute experimental sputtering yield require that the measurements of the parameters involved (sheath width,  $V_{dc}$  and etch rate) are also accurate. Also, SRIM calculation involves the usage of models of surface - plasma interactions which results in errors in calculated results. Nevertheless, useful qualitative information can be obtained using these procedures.

Values of the experimentally determined sputtering yield lower than 1 found in all experiments undertaken in this work suggest that not all incoming ions play an important role. Comparison of the experimental sputtering yield (Figure 4.98) with that obtained using SRIM (Figure 4.105 a)) showed that a SRIM-estimated sputtering yield below 1 is obtained at energies below 150 eV. Knowing that the experimentally determined Y was 1 for ion energies of about 500 eV and also that the code gives overestimated values [Malherbe, 1994], it can be considered that the value of 150 eV given by the code is in reality 500 eV. Thus, the replot of Figure 4.104 a) given in Figure 5.5 becomes more appropriate for describing the plasma - treated surface processes. The new graph shows that the maximum vacancy depth is expected to be about 2 nm and the ion penetration depth 3 nm.

The ions formed in the plasma have a distribution of energies. Thus, only a fraction of them have the maximum energy. Therefore, the predicted maximum depth of damage for a certain value of ion energy is expected to be less in the case of plasma than for ion

bombardment.

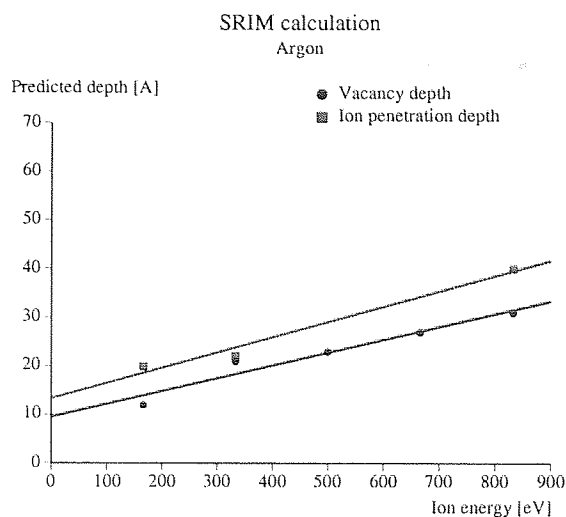


Figure 5.5 Replot of Figure 4.104 a)

As observed in Figure 4.106 a), with increasing ion energy the density of argon implantation is predicted to be lower. This fact was also reported by Singer [1981]. Knowing that sputtering yield increases with ion energy (Figure 4.98), it can be concluded that the density of implanted argon is inversely dependent on the sputtering yield. Knowing that vacancies provide an easy path for diffusion, atomic migration towards the surface is expected to occur at these ion energies. The sputtering probability of an atom raised above the surface is much higher than that of an atom situated deeper in the surface. Due to the fact that Ga rich surfaces were obtained at high ion energies, preferential sputtering of As has probably taken place. The reasons for As segregation are not clear yet, but some explanation for this behaviour is presented in the following.

The difference in surface binding energy between the two constituents of the target may be the explanation for As segregation. For As, this value is 1.26 eV whereas for Ga is 3.075 eV [Pan et al, 1997]. As discussed previously [Wei, 1995], the mass difference between As and Ga cannot be taken as explanation for preferential segregation of As. The large difference in sublimation energy (29 kcal/mole for As and 64.9 kcal/mole for Ga) also results in the preferential sputtering of As.

With increasing ion energy, the predicted increase in vacancy creation may induce further As segregation. Smentkowski et al. [2000] also found that Ga enrichment of the GaAs surface increased with either increasing Ar bombarding energy or the ion current density. This result was also reported by Singer [1981].

The explanation that Ga enrichment of the surface found when using argon plasmas is due, at least partially, to formation of volatile As-H compounds is not valid at high ion energies (e.g. *strong* plasmas). This is because, as explained earlier, contamination in the plasma (with oxygen and hydrogen compounds) is only important in the case of *weak* plasmas, where sputtering is very low.

#### 5.3.2.1.4 Summary of results - argon

With increasing ion energy, firstly arsenic segregation takes place. At a certain point, sputtering becomes important and the segregated As is removed. Surface oxidation during plasma processing takes place at low ion energies only and  $\text{Ga}_2\text{O}_3$  is formed. At high ion energies, surface oxidation can only be found after plasma treatment and only  $\text{Ga}_2\text{O}$  is formed.

#### 5.3.2.2 Neon etching of GaAs

Similar to the case of argon, the oxide thickness increased with pressure at 150 W during Ne plasma etching from about 0.5 nm to 1.2 nm due to formation of  $\text{Ga}_2\text{O}_3$  (Figure 4.49 a)). Also, no arsenic oxides were formed on the surface of the neon-treated samples (Figure 4.47). These results are very similar to those found for *weak* argon plasmas at 50 W (Figure 4.43 a)). Under these supposed similar conditions, etch rate values of over 150 nm for neon (Figure 4.99) and about 50 nm for argon (Figure 4.97) were measured. Although mass and plasma density were lower than for argon (Figure 4.5), the ion energies for the same power-pressure combination in neon plasmas are expected to be higher. This is also the explanation for the high sputtering yield of just little less than 1 found at 200 W and 10 mT. As will be shown in the following, higher ion energies for neon than for argon are also predicted by the SRIM code.

As revealed by SRIM results for neon (Figure 4.105 b)), sputtering yields of about 1 are obtained at about 220 eV, which is higher than for argon. As shown earlier, the SRIM code gives overestimated values of about 3.3 times the experimental values for the sputtering yield. Thus, if the values for  $Y$  are overestimated with the same proportion for argon and neon, a maximum ion energy for neon of about 730 eV is expected. Accordingly, more accurate values for ion penetration and vacancy depth can now be obtained for neon also (Figure 5.6).

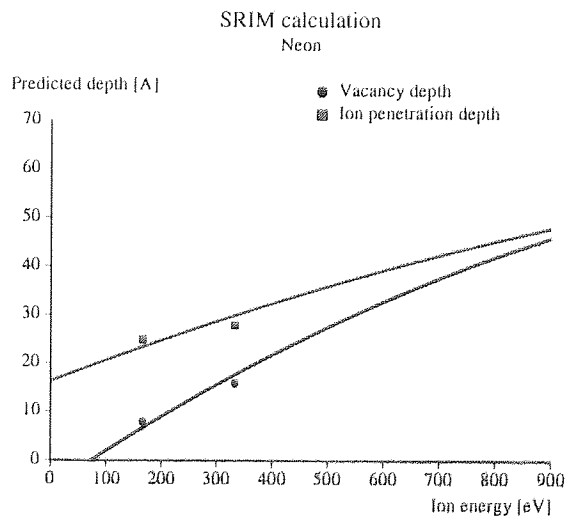


Figure 5.6 Replot of Figure 4.104 b)

Comparison of Figures 5.5 and 5.6 shows that higher values of vacancy depth and ion penetration are predicted, at maximum energy, for neon than for argon. This implies that at 200 W and 10 mT a deeper surface damage is expected in the case of neon than for argon. This result, correlated to the fact that the ion density for neon was lower than for argon shows that surface damage is shallower and denser for argon, as shown in Figure 5.7.

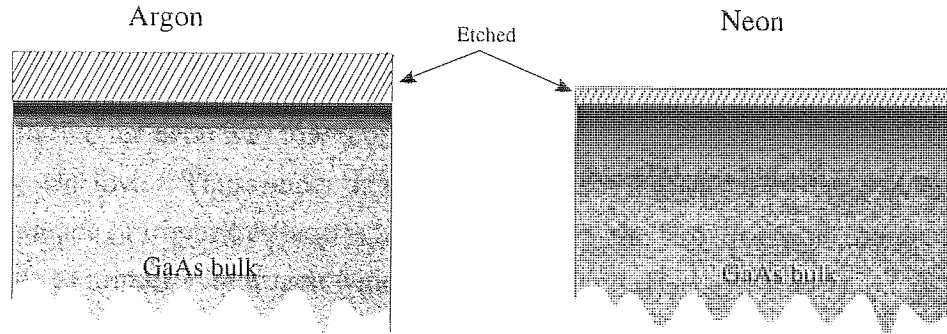


Figure 5.7 Comparative profile of surface damage for Ar and Ne for the same ion energy. The dark areas represent the damage

The increase in oxide thickness during neon plasma processing with increasing pressure at 150 W was due to formation of  $\text{Ga}_2\text{O}_3$  only, as can be observed in Figure 4.47. Because of the fact that similar processes are expected to govern surface oxidation in argon and neon plasmas, it is believed that  $\text{Ga}_2\text{O}_3$  has also formed during neon plasma processing of the surface, as in the case of argon. Also, similar reasons (explained earlier in Subsection 3.2.1.2 of this chapter) for formation of the higher oxidation state of Ga are believed to be valid here. In the case of neon etching, the arsenic enrichment observed with increasing pressure is mainly due to a lower removal rate of the segregated arsenic compared to the case of argon.

#### Weak plasma

In the case of neon plasma, the higher limit for *weak* plasmas represented by the plasma during which no oxidation takes place is 150 W and 10 mT. A qualitative representation of the variation of the plasma strength with pressure and power is given in Figure 5.8.

	5 W	25 W	50 W	100 W	150 W	200 W
10 mT						
20 mT						
30 mT						
50 mT						
80 mT						
90 mT						

Figure 5.8 Qualitative representation of the variation of the plasma strength with power and pressure for neon plasma. The brighter areas represent a stronger plasma

A surprisingly high difference in the relative concentrations of As and Ga was found in the case of neon. As can be observed in Figure 4.47, the As enrichment with pressure is associated with oxidation of Ga in the form of  $\text{Ga}_2\text{O}_3$ . Preferential formation of this compound with increasing pressure was also found in the case of argon plasma treatment. Based on experimental evidence, this phenomenon was explained earlier in this Chapter by the presence of oxygen impurity in the plasma introduced with the feed gas. This explanation is valid for neon also, the only difference here being in the sputtering rate which is lower than oxidation rate.

As the etch rate for neon was low (compared to argon), removal of arsenic depletion by sputtering was lower. Thus, under these plasmas, sputtering was lower than oxidation. The importance of impurities here is also suggested by the lack of arsenic oxides on the surface due to impurity hydrogen which forms volatile  $\text{AsH}_3$ .

#### *Strong plasma*

The thickness of the oxide formed at 150 W and 10 mT was about 0.5 nm and consisted of  $\text{Ga}_2\text{O}$  only, as in the case of argon. The layer diagram of the surface resulting from the ARXPS analyses is presented in Figure 5.9 a). At higher pressure, the segregated As is not completely removed by the ions which are less energetic than at low pressures. The layer diagram of the surface is presented in Figure 5.9 b).

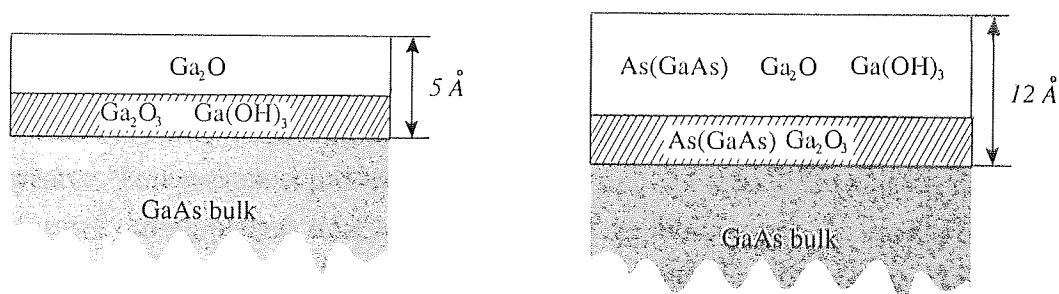


Figure 5.9 Layered structure for Ne plasma treated GaAs at 150 W, for 30 min and a) 10 mT, b) 80 mT

No stoichiometry changes with power were observed at 10 mT. Due to the relatively high etch rates observed here, there is a high probability that the surface was initially arsenic depleted and then balanced by oxidation in air of the excess Ga, as in the case of argon. It is likely therefore, that at low ion energies/low etch rates surface oxidation due to plasma impurities dominates, whereas at higher energies/high etch rates preferential sputtering of the segregated layer dominates. The etch rates refer to physical processes only.

#### 5.3.2.2.1 Summary of results - neon

Similar results were found for neon etching, as for argon etching.  $\text{Ga}_2\text{O}_3$  formed during plasma treatment whereas  $\text{Ga}_2\text{O}$  formed after plasma treatment. The only difference is that

for similar plasma conditions, less sputtering takes place in the case of neon. Thus, less segregated As was removed from the surface.

### 5.3.3 Oxygen etching of GaAs

Interpretation of the XPS results for the oxygen-etched surfaces is more difficult than for the inert gas treatment due to the fact that sputtering and oxidation during and after plasma treatment were due to oxygen. Thus, their separation is more difficult. Also, finding the separation point for *strong* and *weak* plasmas is more complicated here.

Due to the fact that no volatile oxygen compounds can be formed with GaAs, an increase in the etch rate can only be associated with physical sputtering. As observed in the case of inert-gas etching, higher etch rates are associated with lower oxidation during plasma processing. In the case of oxygen plasma, with increasing ion energy, oxidation during plasma processing and sputtering are expected to increase simultaneously. This is because of the fact that with increasing ion energy penetration depth of oxygen ions is expected to increase (as predicted by SRIM, Figure 4.108) increasing the probability of formation oxides. In the same time, sputtering and oxidation during plasma treatment are concurrent processes.

As expected, a stoichiometry change has taken place with increasing ion energy (see Chapter 2). An increase in arsenic depletion was found at 10 mT with increasing power. With increasing power, the increase in oxygen ion energy implied a decrease in the concentration of  $\text{Ga}_2\text{O}_3$  and  $\text{As}_2\text{O}_5$  up to a point where these compounds completely disappeared. This was most probably due to sputtering. At least these two compounds were formed during plasma treatment. The arsenic depletion observed has not been balanced by oxidation and relaxation. Minimization of surface free energy is thought to have taken place in air by formation of the lower oxidation states of Ga and As at the outermost layers, leaving deep damage underneath. This fact is also evident from the ARXPS analysis at 10 mT, 150 W (Figure 4.56 a) where the deep Ga rich layer becomes stoichiometric closer to the surface. The layer diagram of the surface as resulted from the ARXPS data is presented in Figure 5.10.

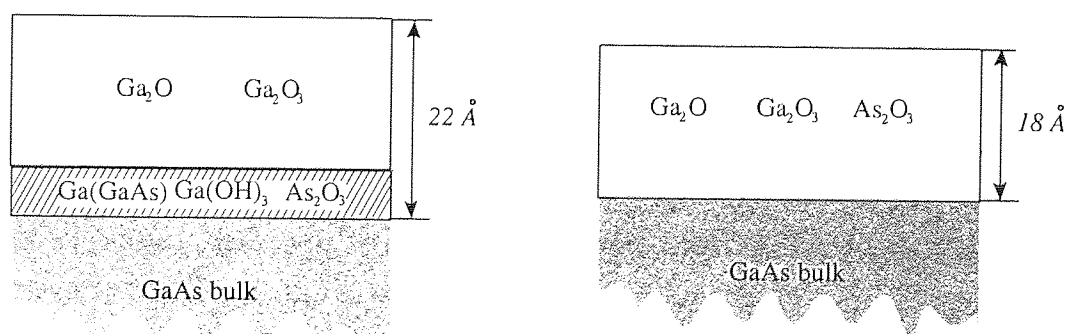


Figure 5.10 Layered structure for  $\text{O}_2$  plasma treated GaAs at 150 W, for 30 min and a) 10 mT; b) 90 mT

Formation of As-H compounds due to the presence of hydrogen impurities cannot account for the relatively high stoichiometry changes observed at high ion energies mainly because sputtering yield was much more important. Also, free H is unlikely to occur in an oxygen plasma.

As can be seen in Figure 4.54 b), no stoichiometry changes were found with increasing power at 90 mT. Here, the ion energies were lower than at 10 mT and oxidation during plasma processing was comparable to the rate of sputtering. At higher pressure (90 mT, Figure 4.56 b)), oxidation during plasma processing (represented by  $\text{Ga}_2\text{O}_3$ ) was higher than sputtering rate and also higher than at 10 mT. As the total oxide was lower than at 10 mT, oxidation in air must have been lower. At 50 W, oxidation and sputtering were balanced and no compositional changes were observed.

The simultaneous decrease of the concentration of all oxides except for  $\text{Ga}_2\text{O}$  resulted in a slight decrease in the total oxide thickness with pressure at 150 W. As with increasing pressure ion energies decreased, oxidation during plasma treatment and sputtering decreased also. Thus, the damage and stoichiometry changes were balanced by oxidation after plasma treatment (immediately after the plasma was extinguished or on exposure to air prior surface analysis).

There is no clear evidence that the native oxide was removed at 5 W, but a model of the phenomena is proposed in the following. Within the error limits, the ARXPS results at 5 W and 90 mT showed that no preferential oxidation of Ga or As has taken place. The layered structure of the surface is presented in Figure 5.11. Similar result was found for the native oxide. Also, in both cases,  $\text{Ga}_2\text{O}_3$  and  $\text{As}_2\text{O}_5$  were formed closer to the substrate, prior to formation of the other oxides. The only difference was in the oxide thickness which was about double in the case of oxygen treatment due to formation of more  $\text{Ga}_2\text{O}$  and  $\text{As}_2\text{O}_3$ . Most probably, no sputtering has taken place here and oxidation of Ga and As were simultaneous during and also after plasma treatment. There is a high probability that the supplementary surface oxidation has only increased the density of the oxide by oxidation of the GaAs present in the native oxide. This process has probably taken place after plasma treatment on the activated surface. As explained earlier in this chapter, the calculation of the oxide thickness was made by using a model where the surface oxide was considered "pure" and homogeneous. Thus, although all XPS signal corresponding to the oxides was taken into account, its distribution within the surface was deliberately changed.

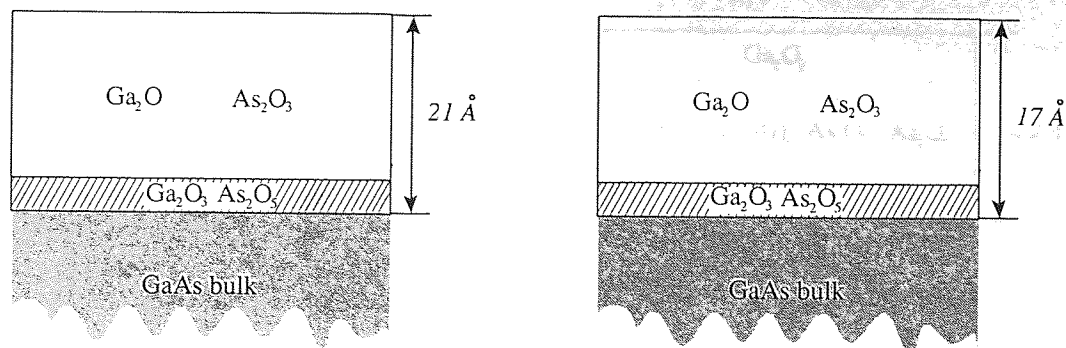


Figure 5.11 Layered structure for  $O_2$  plasma treated GaAs at 5 W, for 30 min and a) 10 mT; b) 90 mT

### 5.3.3.1 Summary of results - oxygen

$Ga_2O_3$  and  $As_2O_5$  were formed during plasma treatment whereas  $Ga_2O$  and  $As_2O_3$  formed in air on the activated surface, after etching. It is important to observe that oxygen plasma was the only plasma favouring formation of arsenic oxides. The highest oxide thickness obtained with oxygen plasma was lower than that obtained with argon plasma.

### 5.3.4 GaAs etching with oxygen-argon plasma

Due to the fact that the electron affinity of oxygen is high, low density of argon ions is expected to exist in argon-oxygen plasmas. This is the explanation for the very low etch rates measured in all argon-oxygen plasma conditions studied in this work (Figure 4.102). Also, within the experimental errors, the changes of the etch rate with pressure, power or oxygen concentration in the mixture were less pronounced than for the pure plasmas. This shows that, in contrast to what was expected, argon ions had low energies and did not cause high sputtering of the surface. This result also suggests that the plasmas of argon-oxygen mixtures used here are *weak* plasmas.

As observed in Figures 4.46 a) and b), arsenic depletion increased with ion energy (high powers, low pressures) and the fact that this stoichiometry change could still be observed after air exposure shows that the process of oxidation left no chance for surface relaxation. This phenomenon was also observed in the case of pure oxygen plasma treatment. The simultaneous increase of the oxide thickness (Figure 4.62 b)) due to  $Ga_2O$  formation observed with increasing ion energy comes to support this model. As found before, this oxide is usually formed after plasma treatment on the activated surface.

The layer diagram resulting from the ARXPS data for the surface exposed to two different plasma conditions is presented in Figure 5.12. The diagrams show that, with increasing  $O_2$  concentration in the plasma, more  $Ga_2O_3$  is formed on the surface of GaAs. Also, this compound is formed at the outermost surface.

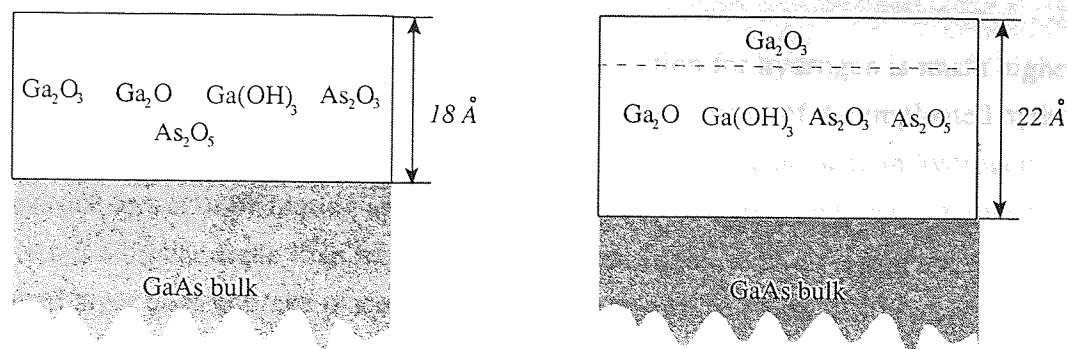


Figure 5.12 Layered structure for Ar + O<sub>2</sub> plasma treated GaAs for 30 min at 150 W, 90 mT and a) 94.5% Ar + 5.5% O<sub>2</sub>; b) 89.8% Ar + 10.2% O<sub>2</sub>

A surprisingly high concentration of Ga(OH)<sub>3</sub> was observed with decreasing ion energy, the highest amount found in this work. As sputtering was relatively low, the presence of impurities must have been important here. Argon ions are known to be the most efficient for removal of water from the chamber walls thus becoming a source for O-H species in the plasma. As presented in Section 4.2.1.4, formation of Ga(OH)<sub>3</sub> on the surface of GaAs may take place in the presence of water at high temperature. Similar processes must have taken place in the case of surface exposure to oxygen-argon plasmas and here the role of temperature is played by the ion energy. In the case of pure argon etching, the etch rates were much higher and therefore this effect could not be observed.

#### 5.3.4.1 Summary of results - Ar + O<sub>2</sub>

Argon ion energies were much lower than in the case of pure argon plasma. The highest amount of Ga(OH)<sub>3</sub> found in this work was observed for Ar + O<sub>2</sub> plasma treatment of GaAs. Also, it was found that more Ga<sub>2</sub>O<sub>3</sub> was formed on the samples treated in higher oxygen content plasmas.

#### 5.3.5 Hydrogen etching of GaAs

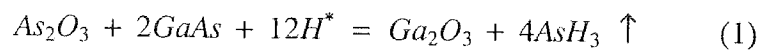
Etching with hydrogen resulted in surface compositional changes only. No sputtering was observed although high ion energies of a few hundred eV were reported to exist in certain power-pressure combinations [Layberry et al, 1999]. Here, the energy transferred to the surface atoms was very much smaller than for the other gases due to the low mass of hydrogen, which implies a very low momentum transfer.

With increasing sputtering, a decrease of surface oxidation was observed on the samples exposed to inert gas and oxygen plasmas. In the case of hydrogen treatment, no etching occurred; thus no correlation between sputtering and oxidation of the excess target atoms can be made. Here, ion implantation and As removal via formation of As-H compounds are the only factors responsible for surface compositional changes during plasma

treatment.

SRIM results have shown that the depth of ion penetration for hydrogen is much higher than that of any other ion studied in this work. Also, the density of the implanted hydrogen ions is predicted to be lower (Figure 4.113). Thus, total surface damage in hydrogen plasma (due to ion implantation and chemical reactions) is expected to have a lower density but a higher depth than for the other plasmas. In the same time, sputtering of the damaged layer does not take place here and therefore surface composition is the result of the accumulated damage over the etching time. The presence of the native oxide makes the model of surface - plasma interaction more difficult.

With the exception of 5 W and 10 mT, no arsenic oxides were found on the hydrogen plasma treated GaAs. As proposed by Sullivan *et al* [1998], reaction



is likely to occur on the surface of GaAs during hydrogen plasma treatment and may explain these findings. The increase of  $\text{Ga}_2\text{O}_3$  with increasing pressure found (Figure 4.65) cannot be the result of the above reaction due to the fact that the arsenic oxides were no longer available to further maintain the reaction. Thus, the presence of oxygen impurities introduced by the feed gas (as explained in Chapter 3) probably accounts for the  $\text{Ga}_2\text{O}_3$  increase with pressure observed, as in the case of inert plasma etching.

The layer diagram for the surface of a sample exposed to hydrogen plasma at high ion energy is presented in Figure 5.13. The diagram shows that the surface remained activated after plasma processing and  $\text{Ga}_2\text{O}$  was formed in relatively high amounts.

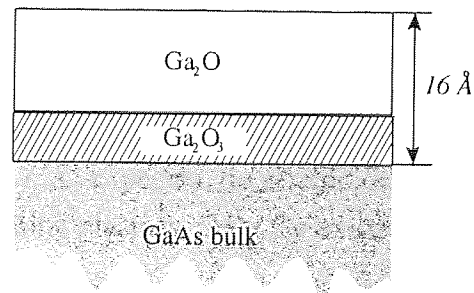


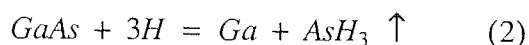
Figure 5.13 Layer structure for  $\text{H}_2$  plasma treated GaAs at 200 W, 10 mT, 30 min

The reason for the preferential formation of  $\text{Ga}_2\text{O}$  with increasing ion energy is not clear, but it may be due to the following process.

A loss of reactivity towards oxygen in air after treatment in hydrogen plasmas of GaAs was reported by Debiemme-Chouvy [1993]. This effect was explained by accumulation of hydrogen at the surface which hindered surface oxidation in air. With increasing ion energy, more hydrogen is implanted deeper in the target and hydrogen accumulation at the surface decreases. This probably accounts for the increase in  $\text{Ga}_2\text{O}$  concentration with power observed (Figure 4.66). This effect is also responsible for the decrease of  $\text{Ga}_2\text{O}$

concentration with pressure.

H<sub>2</sub> plasma etching of GaAs induced As enrichment with increasing pressure (Figure 4.65). Chemical processes are the only processes inducing stoichiometry changes in the case of hydrogen plasma. Thus, this result must be due to preferential oxidation of Ga in the presence of impurity oxygen, which takes place in the plasma forming Ga<sub>2</sub>O<sub>3</sub>. Appearance of Ga<sub>2</sub>O is associated with As removal via formation of volatile AsH<sub>3</sub> which freed some Ga to oxidize in air. This process may be described by the following reaction:



Appearance of Ga(OH)<sub>3</sub> may be related to the presence of hydrogen, but cannot be unequivocally explained as this compound was found in low quantities.

### 5.3.5.1 Summary of results - hydrogen

No sputtering was observed in the case of hydrogen plasma treatment of GaAs. It is important to observe that the arsenic oxides were completely removed from the surface here. Also, Ga<sub>2</sub>O<sub>3</sub> formed during plasma treatment and Ga<sub>2</sub>O formed after the treatment only at high ion energies.

A loss of reactivity towards oxygen in air after treatment in hydrogen plasmas of GaAs was observed at low ion energies. This process hindered Ga<sub>2</sub>O formation under the mentioned conditions.

### 5.3.6 Hydrogen - argon plasma etching of GaAs

Due to the argon content of these plasmas, the native oxide was completely removed in all samples treated in high ion-energy plasmas (at least above 100 W, all pressures and concentrations, Figures 4.61). As expected, no arsenic oxides were found on the surfaces exposed to hydrogen-containing plasmas. Only Ga oxides formed on these surfaces.

In hydrogen-argon plasmas, similar chemical surface processes are expected to take place, as in the case of hydrogen. Thus, the increase of Ga<sub>2</sub>O concentration with power found here can be also explained by reaction (2) followed by oxidation of free Ga presented above. Therefore, surface stoichiometry found in all samples processed in the hydrogen - argon plasma is probably due to removal of the accumulated hydrogen at the surface by argon ions. All samples contained Ga<sub>2</sub>O here, in contrast to the case of hydrogen treatment.

An increase in oxide thickness with hydrogen concentration was observed at low pressure as well as at high pressure (Figures 4.58 c) and d)). This result is due to a lower etch rate (which implies a higher Ga<sub>2</sub>O<sub>3</sub> concentration) together with an increase of the rate of reaction (2) (which is followed by formation of Ga<sub>2</sub>O in air).

The increase in arsenic depletion with decreasing depth at 75% H<sub>2</sub> observed in Figures 4.60 a) and b) shows that not all free Ga oxidised. This can be seen in the layer diagram for the surface of GaAs exposed to Ar + 75% H<sub>2</sub> plasma at 150 W, 10 mT, 30 min is presented in Figure 5.14.

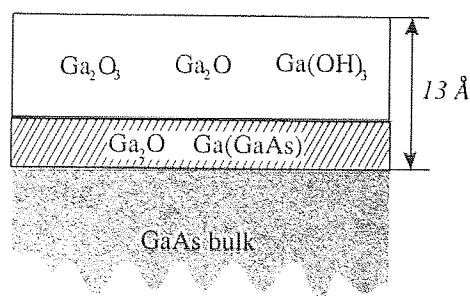


Figure 5.14 Layer structure for Ar + 75% H<sub>2</sub> plasma treated GaAs at 150 W, 10 mT, 30 min

The experiments with hydrogen-argon plasmas were meant to simulate methane-hydrogen mixtures, as these plasmas are used in industry. CH<sub>4</sub>-H<sub>2</sub> plasmas contain a multitude of species and their effect on surface is extremely difficult to follow. Separation of the chemical effects of CH<sub>4</sub> by replacement with an inert gas is thought to be useful in studying surface phenomena induced by hydrogen as part of a gas mixture. Similar surface-chemical effects found in pure hydrogen were also observed in argon - hydrogen mixtures and are expected to be found in most of the hydrogen-containing plasmas.

Physical processes (sputtering) were much higher in the case of pure argon plasmas than in argon - hydrogen mixtures, even at the lowest hydrogen concentration. This result was expected as new plasma reactions take place on addition of a gas while the original ones lower their probabilities. Therefore, this phenomenon limits the usefulness of the study of alternative plasmas, especially for physical processes.

### 5.3.6.1 Summary of results - Ar + H<sub>2</sub>

The etch rates in the case of argon - hydrogen plasma treatment were much lower than in the case of etching with pure argon. Also, no arsenic oxides were formed on the argon - hydrogen plasma etching of GaAs, as in the case of pure hydrogen treatment.

All samples contained Ga<sub>2</sub>O here, in contrast to the case of pure hydrogen treatment and Ga<sub>2</sub>O<sub>3</sub> was formed after plasma processing of the surface.

### 5.3.7 Summary of the overall processes

Due to the multitude of possible experimental conditions and also due to the diversity of tools used for surface analysis, a comprehensive understanding of surface processes is not available yet. The study of surface - plasma interactions can be divided into the study of

physical and chemical processes.

As shown in this work, after plasma processing the surface remains activated and further surface changes take place. Therefore, the term *final* surface is relative and must be used in conjunction with at least two parameters: duration of exposure and type of ambient atmosphere the sample is exposed to after plasma processing. Thus, when defining the optimal condition for minimal surface damage a set of parameters describing the particular treatment have to be specified.

A summary of the processes responsible for the surface changes in GaAs observed in this work is presented in the following.

#### **5.3.7.1 Physical processes**

Removal of surface atoms due to momentum transfer depends on type, energy and incidence angle of impinging particle and also duration of treatment. Previous studies of ion bombardment of GaAs provided a starting point in the study of plasma processing of this material.

The main complication in sputtering of multiple component targets is that the components are not removed stoichiometrically which implies changes in the composition of the surface layers. As a consequence of preferential sputtering, a stationary state of surface composition is reached only after a certain duration of bombardment.

From the point of view of physical processes, surface composition here refers to the relative composition of As and Ga atoms and the damaged layer will have a composition different from that of bulk material.

An increase of Ga enrichment due to arsenic segregation with ion energy and current density was observed in all plasmas used in this study, except for hydrogen plasmas. This process will take place up to a point where sputtering becomes more dominant over As segregation. This implies that an optimum ion energy for a complete removal of segregated atoms can be found for any plasma. Thus, surface stoichiometry can ideally be obtained during plasma processing at the energies employed in this investigation. The main problem related to maintaining this surface composition is related to the fact that most of the ions striking the surface are implanted and the surface is far from equilibrium immediately after plasma processing. Thus, a surface layer corresponding to the ion range will be damaged. After the plasma is extinguished, depending on the ambient conditions, surface changes continue to take place via relaxation and oxidation.

The highest etch rates in this work were found for argon etching.

### 5.3.7.2 Chemical processes

If no preferential treatment is given to As or Ga (e.g. mechanic polishing of the surface), these two components oxidize simultaneously. During and after plasma treatment, preferential oxidation was observed, this result showing that plasma treatment induces preferential processes.

#### 5.3.7.2.1 Surface changes during plasma processing

Oxidation during inert-gas plasma processing was found only at low powers and high pressures and was due to the presence of impurities in the process chamber. Also, arsenic reduction via formation of volatile  $\text{AsH}_3$  is believed to have some influence on surface composition. At higher powers and lower pressures, sputtering was more important than oxidation. The only oxide formed during inert-gas plasma treatment was  $\text{Ga}_2\text{O}_3$ , at low ion energies only.

Removal of surface layers containing oxides formed during plasma treatment increased with increasing ion energy. During oxygen-containing plasma etching of GaAs, preferential oxidation of Ga in the form of  $\text{Ga}_2\text{O}_3$  was found. This result was explained in terms of arsenic segregation followed by sputtering due oxygen ions and a simultaneous interdiffusion between arsenic and oxygen. Hydrogen-containing plasmas also induced formation of  $\text{Ga}_2\text{O}_3$ . The preferential appearance of  $\text{Ga}_2\text{O}_3$  during plasma processing was attributed to the fact that a higher energy is necessary at the surface for its formation.

#### 5.3.7.2.2 After plasma processing

After all plasma treatments studied here, minimization of free energy of the activated surface has taken place mainly via formation of  $\text{Ga}_2\text{O}$  in air. It was observed that surface activation was higher at lower ion energies (lower powers and higher pressures).

In the case of hydrogen etching, temporary neutralization of the surface was obtained especially at lower ion energies and surface oxidation in air was hindered.

A logarithmic growth in air of surface oxide was observed after the inert-gas etching of GaAs. The first oxide to be formed on the surface immediately after plasma treatment was  $\text{Ga}_2\text{O}$ . Formation of  $\text{Ga}_2\text{O}_3$  was observed only after a certain period of exposure to air and was realised by a further oxidation of  $\text{Ga}_2\text{O}$ .

## Chapter 6. Conclusions

Progress in the field of electronic device fabrication is driven by the ability to improve quality, increase integration, decrease cost and develop new applications.

This work is meant to contribute to the understanding of surface reactions in industrial plasmas for a better control of the industrial process.

### 6.1 Peak assignment in the XPS of GaAs

Hence not all surface compounds and the conditions for their appearance on the GaAs are yet completely known, the first part of this work was concerned with their study.

The assignment of the XPS peaks proposed here is: 19.1 eV for Ga(-As), 20.1 eV for Ga<sub>2</sub>O, 20.7 eV for Ga<sub>2</sub>O<sub>3</sub>, 21.7 eV for Ga(OH)<sub>3</sub>, 41.1 eV for As(-Ga), 44.3 eV for As<sub>2</sub>O<sub>3</sub> and 45.3 eV for As<sub>2</sub>O<sub>5</sub>.

### 6.2 GaAs surface modification

The main experimental observations are related to changes in surface stoichiometry, surface oxidation due to impurities in the plasma and also due to air exposure of the activated surface prior to analysis.

Two plasma regimes inducing different phenomena on the GaAs surface were put in evidence. Discussion of the results was based on their separation by ion energy into *weak* and *strong* plasmas. Since the ions in the plasma have a distribution of energies, this separation cannot be sharp and precise.

#### 6.2.1 Inert-gas plasmas

Inert ion etching of GaAs resulted in surface stoichiometry changes, sputtering and oxidation. These phenomena were found to have different intensities depending on ion energy. For similar input plasma parameters, neon ions have higher ion energies and lower density than the argon ions. Neon ions have a higher penetration depth in GaAs and the sputtering yield is lower. Thus, neon plasmas induce formation of a deeper damage layer, but the density of the damage is lower.

At low energies, an important role in surface compositional changes during inert gas plasma processing was found to be played by impurities in the plasma. Due to low sputtering, oxidation during neon plasma treatment is important at higher energies also. The rate of sputtering is lower than the rate of surface oxidation during *weak* plasma treatment in argon, also. Impurity oxygen in the plasma induces formation of the higher

oxidation states of Ga and As, e.g.  $\text{Ga}_2\text{O}_3$  and  $\text{As}_2\text{O}_5$  whereas impurity hydrogen removes As from the surface.

The oxide formed in the air by oxidation of free Ga and As is firstly formed by the lower oxidation states of Ga and As (e.g.  $\text{Ga}_2\text{O}$  and  $\text{As}_2\text{O}_3$ ) and with increasing exposure the higher oxidation states also appear. The surface remains highly activated after *weak* plasma treatment and oxidation in air can reach over 20 Å thickness within a month of exposure. At higher energies, the incident ions produce large etch rates. Sputtering is important and impurities in the plasma do not play an important role in surface composition. Also, the amount of Ga at the outermost surface depends on the relative intensity of sputtering and oxidation in air.

### 6.2.2 Oxygen-containing plasmas

Sputtering and surface oxidation during plasma treatment are concurrent processes for plasmas which do not contain oxygen. For oxygen-containing plasmas, this effect is superimposed with a simultaneous increase of oxidation during plasma processing and sputtering with increasing ion energy. At high ion energies, arsenic depletion for both pure oxygen and oxygen-argon plasmas is deep and minimization of surface free energy takes place by oxidation only at the outermost layer.

$\text{Ga}(\text{OH})_3$  is formed during plasma treatment due to the presence of water impurities. This result is mostly observed when argon is present in the process chamber.

### 6.2.3 Hydrogen-containing plasmas

Hydrogen treatment of the GaAs surface resulted in surface compositional changes only. No physical sputtering occurred. Chemical removal of As by formation of As-H volatile compounds and ion implantation caused surface damage which was balanced by oxidation.

The reported loss of reactivity towards oxygen of the surfaces previously treated in hydrogen-containing plasmas was confirmed in this work also.

## 6.3 Relevance of the work to the general field

In industry, the usual etchant for GaAs is  $\text{CH}_4/\text{H}_2$  plasmas. These plasmas are very complex and an accurate information of the type of ions present and their energies is very difficult to obtain. Furthermore, the surface reactions induced by these ions are complicated. Therefore, a separation of chemical effects from physical effects is necessary for a better understanding of these complex processes. This is also the aim of this work.

Many studies on surface - plasma interaction in GaAs are reported, but due to the diversity of experimental conditions and surface analysis tools used, a comprehensive theory of surface processes is not available yet.

The study of surface - plasma interaction was undertaken here by correlating results of surface analysis with plasma diagnosis. Based on published data and measurements reported here, a general understanding of the plasmas used is proposed here. Plasmas of inert gases and mixtures with hydrogen and oxygen were employed.

Qualitative information on the variation of vacancy depth, ion penetration and sputtering yield with ion energy for different bombarding ions was obtained using SRIM code.

In the current literature, characterization of surface oxides of GaAs is still an open issue. A separate study aiming the identification of the GaAs surface oxides was undertaken in this work and an assignment of all the photoelectron peaks found in the 3d region of the XPS spectra is proposed. Comparisons of proposed models with those found in current literature were also presented.

Under certain conditions, impurities in the plasma and surface modification in air prior to analysis were found to play an important role in the final surface composition. Therefore, an estimation of the amount of impurities present in the plasma is given in this work. Samples exposed to ambient air for different periods of time and also to pure oxygen were analysed.

During plasma processing, low surface damage is obtained at high oxidation. As these plasma conditions have low sputtering yields, a compromise has to be made in choosing the best condition for high sputtering and low damage. Surface stoichiometry and relatively high sputtering rates can theoretically be obtained for any gas (except for low mass ions) immediately after processing. Problems arise due to the fact that after treatment the surface is not stable. Subsequent handling of the sample implies exposure to air and/or surface relaxation, changing surface composition.

Formation of  $\text{Ga}_2\text{O}_3$  was found to take place during plasma treatment or after a certain time of exposure to air. Its presence on the surface was found to decrease with increasing etch rate. Monitoring the presence of  $\text{Ga}_2\text{O}_3$  on the surface shortly after plasma processing is a potential tool for determination of surface oxidation during treatment.

$\text{Ga}_2\text{O}$  was found to be formed after plasma treatment, on exposure to air or oxygen. Hydrogen plasma treatment at low powers proved to be a good method of surface passivation in air.

Formation of  $\text{Ga}(\text{OH})_3$  was found to be favoured by the presence of water in experiments with boiling of GaAs wafer. This compound was also present in the plasma treated samples, but in relatively small amounts. Its formation was found to be subjected to energy availability at the surface, as in the case of  $\text{Ga}_2\text{O}_3$ .

## Chapter 7. Further work

The study of plasma induced surface modification of GaAs is far from being complete. A better understanding of surface processes may be achieved by improving the experimental setup and also the mathematical models.

### *A better plasma process chamber*

For reducing the presence of impurities in the process chamber, ultra high vacuum and also research grade purity gases should be used. A load lock would also be most useful. Also, impurities in the process chamber are to be monitored more precisely.

Accurate measurements of the absolute sputtering yield require that the experiments are performed under UHV conditions so that contaminants do not deposit onto the sample during analysis.

Systems where direct contact of the just treated surface with the ambient air can be avoided should also be used. This can be achieved by either integration of plasma cell and surface analysis tools or by using a vacuum suitcase for transportation of samples.

For studies of lowering surface damage by etching, inductive coupling (IC) may be more appropriate [Maeda et al, 1999]. Inductively coupled plasma configurations are capable of producing high density plasmas at low pressure (less than 20 mT) etching anisotropic features over large wafers with less surface damage.

### *Plasma modelling*

Comprehensive codes for the prediction of ion energy, density and angle distributions for all plasmas would be most useful in the studies of surface - plasma interactions. There are commercially available plasma simulations like PHOENICS-CVD (from Cham, UK) and Chemkin (from Reaction Design, USA) and there are also many research groups developing their own codes for specific geometries of plasma sources [Lymberopoulos & Economou, 1995], [Collision, 1996], [Grappenhau, 1997].

### *Surface analysis*

Complementary surface analytical techniques should be used for complete unequivocal depth profile analysis.

More studies of the oxides are needed. Core level shifts are sometimes unable to

distinguish between compounds with close binding energies. The valence region, because it probes the electrons taking part in the chemical bonding, can potentially be useful.

#### *Modelling of surface processes*

Quantum mechanical codes like CASTEP or Hyperchem [309 Russ] would give more insight into surface chemistry.

#### *Experimental conditions to be explored*

The influence of flow rate of the feed gas on surface compositional changes may also bring more information on the processes governing redeposition of just sputtered particles.

Other experiments giving useful information on surface oxidation and formation of hydroxides may be the study of the influence of humidity in air and also in the process chamber. There are commercially available devices for inducing and monitoring humidity in reactors.

Studies of surface changes on exposure to different neutral gases immediately after extinguishing the plasma may help to understand the processes involved in minimization of free energy of the just activated surface. Also, the dependence of surface composition on duration of etching may reveal surface processes that take place before equilibrium between sputtering and segregation is established.

Systematic studies of surface changes with angle of incidence, mass and type of incident particle using ion bombardment are also needed for a better understanding of the physical processes occurring in the plasma.

## References

- Alay JL, Journal of Applied Physics 77(7) (1995) 3010 - 3022.
- Alay JL, Vandervorst W, J. Vac. Sci. Technol. A10(4) (1992) 2926.
- Albanesi EA, Sferco SJ, Lefebvre I, Allan G, Hollinger G, Physical Review 46(20) (1992) 13260-13267.
- Allwood DA, Carline RT, Mason NJ, Pickering C, Tanner BK, Walker PJ, Thin Solid Films 364 (2000) 33.
- Allwood DA, Cox S, Mason NJ, Palmer R, Young R, Walker PJ, Thin Solid Films 412(1) (2002) 76.
- Alnot P, Wyczisk F, Friederich A, Surface Science 162 (1985) 708 - 716.
- Ando S, Schinohara M, Takayama K, Vacuum 49(2) (1998) 113 - 120.
- Aoyama T, Tanemura M, Okuyama F, Applied Surface Science 100(101) (1995) 351-354.
- Aydil ES, Giapis KP, Gottscho RA, Donnelly VM, Yoon E, Journal of Vacuum Science and Technology B11(2) (1993) 195-205.
- Ayzenshtat GI, Kanaev VG, Khan AV, Potapov AI, Nucl. Instrum. in Phys. Research A 466(1) (2001) 162.
- Ballutand D, Debiemme-Chouvy C, Etcheberry A, De MP, Svob L, Appl. Surf. Sci. 84 (1995) 187 - 192.
- Barrett NT, Greaves GN, Pizzini S, Roberts KJ, Surface Science 227 (1990) 337 - 346.
- Beerbom M, Henrion O, Klein A, Mayer T, Jaegermann, Electrochem. Acta 45 (2000) 4663-4672.
- Behrisch R. Sputtering by particle bombardment: Topics in Applied Physics. Series Eds: Lotsch HKV, Berlin, Springer Verlag. (1981).
- Belengeur P, Beouf JP, Phys. Rev. 41(8) (1990) 4447-4459.
- Bertolucci E, Bottigli U, Ciocci MA, Cola A, Nuclear Physics B - Proceedings Supplements 61(3) (1998) 633-637.
- Bertrand PA, J. Vac. Sci. Technol. 18 (1981) 28-33.
- Blakely JM, Surface physics of materials, 2 nd ed., UK, (1975).
- Boenig HV, Fundamentals of Plasma Chemistry and Technol., Technomic (1998).
- Bohr MT, Applied Surface Science 100(101) (1996) 534-540.

- Bond P, Brier PN, Fletcher J, Jia WJ, Price H, Gorry PA, Surface Science 418(1) (1998) 181-190.
- Breeze PA, Hartnagel HL, Sherwood PM, J. Electrochem. Soc. 127 (1980) 454-461.
- Bresse J, Cardinaud C, Scanning Microscopy 8(4) (1994) 976-986.
- Briggs D, Brown A, Vickerman JC, Handbook of Static Secondary Ion Mass Spectrometry, 2 nd ed., NY (1989).
- Briggs D, Seah MP, Practical Surface Analysis, 2 nd ed., Chichester (1990).
- Brozel MR, Stillman GE, Gallium arsenide, 2 nd ed., UK (1996).
- Carli R, Bianchi CL, Applied Surface Science 74 (1994) 99-102.
- Chapman B, Glow discharge processes, sputtering and plasma etching, 2 nd ed., New York, Chichester (1980).
- Chester MJ, Jach T, Journal of Vacuum Science and Technology B11(4) (1993) 1609-1613.
- Chester MJ, Terrence J, Dagata JA, Journal of Vacuum Science and Technology A11(3) (1993) 474-480.
- Ching-Hui C, Green DL, Hu EL, Journal of Vacuum Science and Technology B13(6) (1995) 2355-2359.
- Choudhury T (1991). An XPS study of the effect of ion bombardment on transition metal oxides. PhD Aston University, UK.
- Christie AB, Methods of Surface Analysis, 2 nd ed., NY (1980).
- Christmann K, Introduction to Surface Physical Chemistry, 1 st ed., Chichester (1991).
- Christophorou LG, James DR, Mathis RA, 12 (1979) 1223-1236.
- Cochran CN, Foster LM, Journal of Electrochemical Society 109 (1982) 144-148.
- Collision WZ, Kushner MJ, Journal of Applied Physics Letters 68(7) (1996) 903.
- Cossu G, Ingo GM, Mattogno G, Padeletti G, Proietti GM, Applied Surface Science 56 - 58 (1992) 81-88.
- Croydon WF, Parker EHC, Dielectric Films on Gallium Arsenide, 2 nd ed., New York (1981).
- Cuberes MT, Sacedon JL, Surface Science 269(270) (1992) 929-933.

- Dautremont-Smith WC, Mater. Res. Soc. Symp. Proc.(USA) 104 (1988) 313.
- Debiemme-Chouvy C, Ballutand D, Pesant JC, Severac C, Etcheberry A, Appl. Surf. Sci. 65-66 (1993) 643-645.
- Deng ZW, Kwok RWM, Lau WM, Cao LL, Appl. Surf. Sci. 158 (2000) 58-63.
- Flesch GD, Nourbakhsh S, Ng CY, J.Chem.Phys. 92(6) (1990) 3590-3603.
- Foad MA, Thomas S, Wilkinson CDW, J. Vac. Sci Tech. B 11(1) (1993) 20-25.
- Gatos HC, The Surface Chemistry of Metals and Semiconductors, 2 nd ed., New York (1980).
- Ghidaoui D, Lyon SB, Thompson GE, Walton J, Corrosion Science 44(3) (2002) 501-521.
- Godyak VA, Piejak RB, Sternberg N, IEEE Transactions on Plasma Science 21(4) (1993) 378-381.
- Gourier S, Friedel P, Larsen PK, Surf. Sci. 152 (1985) 1147-1150.
- Grapperhaus MJ, Kushner MJ, Journal of Applied Physics 81(2) (1997) 569-578.
- Grigonis A, Galdikas A, Silinskas M, Applied Surface Science 138/139 (1999) 581-586.
- Hahn YB, Hays DC, Cho H, Jung KB, Abernathy CR, Pearton SJ, Appl. Surf. Sci. 147(1) (1999) 207-210.
- Hollinger G, Skheyta-Kabbani, Gendry M, Physical Review B49 (1994) 11159-11167.
- <http://physics.nist.gov/PhysRefData/XrayMassCoef/tab3.html>.
- <http://srdata.nist.gov/xps>.
- <http://jas2.eng.buffalo.edu/applets/education/solid/unitCell/home.html>.
- Ingre S, Lau WM, McIntyre, Journal of Vacuum Science and Technology A 4(3) (1986) 984 - 988.
- Iwami M, Watanabe Y, Kato H, Nakayama M, Sano N, Thin Solid Films 146 (1987) 291-297.
- Janes J, Huth C, Journal of Vacuum Science and Technology A 10(5) (1992) 3086-3091.
- Kaminsky M, Radiation Effects on Solid Surfaces, 3 rd ed., (Washington, D.C., 1976).
- Kikawa T, Ochiai I, Takatani S, Surf. Sci. 316 (1994) 238-246.
- Kubaschewski O, Hopkins BE, Oxidation of Metals and Alloys, 2 nd ed., (London, 1953).

- Kuen-Sane D, Rong-Yih H, Materials Science and Engineering B - Solid State Materials for Advanced Technology B9(1-3) (1991) 57-60.
- Kumar J, Sumathi RR, Udhayasankar M, Jayavel P, J. of Crystal Growth 178(3) (1997) 229.
- Kushner MJ, J. Appl. Phys. 58(11) (1985) 4024-4031.
- Kuypers AD, Hopman HJ, J. Appl. Phys. 63 (1988) 1894-1899.
- Kwei CM, Tung CJ, Journal of Physics D 19 (1986) 255-263.
- Lamontagne B, Guay D, Roy D, Sporken R, Caudano R, Applied Surface Science 90 (1995) 481-487.
- Law VJ, Ingram SG, Tewordt M, Jones GAC, Semicond. Sci. Technol 6 (1991) 411-413.
- Layberry LR, Wronski, Pearce CG, Sullivan J, J.Phys. D, Appl. Phys. 32 (1999) 1-13.
- Layberry RL (1999). Computer simulation of radio-frequency methane/hydrogen plasmas and their interaction with GaAs surfaces. PhD. Aston University, UK.
- Lee JW, Jeon MH, Devre M, Mackenzie KD, Solid - State Electronics 45(9) (2001) 1683-1691.
- Lee JW, Jung PG, Devre M, Westermann R, Solid-State Electronics 46(5) (2002) 685-698.
- Lefebvre PR, Irene EA, Journal of Vacuum Science and Technology B15(4) (1997) 1173-1181.
- Leyral P, Litty F, Loualiche S, Nouailhat N, Guillot G, Solid State Commun. (USA) 38 (1981) 333-339.
- Li K, Lin J, Wee ATS, Tan KL, Feng ZC, Webb JB, Appl. Surf. Sci. 99 (1996) 59-66.
- Lieberman MA, IEEE Trans. Plasma Sci. 16 (1994) 638-645.
- Lieberman MA, Lichtenberg AJ . Capacitive discharges, in: Principles of plasma discharges and materials processing, New York, John Wiley and Sons. 326-372.
- Liu J, Huppert GL, Sawin HH, Journal of Applied Physics 68 (1990) 3916-3934.
- Liu L, Edgar JH, Materials Sci. and Engineering 37(3) (2002) 61-64.
- Lu ZH, Bryskiewicz, McCaffrey J, Wasilewski Z, Graham MJ, J. Vac. Sci. Technol. B(11) (1993) 2033-2037.
- Lymberopoulos DP, Economou DJ, IEEE Trans. on Plasma Science 23(4) (1995) 573-

- Maeda T, Cho H, Hong J, Pearton SJ, *J of Electronic Materials* 28(2) (1999) 118-121.
- Maeda T, Lee JW, Shul RJ, Han J, Hong J, Lambers ES, *Appl. Surf. Sci.* 143(1) (1999) 174-180.
- Malherbe JB, *Critical Rev. in Solid State Mat. Sci.* 19(2) (1994) 55-127.
- Malherbe JB, Barnard WO, Strydom I, Louw CW, *Surface and Interface Analysis* 18 (1992) 491-495.
- Malherbe JB, Odendaal RQ, *Appl. Surf. Sci.* 144-145 (1999) 192-200.
- Man KF, Smith ACH, Harrison MFA, *Journal of Physics B* 20 (1987) 5865-5870.
- Massies J, Contour JP, *Journal of Applied Physics* 58(2) (1985) 806-810.
- Masuda A, Yonezawa Y, Morimoto A, Shimizu T, *Jpn. J. Appl. Phys.* 34(2B) (1995) 1075-1079.
- McDaniel EW, *Collision Phenomena in Ionized Gases*, 1 st ed., John Wiley, New York (1964).
- Meichsner J, Zeuner M, Krames B, Nitschke M, Rochotzki R, Barucki K, *Surface and Coatings Technol.* 98 (1998) 1565-1571.
- Mihailova T, Velchev N, Krastev V, Marinova T, *Appl. Surf. Sci.* 120 (1997) 213-219.
- Mikhailov GM, Bilkin PV, Khudobin SA, Chumakov AA, Yu SS, *Vacuum* 43 (1992) 199-201.
- Morgan R, *Plasma Etching in Semiconductor Fabrication*, 2 nd ed., Amsterdam, Elsevier, Oxford (1985).
- Nahlah E, Srinivasa RS, Major S, Sabharwal SC, Muthe KP, *Thin Solid Films* 333 (1998) 9-12.
- Naito S, Ito N, Hattori T, Goto T, *Japanese Journal of Appl. Phys.* 34(1) (1995) 302-303.
- Olthoff JK, Van BRJ, Radovanov SB, *Journal of Research of National Institute of Standards and Technology* 100(4) (1995) 383-400.
- Pan JS, Wee ATS, Huan CHA, Tan HS, Tan KL, *Journal of Physics D: Applied Physics* 30 (1997) 2514-2519.
- Passeggi MCGJ, Vaquila I, Ferron J, *Applied Surface Science* 133 (1998) 65-72.
- Passeggi MCG, Koropechi RR, Ferron J, Molinas B, Guadalupi GM, *Surface and*

- Coatings Technology 122 (1999) 56-59.
- Passeggi MCG, Koropeccki RR, Ferron J, Molinas B, Guadalupi GM, Surface and Coatings Technology 122 (1999) 56-59.
- Pearton SJ, Mater. Sci. Rep. (Netherlands) 4 (1990) 313-318.
- Pearton SJ, Int. J. Mod. Phys B (Singapore) 8(10) (1994) 1247-1342.
- Pearton SJ, Materials Sci. and Engineering B 40 (1996) 101-111.
- Phelps AV, Journal of Physical and Chemical Reference Data 20(3) (1991) 557-573.
- Phelps AV, Journal of Physical and Chemical Reference Data 21(4) (1992) 883-897.
- Popov OA, Godyak VA, J. Appl. Phys, 57(1) (1985), 53-58.
- Qian G, Martin RM, Physical Review B, 38(11) (1998) 7649-7663.
- Quagliano LG, Applied Surface Science 153 (2000) 240-244.
- Rahman M, Deng LG, van BJ, Wilkinson CDW, Journal of Applied Physics D 34 (2001) 2792-2798.
- Raizer YP, Shneider MN, Yatsenko NA, Radio-Frequency Capacitive Discharges, 2 nd ed., USA (1995).
- Rauf S, Kushner MJ, J. Appl. Phys. 82(6) (1997) 2805-2809.
- Roth JR, Applications to Nonthermal Plasma Processing, 2 nd ed., Bristol (2001).
- Rusu IA (2001). Contributions to the microscopic and macroscopic studies of the inhomogeneous regions of low temperature plasmas. Ph D. A.I. Cuza University, Romania.
- Sanghera HK (1998). Investigation of the effects of low energy high dose ion bombardment in metals and compound semiconductors. Ph D. Aston University, UK.
- Schmuki P, Hussey RJ, Sproule GI, Tao Y, Wasilewski ZR, McCaffrey JP, Graham MJ, Corrosion Science 41 (1999) 1467-1477.
- Schwartz GP, Gualtieri GJ, Kammlott GW, Schwartz B, Journal of Electrochemical Society 126(10) (1979) 1737-1749.
- Schwierz F, Liou JJ, Microelectrincs Reliability 41(2) (2001) 145-168.
- Seah MP, Auger and x-Ray Photoelectron Spectroscopy, 2 nd ed., Chichester, UK (1990).
- Seah MP, Dench WA, Surf. and Interf. Analysis, vol.I, 2 nd ed., Chichester, UK (1979).
- Senemaud C, Belin E, Gheorghiu A, Theye ML, Journal of Non-Crystalline Solids 77/78

(1985) 1289-1292.

Sharma BL, Diffusion in Semiconductors, 1 st ed., Germany (1970).

Sheka IA, Chaus IS, Mityureva TT, The Chemistry of Gallium, 3 rd ed., Chichester (1966).

Shin J, Geib KM, Wilmsen CW, Chu P, Wieder HH, J. Vac. Sci. Technol A9(3) (1991) 1029-1034.

Sigmund P, Nuclear Instruments and Methods in Physics Res. B 27(1) (1987) 1-20.

Singer IL, Murday JS, Comas J, Journal of Vacuum Science and Technology 18(2) (1981) 161-170.

Singer IL, Murday JS, Cooper LR, Surface Science 108(1) (1981) 7-24.

Singh NK, Bolzan A, Foord JS, Wright H, Surface Science 409(2) (1998) 272-280.

Smentkowski VS, Progress in Surface Science 64 (2000) 1-58.

Smith R, Atomic and Ion Collisions in Solids and at Surfaces. Theory, Simulation and Applications. Cambridge, Cambridge University Press. (1997),

Snijkers RJMM, Sambeek MJM, Kroesen GMW, Hoog FJ, Appl. Phys. Lett. 63(3) (1993) 308-314.

Sobolewski MA, IEEE Trans. on Plasma Sci., 23(6) (1995), 1006-1022.

Steer CA, Weng GS, Luo JL, Ivey DG, Electrochemistry Communications 2 (2000) 754.

Stuart RV, Vacuum Technology, Thin Films and Sputtering. An Introduction, 2 nd ed., (Orlando, Florida, 1983).

Sullivan JL, Saied SO, Layberry R, Cardwell MJ, Journal of Vacuum Science and Technology 16(4) (1998) 2567-2571.

Sullivan JL, Yu W, Saied SO, Surf. and Interf. Analysis 22 (1994) 515-519.

Sullivan JL, Yu W, Saied SO, Applied Surface Science 90 (1995) 309-319.

Surdu-Bob CC, Saied SO, Sullivan JL, Applied Surface Science 183 (2001) 126-136.

Surendra M, Plasma Sources Sci. Technol. (1995), 56-73.

Swart M, Auret FD, Goodman SA, Materials Science in Semiconductor Processing 3 (2000) 97-101.

Takuo S. Applications of Plasma Processes to VLSI Technology. From: Series Eds:

- Takuo S, New York, John Wiley & Sons. (1985).
- Tereshchenko OE, Chikichev SI, Terekhnov AS, Applied Surface Science 142 (1999) 75-80.
- Thurmond CD, Schwartz, Kammlot GW, Schwartz B, J. Electrochem. Soc 127(6) (1980) 1366-1371.
- Tone K, Yamada M, Ide Y, Katayama Y, Jpn. J. Appl. Phys 31 (1992) L721-L724.
- Tosi P, Bassi D, Brunetti B, Vecchiocattivi F, Internat. Journal of Mass Spectrometry and Ion Processes 149 - 150 (1995) 345-353.
- Tuck B, Introduction to Diffusion in Semiconductors, 2 nd ed., UK (1974).
- Turner MM, Journal of Physics 48 (1998) 59-69.
- Vasquez RP, Lewis BF, Grunthner FJ, Applied Physics Letters 42(3) (1983) 293-295.
- Ventzek PLG, Hoekstra RJ, KushnerMJ, J. Vac. Sci. Technol. B(12) (1994) 461-477.
- Vodjdani N, Parrens P, J. Vac. Sci. Technol. B 5(6) (1987) 1591-1598.
- Wagner CD, Riggs WM, Davis LE, Moulder JF, Handbook of x-Ray Photoelectron Spectroscopy, 2 nd ed., USA (1979).
- Webb AP, Wilkinson CDW, Vacuum 34(1-2) (1984) 159-162.
- Wei Y (1995). Ion bombardment induced compositional changes in compound semiconductor surfaces studied by XPS combined with LEISS. PhD. Aston University. UK.
- Wild C, Koidl P, J. Appl. Phys. 69(5) (1991) 2909-2917.
- Wilmsen CW. Oxidation of GaAs, Chichester (1989).
- Wolan JT, Mont CK, Hoflund GB, Applied Physics Letters 72 (1998) 1469.
- Yokoyama S, Inoue T, Yamakage Y, Hirose H, Proc. Inst. Phys. Conf. 79 (1985) 325-330.
- Ziegler JF, Biersack JP, Littmark U, The Stopping and Range of Ions in Solids, 2 nd ed., Chichester (1985).
- Zommer L, Lesiak B, Jablonski A, Gergely G, Menyhard M, Sulyok A, Gurban S, Journal of Electron Spectroscopy and Related Phenomena 87 (1998) 177-185.

**Published work**



Applied Surface Science 202 (2002) 183–198

applied  
surface science

[www.elsevier.com/locate/apsusc](http://www.elsevier.com/locate/apsusc)

## Surface compositional changes in GaAs subjected to argon plasma treatment

C.C. Surdu-Bob<sup>a</sup>, J.L. Sullivan<sup>a,\*</sup>, S.O. Saied<sup>a</sup>, R. Layberry<sup>a</sup>, M. Aflori<sup>b</sup>

<sup>a</sup>*Surface Science Group, School of Engineering and Applied Science, Aston University, Birmingham B47ET, UK*

<sup>b</sup>*Plasma Physics Department, A.I.I. Cuza University, Iasi 6600, Romania*

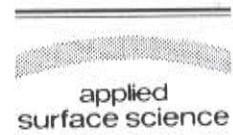


Aston University

Content has been removed due to copyright restrictions



Applied Surface Science 183 (2001) 126–136



[www.elsevier.com/locate/apsusc](http://www.elsevier.com/locate/apsusc)

## An X-ray photoelectron spectroscopy study of the oxides of GaAs

C.C. Surdu-Bob, S.O. Saied, J.L. Sullivan\*

*Surface Science Research Group, School of Engineering and Applied Science, Aston University,  
Aston Triangle, Birmingham B4 7ET, UK*

Received 27 March 2001; accepted 12 September 2001



**Aston University**

**Content has been removed due to copyright restrictions**